

Nonwoven Coalescing Fuel-Water Filter Media for Diesel Engines

Hamidreza Arouni

Submitted in accordance with the requirements for the degree of

Doctor of Philosophy

The University of Leeds

School of Design

June 2017

The candidate confirms that the work submitted is his own and that appropriate credit has been given where reference has been made to the work of others.

This copy has been supplied on the understanding that it is copyright material and that no quotation from the thesis may be published without proper acknowledgement

© 2013 The University of Leeds and Hamidreza Arouni

The right of Hamidreza Arouni to be identified as Author of this work has been asserted by him in accordance with the Copyright, Designs and Patents Act 1988.

Acknowledgements

Undertaking this PhD has been a life-changing experience for me and it would not have been possible to do it without the help of God and support and guidance that I received from many people.

Firstly, I would like to thank Prof Stephen Russell, my main supervisor, for his continued support, enthusiasm and guidance throughout this PhD. This work would not have been achievable without his guidance and feedbacks. I would also like to thank my second supervisor, Dr. Parikshit Goswami, academic advisor Prof Nik Kapur (School of Mechanical Engineering), and industrial advisor, Dr. Umer Farooq (Parker Racor Filter Division), for their advice, help and supports received through this collaborative work.

This research work benefited from financial and technical supports from Parker Hannifin Manufacturing (UK) Ltd., Racor Filter Division Europe (Dewsbury, UK) as the industrial advisor of the project, and I do appreciate their contribution during this research.

I wish to express my deepest appreciation and love to my parents, Davoud Arouni and Hamila Alidousti for their encouragement, inspiration and reassurance.

Finally, special thanks to my loving wife, Zohreh Gharaei, for her endless love and supports that kept me strong and motivated throughout this journey.

Abstract

Fuel-water filters are a promising solution for the removal of water from diesel fuel and frequently rely on a depth coalescing nonwoven medium and a barrier mesh. Water is a fuel contaminant that can cause severe damage to engine injectors by promoting corrosion and microbial growth. Coalescing water out of diesel fuel has become challenging because of the increasing amount of bio-diesel and performance enhancing additives that are present to meet emission control regulations. High water content and the reduction in interfacial tension (IFT) between the water and diesel are associated with formation of more stable emulsions and the generation of smaller water droplets that are harder to remove. This research systematically investigates the characteristics of bio-diesel and surfactant (monoolein) blends with standard diesel fuel, and explores the factors affecting the efficient removal of water from fuel by means of depth coalescing media composed of poly(butylene terephthalate) (PBT) meltblown fabrics. It was established that bio-diesel and monoolein do not influence the IFT of water in fuel in a comparable manner and the resulting water droplet size distributions (DSD) are substantially different, which has implications in terms of the interpretation of results from commonly used ISO and SAE standard test methods. Fuels blended with bio-diesel exhibited higher viscosity and water content than fuel freshly blended with monoolein. Online measurement of water droplet sizes revealed substantially smaller water droplets in bio-diesel blends compared to monoolein blends at the same IFT measured using offline tensiometry.

The surface wetting characteristics of PBT meltblown media were modified by alkaline hydrolysis independently of fabric geometric configuration and treated fabrics exhibited greater coalescence efficiencies (up to a 150% increase) but a lower quality factor than untreated samples due to a higher pressure drop attributed to increased water retention. The

optimal wetting behaviour of fibres for achieving maximal coalescence efficiency was not the same for reference diesel and fuel containing surfactant, i.e. monoolein. A universal filter medium with a high coalescence performance cannot therefore be readily achieved if based solely on tuning fibre wetting properties. It was found that the fundamental trade-off between coalescence efficiency and pressure drop could be addressed by dynamic modification of fabric porosity (from 93% to 98%). By enabling fabric dimensions and geometric configuration to be modified in forced flow conditions, improvements in both coalescence efficiency (up to a 150% increase) and quality factor (up to 99 times greater) compared to the control flat sheet filter samples were achieved for both bio-diesel and monoolein-blended fuels.

Table of contents

Acknowledgements	III
Abstract.....	IV
Table of contents	VI
List of Tables	XIII
List of Figures.....	XVII
List of Abbreviations	XXVI
1 CHAPTER 1 Introduction	1
1.1 Fuel filtration systems in diesel engines.....	3
1.2 Nonwoven fuel filter media.....	7
1.3 Challenges in the separation of water from standard diesel fuel	8
1.4 Aims and objectives	9
1.5 Dissertation layout.....	10
2 CHAPTER 2 Literature Review.....	12
2.1 Introduction	13
2.2 Diesel and bio-diesel fuels.....	13
2.2.1 Resources and compositions	13
2.2.2 Emission problems	15
2.2.3 Fuel specifications.....	15
2.3 Water-in-diesel emulsion.....	17
2.3.1 Formation of water-in-fuel emulsion in a fuelling system	18
2.3.1.1 Dissolved water in fuel.....	18
2.3.1.2 Free water in fuel	19
2.3.1.3 Emulsified water in fuel	20
2.3.2 Effective parameters on water droplet size in the emulsion.....	23
2.3.3 Destruction of the emulsion and phase separation	24
2.3.3.1 Droplet coalescence	25
2.3.3.2 Droplet settlement	26
2.3.4 Surfactants in the emulsion	27
2.3.4.1 Influence of surfactants on new droplets.....	28
2.3.4.2 Influence of surfactants on droplet stability	29
2.4 Separation of water from diesel fuel.....	30

2.4.1	Separation mechanisms: filtration and sedimentation	30
2.4.2	Nonwoven water separator media	32
2.4.2.1	Barrier type nonwoven water separator media.....	32
2.4.2.2	Transmissive coalescing type nonwoven water separator media.....	33
2.4.3	Filtration/Coalescing performance of nonwoven fuel-water separators.....	39
2.4.3.1	Separation efficiency.....	39
2.4.3.2	Quality factor	40
2.4.3.3	Coalescence efficiency.....	43
2.5	Existing filtration test procedures.....	44
2.5.1	BS ISO 4020:2001 procedure [101].....	45
2.5.2	ISO 16332:2006 procedure [48].....	47
2.5.3	SAE J1488 procedure [102]	50
2.5.4	SAE J1839 procedure [104]	51
2.6	Influential parameters on the water separation performance of nonwoven coalescing media 53	
2.6.1	Fuel and emulsion characteristics.....	53
2.6.2	Structure-property-performance relationships of nonwoven coalescence media	54
2.6.2.1	Properties of nonwoven fuel-water separation media	55
2.6.2.2	Fibre properties	56
2.7	Summary.....	59
3	CHAPTER 3 Fuel Characterisation.....	61
3.1	Introduction	62
3.2	Stock fuels and additives	63
3.3	Experimental methods and apparatus	64
3.3.1	Preparation of the test fuel blends	64
3.3.2	Interfacial tension (IFT) measurements.....	65
3.3.2.1	Experimental setup and procedure	67
3.3.3	Determination of water in fuel	68
3.3.3.1	Experimental setup and procedure	70
3.3.4	Determination of saturation level of dissolved water in fuel.....	71
3.3.4.1	Experimental setup and procedure	71
3.3.5	Density measurement	72
3.3.5.1	Experimental setup and procedure	73

3.3.6	Dynamic viscosity test.....	74
3.3.6.1	Experimental setup and procedure	75
3.4	Results and discussion.....	77
3.4.1	Interfacial tension (IFT) measurements.....	77
3.4.2	Water content and saturation level of dissolved water in fuel.....	79
3.4.3	Density and dynamic viscosity tests.....	81
3.5	Summary.....	84
4	CHAPTER 4 Water-in-Fuel Emulsion Characterisation.....	85
4.1	Introduction	86
4.2	Stock fuels and additives	87
4.3	Experimental methods and apparatus	87
4.3.1	Laser diffraction technology and particle sizing	87
4.3.1.1	Experimental setup and procedure	91
4.3.2	Refractive index measurement	92
4.3.2.1	Experimental setup and procedure	93
4.3.3	DSEP rating.....	94
4.3.3.1	Experimental setup and procedure	95
4.3.4	Water separation via the sedimentation test (water separability test)	97
4.3.4.1	Experimental setup and procedure	97
4.4	Development of the emulsion generation test rig.....	98
4.4.1	Design of the emulsion generation test rig.....	98
4.4.2	Construction of the emulsion generation test rig.....	100
4.4.2.1	Piping and hose fittings.....	100
4.4.2.2	Fuel tanks (F1 and F2)	100
4.4.2.3	Water reservoir (w)	101
4.4.2.4	Water injection valve (V) and the injector device.....	101
4.4.2.5	Adjustable pressure valve (PV).....	101
4.4.2.6	Pressure gauge (PG).....	101
4.4.2.7	Main pump (P)	101
4.4.2.8	Flowmeter (FM).....	102
4.4.2.9	Clean-up filters (CF)	102
4.4.2.10	Particle sizer device (M)	102
4.4.3	Commissioning the test rig.....	102

4.4.3.1	Pre-test procedure.....	102
4.4.3.2	Emulsion generation procedure.....	103
4.5	Results and discussion.....	104
4.5.1	Determination of the refractive index of the test fuels	104
4.5.2	Water droplet size distribution (DSD) in the test fuels	105
4.5.3	DSEP rating.....	121
4.5.4	Water separation via the sedimentation test	122
4.6	Summary.....	125
5	CHAPTER 5 Design and Construction of the Coalescence Test Rig.....	127
5.1	Introduction	128
5.2	Scope	128
5.3	Design of the new test rig.....	128
5.3.1	Filter housing design	129
5.3.2	Design of test system.....	135
5.3.3	Test liquids	137
5.3.4	Filter sample.....	137
5.3.5	Laboratory equipment	137
5.3.6	Rig frame design	138
5.3.7	Operating conditions and parameters for the test stand.....	139
5.3.7.1	Temperature	139
5.3.7.2	Total test duration	139
5.3.7.3	Volume of fuel	139
5.3.7.4	Test flow rate and filtration face velocity	139
5.3.7.5	Undissolved water concentration	140
5.3.7.6	Operating procedure.....	140
5.4	Construction of the test rig	140
5.4.1	Test stand tubing and fittings	141
5.4.2	Fuel tank (1)	142
5.4.3	Main pump (6).....	142
5.4.4	Water tank (2).....	143
5.4.5	Water pump (3)	143
5.4.6	Water flowmeter (4), and fuel flowmeters (5, 8).....	144
5.4.7	Adjustable valves (7, 14, 16).....	144

5.4.8	Sampler unites (9, 13, 17)	145
5.4.9	Parker test filter housing (10)	145
5.4.10	Manometer	148
5.4.11	Static mixer (12)	148
5.4.12	Clean-up filters	148
5.5	Test procedure	148
5.5.1	Pre-test preparation	149
5.5.2	Separation efficiency measurement	150
5.5.3	Coalescence efficiency test	152
5.6	Test stand validation	153
5.7	Summary	155
6	CHAPTER 6 Characterisation of Meltblown Depth Coalescence Fuel Filter Media	156
6.1	Introduction	157
6.2	Test filter media and test fuels	157
6.3	Experimental methods and apparatus	162
6.3.1	Determination of area density (GSM)	162
6.3.2	Calliper or thickness	162
6.3.3	Air permeability	163
6.3.4	Determination of density, bulk, solidity, and porosity of nonwovens	164
6.3.5	Pore size characterisation	165
6.3.6	Fourier transform infrared spectroscopy - attenuated total reflectance (FTIR - ATR)	167
6.3.7	Differential scanning calorimetry (DSC)	169
6.3.8	Scanning electron microscopy (SEM) and fibre diameter measurement	170
6.3.9	Determination of wetting tension of nonwoven strips	171
6.3.10	Separation performance evaluation	172
6.3.11	Coalescence performance evaluation	173
6.4	Results and discussions	173
6.4.1	Determination of area density (GSM)	173
6.4.2	Calliper or thickness	174
6.4.3	Air permeability	175
6.4.4	Determination of density, bulk, solidity, and porosity of benchmark media	177
6.4.5	Pore size characterisation	178

6.4.6	Fourier transform infrared spectroscopy - attenuated total reflectance (FTIR - ATR)	181
6.4.7	Differential scanning calorimetry (DSC)	188
6.4.8	Fibre diameter measurement	190
6.4.9	Determination of wetting tension of nonwoven strips	194
6.4.10	Separation performance evaluation	195
6.4.11	Coalescence performance evaluation	196
6.5	Summary	197
7	CHAPTER 7 Effects of Fibre Hydrophilicity and Meltblown Fabric Geometric Configurations on the Performance of Depth Coalescing Fuel Filter Media	199
7.1	Introduction	200
7.2	Test filter media and test fuels	200
7.3	Experimental methods and apparatus	201
7.3.1	Modification of the surface wettability	201
7.3.1.1	Wettability characterisation	202
7.3.1.2	Characterisation of treated and untreated nonwoven coalescing media	204
7.3.2	Effect of geometrical arrangement to the coalescing media	206
7.3.2.1	Double layer of PMB media operating in tandem with a filter support	207
7.3.2.2	Surface hairiness: single layer of PMB media with projecting surface fibres in tandem with a filter support	208
7.3.2.3	Static porosity: double layers of PMB media with a spacer in tandem with a filter support	209
7.3.2.4	Dynamic porosity: single layer of PMB media without filter support (bowing arrangement)	211
7.3.2.5	Results	212
7.3.3	configurational characterisation of the bowing configuration	212
7.3.4	Evaluation of coalescing performance: flat vs. bowing configurations	217
7.4	Results and discussion	218
7.4.1	Surface wettability modifications of the filter medium	218
7.4.2	Structural characterisation of the bowing configuration	230
7.4.3	Coalescing performance of new filter media arrangements	233
7.4.3.1	Alkali-treated PMB fabrics with increased wettability in a flat configuration	233
7.4.3.2	Untreated PMB filter fabrics in the bowing configuration	238
7.5	Summary	241

8	CHAPTER 8 Conclusions	243
8.1	General Conclusion	244
8.2	Recommendations for further work.....	249
9	Appendix (A) Source Tables of the Figures Presented In the Text.....	251
10	Appendix (B) Reinforcement of the Bowing Configuration.....	256
10.1	Dynamic porosity with back support: single layer of PMB media with upstream filter support	257
10.2	Local dynamic porosity: single layer of PMB media with reinforced configuration via local stitches	259
10.3	Results	260
11	References.....	262

List of Tables

Table 2-1: General requirements for automotive diesel and bio-diesel fuels [14]	17
Table 3-1: Fuel and fuels additives used in the project	63
Table 3-2: Description of the test fuel blends compositions.....	65
Table 3-3: Test fuel blends for the IFT measurement.....	67
Table 3-4: Test fuel blends for the water content measurement	70
Table 3-5: Test fuel blends for the determination of water saturation point	72
Table 3-6: Test fuel blends for the density measurement	73
Table 3-7: Test fuel blends for the viscosity measurement	75
of the bio-diesel and monoolein blends (source Table 3-8 in Appendix (A))	78
Table 4-1: Test fuel blends for DSD measurement	92
Table 4-2: Test fuel blends for the sedimentation test.....	97
Table 4-3: Refractive Indexes for test fuels.....	105
Table 4-4: Dv_{50} of dispersed water droplets in monoolein and bio-diesel blends at atmospheric pressure	111
Table 4-5: Dv_{50} of dispersed water droplets in monoolein and bio-diesel blends at the 4 bar pressure based on results presented in Figure 4-22 to Figure 4-29.....	115
Table 4-6: Dynamic DSEP of the test fuels	121
Table 4-7: Water separation/settlement in the test fuels (ml).....	123
Table 4-8: Visual assessment of water separation in fuel blends	124

Table 5-1: The validation results of the coalescence test rig	154
Table 6-1: Number of fabric windings in the test filter packs	158
Table 6-2: Layer specification of the WB filter.....	160
Table 6-3: Layer specification of the B16 filter.....	160
Table 6-4: Layer specification of the B41 filter.....	161
Table 6-5: Layer specification of the B45 filter.....	161
Table 6-6: Strip specification of the benchmark media	162
Table 6-7: filter Strips for the ATR-FTIR analysis	169
Table 6-8: Average GSM of the benchmark filter media	174
Table 6-9: Average GSM of strips of the benchmark filter media	174
Table 6-10: Average thickness of the benchmark filter media	175
Table 6-11: Average thickness of strips of the benchmark filter media	175
Table 6-12: Average air permeability of the benchmark filter media	176
Table 6-13: Average air permeability of strips of the benchmark filter media	176
Table 6-14: Density, bulk, solidity, and porosity of benchmark media.....	177
Table 6-15: Density, bulk, solidity, and porosity of strips of the WB medium.....	177
Table 6-16: Density, bulk, solidity, and porosity of strips of the B16, B41, and B45 media	178
Table 6-17: Average bubble point pore size of strips of the benchmark filter media	179
Table 6-18: Average mean flow pore size of strips of the benchmark filter media.....	179
Table 6-19: Average smallest detected pore size of strips of the benchmark filter media	180

Table 6-20: main FTIR spectra peaks for all coalescer layers (cm-1) (for codes see Table 6-6)	187
Table 6-21: Band assignment of main peaks of PET/PBT polymer	188
Table 6-22: Average fibre diameters of strips of the benchmark filter media (for codes see Table 6-6)	193
Table 6-23: Wetting energy test for the WB filter (for codes see Table 6-6)	194
Table 6-24: Wetting energy test for the B filters (for codes see Table 6-6)	194
Table 6-25: Separation efficiency of the benchmark filters measured in the flat configuration with the hydrophobic mesh using the REF diesel fuel	195
Table 6-26: Coalescence efficiency of the benchmark filters measured in the flat configuration using the REF diesel fuel without using the hydrophobic mesh	196
Table 7-1: Sample codes for the hydrolysis test conditions	202
Table 7-2: Samples prepared for wettability evaluations (for sample codes see: Table 7-1)	204
Table 7-3: Nonwoven characterisation test procedures	205
Table 7-4: Effect of different filter arrangements on the coalescence efficiency	212
Table 7-5: L/H values for test filter fabrics (for codes see: Table 7-1)	225
Table 7-6: Dimensional and structural properties of the filter fabrics (for codes see: Table 7-1)	226
Table 7-7: Bursting strength of the filter fabrics (b) (for codes see: Table 7-1)	226
Table 7-8: Coalescence efficiency of the filter fabric using 3D printed spacer filter support	230

Table 7-9: Structural measurement of the flat and bowed PMB media under dynamic conditions	232
Table 7-10: Coalescence efficiency of the untreated PMB in the flat configuration for different fuel blends	239
Table 7-11: Coalescence efficiency of the untreated PMB in the bowing configuration for different fuel blends	239
Table 9-1: Interfacial tension (IFT) of the test fuels	252
Table 9-2: Water content of the test fuels	252
Table 9-3: Water saturation level values of the bio-diesel blends	253
Table 9-4: Density values of test fuels at 25°C	253
Table 9-5: Kinematic and dynamic viscosity values of the test blends at 25°C	254
Table 9-6: Coalescence efficiency of the untreated and alkali-treated PMB media measured in the flat configuration using the REF diesel fuel (see Table 7-1 for the sample code)	254
Table 9-7: Coalescence efficiency of the untreated and alkali treated PMB media in the flat configuration using the M200 fuel (see Table 7-1 for the sample code)	255
Table 10-1: Effect of different filter arrangements on the average coalescence efficiency ..	260

List of Figures

Figure 1-1: Typical fueling system in heavy-duty vehicles [28, 29]	4
Figure 1-2: Typical fueling system in light-duty vehicles [28, 29]	5
Figure 1-3: Simple schematic of a typical single-stage separation fuel filter [29-34].....	6
Figure 1-4: Simple schematic of a typical double-stage separation fuel filter [29-34]	6
Figure 1-5: Simple schematic of a secondary fuel filter consisting of particle separator, coalescer, and barrier media [29-34]	7
Figure 2-1: Simple schematic of a high-pressure common rail (HPCR) fueling system: orange arrows show the fuel feeding direction and red arrows shows return of excess fuel to the tank	18
Figure 2-2: Change of water from the free (settled) state to the emulsified state in the fueling system	20
Figure 2-3: Schematic summary of the factors controlling successful coalescence: A) control of the movement of droplets; B) control of the velocity of droplets; C) Sufficient collision and residence time	26
Figure 2-4: Filtration mechanism [34, 77, 78].....	31
Figure 2-5: Simple schematic of a coalescing fuel filter: A) particulate separator compartment; B) water separator compartment.....	35
Figure 2-6: Three anticipated modes of droplet coalescence upon a fibre surface [92].....	37
Figure 2-7: Schematic of the ISO 4020 test rig [101].....	46
Figure 2-8: Schematic of the ISO16332 test rig [48].....	48

Figure 2-9: Schematic of the SAE J1488 test rig [102]	51
Figure 2-10: Schematic of the SAE J1488 test rig [104]	52
Figure 3-1: A) 100% Bio-diesel, B) Reference diesel fuel	64
Figure 3-2: Capillary-stoppered pycnometers density bottle	72
Figure 3-3: U-shape glass viscometers [132]	76
Figure 3-4: Controlling temperature bath set-up	76
Figure 3-5: IFT of the bio-diesel and monoolein blends (source Table 3-8 in Appendix (A))	78
Figure 3-6: Schematic of the interface of water and monoolein blends	79
Figure 3-7: Schematic of the interface of water and bio-diesel blends	79
Figure 3-8: Water content of the bio-diesel and monoolein blends (source table - Table 9-2 in Appendix (A))	80
Figure 3-9: Water saturation level of bio-diesel blends (source table - Table 9-3 in Appendix (A))	81
Figure 3-10: Density of the bio-diesel and monoolein blends (source table - Table 9-4 in Appendix (A))	82
Figure 3-11: Dynamic viscosity of the bio-diesel and monoolein blends (source table - Table 9-5 in Appendix (A))	83
Figure 4-1: Young's double slit experiment [134]	88
Figure 4-2: Light diffraction pattern on a spherical particle [134]	88
Figure 4-3: Light scattering angles for small and large particles [134]	89
Figure 4-4: Insittec Wet Malvern® particle size analyser	92

Figure 4-5: Refractometer setup and the theory of refraction index measurement	93
Figure 4-6: Microsep set-up.....	95
Figure 4-7: Schematic of the emulsion generation test rig	99
Figure 4-8: The final constructed emulsion generation test rig	100
Figure 4-9: DSD of the water phase in REF at atmospheric pressure	106
Figure 4-10: DSD of the water phase in B5 at atmospheric pressure	106
Figure 4-11: DSD of the water phase in B10 at atmospheric pressure.....	107
Figure 4-12: DSD of the water phase in B20 at atmospheric pressure.....	107
Figure 4-13: DSD of the water phase in B30 at atmospheric pressure.....	108
Figure 4-14: DSD of the water phase in B50 at atmospheric pressure.....	108
Figure 4-15: DSD of the water phase in B100 at atmospheric pressure.....	109
Figure 4-16: DSD of the water phase in M200 at atmospheric pressure.....	109
Figure 4-17: DSD of the water phase in M400 at atmospheric pressure.....	110
Figure 4-18: DSD of the water phase in M600 at atmospheric pressure.....	110
Figure 4-19: DSD of the water phase in M1000 at atmospheric pressure.....	111
Figure 4-20: D_{V50} for dispersed water droplets, related to the IFT of the monoolein and bio-diesel blends at atmospheric pressure	112
Figure 4-21: Effects of molar concentration of A) bio-diesel and B) monoolein in changing fuel-water interface characteristics in static and dynamic conditions	114
Figure 4-22: DSD of the water phase in REF at 4 bar pressure.....	116

Figure 4-23: DSD of the water phase in B10 at 4 bar pressure	116
Figure 4-24: DSD of the water phase in B20 at 4 bar pressure	117
Figure 4-25: DSD of the water phase in B30 at 4 bar pressure	117
Figure 4-26: DSD of the water phase in B50 at 4 bar pressure	118
Figure 4-27: DSD of the water phase in B100 at 4 bar pressure	118
Figure 4-28: DSD of the water phase in M200 at 4 bar pressure	119
Figure 4-29: DSD of the water phase in M400 at 4 bar pressure	119
Figure 4-30: Dv_{50} of dispersed water droplets at atmospheric and 4 bar pressures in monoolein and bio-diesel blends.....	120
Figure 5-1: Initial design of the filter housing.....	130
Figure 5-2: Design details of the outer flange of the filter housing.....	131
Figure 5-3: Design details of the inner flange of the filter housing.....	131
Figure 5-4: Design details of the main body of the filter housing.....	132
Figure 5-5: Design details of the new test filter housing with its three parts clamped together	132
Figure 5-6: Design details of the filter support (A) and barrier mesh (B).....	133
Figure 5-7: Housing configuration for the separation tests	134
Figure 5-8 : Housing configuration for the coalescence tests.....	134
Figure 5-9: Schematic of the coalescing test rig built in-house for the efficiency tests	135
Figure 5-10: Frame (trolley) of the coalescence test rig.....	138

Figure 5-11: The coalescence test rig	141
Figure 5-12: DSD of the water phase in REF at atmospheric pressure generated by the main fuel pump	143
Figure 5-13: Filter housing of the coalescence test rig	145
Figure 5-14: Steps for assembling/disassembling the filter housing	147
Figure 6-1: An example of the benchmark sample	158
Figure 6-2: Schematic of different strip arrangements when assembling the coalescence filters	159
Figure 6-3: Determination of mean flow pore size [34]	166
Figure 6-4: ATR-FTIR spectrum for WB filter - SB_{WB} strip (for codes see Table 6-6)	181
Figure 6-5: ATR-FTIR spectrum for WB filter - CM_{WB} strip (for codes see Table 6-6)	182
Figure 6-6: ATR-FTIR spectrum for WB filter - MB1 strip (for codes see Table 6-6)	182
Figure 6-7: ATR-FTIR spectrum for WB filter-MB2 strip (for codes see Table 6-6)	183
Figure 6-8: ATR-FTIR spectrum for WB filter - MB3 strip (for codes see Table 6-6)	183
Figure 6-9: ATR-FTIR spectrum for B filters - SB_B strip (for codes see Table 6-6)	184
Figure 6-10: ATR-FTIR spectrum for B filters - CM_B strip (for codes see Table 6-6)	184
Figure 6-11: ATR-FTIR spectrum for B filters - MB5 strip (for codes see Table 6-6)	185
Figure 6-12: ATR-FTIR spectrum for B filters - MB15 strip (for codes see Table 6-6)	185
Figure 6-13: ATR-FTIR spectrum for B filters - MB20 strip (for codes see Table 6-6)	186
Figure 6-14: ATR-FTIR spectrum for B filters - MB30 strip (for codes see Table 6-6)	186

Figure 6-15: DSC graph for SB _{WB} strip (for codes see Table 6-6)	189
Figure 6-16: DSC graph for MB30 strip (for codes see Table 6-6)	189
Figure 6-17: SEM images of the WB filter strips (for codes see Table 6-6).....	191
Figure 6-18: SEM images of the B series sample strips (for codes see Table 6-6)	192
Figure 7-1: Control filter sample arrangement in the filter housing for the coalescence efficiency test	207
Figure 7-2: Single (control) and double layer filter assemblies operating with a support layer	207
Figure 7-3: Single (control) layer filter assembly with a hairy surface operating with a support layer.....	209
Figure 7-4: Generation of a ‘gap in between’ arrangement using a porous spacer disk.....	210
Figure 7-5: Bowing arrangement	211
Figure 7-6: 3D printed convex filter supports.....	213
Figure 7-7: Modified filter housing to aid visualisation of the bowing arrangement.....	213
Figure 7-8: 3D printed flat filter supports.....	214
Figure 7-9: detailed design of the filter housing for the bowing characterisations	215
Figure 7-10: Methodology used to capture the bowed filter fabric configuration under dynamic flow conditions.....	216
Figure 7-11: Measuring flag used for measuring for concave deformation of the medium ..	217
Figure 7-12: Wetting curves and repellency of the untreated PMB samples in REF diesel and distilled water respectively (see Table 7-1for the sample code).....	219

Figure 7-13: Wetting curves and repellency of the PMB-0-40 in REF diesel and distilled water respectively (see Table 7-1 for the sample code).....219

Figure 7-14: Wetting curves of the PMB-0.25-40 in distilled water and REF diesel (see Table 7-1 for the sample code)220

Figure 7-15: Wetting curves of the PMB-1-40 in distilled water and REF diesel (see Table 7-1 for the sample code)220

Figure 7-16: Wetting curves of the PMB-3-35 in distilled water and REF diesel (see Table 7-1 for the sample code)221

Figure 7-17: Wetting curves of the PMB-3-40 in distilled water and REF diesel (see Table 7-1 for the sample code)221

Figure 7-18: Wetting and repellency slopes of the untreated PMB samples in REF diesel and distilled water respectively (see Table 7-1 for the sample code).....222

Figure 7-19: Wetting and repellency slopes of the PMB-0-40 in REF diesel and distilled water respectively (see Table 7-1 for the sample code).....222

Figure 7-20: Wetting slope of the PMB-0.25-40 in distilled water and REF diesel (see Table 7-1 for the sample code)223

Figure 7-21: Wetting slope of the PMB-1-40 in distilled water and REF diesel (see Table 7-1 for the sample code)223

Figure 7-22: Wetting slope of the PMB-3-35 in distilled water and REF diesel (see Table 7-1 for the sample code).....224

Figure 7-23: Wetting slope of the PMB-3-40 in distilled water and REF diesel (see Table 7-1 for the sample code)224

Figure 7-24: SEM images of the untreated PMB sample (see Table 7-1for the sample code)
.....227

Figure 7-25: SEM images of the PMB-0-40 sample (see Table 7-1for the sample code).....227

Figure 7-26: SEM images of the PMB-0.25-40 sample (see Table 7-1for the sample code)228

Figure 7-27: SEM images of the PMB-1-40 sample (see Table 7-1for the sample code).....228

Figure 7-28: SEM images of the PMB-3-35 sample (see Table 7-1for the sample code).....229

Figure 7-29: SEM images of the PMB-3-40 sample (see Table 7-1for the sample code).....229

Figure 7-30: Magnitude of filter deformation during the bowing arrangement observed in the
water flow-through experiment.....231

Figure 7-31: Changes in the thickness of the PMB medium as a result of the bowing
deformation: performed at air pressure and velocity of A) 11.9 mbar and 44 cm/s, B) 370 Pa
and 18 cm/s232

Figure 7-32: Effect of wettability (L/H) on coalescence efficiency of the PMB media using
REF diesel fuel (source Table 9-6 in Appendix (A)).....233

Figure 7-33: Effect of wettability (L/H) on pressure drop of the PMB media using REF diesel
fuel (source Table 9-6 in Appendix (A))234

Figure 7-34: Effect of wettability (L/H) on quality factor of the PMB media using REF diesel
fuel (source Table 9-6 in Appendix (A))234

Figure 7-35: Effect of wettability on coalescence efficiency of the PMB media using M200
fuel (source Table 9-7 in Appendix (A))235

Figure 7-36: Effect of wettability on pressure drop of the PMB media using M200 fuel (source Table 9-7 in Appendix (A))	235
Figure 7-37: Effect of wettability on quality factor of the PMB media using M200 fuel (source Table 9-7 in Appendix (A))	236
Figure 7-38: Schematic of the water droplet interactions that are believed to take place with fibre surfaces of low (a), high (b), and medium (c) hydrophilicity, when immersed in REF diesel fuel. Where, γ_{fd} , γ_{fw} , γ_{wd} , WA, and WS are the interfacial tensions of fibre-diesel, fibre-water, water-diesel, work of adhesion, and work of spreading respectively	237
Figure 7-39: Schematic of water droplet interactions with the fibre surface with a low (a), high (b), and medium (c) hydrophilicity, immersed in a monoolein blended diesel fuel (M200), where γ_{fd} , γ_{fw} , γ_{wd} , WA, and WS are the interfacial tension of fibre-diesel, fibre-water, water-diesel, work of adhesion, and work of spreading respectively	238
Figure 7-40: Comparison between coalesced water droplets coming off the flat and bowing filter configurations at a same filtration test condition	241
Figure 10-1: Design details of the filter support.....	257
Figure 10-2: Dynamic porosity arrangement with back support	258
Figure 10-3: The bowing configuration in dynamic porosity arrangement with back support	258
Figure 10-4: Local dynamic porosity arrangement.....	259
Figure 10-5: The bowing configuration in local dynamic porosity arrangement	260

List of Abbreviations

B5, B10, B15, B20, B30, B50, B100

Bio-diesel fuel blends (blend of different percentage of bio-diesel in reference diesel)

CN

Cetane number..... 14

DSC

Differential scanning calorimetry:.....162, 169, 181, 188, 189, 197, 247

DSD

Droplet size distribution:IV, 23, 45, 86, 87, 92, 98, 99, 102, 103, 104, 105, 106, 107, 108, 109, 110,
111, 112, 114, 116, 117, 118, 119, 125, 126, 136, 142, 143, 145, 245, 246

DSEP

Determination of separation characteristics:50, 52, 94, 95, 96, 121, 125, 126, 245, 246

EPA

Environmental Protection Agency: 2

FAMEs

Fatty Acid Methyl Esters: 14

FTIR

Fourier transform infrared spectrometer: 162, 167, 168, 169, 181, 182, 183, 184, 185, 186, 187, 188,
190, 197, 247

HPCR

High-pressure common-rail injection system:.....2, 3, 4, 10, 18, 35, 55

IFT

Interfacial Tension:IV, 9, 17, 19, 24, 26, 27, 28, 36, 37, 39, 45, 46, 47, 48, 50, 53, 54, 62, 64, 65, 66, 67,
68, 77, 78, 79, 84, 86, 98, 102, 112, 113, 125, 126, 137, 149, 155, 172, 244, 245, 246, 252

M200, M400, M600, M100	
Monoolein fuel blends (blend of different percentage of monoolein in reference diesel)	
OEMs	
Original Equipment Manufacturers:.....	3, 4, 32, 244
PA	
Poly(amide):	8, 33
PBT	
Poly(butylene terephthalate): ...IV, 8, 10, 33, 157, 164, 187, 188, 189, 197, 200, 201, 230, 241, 247, 249	
PET	
Poly(ethylene terephthalate):.....	8, 33, 57, 133, 157, 158, 164, 181, 187, 188, 189, 197
PM	
Particulate matter:	2, 15
QF	
Quality factor:	40, 198, 247
REF diesel	
Reference grade diesel fuel:	XV, XVI, XXII, XXIII, XXIV, XXV, 82, 195, 196, 200, 204, 206, 212, 218, 219, 220, 221, 222, 223, 224, 233, 234, 237, 242, 248, 254, 260
SEM	
Scanning electron microscopy:	170, 190, 191, 192, 205, 225, 227, 228, 229, 230
ULSD	
Ultra-Low Sulphur Diesel:	2, 16, 35, 50, 54, 57, 63

CHAPTER 1

Introduction

In a compression-ignition diesel engine, fuel is combusted as it is injected into compressed air within the combustion chamber of the system [1, 2]. The main concern associated with diesel fuel combustion is the emission of hazardous air pollutants such as sulphur oxides (SO_x), nitrogen oxides (NO_x), carbon monoxide (CO), carbon dioxide (CO₂), unburned polycyclic aromatic hydrocarbons (PAH), and particulate matter (PM), because of the potential human and environmental health risks [3-9]. As a result, the United States Environmental Protection Agency (EPA) and the council of the European Union have established stringent emission control regulations. These include Tier 4 [3], Euro 6 [5], and Euro VI [4] regulations that have resulted in major technological advancements in engine design as well as improvements in fuel quality.

A high-pressure common-rail injection system (HPCR) is state of the art in modern high efficiency diesel engines because it enables complete and clean combustion. In HPCR injection systems, the clearances for fuel injection have reduced to micro-scale dimensions. The clearance can be as small as 5µm and the spray hole diameter within the injector may only be 150 µm. During operation, many microlitres of fuel are injected, multiple times in every combustion cycle of the engine at very high pressures of about 2500 bar [10-13]. Moreover, in accordance with the regulations, fuel suppliers are obliged to provide standard grade diesel fuel with a reduced sulphur content. The current EN 590 fuel is a standard grade diesel fuel whose composition and specifications are regulated based on BS EN 590:2013 [14]. The EN 590 diesel fuel is composed of Ultra-Low Sulphur Diesel (ULSD), with a sulphur content of 10 ppm (m/m), up to 7% (v/v) bio-diesel, and a variety of fuel performance enhancement additives.

The high operating pressure and small tolerances of a modern HPCR injection system make it vulnerable to damage or malfunction if fuel contaminants such as water are present [10-13, 15-17]. The presence of water in a fuel system can cause serious damage to fuel lines, pumps, and the injection system itself [1, 2, 12, 13, 15-19]. It can serve as an electrolyte causing corrosion, which may be exacerbated by the dissolution of other chemicals in the fuel. Water also promotes bacterial growth at its interface with the fuel leading to the formation of biological sludge and sediments. Moreover, if water is trapped in small cracks in the engine components and then expands rapidly on heating, wear and equipment failure can ensue. Water is present in diesel fuel as a remnant of fuel refining or it can enter the vehicle fuel tank from the outside environment, for example during re-fuelling of the vehicle, or through humidity and condensation. A threshold of 200 *ppm* (*v/v*) total water content in diesel fuel is defined by the EN 590 standard as an acceptable level by the Original Equipment Manufacturers (OEMs) in both Europe and North America [11, 20]. However, in practice the total water content of diesel measured in the tank of a vehicle can substantially exceed this threshold, with values as high as 5000 (*v/v*) *ppm* being reported [11, 21]. It is also known that the presence of bio-diesel in standard fuel increases the overall water content of the fuel because it is more hygroscopic than mineral diesel, with a greater affinity to water [20, 22-27]. Therefore, to avoid the possibility of damage, water separation is required in the fuel circuit to reduce the maximum total water content to a value below 200 *ppm*, before it reaches the injection system of the engine.

1.1 Fuel filtration systems in diesel engines

From the late 1990's, water separation systems in diesel engines have developed rapidly, achieving high efficiencies of >95%, in accordance with the pressing needs of the Original

Equipment Manufacturers (OEMs) to minimise the total water content reaching the injection system by maintaining the water content below 200 ppm [11, 20]. A typical HPCR fuelling system of a diesel engine comprises fuel lines, a transfer pump that moves fuel from the fuel tank to the lines, fuel filters, a high pressure pump to feed the high pressure fuel lines and the injection system. The rail system connects to the fuel injectors. Simple schematics of commercially employed systems found in heavy-duty and light-duty vehicles are shown in Figure 1-1 and Figure 1-2 respectively [28, 29].

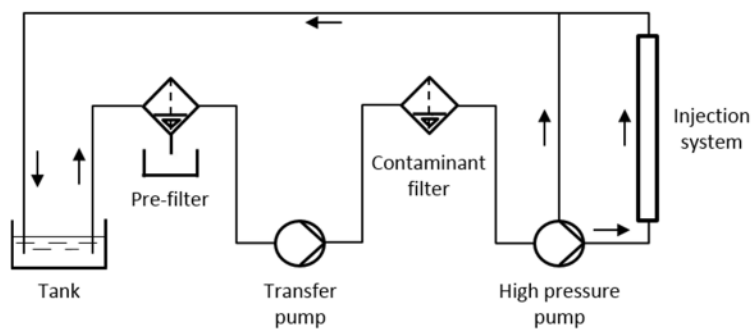


Figure 1-1: Typical fueling system in heavy-duty vehicles [28, 29]

Heavy-duty engines used in for example, buses and trucks, usually have two filters. A water separator is placed at the suction side of the fuel pump (pre-filter or primary filter), and a contaminant filter is placed on the pressure side of the pump to separate hard particulate contaminants. By contrast, in light-duty engines, a single filter is employed to separate both water and particles at the pressure side of the fuel pump, which is known as a secondary filter.

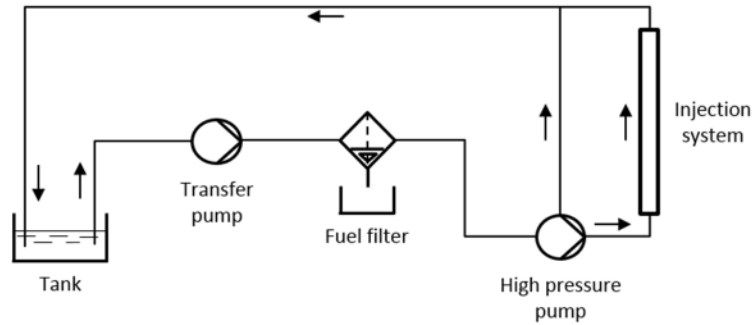


Figure 1-2: Typical fueling system in light-duty vehicles [28, 29]

Water separator filters commonly adopt one of two main separation mechanisms and nonwoven fabrics are commonly encountered in both [29-34]:

(a) Single stage separation – shown in Figure 1-3, this involves a hydrophobic barrier medium to separate water droplets by surface filtration or,

(b) Double stage water separation – shown in Figure 1-4, this involves a two-step process in which water droplets are first captured and coalesced in a depth coalescing medium and then a hydrophobic barrier medium is used on the downstream side of the coalescer to separate enlarged water droplets from the fuel stream.

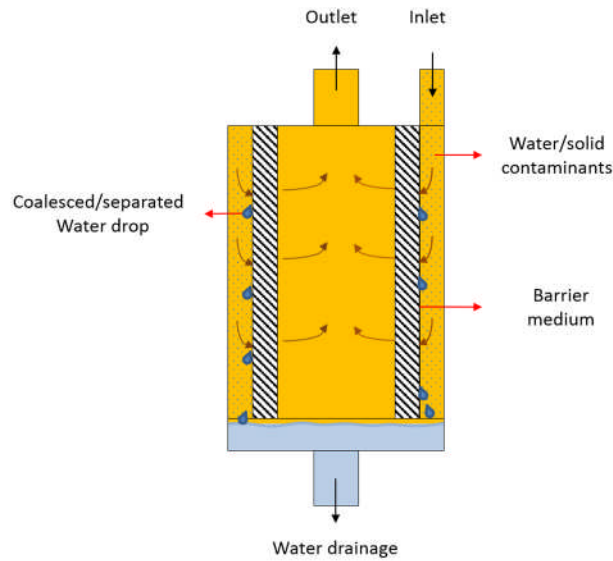


Figure 1-3: Simple schematic of a typical single-stage separation fuel filter [29-34]

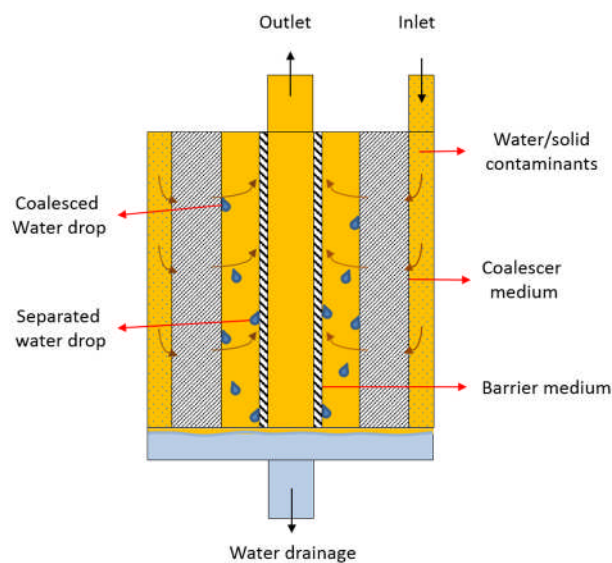


Figure 1-4: Simple schematic of a typical double-stage separation fuel filter [29-34]

In the single stage system, hard particulate matter present in the fuel is removed by the barrier medium, which can affect its performance, whilst in the double stage system the particles are

captured by the coalescer before they reach the barrier medium. In some other filter configurations, another pleated medium may be placed upstream of the barrier and coalescer media to function as a hard particle separator (Figure 1-5).

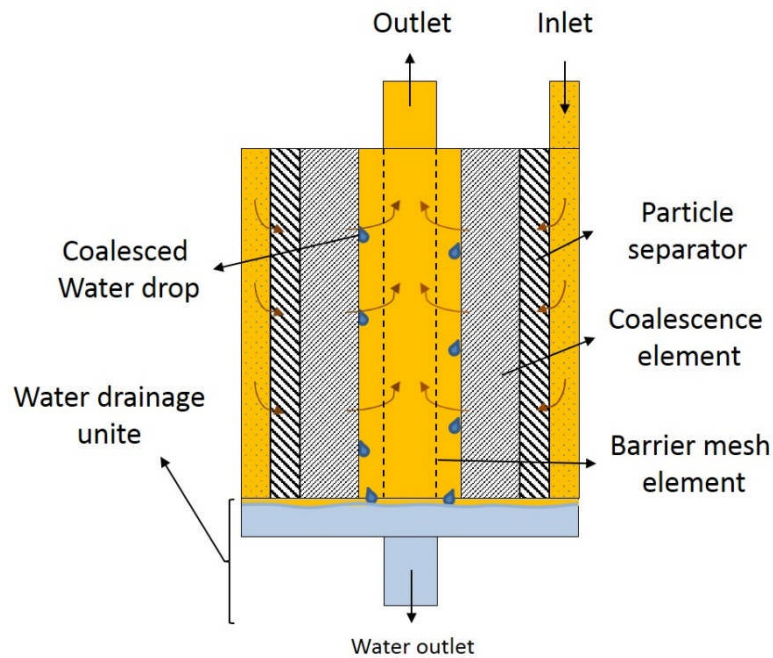


Figure 1-5: Simple schematic of a secondary fuel filter consisting of particle separator, coalescer, and barrier media [29-34]

Commercially, the double/three stage water separation configuration has become more attractive because of the superior coalescence performance resulting from the 3D structure and the higher solid surface area that is provided by the thickness of the depth medium [28, 29].

1.2 Nonwoven fuel filter media

Nonwoven filter media are extensively used in liquid and fuel filtration [34]. Nonwoven fabrics are highly porous and are composed of directionally or randomly oriented fibres, which depending on their diameter, can provide a high solid surface area for capturing impurities from a fluid stream [16, 17, 34-46]. Production of nonwoven fabrics consists of two main steps

[45]: web formation in which uniform assemblies of fibres or filaments are manufactured in sheet form, followed by mechanical, thermal or chemical bonding. One of the attractive aspects of nonwoven fabrics is their ability to be structurally modified during manufacture to modulate porosity, fibre dimensions, fibre orientation, pore size distribution and intrinsic permeability. Nonwoven fabrics used as barrier media in pre-filters commonly have a higher porosity than do secondary filter fabrics. This is because of the pre-filter is closest to the fuel tank and is exposed to a greater quantity of contaminants compared to secondary filters. The higher porosity therefore helps to promote a longer operational lifetime and also avoids a high pressure drop in the system by minimising flow resistance. The pre-filter is traditionally made of a pleated cellulosic wetlaid nonwoven with a silicon-based hydrophobic surface treatment [34]. Secondary filters responsible for removing water, are usually exposed to a higher temperature, pressure and also finer water droplets compared to the pre-filters, because by this stage the contaminated fuel has passed the transfer pump in which it is subjected to shear stress. These filters contain nonwoven fabrics whose role is specifically to capture and coalesce free water in the fuel by exploiting the thickness or ‘depth’ of the fabric to provide multiple surfaces to remove the contaminant. These filters typically comprise multiple layers of meltblown nonwoven fabric to remove small water droplets and are composed of synthetic polymers comprising of poly(amide) (PA); poly(butylene terephthalate) (PBT), or poly(ethylene terephthalate) (PET).[34].

1.3 Challenges in the separation of water from standard diesel fuel

The nonwoven coalescing medium in the water separation filter may be considered as the heart of the filter. Its function is to capture small (millimetre and micron-scale) diameter water droplets from the main fuel stream and facilitate their coalescence to form larger droplets that

are easier to separate by the barrier medium of the filter. This functionality can be challenging to maintain if the water content of the fuel is high and water droplets are either very small or stabilised in the fuel as an emulsion. This challenging situation increasingly exists in the real world due to presence of bio-diesel and fuel additives in standard diesel fuel composition. Bio-diesel molecules typically have R-C-O polymeric backbones which makes them amphiphilic and capable of absorbing humidity in ambient air. Their presence reduces the interfacial tension (IFT) of water and bio-diesel in the same way as a surface active agent (surfactant) [12, 13, 15-17, 47-50]. The presence of bio-diesel therefore results in a higher water content and the stabilisation of much smaller diameter water droplets compared to those present in mineral diesel fuel. Moreover, the presence of bio-diesel can affect the surface tension of the fibres in the filter, which can potentially adversely affect the performance of the coalescing medium [12]. Therefore, improved methods capable of enhancing the coalescence efficiency of nonwoven filters are urgently required to ensure water-free fuel can continue to be delivered to high sensitive fuel injection systems in modern diesel engines.

1.4 Aims and objectives

The main aim of this research is to systematically understand underlying relationships between coalescing fuel filter performance and fabric properties using fuel blends containing bio-diesel and/or surfactants. The specific objectives are:

- a) To characterise modern fuels blended with bio-diesel and surfactants to develop an understanding of how bio-diesel and surfactant content affects fuel properties.
- b) To characterise emulsions containing water and fuels blended with bio-diesel and surfactants in terms of water droplet size and resistance to coalescence, to develop an understanding of how bio-diesel and surfactants affect the emulsion properties.

- c) To design, build, and develop a lab scale coalescence test rig to measure coalescence performance of a flat sheet nonwoven fabric in water-in-fuel emulsions containing bio-diesel and surfactants in conditions that simulate real world conditions.
- d) To evaluate depth coalescing fuel filter media composed of poly(butylene terephthalate) (PBT) meltblown fabrics to study their coalescing performance and pressure drop, using the purpose-built coalescing test rig.

1.5 Dissertation layout

This thesis is divided into chapters, which focus on understanding the behaviour of the fuel and water blends, as well as the study of the factors affecting coalescence performance in meltblown fabrics relevant to industrial use.

- Chapter 1 explains the importance of water separation in modern HPCR diesel engines, the role of nonwoven coalescing filters in water separation and the aims and objectives of the research.
- Chapter 2 provides a critical review of literature on the coalescence process, nonwoven coalescing filters as well as the instrumental methods employed to study the coalescence performance of filters.
- Chapter 3 details the experimental methodology and results of the fuel characterisation study.
- Chapter 4 details the experimental approaches and results of water-in-fuel emulsion characterisations, in terms of water droplet sizes and their resistance to coalescence in diesel fuel blended with bio-diesel/surfactant.

- Chapter 5 explains the design and construction of a lab scale coalescence test rig to enable analysis of the separation/coalescence behaviour of flat sheet nonwoven filter media.
- Chapter 6 details the characterisation of nonwoven coalescence depth filter media as part of a benchmark study.
- Chapter 7 discusses experimental methodologies and results regarding the enhancement of coalescing performance in nonwoven media in relation to wettability and fabric geometry.
- Chapter 8 summarises the main findings and provides recommendations for further work.

CHAPTER 2

Literature Review

2.1 Introduction

The purpose of this chapter is to critically review the relevant science and technology in the area of fuel-water separation and coalescence relevant to the experimental work that follows. To provide a contextual background, this includes a review of parameters known to affect separation of water from diesel fuel using coalescing filter media.

2.2 Diesel and bio-diesel fuels

In compression-ignition engines such as diesel engines, fuel combustion occurs due to the injection of diesel fuel into compressed air in the combustion chamber [1, 2]. In diesel systems, compared to petrol powered engines, a greater volume of air is introduced to the fuel as combustion occurs and consequently high thermal efficiency is achieved. Specifically, this means the ratio of power output at the flywheel of the engine to the theoretical power available from the combustion of the fuel is greater [1]. Understanding the characteristics of diesel fuel is also important because it affects the ability to coalesce water that may be contained within it. For this reason, it is instructive to briefly review its composition.

2.2.1 Resources and compositions

Diesel fuel is one of the refinery products of crude oil produced via fractional distillation and cracking processes in which heavy and long hydrocarbon molecules are broken down to lighter and shorter ones [51]. Diesel fuel is composed of a mixture of straight-chain saturated alkanes, branched alkanes, aromatics and sulphur- and nitrogen-containing compounds [1, 22-24, 51, 52]. Moreover, diesel can contain contaminants such as dirt and water picked up during transportation and storage [18]. The ignition quality of diesel is graded by the cetane number

(CN). For instance, a fuel having CN=50 has the same ignition quality as a mixture of alpha-methyl-naphthalene ($C_{11}H_{10}$) having the poorest ignition quality (CN=0) with a 50% (v/v) of cetane ($C_{16}H_{34}$) with the highest initiation quality (CN=100) [51]. The required fuel CN for high speed engines is in the range of 45-50, i.e. equivalent to the ignition of a mixture of $C_{11}H_{10}$ with 45%-50% cetane (v/v), and for railway vehicles it is about 30 [1, 51]. Production of diesel fuel is easier than petrol fuel and it can provide higher energy than petrol (35.86 MJ/L vs. 32.18 MJ/L) and it is less volatile [53].

Bio-diesel is the term given to Fatty Acid Methyl Esters (FAMEs), which yield CNs of ≈ 50 , and possess sufficient lubricity to be used in diesel engines [22-27]. Bio-diesel is typically produced by trans-esterification of ethanol and oilseed crops (vegetable oils), both of which usually originate from edible feedstock [22-27]. Concerns about the food-fuel conflict in bio-diesel production have led to development of “renewable” fuels which are mostly based on ethanol and lipids from inedible feedstock produced by processes such as fermentation, fisher-tropsch, or hydrotreatment [22-24]. Bio-diesel and renewable fuels have been very successful in controlling emissions, however, there are still concerns about bio-diesel in terms of its viscosity, low-temperature behaviour, degradability in storage and compatibility with infrastructure and after-treatment devices [22-27].

The typical composition of bio-diesel fuels is methyl palmitate ($C_{17}H_{34}O_2$), methyl stearate ($C_{19}H_{38}O_2$), methyl oleate ($C_{19}H_{36}O_2$), methyl linoleate ($C_{19}H_{34}O_2$), and methyl linolenate ($C_{17}H_{32}O_2$) [54]. The proportions by mass of these components depends on the origin of the bio-fuel. For instance, soybean bio-diesel contains 20-30% methyl oleate, whilst rapeseed bio-diesel (RME) contains up to 60%.

2.2.2 Emission problems

Air pollution emissions are one of main concerns relating to use of mineral diesel fuel in engines. Emissions of sulphur oxides (SO_x), nitrogen oxides (NO_x), carbon monoxide (CO), carbon dioxide (CO₂), hydrocarbons (HC), and particulate matter (PM) in diesel exhausts is known to lead to serious human and environmental risks via creation of smog, acidic rain and haze [3].

Diesel fuel does not evolve lead emissions like petrol and it emits lower greenhouse gases such as CO, CO₂ (137-178 *g/kg* vs. 158-269 *g/kg*) and NO_x (0.28-0.46 *g/kg* vs. 0.10-0.22 *g/kg*) compared to petrol [55]. However, emission of fine particles, including those with a diameter less than 2.5 micron (PM_{2.5}), in the diesel exhausts is much higher than in petrol (0.015 - 0.049 *g/kg* vs. 0.003 – 0.004 *g/kg*). Such small particles can penetrate deep into the lungs and cause serious health problems [55]. Particulate matter (soot) in diesel exhaust includes aerosols formed via reactions between sulphur dioxide and nitrogen oxides containing compounds, combustion particles as well as re-condensed organic and metallic vapours. The advent of bio-diesel is the result of a desire to overcome the mineral diesel risks to ambient air quality [22-27]. Compared to mineral diesel, bio-diesel molecules have extra oxygen atoms such that carbon atoms have a higher oxidised rate and therefore there is a lower carbon monoxide (CO) content in bio-diesel exhaust fumes [54].

2.2.3 Fuel specifications

BS EN 590:2013 and ASTM D975-16A are the European and American standards respectively that specify diesel fuel requirements. The EN590 standard was introduced in 1993 (EN590) to ensure standard diesel fuel (EN590) for on-road diesel engine vehicles is free of ash as well as heavy hydrocarbon fractions. The specifications of EN590 are regularly reviewed [14]. The

latest version of the standard, EN590:2013, suggests using Ultra-Low Sulphur Diesel (sulphur content of 10 *ppm (m/m)*), up to 7% (*v/v*) bio-diesel, and variety of performance enhancer additives as the main components [14]. ASTM D975 was also introduced in 1993 and defines different diesel fuel grades for both off-road and on-road applications. This standard classifies diesel as “diesel No.1” with sulphur contents of 15 *ppm (m/m)* (grade No. 1-D S15), 500 *ppm (m/m)* (grade No. 1-D S500), or 5000 *ppm (m/m)* (grade No. 1-D S5000); “diesel No.2” with sulphur contents of 15 *ppm (m/m)* (grade No. 2-D S15), 500 *ppm (m/m)*, (grade No. 2-D S500), or 5000 *ppm (m/m)* (grade No. 2-D S5000) and “diesel No.4” (Grade No. 4-D).

Grade 2-D diesel is generally less volatile, denser and of higher viscosity than grade 1-D, and is more commonly used in both off-road and on-road applications. Diesel 2-D S15 (maximum 15 *ppm (m/m)* sulphur) is known as the ultra-low sulphur diesel (ULSD) while diesel 2-D S500 (maximum 500 *ppm (m/m)* sulphur) is referred to as low sulphur diesel fuel.

Hydrodesulphurisation is the process used to reduce sulphur content of the fuel from 2000 *ppm (m/m)* to 10 *ppm (m/m)* according to the EN590 specification in order to produce ULSD fuel. This process results in the removal of some of the oxygen and nitrogen containing compounds which negatively affect the fuel lubricity [14]. Based on EN590 standards, other additives in addition to bio-diesel are being added to the ULSD fuel to improve fuel properties such as lubricity, compressibility, cold flow and oxidation stability, etc. [14]. Improving the lubricity of the fuel is another advantage of blending bio-diesel as a renewable compound [22-27].

Bio-diesel which is blended with EN590 diesel has to meet minimum requirements provided by BS EN 14214:2012+A1:2014 or ASTM D6751 - 15CE1 as standard specifications for bio-

diesel fuel blend stock (B100). Table 2-1 shows key general specifications of mineral diesel and bio-diesel based on the BS EN 590:2013 and BS EN 14214:2012 respectively.

Table 2-1: General requirements for automotive diesel and bio-diesel fuels [14]

Property	Unit	Mineral diesel		Bio-diesel		Test method
		(BS EN 590:2013)		(BS EN 14214:2012)		
		Minimum	Maximum	Minimum	Maximum	
Cetane number (CN)		51.0	-	51.0	-	EN ISO 5165
Density at 15 °C	<i>kg/m³</i>	820.0	845.0	860.0	900.0	EN ISO 3675
Sulphur content	<i>mg/kg</i>	-	10	-	10	EN ISO 20846
Water content	<i>mg/kg</i>	-	200	-	500	EN ISO 12937
Viscosity at 40 °C	<i>mm² /s</i>	2.0	4.5	3.5	5.0	EN ISO 3104
FAMES content	<i>% (v/v)</i>	-	7	96.5	-	EN 14078

Fuel additives in EN590 fuel are known to act as surface active agents (surfactants) which are amphiphilic and able to lower the interfacial tension, IFT, of oil/water emulsion phases as well as form aggregates such as micelles or liquid crystals in the high concentration [12, 56-59]. Bio-diesel molecules typically have R-C-O polymeric backbones which make them amphiphilic molecules capable of absorbing humidity from the ambient air as well as lowering the interfacial tension (IFT) of the water-bio-diesel, in the same way as a surfactant [12, 13, 15-17, 47-50]. This results in a higher water content in bio-diesel compared to mineral diesel.

2.3 Water-in-diesel emulsion

Water can contaminate diesel and must be separated before it reaches the injection system of the engine to avoid wear, corrosion of the engine components as well as filter plugging

resulting from bacterial growth [1, 2, 12, 13, 15-19]. This section discusses the challenge posed by water in the engine and the impact on water separator filter elements.

2.3.1 Formation of water-in-fuel emulsion in a fuelling system

Figure 2-1 shows a simple schematic of a fuelling system in a diesel engine equipped with a high-pressure common-rail fuelling system (HPCR).

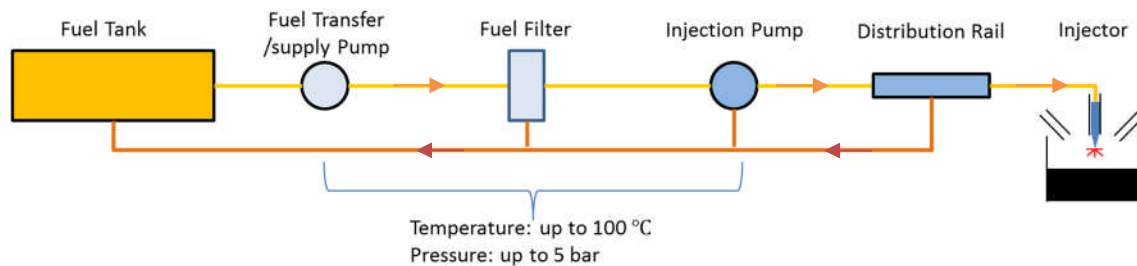


Figure 2-1: Simple schematic of a high-pressure common rail (HPCR) fuelling system: orange arrows show the fuel feeding direction and red arrows shows return of excess fuel to the tank

The system is composed of a fuel tank, low pressure fuel pump, fuel filter, high-pressure injection pump, and high pressure common rail injection parts including injectors [12, 13, 15-17]. Water in the fuelling system can take three forms (Figure 2-2): dissolved water, free (settled) water, or emulsified water, depending on circumstances [12, 30, 58-60].

2.3.1.1 Dissolved water in fuel

A water molecule is a polar molecule due to an uneven distribution of electrons, whilst diesel fuel is composed of nonpolar molecules which do not have charged regions. Hence, mineral diesel fuel dissolves only very slightly in water such that the two liquids are immiscible [32, 58, 61, 62]. Bio-diesel is more hygroscopic than mineral diesel and has affinity to water due to the presence of alkyl-esters and its unsaturated molecular structure [20, 22-27, 54]. This increases the water content of the fuel such that BS EN 14214:2012 has defined a higher

threshold of 500 ppm (v/v) for the water content of pure bio-diesel (B100, Table 2-1). The capability of B100 to dissolve water can be even more than 1300 ppm (v/v) while it is continuously in contact for more than 24 h, i.e. water saturation contents of ≥ 1300 ppm [20, 28, 29].

2.3.1.2 Free water in fuel

Once the water content of the fuel exceeds its saturation level, free water is formed and can settle at the bottom of the vehicle fuel tank where agitation is minimal (thermodynamically low energy state). Consequently, water and diesel form a single interface, with the diesel on top of the free water, where the interfacial tension (IFT) is measured.

The surface tension at the interface of two immiscible liquids is called the interfacial tension (IFT) (N/m) and is measured based on the Fowkes equation (Equation 2-1) [63, 64]. A higher interfacial tension is indicative of weaker intermolecular bonding between the two surfaces. The surface tension (N/m), or the surface free energy (J/m^2) of a liquid is a force (energy) required to increase the surface area of the liquid by one unit [63, 64]. This tension originates from the imbalanced intermolecular forces on the surface of the liquid where the molecules are not completely surrounded by others to be pulled in all directions.

$$\gamma_{12} = \gamma_1 + \gamma_2 - 2(\gamma_1^p \gamma_2^p)^{-2} - 2(\gamma_1^h \gamma_2^h)^{-2} - 2(\gamma_1^{ab} \gamma_2^{ab})^{-2} - 2(\gamma_1^w \gamma_2^w)^{-2}$$

Equation 2-1: Fowkes equation for interfacial tension [63]

Where:

γ_{12} : Interfacial tension of the liquid 1 and 2 (N/m);

γ_{1or2} : Surface tension of liquid 1 or 2 (N/m);

p : Dipole-dipole interactions (N/m);

h : Hydrogen bonding (N/m);

ab : Lewis acid-base interactions (N/m);

w : Van de Waals interactions (N/m).

2.3.1.3 Emulsified water in fuel

Water can be dragged into the engine pipe lines by the fuel circulation from the fuel tank. Such that, the free water in the tank is disturbed when it is exposed to the shear stress of the fuel moving through the fuel pump, such that it forms a spherical interface in the form of an emulsified water droplet in the fuel (Figure 2-2).

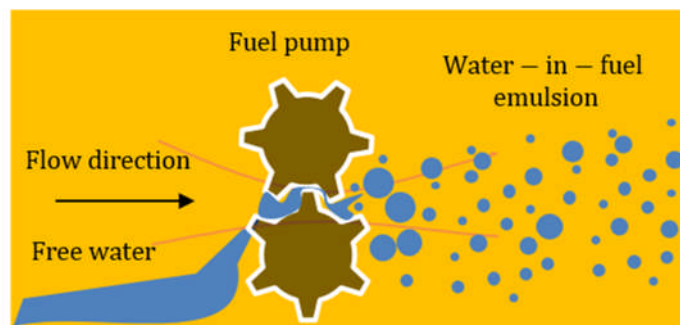


Figure 2-2: Change of water from the free (settled) state to the emulsified state in the fueling system

The conservation of energy during the emulsion generation process can be explained by Bernoulli's equation (Equation 2-2) [65, 66]. The equation is the sum of pressure energy per unit volume (Pv), kinetic energy per unit volume ($v^2/2$), and the potential energy per unit volume (gZ) of the liquid is always constant.

$$gZ + Pv + \frac{v^2}{2} = \text{constant}$$

Equation 2-2: Bernoulli's Equation [65, 66]

Where:

Z : Elevation of the point above a reference plane (m);

P : Static pressure at the chosen point (Pa);

V : Fluid flow speed at a point on a streamline (m/s);

g : Acceleration due to gravity (m/s^2);

v : Specific volume of the liquid (m^3/kg).

Considering the emulsification of two immiscible liquids and taking the input mixing energy (W) and heat (Q) into account in the Bernoulli's equation, Equation 2-3 demonstrates how the input energy can change the fluid internal energy (U) as well as its pressure, kinetic, and potential energies in the emulsified state (denoted by subscript 2).

$$gZ_1 + P_1v + \frac{V_1^2}{2} + U_1 + W + Q = gZ_2 + P_2v + \frac{V_2^2}{2} + U_2$$

Equation 2-3: Bernoulli's Equation including input mixing work and heat [65, 66]

Assuming a constant potential and kinetic energy of the system before and after emulsification, Equation 2-3 can be expressed as Equation 2-4, showing that the mixing energy is equal to the difference of changes in the enthalpy of the system ($\delta H = v\delta P + \delta U$) and the input heat.

$$W = v\delta P + \delta U - Q$$

Equation 2-4: Mixing energy of the emulsification process [65, 66]

Assuming adiabatic conditions ($Q = 0$) and constant pressure ($\delta P = 0$) in Equation 2-4, the input mixing energy affects the internal energy of the emulsion, which is equal to the total interfacial energy of the emulsified phase in the bulk medium (Equation 2-5) [12, 30, 58, 59]. Based on this, lowering the interfacial tension of the emulsion phases results in an increase in the interfacial area of the phases by formation of a finer emulsion containing a greater number of dispersed droplets of smaller sizes [12, 30, 58, 59].

$$W = \delta U = \gamma \delta \sigma, (\sigma = \frac{A}{V} \times \varphi)$$

Equation 2-5: Available energy in the emulsion [12, 30, 58, 59]

Where:

σ : Specific surface area (m^{-1});

γ : Interfacial tension $N \cdot m^{-1}$ ();

A : Surface area of a droplet (m^2);

V : Volume of the droplet (m^3);

φ : Volume fraction of the emulsion (dispersed phase/ continuous phase).

Equation 2-4 is equivalent to the Gibbs free energy equation (Equation 2-6) showing the available energy of the system to do work. When applied to a process, the Gibbs free energy indicates whether the process is able to proceed spontaneously or not. There are three possibilities: 1) if the available energy of the system is decreasing during the process ($\delta G < 0$), then it proceeds spontaneously; 2) if the energy is not changing ($\delta G = 0$) then it is at an equilibrium state; and 3) if changes in the available energy of the system are positive ($\delta G > 0$), then the process requires external energy to initiate. Based on this, the positive change in the energy of the mixture during the emulsification of water in diesel (Equation 2-5) indicates that the emulsification process is not spontaneous, and external energy (W) is required to initiate it [12, 30, 58].

$$\delta G = \delta H - T \delta S = \delta U + v \delta P - T \delta S$$

Equation 2-6: General equation for Gibbs free energy [12, 30, 58]

Where:

δG : Changes in Gibbs free energy (J/kg);

δH : Changes in total energy of enthalpy (J/kg);

T : Temperature ($k - kelvin$);

δS : Changes in entropy of the system ($J/(kg \cdot k)$);
 δu : Changes in internal energy of the system (J/kg);
 δP : Changes in the pressure of the system (N/m^2);
 v : Specific volume of the mixture (m^3/kg).

2.3.2 Effective parameters on water droplet size in the emulsion

The input work of mixing changes the single interface between the fuel and free water to a spherical interface. This takes the form of an emulsified water droplet in the fuel leading to a larger water and fuel interfacial area (Equation 2-5). The initial water droplet size distribution (DSD) depends on the shear stress of the fuel (Equation 2-7), which is influenced by the flow rate as well as the Laplace pressure (pressure across the surface of a spherical droplet - Equation 2-8) of the droplets, which influences their ability to rupture (Figure 2-2) [13, 58, 59, 67].

$$\tau = \mu_c \times \omega, \quad \omega = \frac{du}{dy}$$

Equation 2-7: Shear stress in the fluid [13, 58, 59, 67]

Where:

τ : Shear stress (Pa);
 μ_c : Dynamic viscosity of the continuous phase ($Pa \cdot s$);
 ω ($\frac{du}{dy}$) : Velocity gradient of the fluid layers divided along its thickness (s^{-1}).

$$P_l = \frac{2\gamma}{r}$$

Equation 2-8: Laplace pressure across the surface of a spherical droplet [13, 58, 59, 67]

Where:

P_l : Laplace pressure of a spherical droplet (N/m^2);
 γ : Surface tension (N/m);

r : Droplet radius (m).

The Laplace pressure of a droplet is derived from its surface tension, which maintains its integrity, and the fluid shear stress depends on the fluid viscosity and flow rate. Depending on whether the ratio of the shear stress to the Laplace pressure of the droplet, known as Weber number (We), is high enough, it may be split into smaller droplets. Therefore, the initial water droplet size in the fuel-water emulsion is a function of the mixing energy (*shear stress* – τ), the viscosity of the *fuel* (μ) as well as the IFT of the water and fuel (γ).

Once the emulsion is formed, however, dispersed droplets which have acquired kinetic energy, start to move around in the bulk fuel and collide into each other. Depending on how well stabilised the emulsion is (see Section 2.3.4), this can lead to coalescence of droplets and destruction of the emulsion via phase separation.

2.3.3 Destruction of the emulsion and phase separation

As explained in Section 2.3.1, an emulsion acquires an unfavourable thermodynamic state due to the positive changes in its available energy resulting from unfavourable molecular interaction between the immiscible phases [62]. Therefore, dispersed droplets tend to return to the form of free water to decrease their total surface energy and reach a favourable thermodynamic state. This happens by droplets merging together (droplet coalescence) to form bigger drops, and then by settlement such that they become separated from the bulk liquid, i.e. the diesel fuel [12, 30, 59, 61, 67, 68]. Thus, destruction of an emulsion happens via two steps: droplet coalescence followed by droplet settlement.

2.3.3.1 Droplet coalescence

A film drainage model has been developed to explain the coalescence of two droplets in a three step process consisting of droplet collision, film drain-out and film rupture [58, 61]. In this model, two dispersed droplets are assumed to move towards each other and collide while a volume of the bulk liquid is trapped between the droplets and forms a thin film between. The kinetic energy as well as intermolecular forces of the droplets (van der Waals forces) pull the droplets towards each other such that the trapped film of the bulk liquid is drained out. As a result, the film becomes thinned down to its critical thickness where it is unable to keep the droplets apart anymore resulting in film rupture and coalescence of the droplets. This model emphasises the effect of intermolecular forces and the need for a sufficient residence time of the droplets adjacent to each other [58, 61].

Howarth (1964) and Lehr et al. (2002), however, claimed that the molecular forces between two droplets are not so strong to solely initiate the coalescence of the droplets, and the kinetics of the droplets play the main role [58, 69]. They believe that the main factor for successful coalescence is a sufficient “approach velocity” of the droplets as they collide [58, 69]. Following this critical approach velocity model, Lio et al., 2010, suggested the five main sources of relative motion between droplets, which can lead to their coalescence [58] as : “(i) motion induced by turbulent fluctuations in the surrounding continuous phase; (ii) motion induced by mean velocity gradients in the flow; (iii) different bubble rise velocities induced by buoyancy or body forces; (iv) bubble capture in an eddy; (v) wake interactions or helical/zigzag trajectories.”

According to existing models, successful coalescence is more likely to occur if (Figure 2-3):

- 1- Proper control of the movement of droplets exists by which droplets are able to get close to each other (Figure 2-3 A).

- 2- Proper control of the velocity of droplets exists to create a sufficient approach velocity (Figure 2-3 B).
- 3- Sufficient force exists to overcome any resistance to coalescence, to drain the bulk liquid film out and to rupture off the droplet surface (Figure 2-3 C).
- 4- Sufficient contact time between droplets to maximise the effect of intermolecular forces as well as the sudden IFT gradient (Figure 2-3 C).
- 5- Control of coalesced droplets to avoid droplet rupture/ re-emulsification.

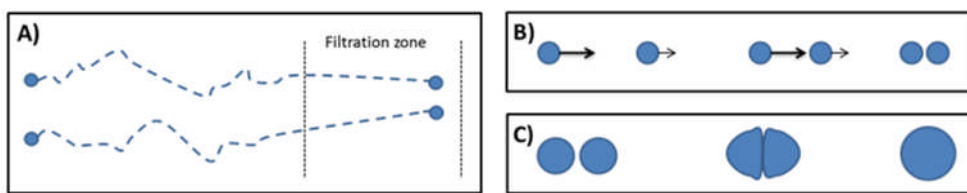


Figure 2-3: Schematic summary of the factors controlling successful coalescence: A) control of the movement of droplets; B) control of the velocity of droplets; C) Sufficient collision and residence time

2.3.3.2 Droplet settlement

Stokes' law describes the settling velocity, V , of a particle in a fluid medium based on Equation 2-9 [70]. The settling velocity of a particle depends on its size, density difference with the bulk medium as well as the medium viscosity. Stokes' Law clearly shows that size of the dispersed droplet is an important factor in its settling velocity and that the settling velocity increases by an order of 2 by increasing the droplet size. This highlights the importance of the coalescence process in the formation of bigger droplets for the rapid separation of the dispersed phase from the bulk phase.

$$V = \frac{2(\rho_w - \rho_f)gr^2}{9\mu}$$

Equation 2-9: Settling velocity of a water droplet dispersed in fuel [70]

Where:

ρ_p : Density of the settling particle (kg/m^3);

ρ_m : Density of the fluid medium (bulk liquid) (kg/m^3);

g : Acceleration due to gravity (m/s^2);

r : Radius of the settling particle (m);

μ : Viscosity of the fluid medium (bulk liquid) ($Pa \cdot s$).

2.3.4 Surfactants in the emulsion

Destruction of an emulsion is favourable from thermodynamic point of view, however, this is not always the goal in some applications found in the chemical and food industries, where a stabilised emulsion is targeted. To achieve this, surfactants are blended with the emulsion to stabilise it and keep the discontinuous phase of the emulsion dispersed in the medium [59, 61, 67, 68, 71].

Surfactant molecular chains have heads and tails with different chemical properties. In an emulsion, one side of the molecular chain has affinity for the medium (continuous phase) and is lyophilic and the other side has no affinity (lyophobic), and is therefore adsorbed on the surface of the dispersed droplets [12, 30]. Some surfactants are amphiphilic with both hydrophilic and hydrophobic groups. In water-in-oil emulsion, they are adsorbed at the interface with their hydrophilic ends bonding to water and their hydrophobic ends bonding to the oil [12, 56-59]. Consequently, they consume energy at the interface resulting in a reduction in the IFT [58, 61, 69].

Surfactants function as stabilisers in emulsions and also influence the coalescence of dispersed droplets by either electrostatic or steric forces once they are generated [12, 30, 59]. He et al. categorise surfactants molecules as either simple molecules or polymeric macromolecules [61]. In this division, small molecule surfactants usually function via electrostatic stabilisation in which PH and ionic strength of the mixture have the greatest effect [61]. Polymeric surfactants, however, function via steric stabilisation by which dispersed droplets are prevented from close proximity, restricting the likelihood of coalescence [61].

As explained in Section 2.2.3 EN590 diesel contains fuel additives including bio-diesel, which tend to act as surfactants and bond with both oil and water, thus reducing the fuel-water IFT (Equation 2-1). Therefore, in water-in-EN590 emulsions, the presence of small stable water droplets ($< 100\mu m$) is to be expected (see Section 2.3.2)[12, 13, 15-17, 32, 35-38, 47-50, 59, 61, 67, 68, 71-74]. In real vehicle situations, 50% of the water droplets after the fuel pump can be smaller than $25\mu m$ ($D_{50} < 25\mu m$) [28], such that the breakdown of the emulsion solely by sedimentation under the influence of gravitational force requires sufficient time, which can be of the order of hours (see Section 2.3.3) [12, 17, 30, 32, 58, 59, 61, 67, 69, 74].

2.3.4.1 Influence of surfactants on new droplets

Once the droplets are generated and start moving in the emulsion, the surfactant molecules are also absorbed on to the surface of droplets as time passes. At the beginning of droplet formation if two new droplets approach each other for coalescence, the layer of the fuel phase containing surfactants between them gets thinner. As the layer become thinner, the surfactant content of the layer is lowered and less surfactant molecules are available in this region for droplets to adsorb compared to the surfactant content of the bulk fuel. Consequently, the IFT of the droplet in the region adjacent to the film locally increases while the rest of the surface has a lower IFT.

This imbalance on the surface of the droplets creates a surface tension gradient (highest tension where the film is thinnest), which causes movement of the bulk liquid containing more surfactant molecules towards the film between two droplets. This phenomenon is known as the Gibbs-Marangoni effect which causes the surfactants being transferred into the area between two droplets which results in creating resistance to coalescence of the droplets [59, 67].

2.3.4.2 Influence of surfactants on droplet stability

When dispersed droplets reach a steady state in which they are surrounded by surfactants, they also interact with each other as they move in the flow. However, due to the electrostatic or steric stabilisation, collision between droplets can initiate film drainage and film rupture. The stability of water droplets in fuel can be evaluated via a test procedure detailed in ASTM D 1401. In this test an emulsion, in which dispersed droplets require more time to sediment, is characterised as the one having the lower “separability”.

However, the equilibrium conditions governing the interaction of the surfactant with the droplet surface can be disturbed, resulting in coalescence due to van der Waals forces and a surface tension gradient [59, 61, 67]. A decrease in surfactant concentration on an aspheric-shaped droplet is most likely to happen when the droplet interacts with another surface, such as fibre in a filter, or indeed another droplet. Once this happens, an interfacial tension gradient occurs and the inherent surface tension value of water is locally measurable on the specific area of the surface that is lacking surfactant [67]. Therefore, the dispersed droplet will be less stable in the emulsion and more ready to initiate coalescence [59, 61, 67, 68] [12, 30, 59, 61, 67, 68].

2.4 Separation of water from diesel fuel

The presence of small, stable water droplets in diesel fuel containing surfactants and those containing bio-diesel mitigates against their efficient separation by sedimentation because removal depends on gravity. Small size droplets therefore possess low settling velocity (see Section 2.3.3) and consequently coalescing media are required to enhance coalescence and provide continuous separation of emulsified water from fuel in diesel engines.

Fuel-water separators conventionally employ barrier and coalescing nonwoven media to mechanically separate unwanted free water from diesel fuel in diesel engines. The coalescing medium is designed to enhance droplet coalescence leading to the formation of larger droplets, which can then be removed more easily by a barrier mesh [12, 30-34, 61]. The water at the barrier mesh is then removed by settlement and drainage on upstream side, either manually or automatically depending on the design of the filter housing.

2.4.1 Separation mechanisms: filtration and sedimentation

The mechanical separation of fluid flows is performed by either filtration using filters or sedimentation using sedimenters [34, 75]. INDA, the Association of the Nonwovens Fabrics Industry defines filtration as “a mechanism or device for separating one substance from another.” [76]. Sedimentation, however, is defined as “separation of liquid droplets or solid particles from a suspending fluid, by allowing them to settle out of suspension under the influence of gravity or of centrifugal force.”[75]. Based on these definitions, filtration is mainly about capturing and holding the dispersed particles on the surface or in depth of a porous medium such that shape and size of the particles/droplets are important factors. In contrast, sedimentation is mainly concerned with the density differences of the emulsion components and particle/droplets sizes, following Stokes law (Equation 2-9).

In filtration, dispersed particles/droplets are separated by the filter via either straining mechanism when size of the particles are greater than pore sizes of the filter, or filtration mechanism when size of the particles/droplets are smaller than pore sizes of the filter and they can be captured by the filter structure through one of the capturing mechanisms of impaction, interception, diffusion, or electrostatic attraction (Figure 2-4) [34, 77, 78].

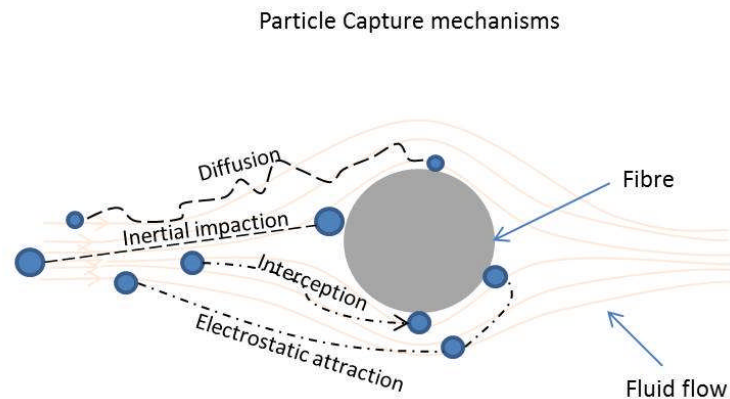


Figure 2-4: Filtration mechanism [34, 77, 78]

The capturing mechanisms are well studied in the air filtration field and it has been reported that the dominant mechanism depends on the particle size [34, 79-82]. Inertial impaction is the dominant capture mechanism for relatively large (e.g. $>1\mu m$) and heavy particles. These particles possess sufficient momentum to escape from the flow and impact the fibres of the medium. By decreasing the fluid flow rate as well as increasing the fibre diameter, particle diameter and its density, particle capture efficiency by this mechanism increases. On the other hand, very small particles ($<0.1\mu m$) have a zig zag motion pattern (Brownian motion) in the flow and this random movement is very likely to cause diffusion and particle delivery to the fibres. By decreasing the flow rate and the particle size as well as increasing fibre diameter and inter-fibre distance particle capture by this mechanism increases. Particles with relative

intermediate sizes ($0.1 \mu m < \text{particle diameter} < 1 \mu m$), are the most difficult to capture and are denoted as the most penetrating particle size, MPPS. These particles are mostly attached to the fibre by the interception mechanism. This mechanism refers to the particle adsorption on the fibre surface by the intermolecular forces as it becomes very close to the fibre, i.e. distance to fibre should be less than the particle radius. Unlike other two mechanisms, the capturing efficiency through interception is independent of the velocity of the fluid, however, as the particle radius increases or the fibre diameter and the inter-fibre distance decreases, the capture increases.

Nonwoven media are widely used in surface and depth filtration, however, to obtain more uniform pore size woven fabrics, screens and membranes are also associated with surface straining [34]. Nonwoven filter media with very small pore sizes composed of sub-micron diameter nanofibres are also used as membranes for micro- and ultra-filtration [34].

2.4.2 Nonwoven water separator media

Nonwoven media are used in the fuelling system of diesel engines as both filters, operating as barrier type media or as sedimenters, operating as coalescing type media. The configurations and product formats vary in line with the demands of each Original Equipment Manufacturer (OEMs), but the overall objective is to maintain the total water content of the fuel within the vehicle below 200 ppm.

2.4.2.1 Barrier type nonwoven water separator media

Conventional barrier type water separators consist of silicone treated cellulose fabrics made by the wetlaid process and they are designed to function by the surface straining filtration mechanism [34, 83]. Such barrier media possess a hydrophobic upstream surface, such that water droplets will not wet the surface, promoting droplet formation, while the fuel is flowing

through. This together with the small pore or aperture size, prevents large droplets from passing through, aiding separation from the fuel. As more droplets are rejected by the filter and beads coalesce into larger droplets the water drains out of the filter housing. Since such barrier media function using a filtration rather than a sedimentation mechanism, the pore sizes must be small enough to separate dispersed water droplets from the fuel stream and the fabrics being wetlaid have relatively low porosities. Unfortunately, this can lead to a high pressure drop, especially if the medium becomes plugged, which in the worst case can interrupt fuel flow to the engine. The fabrics are assembled in to cartridge filters and are pleated to increase the surface area and reduce the face velocity during operation [34].

2.4.2.2 Transmissive coalescing type nonwoven water separator media

Coalescence fuel filters as considered as sedimenter media with a high surface area for capturing emulsified water droplets from diesel fuel and enhancing their coalescence [16, 17, 34-45]. Incoming water droplets in the diesel fuel stream enlarge already captured droplets held on fibre surfaces by a coalescence mechanism, eventually enabling their gravitational separation [12, 30-34, 61]. Nonwoven coalescing media are porous fabrics that traditionally take one of three forms [12, 16, 17, 34, 43, 44]:

- 1) Single layer resin bonded wet-laid nonwovens of short fibres consisting of blends of cellulose (wood pulp) and polyester and/or glass microfibre.
- 2) Composite nonwovens, consisting of PET, PA or PBT meltblown fabrics that are laminated to or formed on a cellulosic wetlaid medium [16].
- 3) Multiple layered nonwovens primarily consisting of PET or PBT meltblowns [12, 34].

Meltblown technology is the most widely employed technique mainly because of the ability to produce fibres of micron and sub-micron diameters in a one-step, cost-effective process [34-

38, 45]. Although fibre diameter can range between 0.1 and 30 micrometres, the majority have a mean diameter of 2 to 7 microns, and are formed by attenuation of liquid thermoplastic polymer streams in a heated high velocity airstream at typically just below Mach 1 velocity. A coherent web is formed due to mechanical entanglement and self-bonding of the fibres [34-38, 45]. Such fabrics are highly efficient in the separation of particles bigger than 100 microns [34-38, 45] although in many liquid filtration applications they are employed to remove particles whose dimensions are <10 micrometres by exploiting depth filtration. Utilisation of micro-scale fibres started from the 1960's using asbestos and glass microfibres but today, polymeric fabrics dominate [84, 85]. Meltblowing is also capable of producing sub-micron fibres, enabling an associated increase in the solid surface area, which is highly relevant to the development of advanced water/diesel separation filters [35-38].

Similar to barrier type media, single layer and composite nonwoven coalescing media are frequently pleated during their conversion in to a final filter element, aided by the cellulosic support layer. The media in these elements are constructed with either a constant or gradient density through their thickness, while the multilayer media are wrapped over a plastic support [34, 39-42]. Unlike the barrier type media, depth coalescing nonwoven media do not necessarily have to have a high density structure with pore sizes smaller than the size of dispersed water droplets, therefore, pressure drop across such filter elements can be controlled effectively (see Section 2.4.3.2) [30-33].

A nonwoven coalescing medium in fuel-water separation promotes the collection, growth and removal of the dispersed water such that it is able to drain out of the fuel [34, 75, 83]. According to the newest generation of filtration systems used in diesel engines, coalescing water separator media are used either as primary or secondary filters and in both cases, their performance characteristics have been industrially accepted [2, 14, 86-89].

Operating principles

The operating principle of a coalescing medium is based on three steps: droplet capture, droplet coalescence, and release of the coalesced droplets [12, 30, 32, 34, 47, 90]. Depending on droplet size, the capture mechanisms rely upon inertial impaction, interception, diffusion, and electrostatic attraction, however, the dominant droplet capture mechanism is the interception on the surface or in the depth of medium (see Section 2.4.1) [34, 75, 90]. The captured droplets can coalesce with adjacent droplets as well as incoming droplets in the flow. The coalesced droplets then move or “transmit” within the medium with the flow, leaving the downstream side as they become large enough to be separated from the flow by gravity. Figure 2-5 simplifies the key functions of a coalescing media operating as a secondary filter element alongside a particulate filter and barrier medium (see Section 1.1).

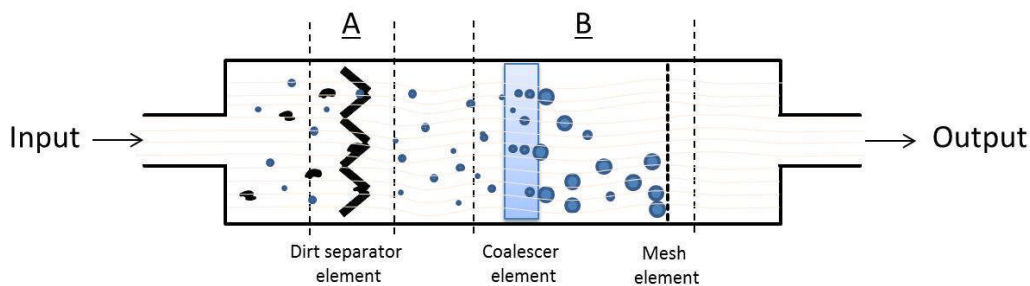


Figure 2-5: Simple schematic of a coalescing fuel filter: A) particulate separator compartment; B) water separator compartment

In conventional diesel fuelling systems, the most penetrating droplet size (MPDS) in terms of fuel-water separation is in the range of $25\ \mu\text{m}$ to $100\ \mu\text{m}$ (see Section 2.3.4), but today the challenge is even greater. In new generation HPCR injection systems working with ULSD fuel, droplet sizes can be even lower (see Section 2.3.4) with the MPDS range dropping to between $3\ \mu\text{m}$ and $25\ \mu\text{m}$ depending on the fuel and system specifications [12, 13, 16, 28]. Some coalescing water separators are made of hydrophilic cellulose/glass microfibre blends to

improve water/fibre interactions for a high efficiency droplet capture [30-34, 75, 83]. The fundamentals of fibre surface wettability can be explained with reference to the Young-Dupre equation (Equation 2-10) [63, 91]. The equation describes the equilibrium state of surface tensions of the solid, liquid, and vapour (air) when a droplet is placed on a perfect surface of the solid and an equilibrium contact angle, θ , is built [91]. If the IFT between the solid and droplet, γ_{sl} , is low, i.e. there is high intermolecular attraction between the solid and liquid (see Section 2.3.1.2), the droplet can wet the surface and consequently create a contact angle lower than 90° [63, 91].

$$\gamma_{sv} = \gamma_{sl} + \gamma_{lv} \cos \theta$$

Equation 2-10: Young-Dupre equation [63, 91]

Interaction between a water droplet and the surface of a fibre immersed in diesel fuel depends on the magnitude of available work of adhesion, W_A (Equation 2-11), as well as work of spreading, W_s (Equation 2-12) [63, 91]. Water droplets are inclined to be adsorbed on the surface of a fibre when the droplet thermodynamically reaches a lower energy state by sitting on the fibre and the work of adhesion is positive ($W_A > 0$). Likewise, the droplet starts to spread on the surface of the fibre when the total energy of the droplet (γ_{wd}) and the wetted surface (γ_{fw}) is lower than that of solid surface itself (γ_{fd}), i.e. the work of spreading is positive ($W_S > 0$).

$$W_A = \gamma_{wd} + \gamma_{fd} - \gamma_{fw} \quad \text{or} \quad W_A = \gamma_{wd}(1 + \cos \theta)$$

Equation 2-11: Available work of adhesion [63, 91]

$$Ws = \gamma_{fd} - \gamma_{wd} - \gamma_{fw} \quad \text{or} \quad Ws = \gamma_{wd}(\cos \theta - 1)$$

Equation 2-12: Available work of spreading [63, 91]

Where:

γ_{wd} : Interfacial tensions (IFT) between water drop and diesel;

γ_{fd} : Interfacial tensions (IFT) between fibre and diesel;

γ_{fw} : Interfacial tensions (IFT) between fibre and water.

Such that, a droplet approaching a fibre with the flow either: 1) cannot wet the surface and because of the fluid energy at the upstream stagnation point of the surface (Figure 2-6 (a) – point A), it moves along the periphery and detaches at an angle on which fluid drag force can affect its stability (Figure 2-6 (a) – point C); or 2) can completely wet the surface and create a film over the fibre as it is fed by the incoming droplets (Figure 2-6 (b)); or 3) has an intermediate wettability towards the surface such that moves on the surface and depends on its dynamic contact angle it can reach to the downstream stagnation point and gets coalesced with the incoming droplets until it is detached (Figure 2-6 (c)) [92].

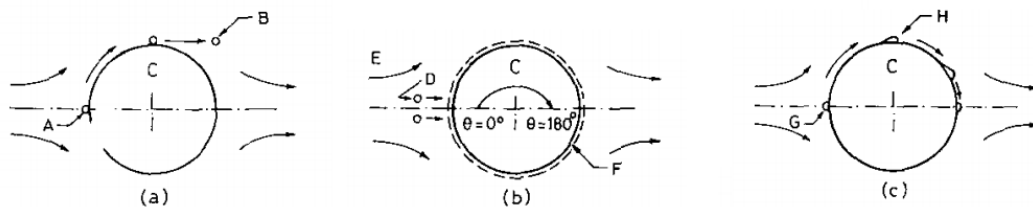


Figure 2-6: Three anticipated modes of droplet coalescence upon a fibre surface [92]

The deposition and detachment of a droplet from the fibre depends on the drag energy of the fluid as well as the adhesion and spreading forces between the droplet and surface. As the droplet completely wets the surface (Figure 2-6 (b)), the drag force can cause re-emulsification

of the water due to a lower Laplace pressure (Equation 2-8 – see Section 2.3.2) of the droplet when it spreads to a larger curvature [93].

Fibrous networks such as nonwovens are also able to control droplet movement within the structure, by wicking and providing capillary channels and accordingly capillary pressure, P_c , (Equation 2-13) for droplets [63, 94, 95]. High capillary pressure provides a mechanism for transporting a liquid within the capillary channel. The Lucas-Washburn equation (Equation 2-14) measures the vertical diffusion of the liquid through capillary spaces (wicking phenomenon regardless of the gravitational forces) as a function of time [63, 94].

$$P_c = \frac{2\gamma_{lv} \cos \theta_a}{r_e}$$

Equation 2-13: Capillary Pressure [63, 94, 95]

$$h^2 = \frac{r_e \gamma_{lv} \cos \theta_a t}{2\tau^2 \eta}$$

Equation 2-14: Lucas-Washburn Equation [63, 94]

Where:

h : Nominal distance travelled by the liquid from the reservoir;

$h\tau$: Actual distance travelled;

τ : Appropriate tortuosity factor;

η : Liquid viscosity;

ρ : Liquid density;

θ_a : Dynamic advancing contact angle;

γ_{LV} : Liquid surface tension.

2.4.3 Filtration/Coalescing performance of nonwoven fuel-water separators

Water separators are usually evaluated by measuring their water separation efficiency and quality factor, which are detailed further in this section.

2.4.3.1 Separation efficiency

One of the fundamental performance measurements to evaluate the performance of a filter element is its filtration efficiency (Equation 2-15) [12, 30, 31, 34, 47].

$$E = \frac{M_{dU} - M_{dD}}{M_{dU}} \times 100$$

Equation 2-15: Calculation of instantaneous water separation efficiency [12, 30, 31, 34, 47]

Where:

M_{dU} : Upstream particle count/amount for particles of diameter d or greater;

M_{dD} : Downstream particle count/amount for particles of diameter d or greater.

Evaluation of the water separation performance depends on the specific end use of the filter medium, and is frequently dictated by industrial standards. These are essentially laboratory test methods are conducted using a base reference grade diesel fuel that is free of solid contaminants or bio-diesel, but is blended with a specified surfactant, which alters the fuel IFT and water separation characteristics. The approach is based on the theory that low IFT will result in small droplet sizes and thereby simulate more challenging fuels such as those containing bio-diesel or surfactant additives, e.g. EN590 diesel. ISO16332:2006 sets out the standard procedure for evaluating fuel-water separation efficiency and defines the efficiency as in Equation 2-16 [48].

$$\eta = \frac{c_u - c_d}{c_u} \times 100$$

Equation 2-16: calculation of water separation efficiency [48]

Where:

η : Water separation efficiency, in %;

c_u : Water concentration at upstream side of the filter element, in ppm by volume;

c_d : Water concentration at downstream side of the filter element, in ppm by volume.

For this measurement, water concentrations both upstream and downstream of the element are measured using a Karl Fischer titrator, which is explained in detail in Chapter 3.

2.4.3.2 Quality factor

Another fundamental performance measurements of a filter element is its quality factor (QF) (Equation 2-17) which takes the pressure drop into the account along with the efficiency of the filter influencing the overall performance of the element [12, 30, 31, 34, 47, 96, 97]:

$$QF = \frac{-\ln(1 - E/100)}{\Delta P}$$

Equation 2-17: Quality Factor [12, 30, 31, 34, 47, 96, 97]

Where:

E: Filtration efficiency of the element (%);

ΔP : Differential pressure across the filter medium (Pa);

Pressure drop between two points in a fluid flowing through a streamline results from resistance to the flow in that region [66]. Pressure drop in a fluid system can be experimentally measured using differential pressure gauges.

The total head or energy of a fluid at a point in the flow (Equation 2-18) can be calculated using Bernoulli's equation (Equation 2-2), and head loss (loss of energy) due to the friction in a region is calculated via the Darcy-Weisbach equation (Equation 2-19), which can be converted to pressure drop via Equation 2-20 [66].

$$H = Z + \frac{P}{\gamma} + \frac{V^2}{2g} \quad \text{or} \quad \rho g H = \rho g Z + P + \frac{\rho V^2}{2}$$

Equation 2-18: Total head of a fluid [66]

Where:

H : Total head or total energy at the point (normalized constant from Bernoulli's equation);

Z : Elevation of the point above a reference plane;

P : Static pressure at the chosen point;

γ : Specific weight of the fluid at all points in the fluid ($\frac{N}{m^3}$);

ρ : The density of the fluid ($\frac{kg}{m^3}$);

V : Fluid flow speed at a point on a streamline;

g : Acceleration due to gravity.

$$H_f = f \times \frac{L}{D} \times \frac{V^2}{2g}$$

Equation 2-19: Darcy-Weisbach Equation [66]

Where:

H_f : Head Loss between two nodes (m);

f : Darcy friction factor which can be found from Moody Chart based on Relative Roughness and Reynold Number of the system (dimensionless);

L : Length of the tube between the two nodes (m);

D : Diameter of the tube (m);

V : Velocity of the fluid at the second node (m/s);

g : Acceleration due to gravity (m/s^2);

$$\Delta P = \rho \cdot g \cdot H_f$$

Equation 2-20: Pressure drop calculation [66]

Where:

H_f : The head loss due to friction (m);

ΔP : Pressure loss due to friction (Pa);

ρ : The density of the fluid (kg/m^3);

g : Acceleration due to gravity (m/s^2).

Mathematically calculation of the pressure drop across a permeable filter medium requires simulation of the flow through the medium. Channel and cell model theories explain fluid dynamics through nonwoven porous materials [34]. The channel theory is usually applied for a compact structure with a high packing density, while the cell model is applied to open structures. For instance, the channel theory considers the fibrous structure as an assembly of cylindrical tubes stretched from one side to the other side of the medium along its thickness. In this model, Darcy's law, Equation 2-21 is a fundamental equation and explains the flow through a porous medium in which the flow is perpendicular to the medium thickness.

$$q = \frac{k}{\mu} \frac{\Delta P}{L}$$

Equation 2-21: Simplified Darcy's law [34]

Where:

q : face velocity of the fluid (m/s);

k : Intrinsic permeability of the medium (m^2), ($k = Cd^2$, C is the pore shape factor and d is mean pore diameter);

μ : Fluid dynamic viscosity (Pa/s);

ΔP : Pressure drop across the thickness (Pa);

L : Medium thickness (m).

The intrinsic permeability of a medium, k , in Darcy's law is defined by the Kozeny-Carman equation (Equation 2-22) in a specific condition in which the fluid flows through a flat porous medium with a solidity of $\chi > 0.2$ and $\chi < 0.8$ ($\chi = 1 - porosity(\varepsilon)$), elliptical pore shapes, and capillary channels oriented at 45° to the medium surface.

$$k = \frac{\varepsilon^3}{5S^2\chi^2}$$

Equation 2-22: Intrinsic permeability of a medium based on Kozeny-Carman equation [34]

Where:

ε : Permeable porosity or void volume expressed as a decimal fraction of the total volume of the medium (m^3/m^3);

χ : Solidity or packing density expressed as a decimal fraction of the total solidity of the medium (m^3/m^3);

S : Specific surface area per unit volume solid material (m^2/m^3).

Darcy's law clearly shows that more compact media lead to a greater flow resistance and therefore pressure drop at a constant fluid face velocity. Practically, this also occur as water or particles are accumulated by the filter leading to plugging of the void volume in the porous structure. Classically, the pressure drop and separation efficiency are interrelated and one is generally sacrificed to improve the other. For instance, modifying the surface chemistry of a nonwoven coalescing media to render it more hydrophilic is a strategy that has been used to improve water removal efficiency, but at the expense of an increased pressure drop, which decreases overall quality factor of the filter element (see Section 2.6.2.2).

2.4.3.3 Coalescence efficiency

Coalescence, which is the state of combining two or more droplets (see Section 2.3.3.1), can be a result of droplet collision among other possible collision consequences such as bouncing

apart [98]. Therefore, the coalescence efficiency, ε , can be defined by the fraction of collisions that results in the coalescence of droplets (Equation 2-23) [99, 100]. This calculation requires numerical models to measure collection, C_{eff} , and collision, E , efficiencies which respectively refer to the fraction of droplets approaching a surface that actually deposit upon that and the fraction of moving droplets that actually make surface contact [99, 100].

$$\varepsilon = \frac{C_{eff}}{E}$$

Equation 2-23: Droplet coalescence efficiency [99, 100]

Where:

ε : Coalescence efficiency;

C_{eff} : Collection efficiency;

E : Collision efficiency.

In the present research, the term coalescence efficiency of a filter medium refers to the volume fraction of the dispersed droplets passing through the medium that are coalesced and become large and heavy enough to be settled and collected downstream of the medium (see Chapter 5).

2.5 Existing filtration test procedures

There are number of SAE and ISO standard water separation test procedures that are commonly being used worldwide such as SAE J1829, SAE J1488, ISO 4020, and ISO 16332. In all these methods, there is a test circuit in which water is continuously injected into a fuel stream such that a water-in-fuel emulsion is created using an emulsifier device that passes through a filter housing holding a filter. The housing possesses a drainage container for collecting separated water. The main difference between the test stands in these methods is the emulsifier device used to generate the water droplets and their resultant sizes.

The ISO 4020 and SAE J1839 are usually employed to test primary filters (Section 1.1) for which generation of a coarse droplet size distribution (DSD) is intended. The ISO 16332 test rig however, is capable of generating a range of droplet size distributions from fine to coarse. ISO 16332 also uses a fuel with a lower IFT of about $15\pm 3 \text{ mN/m}$ while the original IFT of the test diesel is maintained in the ISO 4020 and SAE J1839 around 30 mN/m .

The SAE J1488 test rig is designed to generate fine droplet sizes in fuel with a relatively low IFT of $15\text{-}19 \text{ mN/m}$. In contrast to the ISO 16332, this method does not define the average water droplet size, however, finer droplets than those generated in the ISO 16332 are expected in the SAE J1488 test.

In all these methods, the separation efficiency of the whole filter module (final product) is reported which will not provide required information to evaluate the performance of filter elements inside the product. This is the main limitation of these methods from research and development point of view to understand the performance of nonwoven filter media used in the structure of the final filter product.

2.5.1 BS ISO 4020:2001 procedure [101]

ISO 4020 specifies nine types of test for diesel fuel filters of road vehicles including a test for water separation efficiency. The other tests are: test for cleanliness of new filters, fabrication integrity test, test for differential pressure of new filters, test for instantaneous filtration efficiency and filter life, collapse/burst test of the filter, burst test of complete filters, pulsating pressure fatigue test and the vibration resistance fatigue test.

Figure 2-7 shows the test stand for water separation. Water is injected into the fuel stream under static pressure at the suction side of a low shear pump (6). The water flow rate is controllable by the valve (5) and is kept at 2% of the main pump flow rate. The fuel is first

filtered by Fuller’s Earth or clay cartridge filters with an IFT between 25 and 30 mN/m . The pump directs the emulsion through the filter (11) for 60 min and separated water is collected from beneath the filter. The volume of uncaptured water from the filter is measured by analysing 100 ml of a fuel sample taken from the outlet of the filter housing (15) via a Karl Fischer titration set-up (ISO 760, see Section 3.3.3), every 5 min. The undissolved water content is plotted versus time. It is recommended that the test should be conducted at $23^{\circ}C \pm 5^{\circ}C$.

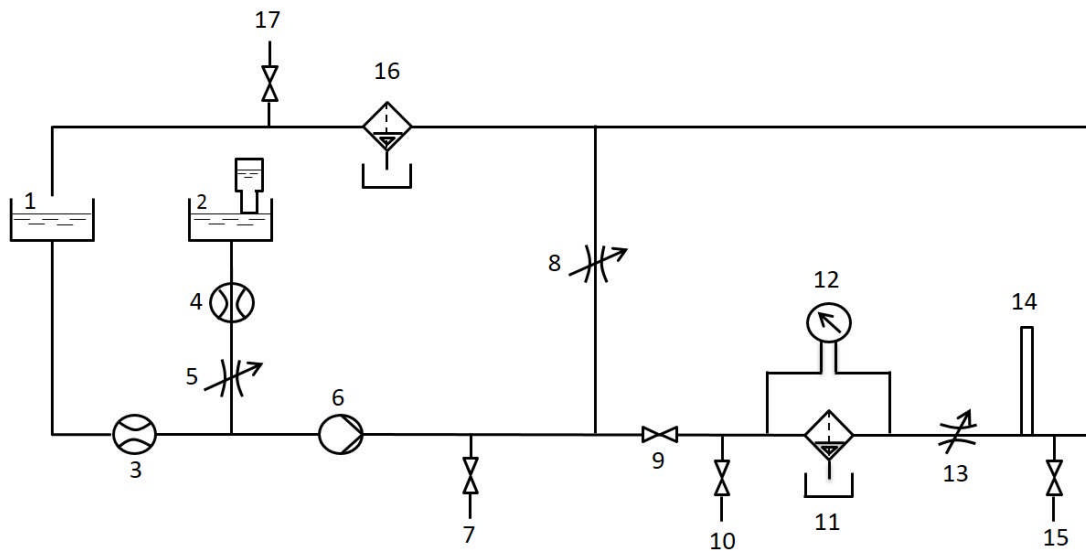


Figure 2-7: Schematic of the ISO 4020 test rig [101]

The test system components are as following:

- | | |
|--|--------------------------|
| 1- Fuel tank | 9- Stopcock, on/off |
| 2- Water tank with constant-level device | 11- Test filter |
| 3, 4- Flow meter | 12- Manometer |
| 5, 8, 13- Adjustable vale | 14- Head tube with scale |
| 6- Main pump | 16- Clean-up filter |
| 7, 10, 15, 17- Sampler | |

The main pump (6) is a diaphragm pump whose flow rate is kept constant at 833 ml/min (50 l/h) to maintain the droplet size distribution uniform during the test. Diaphragm pumps belong to the category of reciprocating-type positive displacement pumps in which the reciprocating motion of the diaphragm creates consecutive positive and negative pressure inside the chamber of the pump. This causes fluid flow in the system. The ISO 4020 does not report the expected droplet size distribution in the test system, however, using a low shear pump at a low flow rate and circulating emulsion with a high water concentration (2%) at a high IFT, all imply that the test rig introduces relatively large water droplets to the filter under the test.

2.5.2 ISO 16332:2006 procedure [48]

The ISO 16332 test stand (Figure 2-8) evaluates the water separation performance of fuel filters for either finely or coarsely emulsified water in diesel fuel at a relatively high flow rate of 0.833 l/min to 15 l/min . The ISO 16332:2006 test standard classifies fuel filters into suction side and pressure side filters depends on their location in the main fuel transfer pump in a vehicle. The test procedure recommends generation of coarse droplets for testing the suction side filters and generation of fine droplets for testing the pressure side filters, however, these recommendations do not necessarily prevent testing each of the filter types with both fine and coarse droplets.

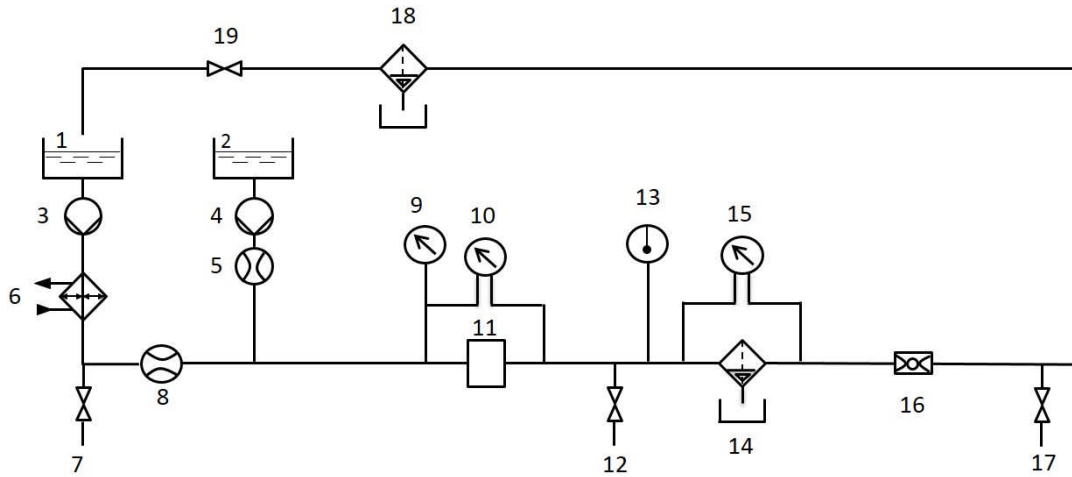


Figure 2-8: Schematic of the ISO16332 test rig [48]

The test system components are as following:

- | | |
|--------------------|--------------------------|
| 1- Fuel tank | 10, 15- Manometer |
| 2- Water tank | 11- Orifice plate holder |
| 3- Fuel pump | 13- Thermometer |
| 4- Water pump | 14- Test filter |
| 5, 8- Flow meter | 16- Static mixer |
| 6- Heat exchanger | 18- Clean-up filter |
| 7, 12, 17- Sampler | 19- Stopcock, on/off |
| 9- Pressure gage | |

Water-in-fuel emulsion is generated by passing the fuel and water through an orifice plate of specified orifice diameter. The differential pressure across the orifice plate, which depends on the orifice size, creates a droplet size distribution with a certain median value (D_{50}). Based on the orifice sizes provided by the standard, the D_{50} of the generated distribution can be as fine as $60 \mu\text{m}$ or as coarse as $300 \mu\text{m}$. Water concentration is specified as either 0.15% or 2%.

The fuel in this test should contain a multifunctional additive, which is commercially available and lowers the fuel IFT down to $12 - 18 \text{ mN/m}$. Moreover, water separability of the fuel,

which can be measured by the sedimentation test according to ASTM D 1401 at 25 °C, see Section 4.3.4, should be 270 s ± 30 s, when 75 % of test fuel is separated. To generate the fine emulsified water droplets (D_{50} of 60 μm) a specific orifice plate which produces a 260 hPa ± 10 hPa differential pressure across the plate is used, and for the coarse droplets (D_{50} of 300 μm) the pressure decreases to 48 hPa ± 5 hPa by changing the plate. The test procedure requires control of the temperature to 23°C ± 2°C for either 60 min if 2% (v/v) water concentration is injected, or for 90 min if 0.15% (v/v) (1500 *ppm*) water is injected into the test fuel.

To measure the filter efficiency, the water content of the test fuel is measured via the Karl Fischer titration set-up, see Section 3.3.3, after 10 min of the test from the sampling point (7), Figure 2-8. Undissolved water is monitored downstream of the filter (sampling point 17) at 10 min intervals by subtracting the original water content from the total water content measured via the coulometer. The instantaneous and average water separation efficiencies are calculated by Equation 2-24 and Equation 2-26 respectively. Note the water concentration refers to the concentration of undissolved water in fuel.

$$\eta_i = \frac{c - c_i}{c} \times 100$$

Equation 2-24: calculation of Instantaneous water separation efficiency [48]

Where:

η_i : Instantaneous water separation efficiency (%);

c : Specified test water concentration (*ppm* (v/v));

c_i : Downstream water concentration (*ppm* (v/v)) of sample i .

$$C_{av} = \frac{\sum c_i}{n}$$

Equation 2-25: calculation of average downstream water concentration [48]

Where:

C_{ac} : Average downstream water concentration (*ppm (v/v)*);

n : Number of samples.

$$\eta_{av} = \frac{c - c_{av}}{c} \times 100$$

Equation 2-26: calculation of average water separation efficiency [48]

Where:

η_{av} : Average water separation efficiency (%);

C_{ac} : Average downstream water concentration (*ppm (v/v)*) - Equation 2-25.

2.5.3 SAE J1488 procedure [102]

The American standard test procedure SAE J1488 (revised in 2010) suggests a test stand (Figure 2-9) that uses a centrifugal pump (5) (3500-rpm, 1Hp) to generate emulsified water in diesel fuel before introducing it to the test filter. The test fuel is a ULSD fuel treated with Fuller's Earth or clay cartridge filters with a controlled IFT between 15 and 19 *mN/m* using monoolein as a surfactant, which is a non-ionic lipid and compound of monoglycerides [103]. The DSEP rate (ASTM D 7261-08), see Section 4.3.3, for the test fuel should be greater than 75. The procedure describes a test in which the fuel flow rate can be as high as 25 *l/min*, and the water injection flow rate is defined as 0.25% of the main flow rate. Although the exact average diameter of droplets is not defined, the droplet size distribution is expected to be fine and suitable to test pressure side filters.

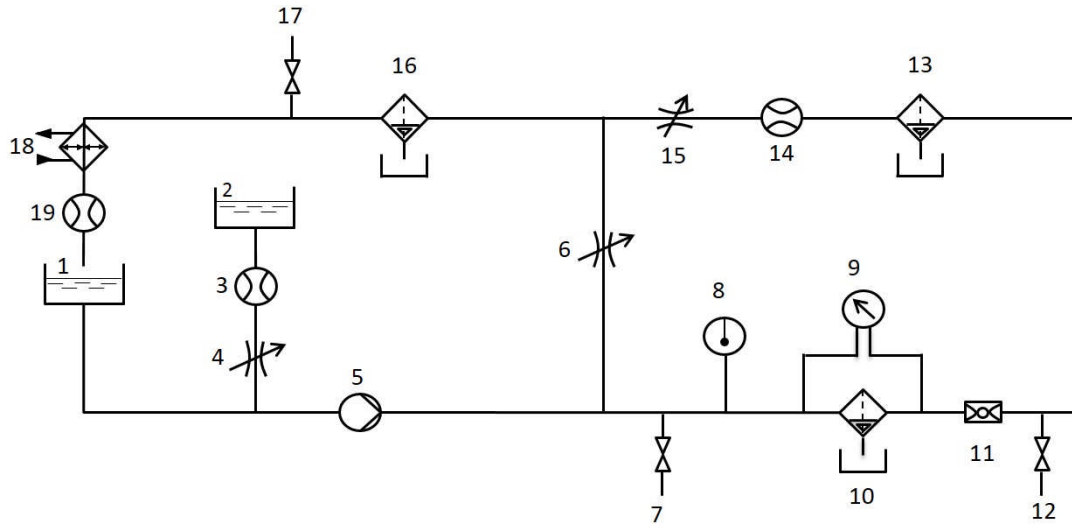


Figure 2-9: Schematic of the SAE J1488 test rig [102]

The test system components are as following:

- | | |
|---------------------------|-------------------------|
| 1- Fuel tank | 8- Thermometer |
| 2- Water tank | 9- Monometer |
| 3, 14, 19- Flow meter | 10- Test filter |
| 4, 6, 15- Adjustable vale | 11- Static mixer |
| 5- Main pump | 13, 16- Clean-up filter |
| 7, 12, 17- Sampler | 18- Heat exchanger |

Similar to the ISO 16332 test procedure, the efficiency of the test filter is calculable by measuring undissolved water content from the effluent sampler (12), in time intervals of 20 min, until either the pressure drop or the water content exceeds an upper limit specified by the user, or an equilibrium pressure drop is obtained at a minimum of 2.5 h in to the test. Testing is recommended to be carried out at $26.6^{\circ}\text{C} \pm 2.5^{\circ}\text{C}$.

2.5.4 SAE J1839 procedure [104]

The SAE J1839 standard defines a test procedure to evaluate the separation efficiency of fuel filters faced with coarse dispersed water droplets. The designated test stand (Figure 2-10)

generates water droplets with a large median size (D_{50}) between $180\ \mu\text{m}$ and $260\ \mu\text{m}$ by using a water dispensing device (6) which has a nozzle and injects water into the main stream on the pressure side of the fuel pump (5).

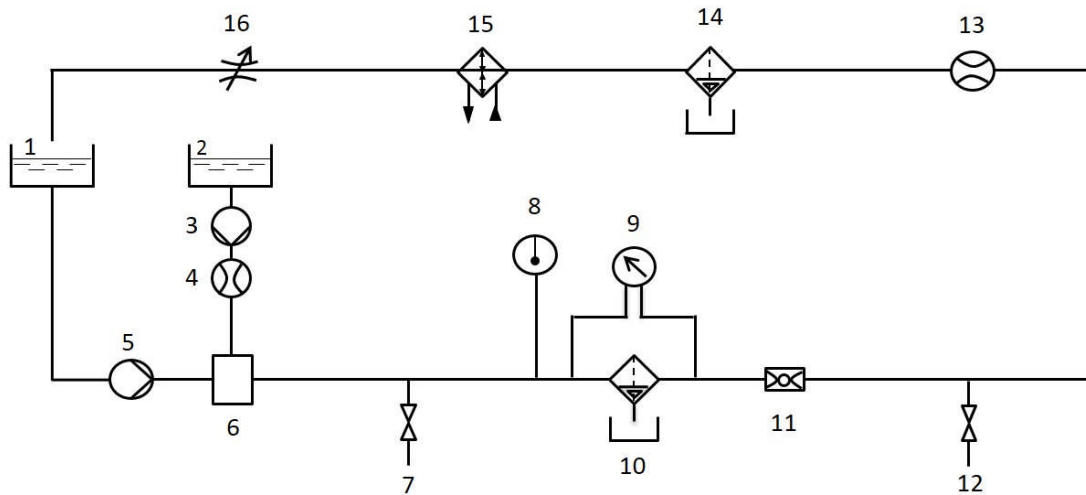


Figure 2-10: Schematic of the SAE J1488 test rig [104]

The test system components are as following:

- | | |
|----------------------------|---------------------|
| 1- Fuel tank | 7, 12- Sampler |
| 2- Water tank | 9- Thermometer |
| 3- Water pump | 10- Test filter |
| 4, 13 - Flow meter | 11- Static mixer |
| 5, Fuel pump | 14- Clean-up filter |
| 6- Water dispensing device | 15- Heat exchanger |

The velocity of both water injection and the main stream as well as the diameter of the nozzle govern the droplet size distribution. The test fuel, flow rates, test temperature and the test procedure are similar to the SAE J1488, however the equilibrium pressure drop potentially arrive at 30 min in to the test. The SAE standard reports the water separability using the separometer giving the DSEP value (see Section 4.3.3).

2.6 Influential parameters on the water separation performance of nonwoven coalescing media

A fuel-water separator medium interacts with the fuel containing emulsified droplets as it passes through. In this section, parameters known to affect the overall performance of the medium and its quality factor are discussed.

2.6.1 Fuel and emulsion characteristics

Fuel properties such as viscosity, IFT and surfactant content affect water droplet size, which consequentially influences the separation efficiency of the coalescing medium. Moreover, fuel chemistry influences the water content of the fuel and the presence of bio-diesel can increase the amount of dissolved water in the fuel. Petiteaux [11] showed that 20:80 blends of bio-diesel/mineral diesel (B20) reduce water separation via the sedimentation test and IFT by 1.5% and 19% respectively, and that B20 can possess a saturation level more than twice that of mineral diesel. Other studies [20, 28, 29] found that the IFT and water separation behaviour of blends containing more than 20% bio-diesel are very similar to pure bio-diesel (B100), and the change in both parameters does not hold as the proportion of bio-diesel increases up to B100. This is because bio-diesel chemistry is dominant at the interface of water and fuel at these concentrations. Tang [20], Tat [105], and Yuan [106] claimed that the fuel viscosity can almost double if bio-diesel is blended into mineral diesel, which can be beneficial for capturing small particles, e.g. $<20\mu m$, by the inertia impaction mechanism as a fuel of high viscosity generates a higher drag force in the fluid than a fuel of low viscosity. Owing to the influence of bio-diesel on IFT and emulsion stabilisation, the same study reported more challenging water separation than in mineral diesel. Using ISO 16332 test stand methodology, the addition of just 5% bio-diesel (B5) has been found to reduce water separation efficiency in the fuel from 95% to 85% due to a decrease in the fuel IFT (22.9 mN/m to 12.9 mN/m) as well as increase the separation

time (13s to 150s - according to the sedimentation test, ASTM D 1401) [28]. In other work, Petiteaux [11] and Schutz [50] reported that water separation from ULSD fuel is more challenging than Low Sulphur diesel (LSD) due to the presence of additives to improve lubricity, cetane number (CN), and deposit control in the ULSD fuel. Schutz [50] also suggested that in the presence of surfactants, the dynamic movement of surfactant molecules from the bulk fluid to the fuel-water interface or fibre/fuel interface (diffusion transport of additives) results in a time-dependent decrease in IFT as well as a time dependent increase in the contact angle of water on the fibre surface. No absolute correlation could be found between changes in IFT and that of water separability (coalescence of water droplets) caused by different surfactants [11, 50]. This is in agreement with the results of Pangestu [12], which suggested that droplet size and its persistence in an emulsion is not only driven by IFT, but also the ability of the surfactant to stabilise dispersed droplets from coalescence.

2.6.2 Structure-property-performance relationships of nonwoven coalescence media

In Sections 2.3.3 and 2.4.2.2, it was explained that the presence of fibrous coalescing media enhances the droplet coalescence but can also cause a pressure drop that can adversely affect the quality factor. In the literature different approaches have been made to reduce the dependency of pressure drop and coalescence efficiency and improve quality factor of coalescing media by improving the efficiency and reducing the pressure drop. To achieve this, researchers have attempted to modulate the macro- or/and micro-structural properties of the fabric, for instance, by utilising different polymers, augmentation of coalescing media with submicron fibres and nanofibres, modification of the medium structure and changing fibre surface wettability.

2.6.2.1 Properties of nonwoven fuel-water separation media

The macro-structural properties of a nonwoven medium such as the compactness, structural isotropy, pore structure and thickness can be expected to affect performance as liquid is passed through, both in terms of pressure drop and separation efficiency. Practically, such parameters depend on the way in which the fabric is manufactured and how the filter medium is constructed.

Media arrangements

Limitations are known to exist with traditional wet-laid coalescing media composed of resin bonded staple fibre cellulose and glass fibres. These include the risk of incompatibility of the resin with the fuel, fibre shedding due to the short fibre length, which can damage engine components and high pressure drop. [15, 16]. In composite nonwoven structures, cellulosic media are usually combined with phenolic resins, which have excellent environmental and heat stability, and the resin also facilitates pleating as well as a mechanical support to the meltblown web which is itself a stable media with broad chemical compatibility and high dirt hold capacity [16]. Both single layer and composite coalescing media have demonstrated excellent separation efficiency in diesel fuelling systems, i.e. 99.9% efficiency in separating particles greater than $25\ \mu\text{m}$, however, their suitability for separation of smaller size droplets ($<25\ \mu\text{m}$) present in HPCR injection system is in serious doubt [12, 13, 16]. It has been claimed that cellulosic media cannot fulfil the requirements for next generation fuel filters due to their relatively high fibre diameter, and glass fibres are increasingly unacceptable because of the risk of fibre migration due to shedding [16]. The third generation of coalescing water separators primarily consist of multiple layers polyester meltblowns, which provide more flexibility to engineer structure and properties in terms of fibre diameter, fabric porosity and other structural features [12, 16, 17, 34, 43, 44].

Viswanadam [107] suggested a tubular geometry of nano-membranes over the flat sheet configuration of a water separation media to improve the quality factor, and this has shown promising results. The improved performance has been attributed to the hypothesis that the tubular structure provides a geometry promoting easy detachment of water droplets from the surface of the nano-membrane. Another attempt to control the pressure drop has been reported using hydrophobic drainage channels embedded into hydrophilic glass microfibre coalescence filter media to aid aerosol filtration [97, 108, 109]. This methodology has been reported as a suitable way to reduce saturation of liquid inside the filter and maintain a low pressure drop. Vibrating the filter holder for both hydrophilic and hydrophobic media was also demonstrated to encourage detachment of large coalesced droplets from the fibre surface [110, 111].

Media thickness

It is known that an increase in both filter thickness and basis weight can lead to an increase in both capture efficiency and pressure drop across the medium, however, there is usually a disproportionate increase in the pressure drop, leading to a deterioration of the quality factor [74]. The increase in separation efficiency can be attributed to a higher solid surface area and lower face velocity, however, the reduced porosity and permeability of the fabric increases flow resistance [30-32, 39-42]. To address the high pressure drop in thick multilayer coalescing media, some researchers have suggested inclusion of submicron fibres integrated within a fabric with a graduated porosity and permeability from the influent side to the effluent side of the medium [32, 112, 113].

2.6.2.2 Fibre properties

Surface wettability of fibres and fibre diameter can also influence coalescing performance by affecting the interaction with the fuel and water.

Fibre wettability

Controlling the wettability of fibres has been a very attractive approach such that several studies have been reported seeking to identify an optimal hydrophilicity for fibre mat assemblies to enable maximum efficiency while controlling pressure drop [12, 30-32, 34, 47, 74, 93, 96, 112, 114-117].

Kulkarni et al. [96] modified the overall hydrophilicity by sandwiching layers of PET and PP microfibre with glass microfibre layers (all the samples were composed of inlet and outlet layers made of glass fibres) and characterised the effect using the L/H ratio (lipophilicity/hydrophilicity – see Section 7.3.1.1). They reported that at a face velocity of about 8.8 mm/s, an L/H ratio of about 3-10 and 25 are the optimum ranges of hydrophilicity for the best quality factor of glass/PP and glass/PET layered media respectively. In other work, Kulkarni et al. [115] also combined the effects of fibre size and intermediate wettability by blending electrospun PP fibres with glass microfibres at a face velocity of around 8.8 mm/s. They suggested a L/H range of about 0.9-1.2 as the best to avoid excess pressure drop using PP fibres with average diameters between 300 and 900 nm. Patel et al. [60, 114] explored the contribution of a hydrophobic inlet layer on the quality factor of a glass fibre substrate for the separation of water from ULSD fuel at different face velocities of 0.33, 0.67, and 1 mm/s. They used electrospun Poly(vinylidene fluoride-co-hexafluoropropylene), PVDF-HFP with an average diameter of 334 nm, as well as electrospun PP submicron fibres with an average diameter of 876, 1082, and 1710 nm, as the inlet layer of the medium. They reported that the hydrophobic nano-layer improved the quality factor of the glass fabric in both cases, although the total porosity of the medium reduced from 96% to 82% in the case of the PVDF-HFP layer and from 96% to 92% in the case of the PP fibre layer by adding the nano-membrane. The study also showed that the quality factor decreases by increasing the face velocity in all cases,

however, the PP composite nonwovens showed better performance due to the limited effect on pressure drop, attributable to the relatively large diameter of these fibres compared to the PVDF-HFP fibres. In other work, Rajgarhia et al. [117] examined the quality factor of glass fibre fabrics coated with a hydrophobic nanofibrous sheet produced by the gas jet fibre method at a face velocity of 0.33 mm/s with a mean droplet size of 20 μm . In this work, the porosity of the medium was slightly reduced by the coating process (97.1% to 96.3%), however, a large increase in quality factor of the single glass fibre layer was reported. The nanofibres were composed of randomly distributed hydrophobic polyvinyl acetate (PVA) and hydrophilic polyvinylpyrrolidone (PVP) in the fibre cross section. Krasinski et al. [116] also claimed that a hydrophobic PP meltblown inlet layer performed better in terms of coalescence performance than a hydrophilic glass fibre inlet layer due to greater deposition of the coalesced droplets from the structure. They also suggested applying an electrostatic charge on the hydrophobic inlet layer to improve the overall efficiency. Manzo [118] used stainless steel microfibre media in aerosol filtration to demonstrate an improved quality factor compared to similar glass fibre fabrics as a result of higher permeability and surface energy towards the liquid droplets.

Fibre diameter

The benefits of decreasing fibre diameter and use of submicron fibres is a well-known strategy to increase separation efficiency for particles smaller than 100 micrometres in diameter, however, the pressure drop can also increase due to a reduction in permeability and porosity [12, 34-38, 45, 119-122].

Patel et al. [97] and Chase et al. [123] showed that augmentation of the fabric by inclusion of sub-micron fibre is promising in improving the quality factor due to higher separation efficiency as well as higher slip-flow enhanced by the sub-micron fibres leading to a lower

pressure drop. They showed that use of submicron fibres can produce lower density structures with large surface area to mass, high pore volume, and high permeability compared to micro-diameter fibres of the same fibre length. In this case, the efficiency is higher as there is higher slip flow on submicron fibres which increases the probability of particle capture, and the pressure drop is lower as a lower drag force is created by the submicron fibres and the permeability is higher. However, in the case of media of equivalent areal density, the pressure drop challenge persists as a result of the high packing density and higher resistance to flow. However, the pressure drop can increase more slowly slower than the efficiency when the fibre diameter decreases in a fabric of equivalent areal density [97, 123]. Wang et al. [124-126] proposed an environmental-friendly solvent-free melt-process technique to produce robust microfibre and nanofibres of PP and PA6 for incorporation into a water/diesel separator element by hydroentanglement. A higher quality factor than for a conventional meltblown medium was obtained attributable to the submicron fibre content and higher solid surface area and porosity. Shin et al. [119, 120] suggested that a quality factor can be achieved by optimising the submicron fibre content to enhance droplet capture by increasing solid surface area and reducing the pore size whilst maintaining a high porosity. Pangestu et al. [12] claimed that filter media can perform efficiently and independently of the fuel surfactant level if the solid surface area is sufficiently high e.g. more than 200 m²/g. Bansal et al. [32] and Agarwal et al. [112] reported in his experiments that a decrease in pore size and an increase in fibre wettability increased coalescence efficiency.

2.7 Summary

Water separation from EN590 fuel containing surfactants including bio-diesel is highly challenging because of the small and stable droplets that are presented to the fuel filter system.

The properties of these emulsion as well as the nonwoven coalescing media used to remove the water from the diesel fuel directly impact the coalescing performance and currently, there is no universally applicable filter media that can fully satisfy current industrial requirements.

In the literature, the impact of bio-diesel and surfactants on water-in-fuel emulsion properties and water separation has been investigated, however, comparative data on water droplet size distributions and water separation performance associated with blends of diesel/bio-diesel and diesel/surfactants is lacking. Therefore, further research is needed on the properties of bio-diesel and mineral diesel as well as characteristics of water-in-fuel emulsion with and without surfactants to provide a clear picture of separation challenges facing coalescing media in fuel-water separation applications.

Based on the literature, it has been established that a coalescing medium should comprise a structure with the desired wettability, high surface area, 3D structure, and porosity to perform adequately. To address this, multilayer coalescing media are more attractive, because of their ability to be engineered to provide a tailored structure. However, there are relatively few systematic studies of their coalescence performance which take account of their wettability especially in presence of surfactants present in the fuel. Moreover, as this type of media is usually supported by a polymeric mesh support, they function in conditions where their configuration may be slightly different to that which applies in a tension-free state because they are compressed by the liquid flow during operation of the engine. Accordingly, the extent to which configurational modifications to existing coalescence media can improve coalescing media needs to be elucidated.

CHAPTER 3

Fuel Characterisation

3.1 Introduction

As reported in Section 2.3.4, fuel additives including bio-diesel (B100) tend to act as surfactants (surface active agents), such that fuel-water interfacial tension (IFT) is reduced and water droplets are more stabilised in the fuel containing these additives [12, 13, 15-17, 47-50]. It has been reported that bio-diesel can change the viscosity of diesel, which influences the shear stress in the fluid and therefore the characteristics of water droplets [20]. Bio-diesel is also more hygroscopic than petroleum-diesel and has affinity to water due to its alkyl-ester groups and unsaturated molecular structure [20, 22-27]. This can lead to an increase in the water content of the fuel such that a water saturation level of ≥ 1300 ppm has been reported for B100 [20, 28, 29]. Accordingly, International standard test methods such as ISO 16332 [48] and SAE J1488 [102] recommend adding monoolein (1-Oleoyl-rac-glycerol) as an universal surfactant to a reference grade diesel for the water separation tests, to adjust the IFT of the test fuel and simulate the presence of fuel additives including bio-diesel. However, to the best of the author's knowledge, no comprehensive data exists in the literature comparing the effects of bio-diesel and monoolein on fuel properties. Accordingly, the main aim was to characterise diesel fuel blended with bio-diesel and with monoolein and compare the effect of blending in relation to their properties. To achieve this, bio-diesel and monoolein were separately mixed into the reference grade diesel fuel in different concentrations and the resultant changes in fuel properties, specifically the IFT, water content, density and viscosity were investigated.

Ultimately, this fuel characterisation work was required to determine the relationship between the fuel properties and the size of water droplets, as well as their separation behaviour when emulsified in a fuel blend. These particular experiments are detailed in Chapter 4.

3.2 Stock fuels and additives

Table 3-1 shows the list of fuels and fuel additives used in the present study. Selection of these materials was guided by current industrial standards and commercially available fuel composition. For consistency, and to enable comparison of data, the same fuels and additives were used throughout.

Table 3-1: Fuel and fuels additives used in the project

Category	Material	Description
Reference fuel	Mineral diesel (REF)	Ultra-Low Sulphur Diesel (ULSD) reference grade fuel, pure and with no bio-diesel content, in accordance with CEC RF-06-03:2003 standard fuel specifications.
Fuel additive	Bio-diesel (B100)	Rapeseed oil methyl ester (RME)
Fuel additive	Monoolein	(1-(cis-9-Octadecenoyl)-rac-glycerol

In this work, the bulk fuel was an additive-free reference grade mineral diesel, denoted as REF. This fuel was a standard Ultra-Low Sulphur Diesel (ULSD) produced by the Hess Corporation (Germany) and based on the specifications of the reference grade test fuel, CEC RF-06-03:2003 fuel, which was provided by CEC secretariat services, as recommended in ISO 16332. The bio-diesel, Carcal B100 RME (Off-road), originated from pure rapeseed oil methyl ester (RME) and was produced by Petrochem Carless Limited (Surrey, UK) and based on specifications of the standard bio-diesel fuel provided by BS EN 14214:2012+A1:2014, denoted as B100 throughout. Bio-diesel oxidation levels were not measured, but all fuels for testing were extracted from unopened barrels. Figure 3-1 illustrates the appearance of the bio-diesel and reference diesel used in this research.

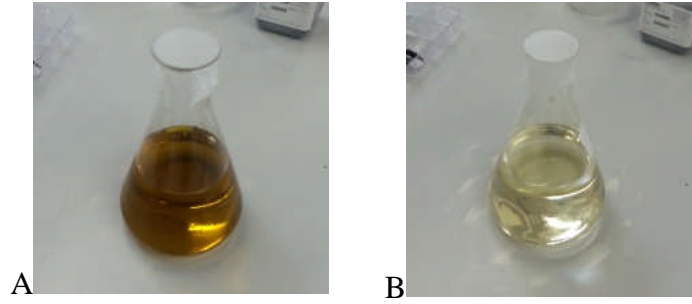


Figure 3-1: A) 100% Bio-diesel, B) Reference diesel fuel

The monoolein surfactant, (1-(cis-9-Octadecenoyl)-rac-glycerol, with a density of 969 kg/m^3 , was purchased from Sigma Aldrich (UK) and along with the REF and B100 fuel was supplied by the external sponsor of this research, Parker Hannifin Manufacturing (UK) Ltd., Racor Filter Division Europe (Dewsbury, UK).

3.3 Experimental methods and apparatus

This section details the test methodology for characterisation of the fuel blends, most importantly the interfacial tension (IFT), water content, density and dynamic viscosity. The IFT and water content measurements were performed using equipment available in the R&D laboratory of the project sponsor, and the density and viscosity of the test fuels were determined in the laboratories of the University of Leeds (Leeds, UK).

3.3.1 Preparation of the test fuel blends

Two sets of test fuels, namely bio-diesel blends and monoolein blends were evaluated in this research because of their practical relevance in industry and their applicability to the ISO testing of fuels. Bio-diesel blends were prepared by mixing volumes of bio-diesel (B100) into the reference grade diesel (REF). Bio-diesel fuel blends were designated as “Bi” where i = the volume fraction of bio-diesel $(v/v) \times 100$. B5 therefore consists of a blend of REF and 5%

bio-diesel. The mineral diesel and surfactant blends were prepared by mixing a specified volume (*ppm*) of monoolein in the reference grade diesel (Mi), where i = the volume fraction of monoolein in *ppm* (v/v) $\times 1,000,000$. M200 therefore refers to a blend of REF with 200 *ppm* (v/v) monoolein. To prepare the blends, the components were volumetrically added into a bucket where they were well agitated manually using a glass rod for a period of time about 1 min. The ambient temperature of the laboratories in the University as well as sponsor site was kept in a range of 22-25 °C as the daily laboratory routine such that a constant fuel temperature was assumed for all the measurements throughout. Table 3-2 summarises the fuel compositions of each blend used in the present study.

Table 3-2: Description of the test fuel blends compositions

Test Fuel	Compositions (v/v)	Test Fuel	Compositions (v/v)
REF	100% REF – 0% bio-diesel	M200	REF – 200 <i>ppm</i> monoolein
B5	95% REF – 5% bio-diesel	M400	REF – 400 <i>ppm</i> monoolein
B10	90% REF – 10% bio-diesel	M600	REF – 600 <i>ppm</i> monoolein
B15	85% REF – 15% bio-diesel	M1000	REF – 1000 <i>ppm</i> monoolein
B20	80% REF – 20% bio-diesel		
B30	70% REF – 30% bio-diesel		
B50	50% REF – 50% bio-diesel		
B100	0% REF – 100% bio-diesel		

3.3.2 Interfacial tension (IFT) measurements

From the macroscopic point of view, surface tension (N/m), or the surface free energy (J/m²) of a liquid is a force (energy) required to increase the surface area of the liquid by one unit [63, 64, 127]. This tension originates from imbalanced intermolecular forces between the molecules

on the surface of the liquid that are not completely surrounded by other molecules to be pulled in all directions. The surface tension at the interface of two immiscible liquids is called the interfacial tension (IFT) (N/m) and is measured based on Fowkes' equation (Equation 2-1 in Section 2.3.1.2) [63, 64]. A higher interfacial tension is therefore indicative of weaker intermolecular interactions between the two surfaces.

The international standard ISO 6889:1986 explains test procedures to measure IFT by using a measuring device (probe) which can be a plate (Wilhelmy plate method), stirrup, or a ring. In principle, the set-up consists of a probe made of platinum which is easy to clean and chemically inert and has a very high surface energy. To measure the IFT of two immiscible liquids, the probe is suspended on a precise balance and its edge is made to touch the interface between the liquids, where the liquid with a lower density is placed on top of the one with a higher density. Once the platinum probe is in contact with the interface, the liquid tends to be drawn up on the probe into the form of a meniscus. This applies a force on the probe that can be measured by the balance. The maximum detected force can then be used to measure the IFT according to Equation 3-1. Due to the high surface energy of platinum, a contact angle of zero with the interface is assumed in the calculation. The same principle is applied for the surface tension measurement except the low-density liquid is replaced by air and the probe is placed at the surface of the liquid (interface of the liquid with air).

$$\gamma_{w/o} = \frac{F}{2l \cos \theta}$$

Equation 3-1: Approximate equation for measuring the IFT [63, 64, 127]

Where:

F : Maximum detected force by tensiometer (N);

$\gamma_{w/o}$: Interfacial tension between water and fuel (N/m);

l : Length of the measuring plate (m);

θ : Contact angle between the interface and the plate.

3.3.2.1 Experimental setup and procedure

In this work, the mean IFT of each fuel blend was determined using the Wilhelmy plate method via tensiometry based on five replicates per fuel sample. For these measurements, the fuel blends listed in Table 3-3 were prepared based on the procedure explained in Section 3.3.1.

Table 3-3: Test fuel blends for the IFT measurement

Fuel type	Fuel ID						
Reference grade	REF						
Bio-diesel blends	B5	B10	B15	B20	B30	B50	B100
Monoolein blends	M200	M325	M400	M600	M1000		

The test setup and requirements included a Kruss K20 Easy Dyne force tensiometer consisting of a fixed positioned balance on top and an adjustable positioning stage beneath the balance, a platinum plate, fire-proof glass sample vessels with an outer diameter of 70 mm, disposable plastic pipettes, a torch/lighter, and Propan-2-ol (Isopropanol-(CH₃)₂CHOH) as a cleaning solvent. All the measurements were carried out at a room temperature of 22-25 °C.

For each measurement, the measuring probe and glass vessels were thoroughly cleaned by washing with isopropanol and drying with clean compressed air in a fume cupboard. The probe and glass vessels were heated using a torch afterwards, to ensure no trace of residual contamination was present. A blue flame is an indication that the vessel and/or probe are free of such contamination. To start the measurement, the clean probe was suspended on the balance, and the approximate volume of 50 ml of the fuel sample (low density phase) was poured into a clean glass vessel positioned on the adjustable positioning stage of the

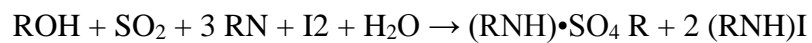
tensiometer. The stage was raised manually such that the clean probe was completely immersed in the fuel (close to, but not touching, the bottom of the vessel). At this stage, the buoyancy/gravitational force acting on the measuring plate was tared such that the balance was calibrated to enable measurement. The stage was then lowered such that the probe was removed from the fuel. The fuel sample was then kept aside, and a new clean vessel was used to pour 40-50 ml of distilled water (high density liquid). The measuring probe was cleaned and suspended on the balance again and the water vessel was positioned right below the measuring plate by adjusting the height of the sample stage. A software command was activated by pressing the “surface detect” button so that the sample stage raised automatically and the tensiometer detected the surface of the liquid once the probe touches the surface. Once the surface was detected, the entire volume of the fuel sample used for the calibration was transferred carefully into the vessel on-board using a plastic pipette. The transfer was performed without disturbing the liquid interface and avoiding creation of any bubbles [63, 64].

To avoid disturbance to the interface or the plate touching the water surface while transferring the fuel, it was found convenient to immerse the probe 3 mm beyond the water surface (without breaking it) and then to relocate it after the transfer. Calculation of the IFT of the liquids in mN/m could therefore be performed using the tensiometer.

3.3.3 Determination of water in fuel

Water content of fuel is usually determined using the Karl Fischer titration technique [128, 129]. Titration, in principle, refers to the calculation of a substance concentration in a solution by carefully monitoring chemical reactions between the solution and a standard reagent with a known concentration. The test apparatus and method are described in ISO 760:1978.

Herein, the coulometric Karl Fischer titration method was used to determine total water content including dissolved and undissolved water in the test fuel blends. The coulometry Karl Fischer titration works based on a reaction between sulphur dioxide, a base (RN), iodine, water, and an alcohol (ROH) as a solvent (Equation 3-2), in which equimolar amounts of water and iodine is consumed. Such that, water content of the solution can be calculated by monitoring the amount of iodine consumed in reaction with water via measuring changes in electrical conductivity of the reaction solution.



Equation 3-2: Simplified chemical reaction of the titration process [128, 129]

The coulometric titration set-up has a titration vessel composed of an anode compartment with a sensor electrode (polarized double-platinum-pin) and a cathode compartment with a generator electrode. The compartments are separated by an ion-permeable membrane. The analyte consists of sulphur dioxide, iodide salts, a buffer, and a solvent in which iodide (I⁻) is oxidized to iodine (I₂) to react with water, and the catholyte consists of a reagent which completes the oxidation reaction by reducing hydrogen ions to hydrogen. The electron transfer happens at the generator electrode by creating current pulses.

The number of moles of electrons used in this iodine generation is used to calculate the amount of water in the sample. The sensor electrode detects when there is a small excess of iodine, which means there is no water to react with in the vessel. This detection, which is in the form of voltage reduction at the sensor electrode, stops current and iodine generation at the generator electrode and calculation begins automatically by the built-in software in the device.

3.3.3.1 Experimental setup and procedure

Mettler-Toledo-C20 Compact Karl Fischer coulometer was used for this test. HYDRANAL® - Coulomat AK and HYDRANAL® - Coulomat CG reagents (Sigma Aldrich) were used as the anolyte and catholyte respectively and the fuel blends, listed in Table 3-4, were prepared for this measurement following the procedure explained in Section 3.3.1. Bio-diesel used in this test was taken from unopened barrels and as such could be considered as fresh fuel. To ensure the same conditions for the monoolein blends, the test fuels were not conditioned or aged, and they were tested immediately after preparation.

Table 3-4: Test fuel blends for the water content measurement

Fuel type	Fuel ID						
Reference grade	REF						
Bio-diesel blends	B5	B10	B15	B20	B30	B50	B100
Monoolein blends	M200	M325	M400	M600	M1000		

The titration started by filling the anode and cathode compartments of the titration vessel with 100 ml Coulomat AK and 25 ml Coulomat CG respectively. Before conducting any measurements, the set-up was calibrated using the built-in software. Once the calibration was complete, 1- 1.5 ml of a fuel sample was taken, weighed using an accurate balance with an accuracy of four decimal places, and injected into the titration vessel (anode compartment). The quantity of the sample mass was inputted for the automatic analysis of the water content via the software.

At the end of the analysis, e.g. less than 5 min, the mass *ppm* of water was obtained and converted to the equivalent volumetric *ppm* using Equation 3-3.

$$\text{Titration reading (ppm v/v)} = \frac{\text{Titration reading (ppm w/w)} \times \text{Fuel density (kg/m}^3\text{)}}{\text{water density (kg/m}^3\text{)}}$$

Equation 3-3: conversion of mass *ppm* to volume *ppm* [102]

For each of the fuel blends, at least five replicates were taken to calculate the average water content. Fresh chemicals were used to refill the titration vessel after every 40-50 measurements.

3.3.4 Determination of saturation level of dissolved water in fuel

The water saturation level of a fuel is characterised by the maximum *ppm* of water by volume that can be dissolved in the fuel during a certain period of time. In principle, if the water content of a fuel exceeds the saturation level, free or emulsified water will be formed, therefore, the water saturation level can be used as an indication of the likelihood of undissolved water being present in the fuel. Moreover, the capability of a fuel to absorb water can be a consequence of aging. The water saturation level measurements were made based on the procedure described in the SAE J1488:2010 standard.

3.3.4.1 Experimental setup and procedure

To measure the saturation level of the test fuels listed in Table 3-5, 75 *ml* of a fuel sample was placed in a clean and dry bottle and 25 *ml* of deionised water was carefully inserted into the bottom of the bottle using a 50 *ml* syringe with a long, large diameter needle and without agitating the fuel-water interface. A PTFE coated magnetic stirrer was placed in the bottle and the bottle was covered by a rubber diaphragm film and placed on a stirrer for 24 h using the lowest possible speed such that no interface agitation occurred. After this initial aging period, a sample from the fuel on top of the bottle was taken by a syringe to be analysed by the Karl Fischer coulometer following the procedure explained in the Section 3.3.3.

Table 3-5: Test fuel blends for the determination of water saturation point

Fuel type	Fuel ID		
Reference grade	REF		
Bio-diesel blends	B5	B50	B100
Monoolein blends	M400		

At least three replicates were used to determine the mean saturation level of each fuel blend. The test fuels were prepared following the procedure explained in Section 3.3.1.

3.3.5 Density measurement

Density is defined as the mass of the substance divided by its volume in units of kg/m^3 [130]. The density was measured according to ISO 3838: 2004, which recommends a test procedure using a capillary-stoppered pycnometers. The density values were required to calculate the dynamic viscosity of the fuel blends.

Based on the ISO 3838:2004 standard procedure, the density of 25 ml of a test liquid, kg/m^3 , is calculated compared to the density of an equal volume of water at the same temperature based on Equation 3-4. An equal volume of each liquid is ensured by using a 25 ml capillary-stoppered pycnometer (Figure 3-2).



Figure 3-2: Capillary-stoppered pycnometers density bottle

$$\rho_t = \frac{(m_t - m_o)\rho_c}{(m_c - m_o)} + C$$

Equation 3-4: Density of a liquid at any temperature [130]

Where:

ρ_t : Test liquid density at the test temperature, (kg/m^3);

ρ_c : Water density at the test temperature (from the reference chart), (kg/m^3);

m_t : Mass of the pycnometer filled with the liquid under test at the temperature, (g);

m_c : Mass of the pycnometer filled with the water at the temperature, (g);

m_o : Mass of the empty pycnometer at the temperature, (g);

C: Correction for air buoyancy (from the reference chart), (kg/m^3).

3.3.5.1 Experimental setup and procedure

The fuel samples (Table 3-6), were prepared according to the method in Section 3.3.1 and conditioned for 30 min by maintaining the temperature of the bath at 22 °C for all measurements.

Table 3-6: Test fuel blends for the density measurement

Fuel type	Fuel ID					
Reference grade	REF					
Bio-diesel blends	B5	B10	B15	B20	B50	B100
Monoolein blends	M400	M1000				

To calculate the fuel density, ρ_t , based on Equation 3-4, the pycnometer was washed by acetone and dried by clean compressed air. Afterwards, it was calibrated by measuring its weight when empty and filled with distilled water to record m_o and m_c respectively. The pycnometer was cleaned and dried again and was filled with the test fuel to measure m_t at 22 °C. ISO 3838 provides the Buoyancy Correction, C, in tables to enable calculation of the

fuel density, ρ_t . Two replicates per sample were used to calculate mean values. The variation was very low, with a range lower than 0.0006 kg/m^3 .

3.3.6 Dynamic viscosity test

A shear stress is required for a fluid to move and there is a natural resistance that prevents a uniform flow of the fluid throughout its cross section. As a result, the fluid layers move with different velocities relative to each other. This internal resistance, which is also known as the fluid drag force, is attributed to the viscosity of the fluid and is defined as a ratio of the shear stress to the velocity gradient in the fluid stream (Equation 3-5).

$$\tau = \mu \times \frac{du}{dy}$$

Equation 3-5: Shear stress in the fluid [13, 58, 59, 67]

Where:

τ : Shear stress (Pa);

μ : Dynamic viscosity ($Pa \cdot s$);

$\frac{du}{dy}$: Velocity gradient of the fluid layers along its thickness (s^{-1}).

There are two types of viscosity namely, dynamic and kinematic. Dynamic (absolute) viscosity of a liquid, $Pa \cdot s$, is described as the tangential force per unit area required to move a horizontal layer of the fluid with respect to another at a unit velocity when a unit distance between two layers is maintained (Equation 3-5). Kinematic viscosity of a fluid, m^2/s , is defined as a ratio of the fluid dynamic viscosity to its density and is a measure of how resistive it is to flow under the influence of gravity. Viscosity, in both cases, is a function of temperature and pressure, however it is not always a function of the shear stress applied on the fluid. A fluid that has a viscosity independent of the quantity of the shear stress is called a Newtonian fluid while others

are termed non-Newtonian fluids. Diesel fuel is considered as a Newtonian fluid and the ISO 3104 standard describes the test conditions required for calculating dynamic viscosity of petroleum products by measuring their kinematic viscosity. ISO 3105 explains the operating instruments and required glass capillary viscometers for such measurements [131].

3.3.6.1 Experimental setup and procedure

The fuel blends listed in Table 3-7 were prepared for the viscosity measurement following the procedure explained in Section 3.3.1. Based on the recommendations of EN ISO 3104:1996, a BTI® glass capillary viscometer (BS/U-tube, size B) was used for the REF, monoolein blends, and B5, whereas a Technico® glass capillary viscometer (BS/IP/SL size 1) was used for bio-diesel blends containing more than 20% (B20) [132]. Both types of viscometer were of very similar design but had different capillary tube dimensions.

Table 3-7: Test fuel blends for the viscosity measurement

Fuel type	Fuel ID			
Reference grade	REF			
Bio-diesel blends	B5	B20	B50	B100
Monoolein blends	M400	M1000		

The clean U-shape glass viscometers, Figure 3-3, comprised two bulbs, A and E, on each side. A test fuel was poured in the viscometer via the tube L such that the bulb A was filled by the fuel sample with respect to the filling mark G. The measurement had to be carried out at a constant temperature, such that the viscometer was placed in the Townson+Mercer® controlling temperature bath (Figure 3-4) for 30 min to acquire the test temperature, i.e. 25°C.

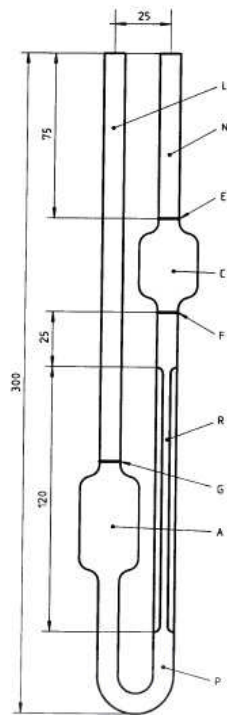


Figure 3-3: U-shape glass viscometers [132]

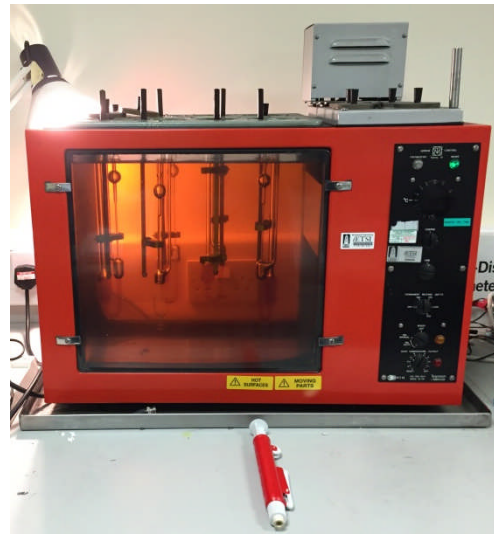


Figure 3-4: Controlling temperature bath set-up

After conditioning the sample, the test liquid was drawn through the bulb C on the tube N to slightly above the timing mark E using a pipette pump. At this point the vacuum was removed and the time, t , taken by the fluid travelling under gravity from mark E to the Mark F through the capillary channel was measured to calculate the kinematic viscosity, ν , using Equation 3-6. The term, C in the equation is the viscometer constant provided by the viscometer manufacturer.

$$\nu = C \times t$$

Equation 3-6: Kinematic Viscosity of a fluid [131]

Based on the ISO 3105 standard, at least two measurements were performed for each test sample to average the flow time for the calculation. The quantity of the kinematic viscosity

(v) of each sample was used to measure their dynamic viscosity (η) using the density (ρ) of each sample according to Equation 3-7.

$$\eta = v \times \rho \times 10^{-3}$$

Equation 3-7: Dynamic Viscosity of a fluid [131]

3.4 Results and discussion

The test fuels were prepared and characterised according to the procedures reported in Section 3.3.1, and the resulting data is now reported to demonstrate the effects of bio-diesel and monoolein content on the overall fluid properties of the fuel blends.

3.4.1 Interfacial tension (IFT) measurements

The bio-diesel and monoolein blends are compared regarding their IFTs (*mean \pm SE*) as shown in Figure 3-5.

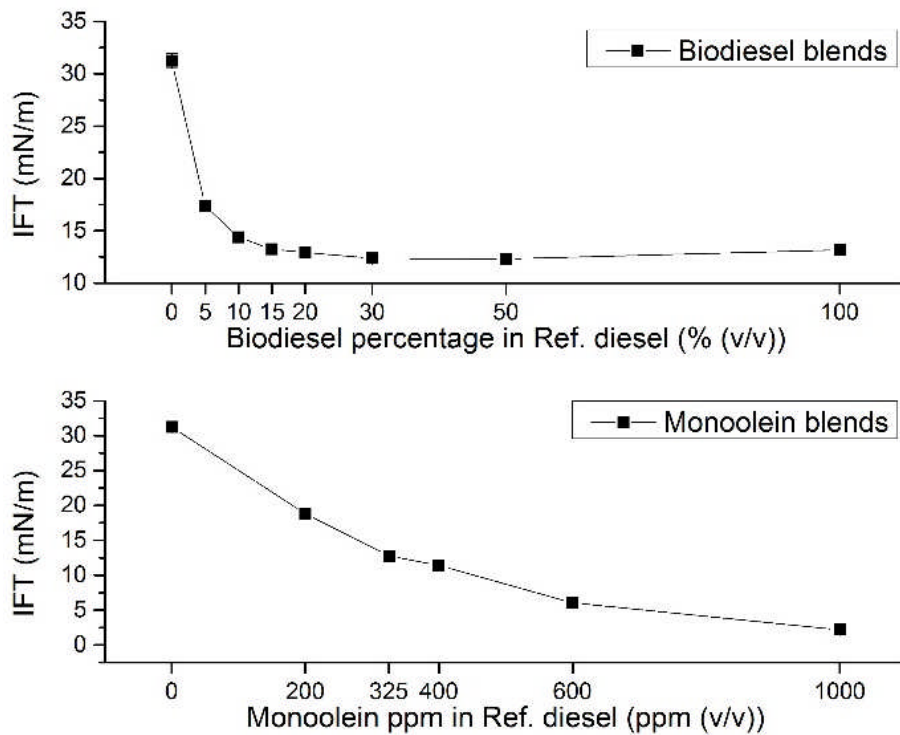


Figure 3-5: IFT of the bio-diesel and monoolein blends (source Table 3-8 in Appendix (A))

The results confirmed that bio-diesel acts as a surface-active agent such that the IFT of the REF fuel reduced from 31.24 ± 0.73 mN/m to 13.17 ± 0.13 mN/m in B100. This is in agreement with findings in the literature [20, 28, 29]. However, note that the trends in the IFT data for the fuels containing bio-diesel and monoolein are not the same when blend proportions increase to B100 and M1000 respectively. As the bio-diesel content increases from B20 to B100, the IFT does not continue to decrease, i.e. the IFT remains almost constant at about 12 mN/m for B20, B30, B50, and B100. However, further decreases in IFT are observed as the monoolein content increases. This can be attributed to the capability of the water and fuel interface to accommodate monoolein molecules to the concentration of 1000 ppm while the interface is not being saturated by them. As a result the IFT decreases by adding more monoolein and the

IFT of 2.18 ± 0.12 mN/m is measured for M1000 (Figure 3-6). This is in contrast to the bio-diesel blends containing more than 20% bio-diesel in which the interface reaches its saturation point and the behaviour of the interface is dominated by the chemistry of the bio-diesel (Figure 3-7). This can be explained by comparing the molar ratios of the bio-diesel and monoolein blends. For instance, the molar concentrations of B20 and M325, which exhibited identical IFTs, are 0.5924 and 0.0009 mol/l respectively (molecular weight of monoolein ($C_{21}H_{40}O_4$) = 356.54 g/mol, bearing in mind that methyl oleate ($C_{19}H_{36}O_2$) has a molecular weight of 296.494 g/mol and is a typical bio-diesel fuel [54]). Thus, a lower number of monoolein molecules are available to saturate the fuel-water interface compared to bio-diesel molecules in each of the fuel blends.

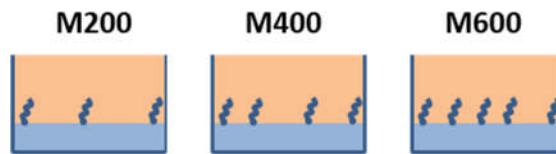


Figure 3-6: Schematic of the interface of water and monoolein blends

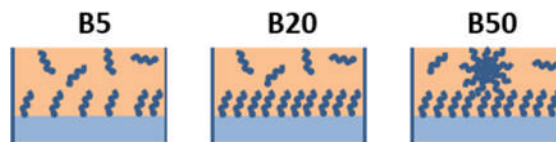


Figure 3-7: Schematic of the interface of water and bio-diesel blends

3.4.2 Water content and saturation level of dissolved water in fuel

The bio-diesel and monoolein blends are compared in terms of their water contents (*mean* \pm *SE*) as shown in Figure 3-8.

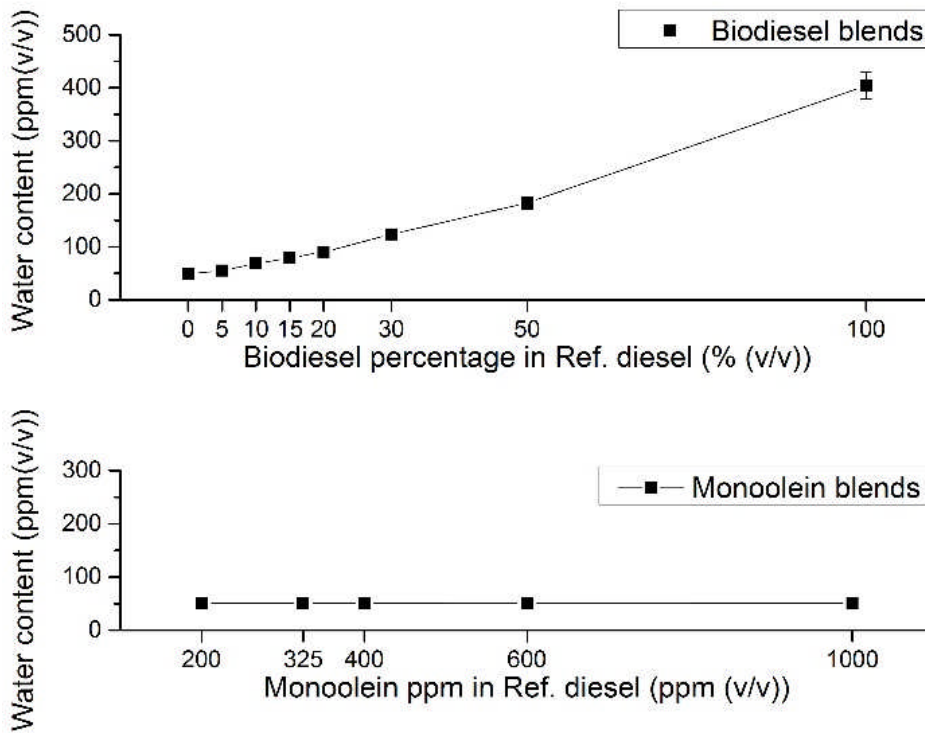


Figure 3-8: Water content of the bio-diesel and monoolein blends (source table - Table 9-2 in Appendix (A))

These results reflect the fact that bio-diesel has more affinity for water than mineral diesel. For example, water contents of $49.13 \pm 2.79 \text{ ppm (v/v)}$ and $403.94 \pm 24.89 \text{ ppm (v/v)}$ were measured for the REF and B100 fuels respectively, which is in agreement with the findings in the literature [20, 22-27, 72, 73]. This is due to the higher polarity of the bio-diesel molecules (alkyl-esters and unsaturated molecular structure) compared to that of mineral diesel. However, it is interesting to note that as the proportion of monoolein increases from zero (REF) up to 1000 ppm (M1000), changes in the water content of the fuel are not noticeable. As explained in Section 3.4.1, this is likely to be attributed to a lower molar ratio of monoolein compared to that of bio-diesel in the test fuels, which results in a lower overall hygroscopicity of the monoolein blends.

The saturation level of fuel blends were measured according to the procedure explained in Section 3.3.4 and the results (*mean ± SE*) are plotted in Figure 3-9.

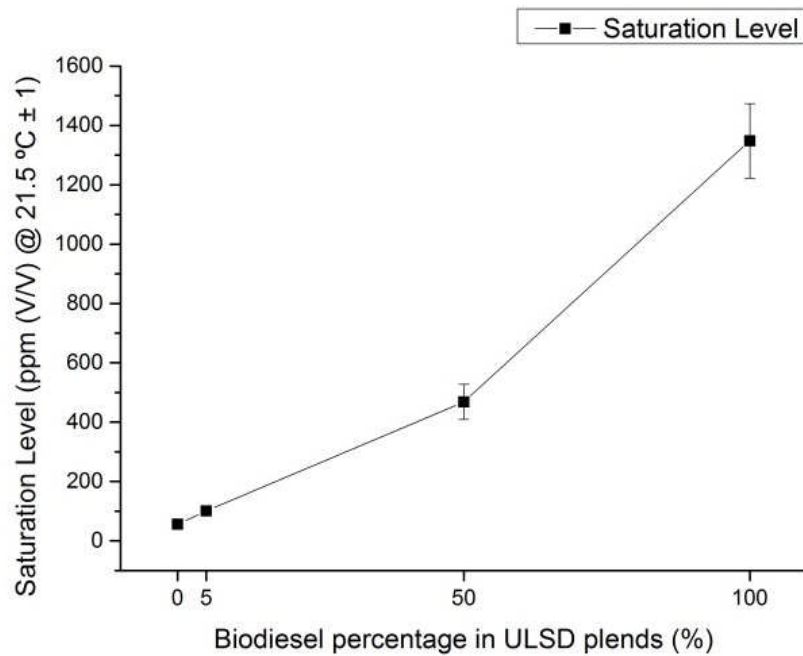


Figure 3-9: Water saturation level of bio-diesel blends (source table - Table 9-3 in Appendix (A))

The high water saturation level of B100 confirmed that bio-diesel has a strong hygroscopicity such that it absorbed more than twenty times the amount of water than the mineral diesel after 24 h aging in direct contact with water. Similar to the water content results discussed earlier above, the lower overall hygroscopicity of M400 compared to the bio-diesel blends can be also attributed to a lower molar ratio of monoolein compared to that of bio-diesel in the test fuels.

3.4.3 Density and dynamic viscosity tests

Figure 3-10 shows the density results (*mean ± SE*) for the fuel blends.

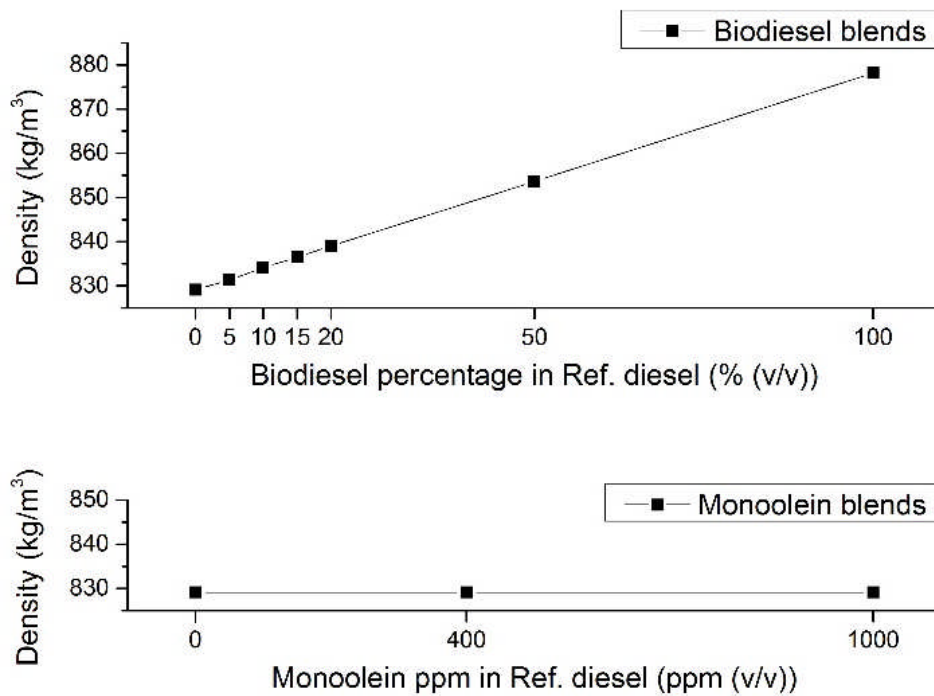


Figure 3-10: Density of the bio-diesel and monoolein blends (source table - Table 9-4 in Appendix (A))

It was found that a fuel blend containing a higher proportion of bio-diesel exhibits a higher density compared to the reference diesel. This is because the bio-diesel (B100) has a higher intrinsic density (878.2 kg/m^3) and water content ($403.94 \pm 24.89 \text{ ppm } (\frac{v}{v})$) compared to the REF fuel with a density and water content of 829.1 kg/m^3 and $49.13 \pm 2.79 \text{ ppm } (\frac{v}{v})$ respectively, which affects the density of the bio-diesel blends. By contrast, there was no marked change in the density of the monoolein blends resulting from the addition of monoolein up to 1000 ppm in the REF diesel.

Figure 3-11 shows the comparative plots of the dynamic viscosity of the bio-diesel and monoolein blends.

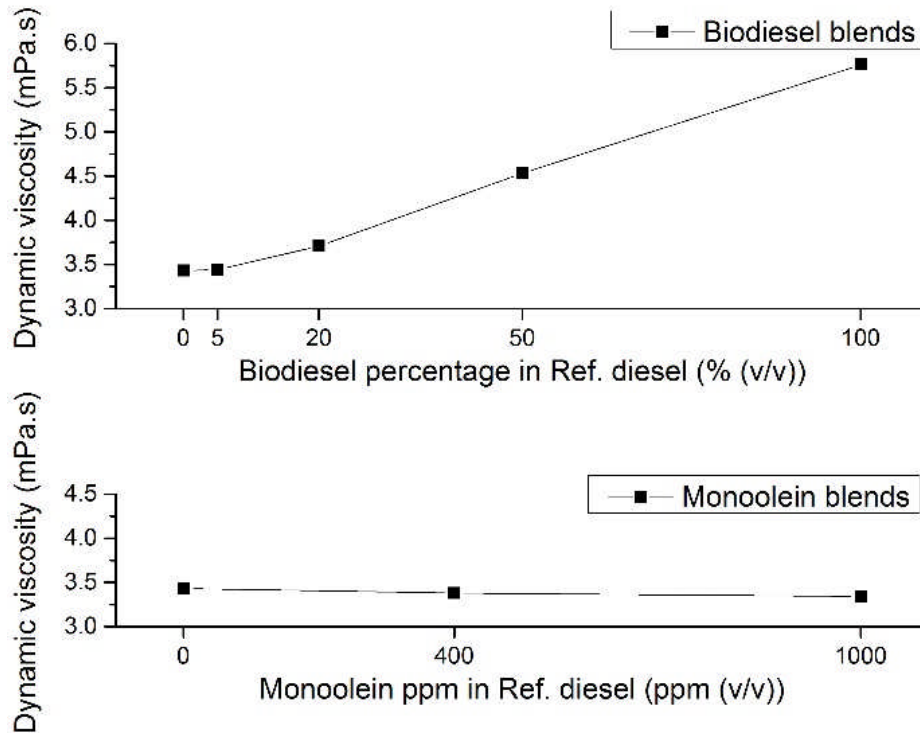


Figure 3-11: Dynamic viscosity of the bio-diesel and monoolein blends (source table - Table 9-5 in Appendix (A))

The bio-diesel blends exhibited higher viscosities than the REF fuel, e.g. $5.76 \text{ mPa} \cdot \text{s}$ in B100 and $3.43 \text{ mPa} \cdot \text{s}$ in REF fuel. On the other hand, no variation was observed in the fuel viscosity of the monoolein blends, which is likely to be connected with the low molar ratio of the monoolein compared to the bio-diesel in the test fuels. For instance, the molar concentrations of the B20 and M325 blends, which exhibited identical IFTs, were 0.5924 and 0.0009 mol/l respectively (molecular weight of monoolein ($\text{C}_{21}\text{H}_{40}\text{O}_4$) = 356.54 g/mol ; based on methyl oleate ($\text{C}_{19}\text{H}_{36}\text{O}_2$) with a molecular weight of 296.494 g/mol , which is a typical bio-diesel fuel [54]).

3.5 Summary

The behaviour of fuel, along with water and the filter medium itself are the main components that interact to control the separation performance of a fuel-water coalescing system. It is therefore important to understand how the properties of the fuel are influenced by common variations in its composition and also to evaluate whether or not the inclusion of surfactant in the form of monoolein is a satisfactory surrogate for bio-diesel. This is particularly important given the widespread use of monoolein in the ISO and SAE water separation test methods. The properties of reference grade diesel fuel in terms of interfacial tension (IFT), dissolved water content and viscosity are substantially affected by addition of bio-diesel, even at low concentrations of only 5% (v/v). However, by contrast, addition of monoolein was only found to affect the IFT of the fuel whereas the water content, density and viscosity of the fuel remained almost constant. The effects of adding monoolein and bio-diesel to a reference fuel are therefore not the same. It was established that monoolein does not saturate the interface of water and fuel at an IFT higher than 2 mN/m , while the interface reaches saturation point in fuels containing more than 20% bio-diesel, i.e. >B20, such that the IFT of the fuel blends is maintained between 12 and 13 mN/m even in the case of B100. This can be attributed to the molar ratio of the bio-diesel in the fuel blends, which is much greater than monoolein in monoolein blends. The results reported herein provided a basis for the design of subsequent experiments concerned with understanding the behaviour and underlying relationships between the fuel properties and water droplet characterisation (chapter 4) and the fuel-water separation performance of filter media (chapters 6 and 7).

CHAPTER 4

Water-in-Fuel Emulsion Characterisation

4.1 Introduction

As highlighted in Section 2.3.4, in a surfactant-stabilised diesel, the presence of small, stable water droplets is to be expected. In a real vehicle, 50% of the water droplets after the fuel pump can be smaller than $25\mu\text{m}$ ($Dv_{50} < 25\mu\text{m}$), such that efficiently capturing them is challenging [28]. Evaluation of the water separation performance of filters depends on their end use and standards such as SAE J1488 and ISO 16332 define the test conditions required [28, 133]. These laboratory tests are usually conducted using a base reference grade diesel fuel that is free of solid contaminants or bio-diesel, but is blended with a specified surfactant such as monoolein, which alters the fuel IFT and water separation characteristics. The approach is based on the theory that a low IFT will result in small droplet sizes and thereby simulate more challenging fuels such as those containing bio-diesel or surfactant additives.

Although the impact of bio-diesel and surfactants on water-in-fuel emulsion properties and water separation has been previously investigated (Section 2.6.1), comparative data on water droplet size distributions (DSD) and water separation performance associated with blends of diesel/bio-diesel and diesel/monoolein is lacking. In Chapter 3, the reference grade fuel and its blends with bio-diesel and monoolein were investigated in detail and differences between the properties of the fuel blends were reported. The present chapter discusses the characteristics of water-in-fuel emulsions with regard to their settlement behaviour as well as the size distribution of water droplets in these two sets of fuel blends. This chapter is also intended to identify some of the important underlying relationships between emulsion characteristics and the fuel properties described in Chapter 3.

ASTM D7261 – 13 and ASTM D1401 - 12E1 are the standard test methods to evaluate separation of water in diesel, i.e. water separability. They use D-SEP rating and settlement tests

respectively, both of which were employed in this research (4.3.3 and 4.3.4) to investigate water separation via gravity in bio-diesel and monoolein blends. Moreover, DSDs in the fuel blends were investigated using an emulsion generation test rig (see Section 4.4) equipped with an online sizing apparatus based on laser diffraction technology.

4.2 Stock fuels and additives

The REF, B100, and monoolein samples used in this research were from the same batches used for the fuel characterisation work (Section 3.2). The test fuel blends were prepared based on the same method as explained in Section 3.3.1.

4.3 Experimental methods and apparatus

This section reports methods and laboratory apparatus used to evaluate droplet size distributions (DSD) as well as water separability in different fuel blends containing bio-diesel or monoolein. This does not include design and construction of the emulsion generation rig which is explained in Section 4.4.

4.3.1 Laser diffraction technology and particle sizing

In emulsion science, laser diffraction is a common technique for the analysis of particle/droplet sizes dispersed in a bulk medium. ISO 13320:2009 explains the method and principles in detail [134]. The method usually employs optical models, such as Fraunhofer and Mie diffraction models, interpreting the scattering pattern, in terms of scattering intensity and angles, created by a particle in the path of a laser beam.

Fraunhofer and Young demonstrated that light rays of a certain wavelength shone at a single or finite number of slits placed between a light source and a screen, are diffracted at the slit edges to form a diffraction pattern on the screen (Figure 4-1). The pattern is composed of light

and dark regions with an intensity reducing from the centre to the sides due to overlapping and interfering light waves at the surface of the screen.

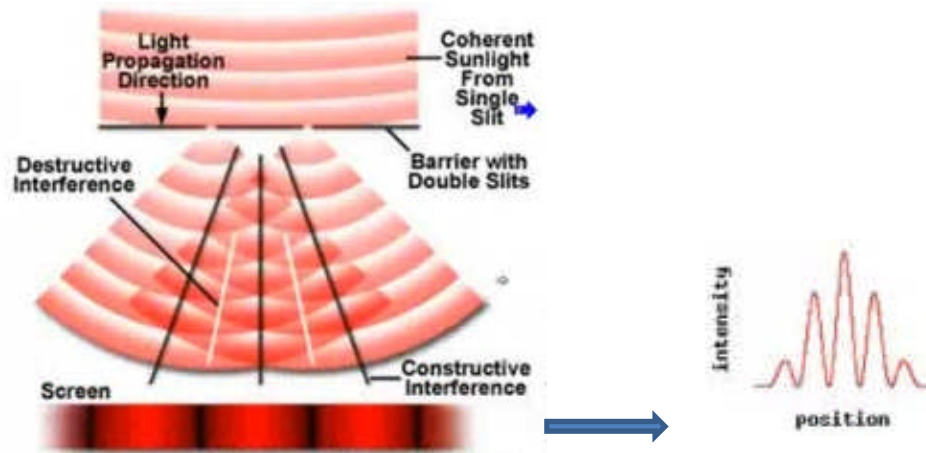


Figure 4-1: Young's double slit experiment [134]

The light points are where the waves have constructive interference and are displacing in the same direction, and the dark regions are where the waves have destructive interference and have a displacement in opposite directions. The same principle is applied to explain the diffraction pattern of light rays shining on a particle which can be diffracted at the particle edges, refracted through the particle, radiated from it or be absorbed by the particle (Figure 4-2).

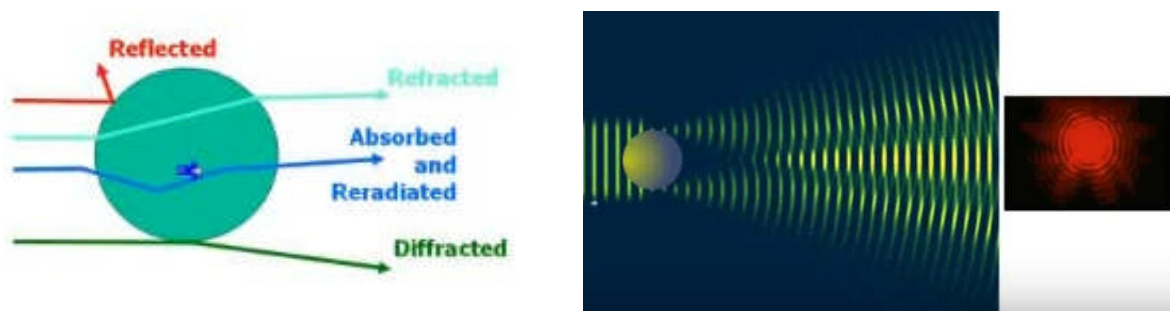


Figure 4-2: Light diffraction pattern on a spherical particle [134]

Small particles diffract the light at larger angles and with less intensity than larger particles (Figure 4-3). Based on this principle, Fraunhofer suggested a model to calculate particle size based on the scattering angle and intensity.

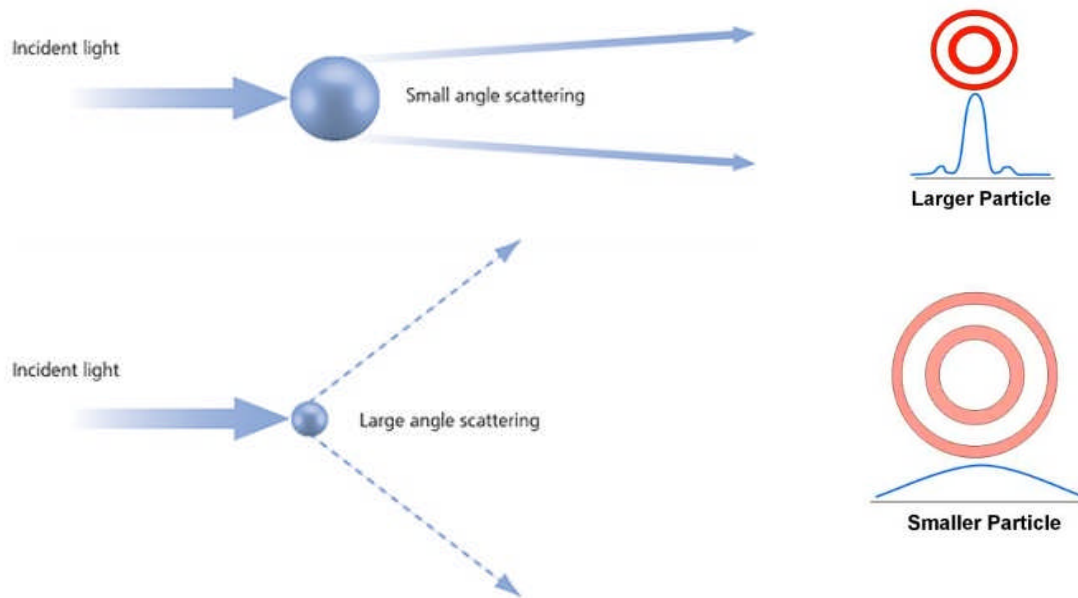


Figure 4-3: Light scattering angles for small and large particles [134]

His model can be used to size particles that have a size much greater than the wavelength of the light being used for the measurements, i.e. larger than $25\mu m$. The share of wave refraction through a small particle, especially when the particle size is approaching the wavelength of the scattering light, is higher than that of a large particle. Here, Mie theory joins Fraunhofer's to measure particle size less than $25\mu m$ as accurately as possible.

Laser diffraction technology typically analyses the particle size based on the equivalent sphere theory by which the size distribution of particles is generated based on their volume equivalent spherical diameter [134]. In this method, the mean particle diameter, is not a number average of the diameter of N number of particles (denoted as $D[1,0]$, Equation 4-1). Rather, it is based on either the ratio of the diameter of a sphere with an average volume of the particle ($D[3,0]$,

Equation 4-3) and diameter of a sphere with an average surface area (D[2,0], Equation 4-3), which is called the Sauter mean denoted as D[3,2], (Equation 4-4) i.e. volume (Equation 4-3)/surface mean (Equation 4-2), or the mean diameter over volume (also called the de Brouckere mean, denoted as D[4,3], Equation 4-5). In this measurement knowing the number of particles is not necessary as the equivalent diameter is measured based on the ratio of two different averages, however, due to light refraction through particles, measuring and recording the refractive indexes of the emulsion phases is compulsory (see Section 4.3.2).

$$D[1,0] = \frac{1}{n} \times \sum_{i=1}^n D_i$$

Equation 4-1: Mean diameter [134]

$$D[2,0] = \sqrt{\frac{1}{n} \times \sum_{i=1}^n D_i^2}$$

Equation 4-2: Surface area mean diameter [134]

$$D[3,0] = \sqrt[3]{\frac{1}{n} \times \sum_{i=1}^n D_i^3}$$

Equation 4-3: Volume mean diameter [134]

$$D[3,2] = \frac{\sum_{i=1}^n D_i^3}{\sum_{i=1}^n D_i^2}$$

Equation 4-4: Sauter mean diameter [134]

$$D[4,3] = \frac{\sum_{i=n}^1 D_i^4}{\sum_{i=n}^1 D_i^3}$$

Equation 4-5: De Brouckere Mean Diameter [134]

4.3.1.1 Experimental setup and procedure

The Insittec Wet Malvern® particle size analyser (Figure 4-4) employing laser diffraction at a wavelength of 670nm was used to measure water droplet sizes over a range of 0.1µm to 2500 µm. The device has a view cell with inlet and outlet hose inserts to stream a water-in-fuel emulsion sample through. The cell is placed between optical and receptor heads perpendicular to a laser beam, such that the beam can pass through the sample containing emulsified droplets. The built-in software uses the Mie optical method to interpret the received data from thirty-two detectors for the angular variation in the intensity of light scattered by dispersed water droplets to calculate their diameter in the sample emulsion. The device was used to characterise test emulsions containing water and a sample fuel (Table 4-1), when connected to the downstream side of an emulsion-generating device. The emulsion-generation device used in this research is explained in Section 4.4. The output was an average distribution for a volume equivalent spherical diameter of the water droplets of the emulsion during water injection, presented in the form of a curve showing the percentage droplet frequencies of different size ranges.

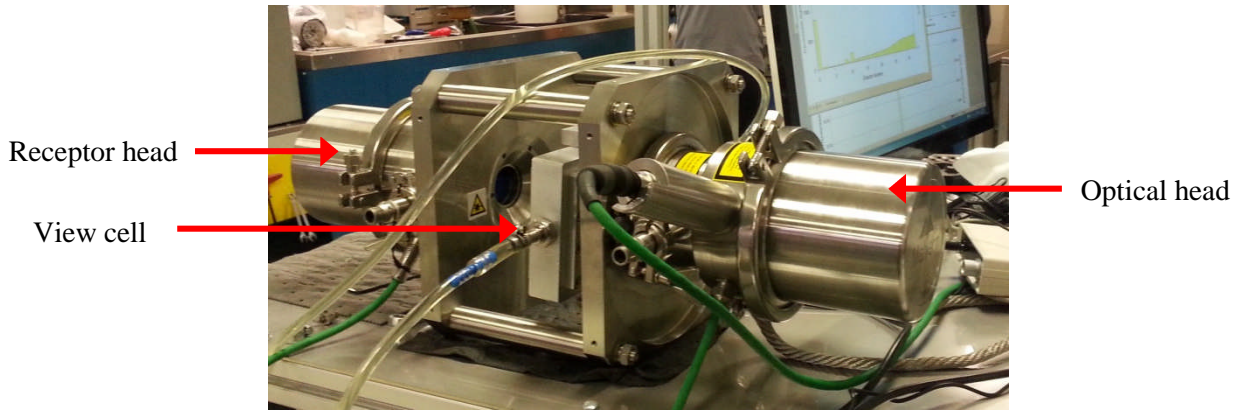


Figure 4-4: Insittec Wet Malvern® particle size analyser

Table 4-1: Test fuel blends for DSD measurement

Fuel type	Fuel ID					
Reference grade	REF					
Bio-diesel blends	B5	B10	B20	B30	B50	B100
Monoolein blends	M200	M400	M600	M1000		

The particle sizer recorded droplet size distributions (DSD), cumulative distributions, and their corresponding volume median diameter, denoted as Dv_{50} , at one second intervals during each test and raw data was processed using OriginPro software to calculate average size distributions, cumulative distributions, and Dv_{50} s during the emulsification. The particle sizer was connected to an emulsion-generating test rig, designed and built in-house exclusively for this research, for online measurement of water DSD, as explained in Section 4.4.

4.3.2 Refractive index measurement

As a first step before droplet size measurements could be made on the bio-diesel and monoolein blends, the refractive index of each test fuel needed to be determined. The refractive index is a dimensionless number quantifying the ratio of the speed of light in a vacuum to its speed in

the test medium, based on Snell's law (Equation 4-6). For instance, the refractive index of water is 1.331, which means the speed of light in the vacuum is 1.331 times faster than its speed in water.

$$\frac{v_a}{v_b} = \frac{\sin \theta_a}{\sin \theta_b} = \frac{n_b}{n_a}$$

Equation 4-6 Snell's law for refraction: a refers to air and b refers to test medium

Where:

v_a and v_b : Speed of light in medium a and b (m/s);

θ_a and θ_b : Angles of incidence and refraction respectively;

n_a and n_b : Refractive indices for medium a and b.

4.3.2.1 Experimental setup and procedure

A CETI® Abbe refractometer was used for this test (Figure 4-5). The apparatus has two prisms, an illuminating prism and a refracting prism, of known refractive indices. A thin layer of the test liquid, typically 1-3 drops, is placed between each prior to measurement.

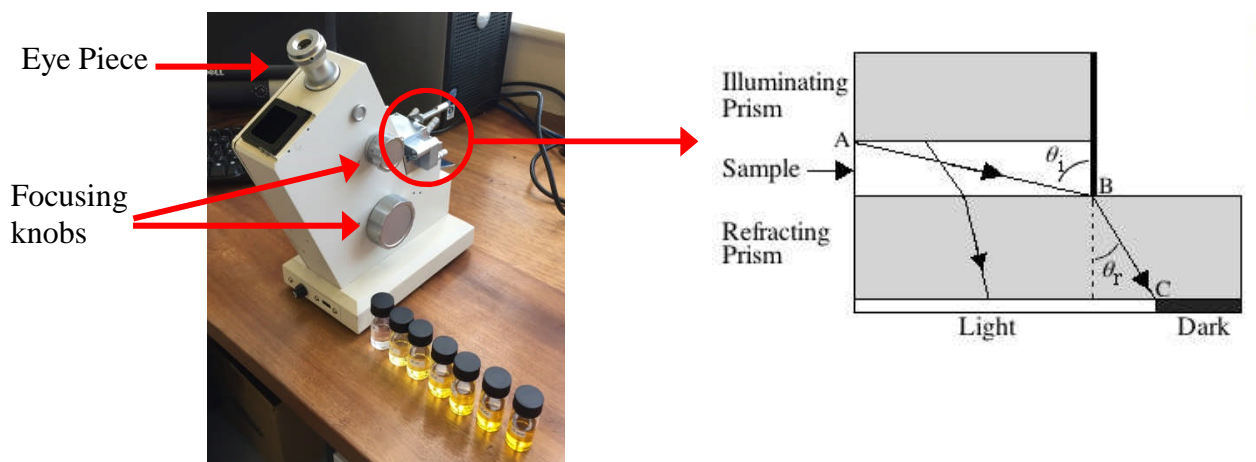


Figure 4-5: Refractometer setup and the theory of refraction index measurement

The refractive index of the refracting prism is chosen to be higher than the test liquid such that the light shone from the illuminating prism through the sample liquid is refracted through the second prism at a smaller angle than the critical angle for the total reflection, i.e. $\theta_r < \theta_i$ (Figure 4-5). The largest possible incidence angle, θ_i , through the sample is known from the specification of the tester, and the largest refracted angle, θ_r , through the refraction prism can be detected by a photodetector built in to the device. Therefore, based on the detected refracted angle, θ_r , the Index of the sample is readable through the eye-piece of the instrument from a scale built-in based on the Equation 4-6. Different refractive indices result from changing the position of the interface of dark and light regions such that a different number from the scale is visible through the eye-piece. The clarity of the interface is adjustable using focusing knobs on the device.

The test fuels used is the same as listed in Table 4-1 and the device was calibrated against distilled water with a known refractive index of 1.331.

4.3.3 DSEP rating

The DSEP rating test, determination of separation characteristics, is a standard test procedure, ASTM D7261 – 13 used to determine the water separation characteristics of diesel fuel when passed through a standard fibreglass coalescing filter. This method, and also the sedimentation test explained in Section 4.3.4, provides a measure of the resistance to coalescence of water droplets induced by surfactants present in the fuel. In principle, mixing a certain amount of distilled water into the test fuel for a certain period of time creates turbidity, or the formation of very tiny water droplets dispersed in the sample fuel. The emulsion is then passed through a standard fibreglass filter such that fuel turbidity, analysed by a turbidimeter, reduces if the sample contains no surfactant. The test apparatus is equipped with a turbidimeter that measures the turbidity of a suspension by radiating a light of known wavelength on to the contaminated

sample. The turbidimeter should be calibrated first using a clean and water-free fuel sample. The turbidity ranges from 0 to 100 and is determined by comparing the intensity of the scattered light through the clean and contaminated samples. The fuel containing less surfactant that is not able to create a stable fuel-water emulsion will have a higher DSEP value, while a fuel with a high level of surfactant has a lower value. The SAE J1488:2010 considers fuels with DSEP values less than 75 to have poor water separability.

4.3.3.1 Experimental setup and procedure

The portable separometer Microsep Mark V Deluxe (Figure 4-6) was employed in this research to measure DSEP values for each test fuel the same as listed in Table 4-1.

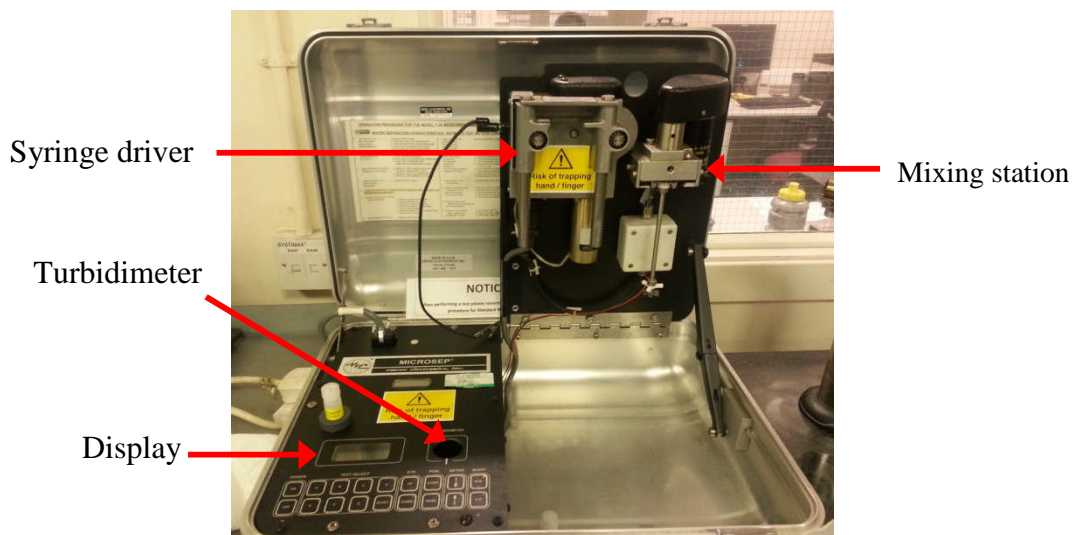


Figure 4-6: Microsep set-up

The test apparatus comprises a control panel with a keyboard, turbidimeter, and meter reading display, a mixing station driven by the MICROSEP® emulsifier ($1000-12500 \text{ min}^{-1}$), and a syringe driver. For each DSEP test, a standard equipment pack including a 60 ml syringe with end plug, turbidimetry glass vial, an ampule of 5 ml distilled water, and Alumicel containing standard fibreglass coalescer is required. The test procedure includes a preparation step by

which the mixer of the Microsep and the sample syringe are washed with the sample fuel to ensure the items are not contaminated with other fuel sample if the device had been used before the test. To conduct the main test procedure, 15 ml of the test fuel was poured in to the turbidimetry glass vial to be placed in the turbidimeter, and was assigned a value of 100 as the clean sample fuel (without free water). Once this calibration step is completed, 50 ml of the fuel sample was poured into the syringe with the plunger removed and a plug was inserted in to the bottom connection of the syringe. Then, 5 ml of distilled water was added into the syringe using a hand pipette and the syringe was placed in the mixing station while the mixer bar was inside the syringe. The start button on the control panel was pressed such that the Microsep started to carry out several functions against a fixed program time scale as follows:

- Emulsification for 30 s;
- Wait for a 30 s interval during which time: (a) the syringe from the mixing station was removed; (b) the plunger was inserted in to the syringe containing the emulsion sample; (c) the plug was removed while the syringe is inverted; (d) the syringe was vented the Alumicel was placed on to it, and finally, (e) the syringe was assembled into the syringe driver and a waste container was placed under the outlet.
- The syringe was driven down for 45 s during which time 15 ml of the emulsion was collected from the syringe using the vial placed in the turbidimeter for the rating measurement.
- The DSEP value for the sample was displayed on the control panel.

In the case of DSEP values of zero, the glass vial was left in the turbidimeter and the sample was rated at 15, 30, 90, and 120 min afterwards to provide a dynamic DSEP measurement.

4.3.4 Water separation via the sedimentation test (water separability test)

The ISO 16332 recommends the ASTM D1401-12E1 test procedure for qualitatively determining water separation characteristics in diesel fuel. The concept is to create a water and oil mixture and to observe how quickly the water is separated from the oil and settles at the bottom of the vessel. Based on this method, a volume of 40 ml oil is taken and poured in to a graduated cylinder placed in a controlled temperature bath. The oil is heated to the test temperature of 54.4 °C (130 °F) and an equal volume of 40 ml distilled water is then gradually added into the cylinder. The liquids are left to equilibrate to the test temperature. Using a stir rod, oil and water are mixed at 1500 min^{-1} for 5 min. Then, the mixture is left undisturbed and the volume of the separated water from oil is recorded versus time.

4.3.4.1 Experimental setup and procedure

Table 4-2 lists the fuel samples tested for water separation via sedimentation, to determine resistance to coalescence modulated by bio-diesel and monoolein content in the test fuels. For this measurement the ASTM D1401-12E1 procedure, was followed with small modifications [135] as now detailed. The small modifications were applied to address a limitation in the availability of the required measuring instruments.

Table 4-2: Test fuel blends for the sedimentation test

Fuel type	Fuel ID		
Reference grade	REF		
Bio-diesel blends	B5	B20	B50
monoolein blends	M200	M325	

40 ml of the test fuels were separately mixed with 10 ml distilled water in a measuring cylinder for 30 s at $1000\text{-}12500 \text{ min}^{-1}$ using a MICROSEP® emulsifier (ASTM D7261 – 13) at room

temperature. After emulsification, the volume of the coalesced water was recorded versus time for the test fuels. It required longer to recover the total volume of water if the water-in-fuel is more stable, or there is more resistance to coalescence in the emulsion, which results in lower settling velocity of the droplets. Equation 2-9 in Section 2.3.3.2 indicates the settling velocity (V) of a droplet with a density of ρ_w and radius of r , settling down in a bulk fuel with a viscosity of μ and density of ρ_f , where g is the acceleration due to gravity.

Sample pairs of B5 and M200, and B20 and M325, were tested due to the similarity of their respective IFTs, i.e. about 18 mN/m and 12 mN/m respectively (see Section 3.4.1), and B50 was used to consider the effect of viscosity on the water separation as it possessed the same IFT as B20 but a higher viscosity than other fuel blends (see Section 3.4.3). REF fuel was used as the control sample and the volume of the separated water from oil was recorded at one minute intervals for the first ten minutes, and then recorded at subsequent intervals, i.e. at the 20th, 30th, 60th, 90th, 120th, 180th, 240th and 300th minute time points of the test.

4.4 Development of the emulsion generation test rig

An emulsion generation test rig equipped with an online droplet size measurement system (Insitac Malvern® particle size analyser – see Section 4.3.1) was built to characterise water droplet size distribution (DSD) in the test fuels. The rig enabled the emulsification of 0.2% (v/v) deionised water in a test fuel and measured DSD at atmospheric and a higher static pressures. 4 bar static pressure was decided for the high pressure tests as it was the maximum feasible static pressure that could be applied to the system without health and safety concerns.

4.4.1 Design of the emulsion generation test rig

The design of the test rig is shown in Figure 4-7 and its operation was based on the following criteria:

- Injection and emulsification of a precise volume of water into a test fuel during a pre-defined period of time, enabling online measurement of water DSD;
- Ability to conduct a single-pass test, i.e. water passes the pump only once, avoiding multiple pumping of the emulsified water to avoid affecting the original water droplet sizes;
- Generation of a uniform and constant flow;
- Maintenance of a constant flow rate at high static pressure up to 4 bar.

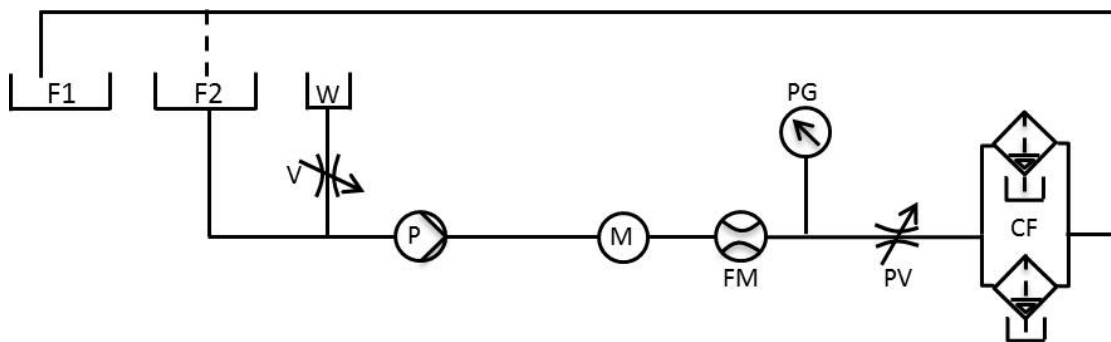


Figure 4-7: Schematic of the emulsion generation test rig

Based on the schematic of the test rig shown in Figure 4-7, the rig design consisted of one circuit for a single-pass test through a particle sizer for the analysis of DSD. The fuel pump (P) circulates a fixed volume of the test fuel from the reservoir (F2) at 6 l/min close to what is encountered in real life applications. The fuel is then passed through the particle size analyser (M), flowmeter (FM), and high efficiency clean-up filters (CF). Deionised water held in the tank (W) at the suction side of the main pump (P) is injected into the system by opening the valve (V) via pump suction as well as the hydrostatic pressure in the water tank. Once injection has started, fuel is collected in the storage reservoir (F1) instead of the tank (F2) to provide a single pass emulsion test. The injection rate has to be constant at 12 ml/min to provide 0.2% (v/v) deionised water in a test fuel during a water injection experiment. To run a test at the

higher pressure, the pressure valve (PV) was adjusted to reach 4 bar static pressure, and the same procedure was followed thereafter.

4.4.2 Construction of the emulsion generation test rig

The final constructed test stand is shown in Figure 4-8.

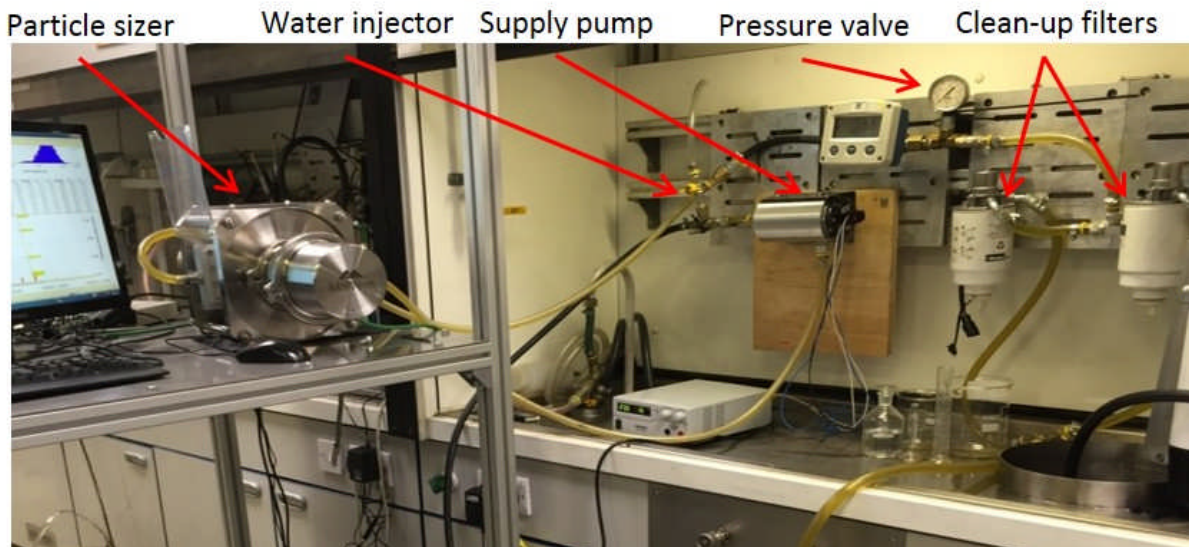


Figure 4-8: The final constructed emulsion generation test rig

Following the system design shown in Figure 4-7, the detailed specification of the test rig components are now outlined.

4.4.2.1 Piping and hose fittings

The hose size of 1/2" [inner diameter of 12.5 mm] was chosen for the piping and all the fitting and hose inserts were chosen accordingly.

4.4.2.2 Fuel tanks (F1 and F2)

Two 20 l stainless steel buckets were used as the fuel feeding and storage tanks. Since the test rig was a temporary one, it did not require permanent fuel reservoirs.

4.4.2.3 Water reservoir (w)

A 30cm piece of 3/8" [inner diameter of 10 mm] PVC transparent hose, volumetrically scaled, was used as the water reservoir.

4.4.2.4 Water injection valve (V) and the injector device

A brass ball valve was fitted to a steel equal 3/8" [outside diameter of 16.7 mm] tee piece to assemble the injector device. To ensure smooth and constant injection of water at 12 ml/min, a small plastic disk with a hole in its centre, i.e. a hole diameter of 1 mm, was fitted inside the tee piece at the water side. The water hose (W) was connected to the valve using a proper size hose insert.

4.4.2.5 Adjustable pressure valve (PV)

A steel ball valve with 3/8" [outside diameter of 16.7 mm] fittings was used to generate pressure in the system for the tests at 4 bar pressures.

4.4.2.6 Pressure gauge (PG)

A USS analogue pressure gauge (0 - 10 PSI, 63 mm glycerine-filled) was used for adjustment up to 4 bar pressure in the system coupled with the PV valve operating with a level of accuracy of $\pm 2\%$. The gauge was installed in the system using an appropriately sized brass tee piece.

4.4.2.7 Main pump (P)

A Parker Nicholas pump (Heavy-Duty Engine Platform Gerotor, 5000 rpm, 24V~7 l/min @ 6 bar) was installed. The pump was able to provide a constant flow rate of 6 l/min for both atmospheric and 4 bar pressure tests. This pump was selected due to its real world application in heavy-duty vehicles.

4.4.2.8 Flowmeter (FM)

A GL turbine flowmeter was used with a large LCD (40mm x 90mm) and accuracy of $\pm 1\%$ over flow rates ranging between 0 and 10 *l/min*.

4.4.2.9 Clean-up filters (CF)

Commercial Dmax® high efficiency clean-up filters were used to provide clean fuel downstream of the particle sizer.

4.4.2.10 Particle sizer device (M)

A Malvern® Insitec Wet particle size analyser (see Section 4.3.1) was used for the DSD analysis. The device was capable of being connected to the system for online measurements.

4.4.3 Commissioning the test rig

Running of the test rig for each test required conducting a pre-test calibration, followed by the emulsion generation test as is now detailed.

4.4.3.1 Pre-test procedure

The 5 min pre-test procedure was designed to enable stable operating conditions such that a steady state flow rate was achieved and air in the entire system was removed. Having a constant, steady state and smooth flow of clear fuel was necessary prior to pre-testing. The pre-test procedure, which was not associated with any water injection, was designed as a multi-pass test, and was performed in the following order:

- 1) Check if the IFT and water content of the test fuel was in range (see Section 3.4.1);
- 2) Fill the fuel tank F2 and take the fuel tank F1 out of the system, i.e. to provide a multi-pass test;
- 3) Open the pressure valve PV (no external pressure in the system);
- 4) Close the water injection valve V, to ensure no water injection in the pre-test;

- 5) Ensure all system components are properly connected and safe to run;
- 6) Start the fuel pump and adjust the flow rate to the test flow rate of 6 l/min ;
- 7) Continue the fuel circulation for 5 min;
- 8) Drain the clean-up filters regularly making sure they are free of water.

4.4.3.2 Emulsion generation procedure

The emulsion generation test procedure was started immediately following the pre-test such that the test rig was not interrupted. Following the pre-test, the pressure valve was left open, the water injection valve was closed and the pump was running at 6 l/min . The test was designed to be a single pass test and was performed in the following order.

- 1) Recover the fuel tank F1 for the outflow;
- 2) 15 ml of deionised water was placed in the water hose ready for the injection;
- 3) The Malvern master sizer was switched on, the manufacturer's calibration procedure for calculating the background signals was carried out, while the fuel was clean and free of water;
- 4) Start the Malvern measurement program;
- 5) Open the water injection valve to inject water in to the system, i.e. an emulsion is generated, and the particle sizer began to measure the DSD of the test fuel;
- 6) Close the water injection valve when 3 ml water remains in the hose, i.e. 12 ml water has been injected during 1 min. The emulsion generation is now stopped and clear fuel passes the particle sizer;
- 7) Stop the Malvern measurement program and save the data file;
- 8) Stop the pump;
- 9) Remove the inflow hose from the tank F2 and place it in the tank F1;

- 10) Start the pump and circulate the fuel for 30 min and drain the clean-up filter regularly to drain the water out;
- 11) Check the water content of the test fuel to make sure all the injected water is removed. If it does not happen in 30 min, circulate the fuel as long as needed to ensure it is clean;
- 12) Stop the pump and put the inflow hose back in the tank F2 and start the pump again at the same flow rate as before;
- 13) Adjust the pressure valve to reach to 4 bar pressure;
- 14) Repeat step 2 to 8 and record the DSD of the same test fuel at 4 bar pressure;
- 15) Discard the fuel using the designated waste procedure.

4.5 Results and discussion

The test fuels were prepared based on the procedure explained in Section 3.3.1, and water in fuel emulsions were generated using the purpose-built test rig (Section 4.4) and characterised according to the procedures reported in Section 4.3. The following section focuses on determining water droplet sizes in fuel blends containing bio-diesel and monoolein as well as evaluating the effect of the fuel additives on the resistance to coalescence of water droplets in the fuel blends.

4.5.1 Determination of the refractive index of the test fuels

Table 4-3 summarises average refractive indices of the test fuels. Each fuel blend was tested in triplicate and the mean value was used for the particle sizer calculations.

Table 4-3: Refractive Indexes for test fuels

Test Fuel	RI	Test Fuel	RI
REF	1.461	M200	1.461
B5	1.461	M325	1.461
B10	1.461	M400	1.461
B15	1.461	M600	1.461
B20	1.46	M1000	1.461
B50	1.458		
B100	1.454		

Based on the results, the refractive index of REF fuel is not changed by addition of monoolein, however, it is changed when more than 20% (v/v) bio-diesel is blended in the fuel. B100 had the lowest index among other test fuels.

4.5.2 Water droplet size distribution (DSD) in the test fuels

To measure the droplet size distribution (DSD) of water droplets, the emulsion generation test rig (Section 4.4) was used to create water-in-fuel emulsion for the different fuel blends, and the particle sizer laser diffraction technology (Section 4.3.1) was employed to plot an average distribution for a volume equivalent spherical diameter of water droplets during water injection for each test fuel. For each emulsion, a volume median diameter, denoted as Dv_{50} [136], was also calculated from their cumulative distribution curves.

The size distributions of water droplets at atmospheric pressure in the test fuels are shown in Figure 4-9 to Figure 4-19 and the corresponding Dv_{50} s of water droplets (mean \pm SE) are listed in Table 4-4.

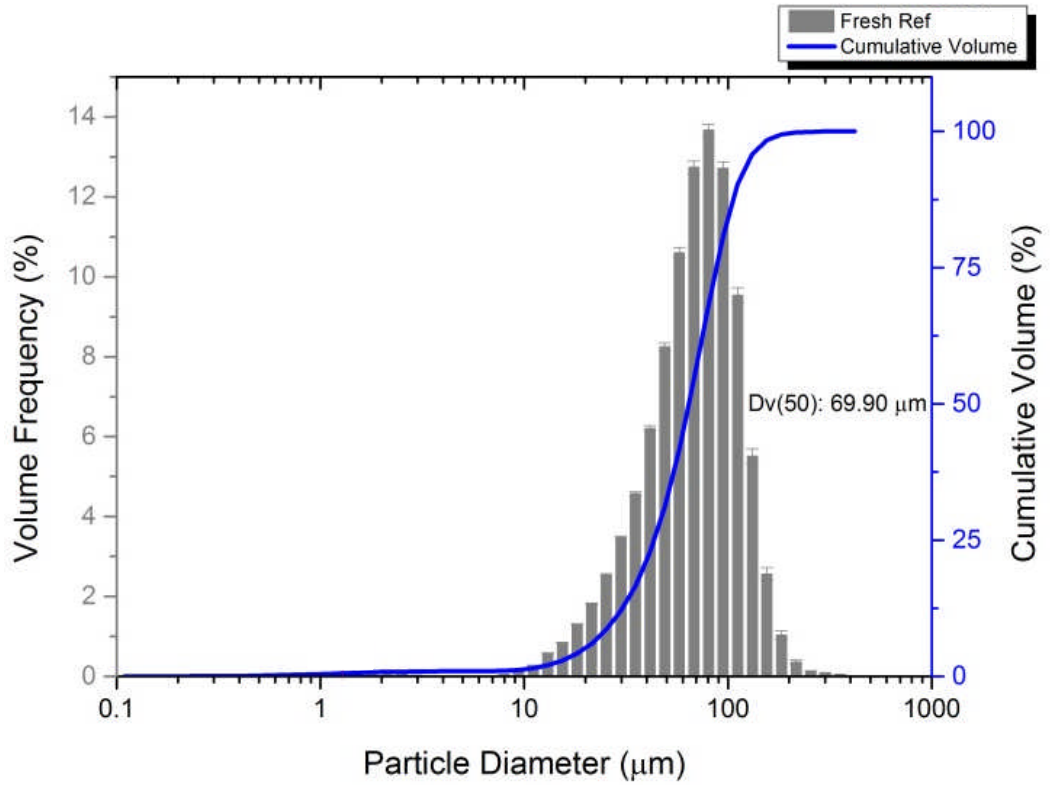


Figure 4-9: DSD of the water phase in REF at atmospheric pressure

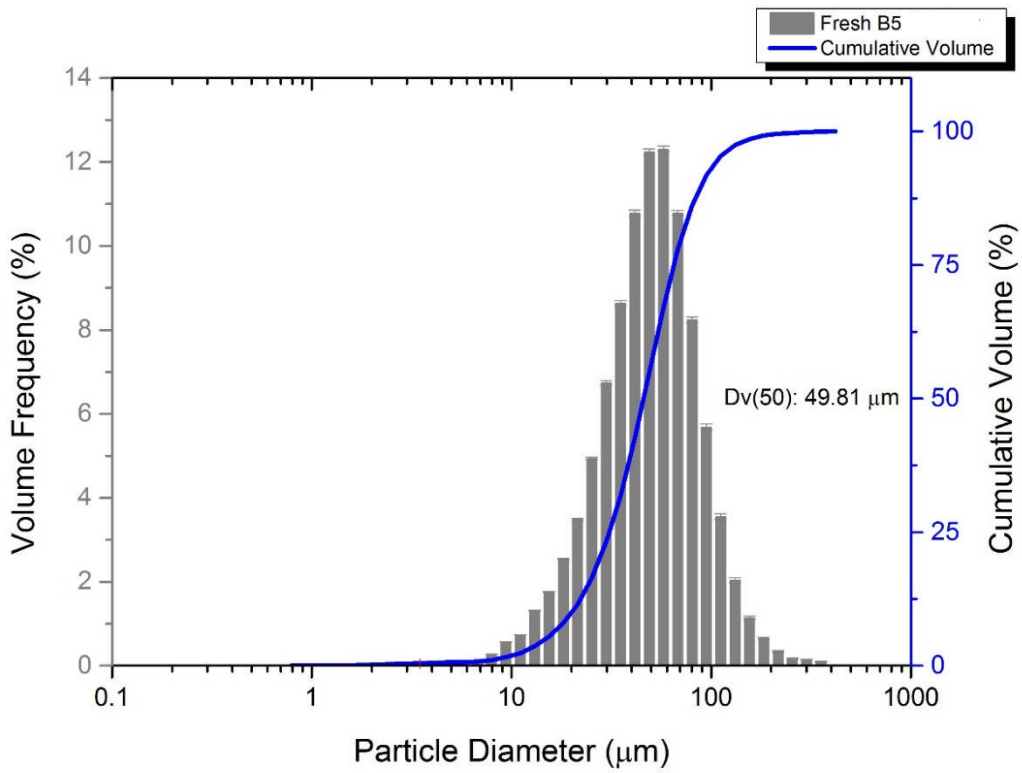


Figure 4-10: DSD of the water phase in B5 at atmospheric pressure

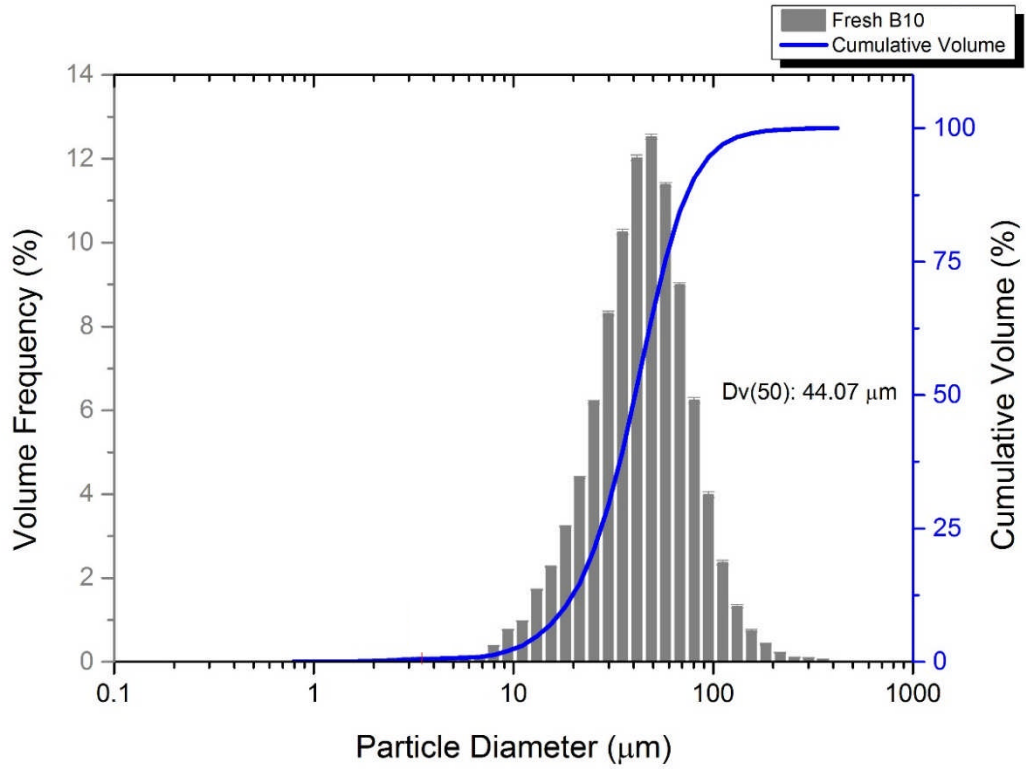


Figure 4-11: DSD of the water phase in B10 at atmospheric pressure

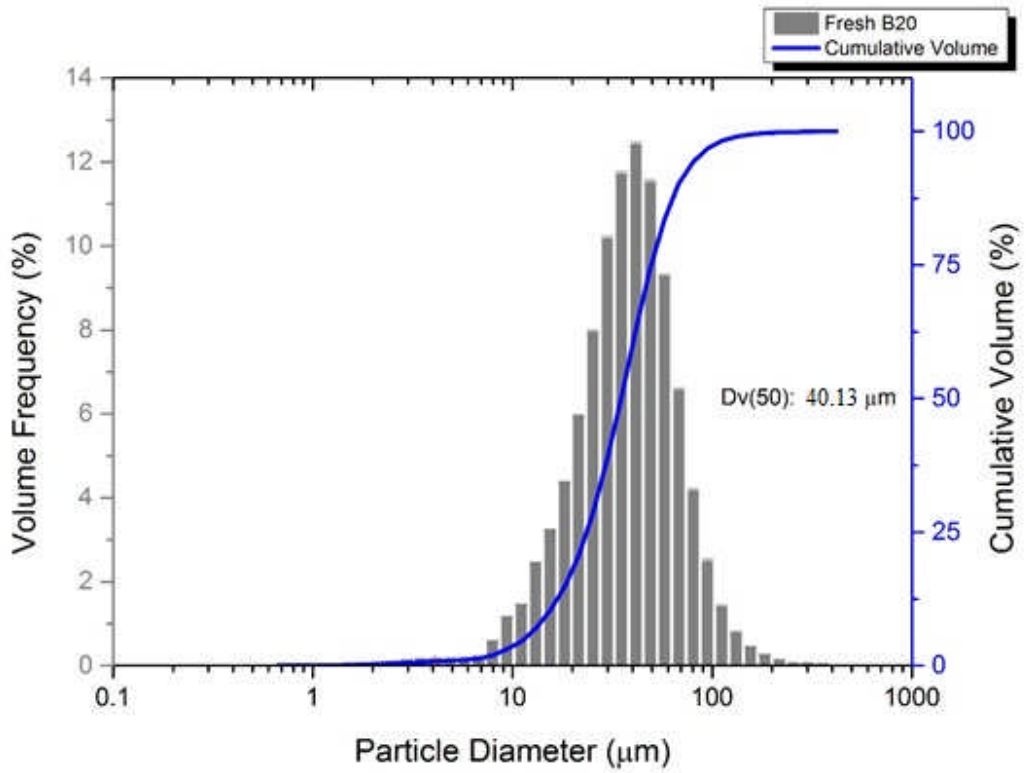


Figure 4-12: DSD of the water phase in B20 at atmospheric pressure

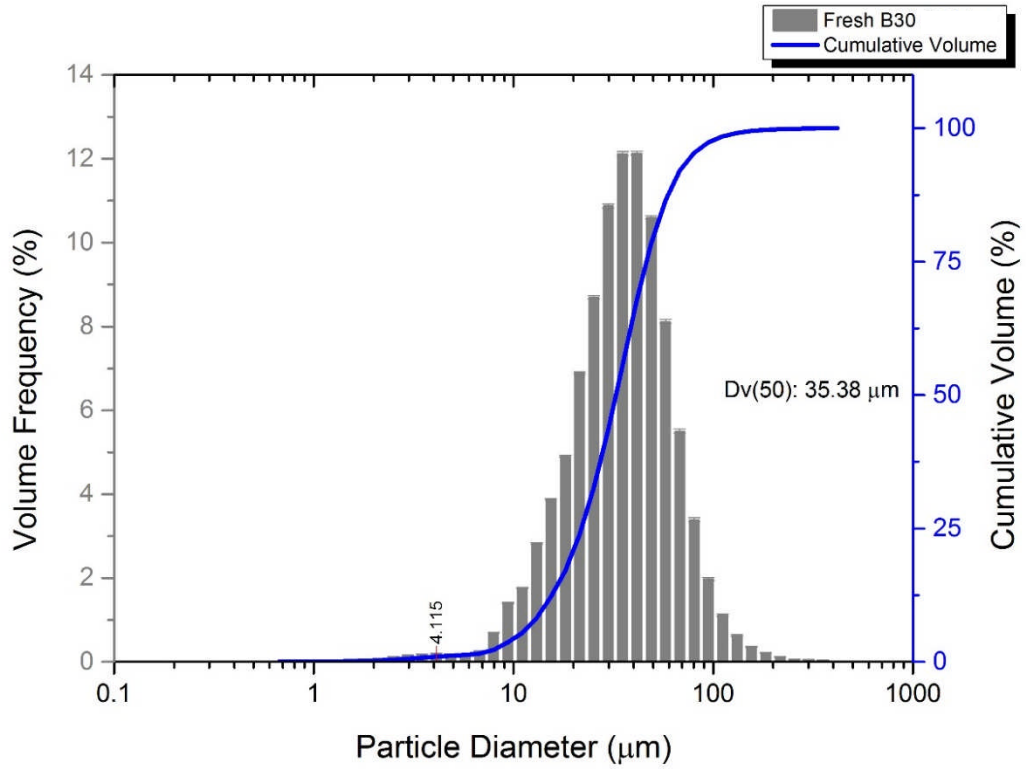


Figure 4-13: DSD of the water phase in B30 at atmospheric pressure

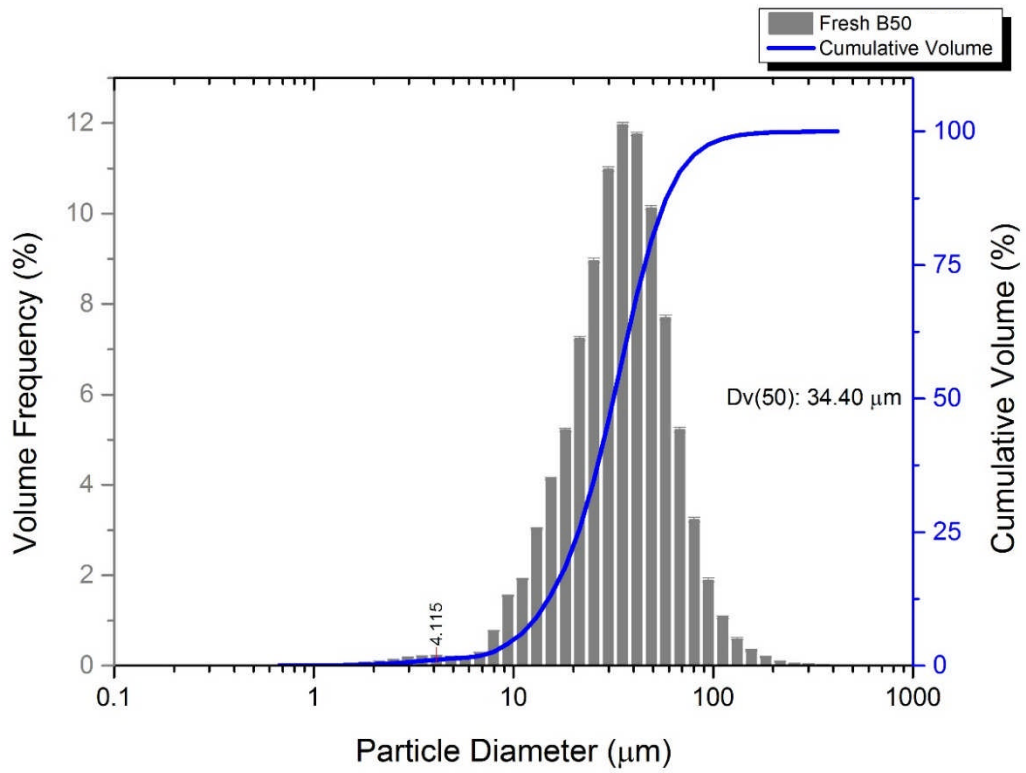


Figure 4-14: DSD of the water phase in B50 at atmospheric pressure

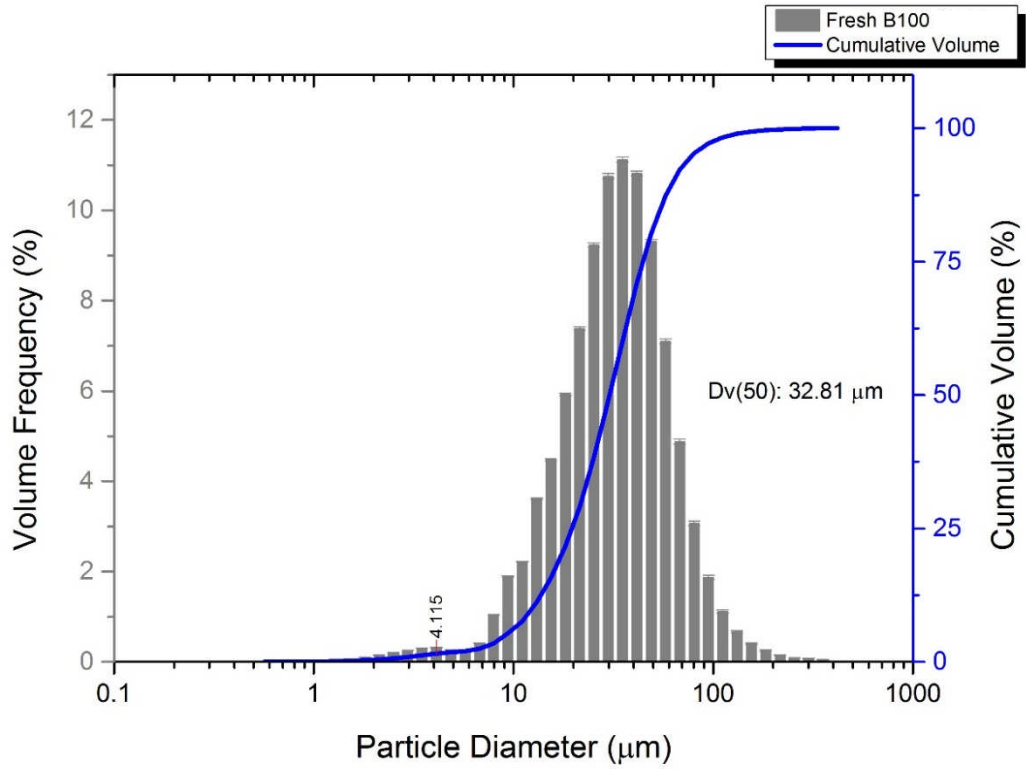


Figure 4-15: DSD of the water phase in B100 at atmospheric pressure

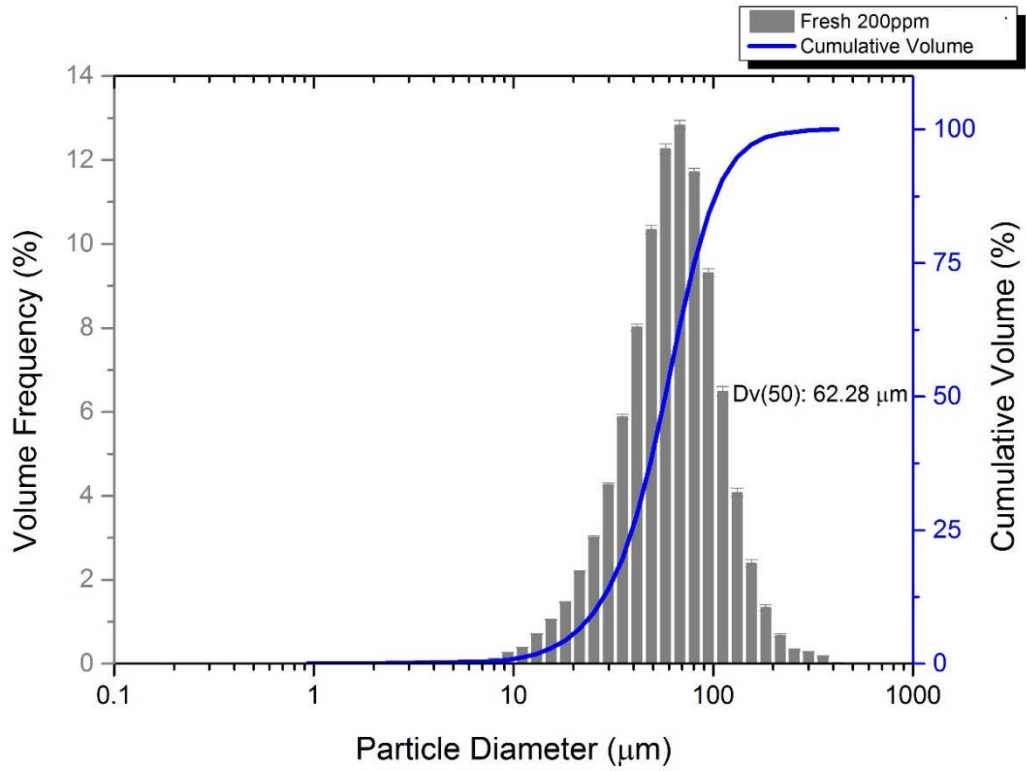


Figure 4-16: DSD of the water phase in M200 at atmospheric pressure

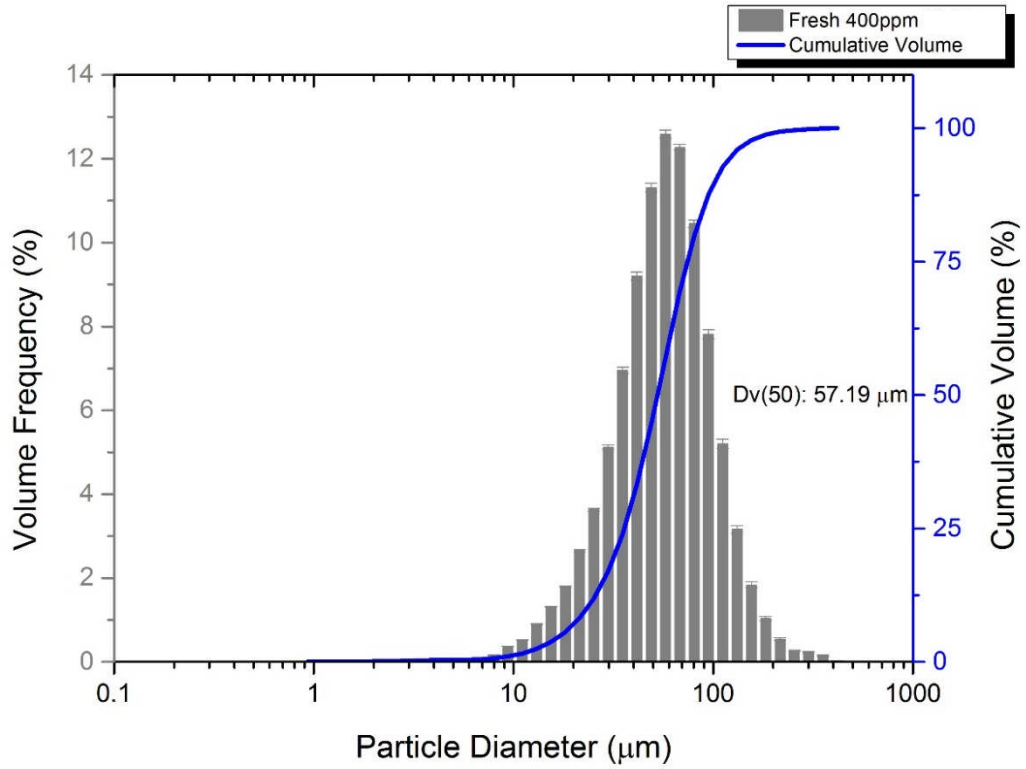


Figure 4-17: DSD of the water phase in M400 at atmospheric pressure

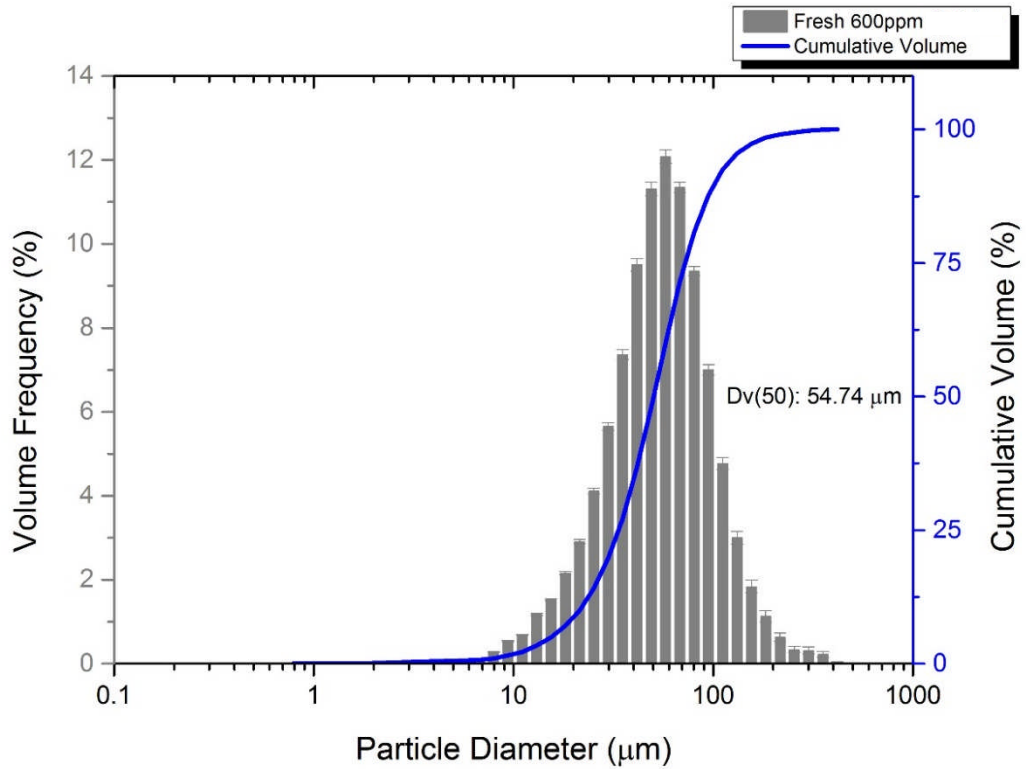


Figure 4-18: DSD of the water phase in M600 at atmospheric pressure

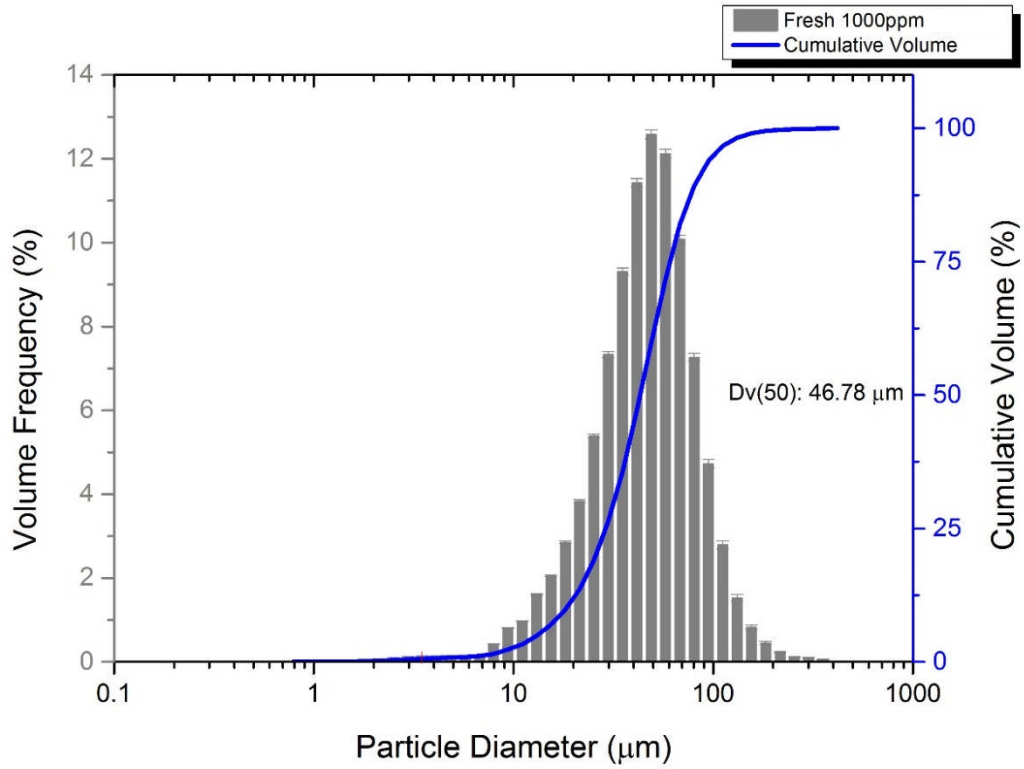


Figure 4-19: DSD of the water phase in M1000 at atmospheric pressure

Table 4-4: Dv_{50} of dispersed water droplets in monoolein and bio-diesel blends at atmospheric pressure

Test Fuel	Dv_{50} (μm)	Test Fuel	Dv_{50} (μm)
REF	69.9 ± 0.23	M200	62.28 ± 0.18
B5	49.81 ± 0.1	M400	57.19 ± 0.17
B10	44.07 ± 0.08	M600	54.74 ± 0.35
B20	40.13 ± 0.06	M1000	46.78 ± 0.13
B30	35.38 ± 0.05		
B50	34.4 ± 0.07		
B100	32.81 ± 0.06		

Comparing the droplet size distributions (DSD) of the fuel blends (Figure 4-9 to Figure 4-19), all the graphs have a clear peak which is close to their Dv_{50} s. The graphs of the bio-diesel blends containing more than 30% (v/v) bio-diesel (Figure 4-13, Figure 4-14, Figure 4-15), however, show another peak which are small and around the size of 4 μm . This can be attributed to the capability of the bio-diesel blends to create small size droplets due to their higher viscosity compared to the REF fuel (see Section 3.4.3). Based on Table 4-4, Dv_{50} of the REF fuel decreased from $69.9 \pm 0.23 \mu\text{m}$ to $34.4 \pm 0.07 \mu\text{m}$ by addition of 50% bio-diesel (B50), and reduced to $46.78 \pm 0.13 \mu\text{m}$ by addition of 1000 ppm monoolein (M200). This data confirms that both monoolein and bio-diesel reduce water droplet size in the fuel and are able to stabilise water droplets at a lower size compared to the reference grade diesel at an identical flow rate. However, to characterise them regarding the water droplet size, the Dv_{50} of water droplets in the fuel blends were plotted with regard to the IFT of the test fuels as shown in the Figure 4-20.

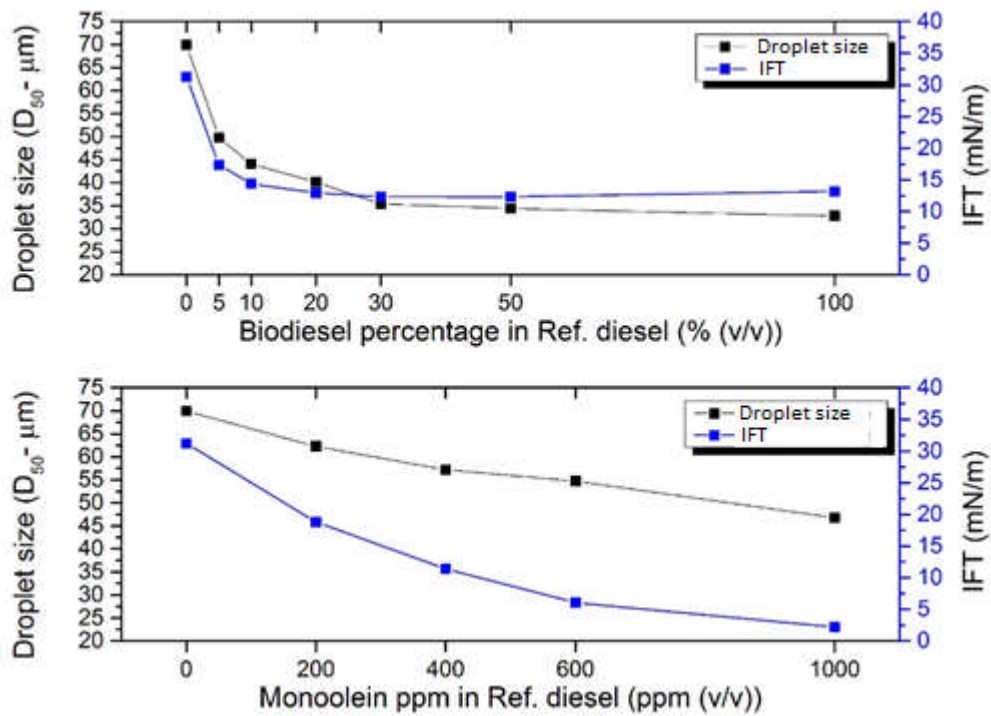


Figure 4-20: Dv_{50} for dispersed water droplets, related to the IFT of the monoolein and bio-diesel blends at atmospheric pressure

Based on Figure 4-20, at an IFT between 17 and 19 mN/m , the Dv_{50} of water droplets in B5 was much smaller than that measured for M200 ($49.81 \pm 0.1 \mu m$ Vs. $62.28 \pm 0.18 \mu m$). The Dv_{50} of the water droplets in B20 was also smaller than that of M400 at an IFT over a range of 11 - 13 mN/m . This indicates that the bio-diesel blends exhibited smaller Dv_{50} values compared to the monoolein blends at corresponding IFT values (Figure 4-20). Regardless of the chemical composition of the monoolein and bio-diesel molecules, this can be attributed to the lower molar ratio of the monoolein than the bio-diesel in the fuel blends, e.g. 0.5924 and 0.0009 mol/l in B20 and M325 respectively (as explained in the Section 3.4.1), resulting in an inability of monoolein to maintain the IFT in the emulsion as low as was measured via tensiometry. During an IFT measurement via tensiometry, the IFT of the interface between the fuel and water phases is measured while the linear interface is stable and has a constant surface area during the measurement. However, when the same volume of water is emulsified in the fuel, the surface area of the fuel-water interface increases, which is because of water droplets dispersed in the fuel. Therefore, a greater number of surfactant molecule is required to maintain the IFT of the emulsion at the same value as what is measured via tensiometry. As explained in Section 3.4.1, in the case of the monoolein and bio-diesel, there are a greater number of bio-diesel molecules in the bio-diesel blends compared to the number of monoolein molecules (Figure 4-21) such that the bio-diesel blends provide many more surfactant molecules compared to the monoolein blends enabling the fuels to stabilize the emulsified droplets at a smaller size. Based on this and also the fact that the bio-diesel blends had a higher viscosity than the monoolein blends at an identical IFT, water droplets are exposed to a greater shear stress competing with their lower Laplace pressure in the bio-diesel blends compared to the monoolein blends, which could contribute to the formation of smaller droplets in bio-diesel blends.

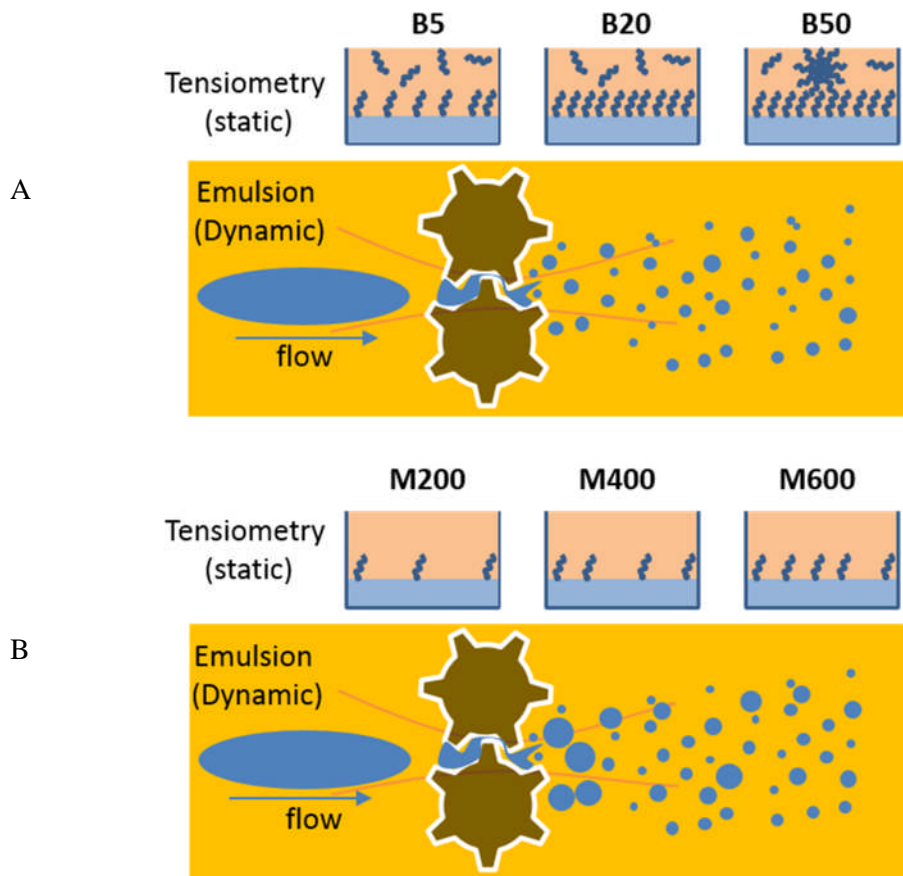


Figure 4-21: Effects of molar concentration of A) bio-diesel and B) monoolein in changing fuel-water interface characteristics in static and dynamic conditions

Table 4-5 lists Dv_{50} of water droplets ($\text{mean} \pm SE$) in the fuel blends at the 4 bar static pressure and Figure 4-22 to Figure 4-29 show the water droplet size distributions (DSD) for this operating condition.

Table 4-5: Dv_{50} of dispersed water droplets in monoolein and bio-diesel blends at the 4 bar pressure based on results presented in Figure 4-22 to Figure 4-29

Test Fuel	Dv_{50} (μm)	Test Fuel	Dv_{50} (μm)
REF	66.27 ± 0.6	M200	58.95 ± 0.21
B10	41.21 ± 0.09	M400	54.77 ± 0.19
B20	38.03 ± 0.07		
B30	33.79 ± 0.05		
B50	31.78 ± 0.05		
B100	31.54 ± 0.05		

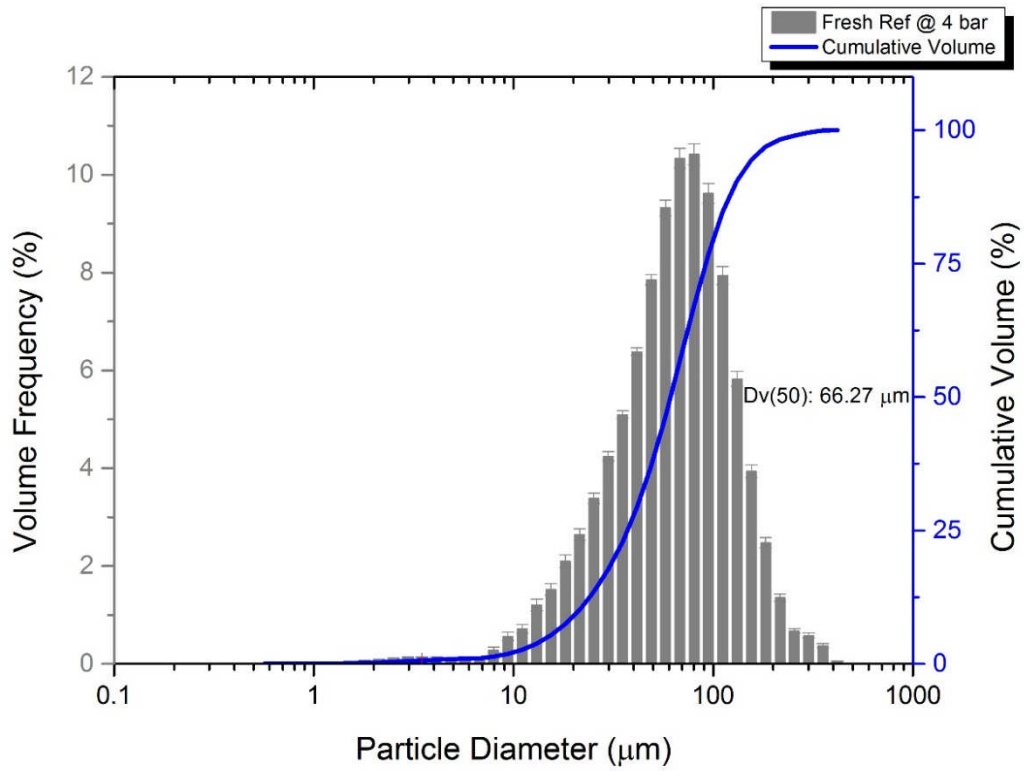


Figure 4-22: DSD of the water phase in REF at 4 bar pressure

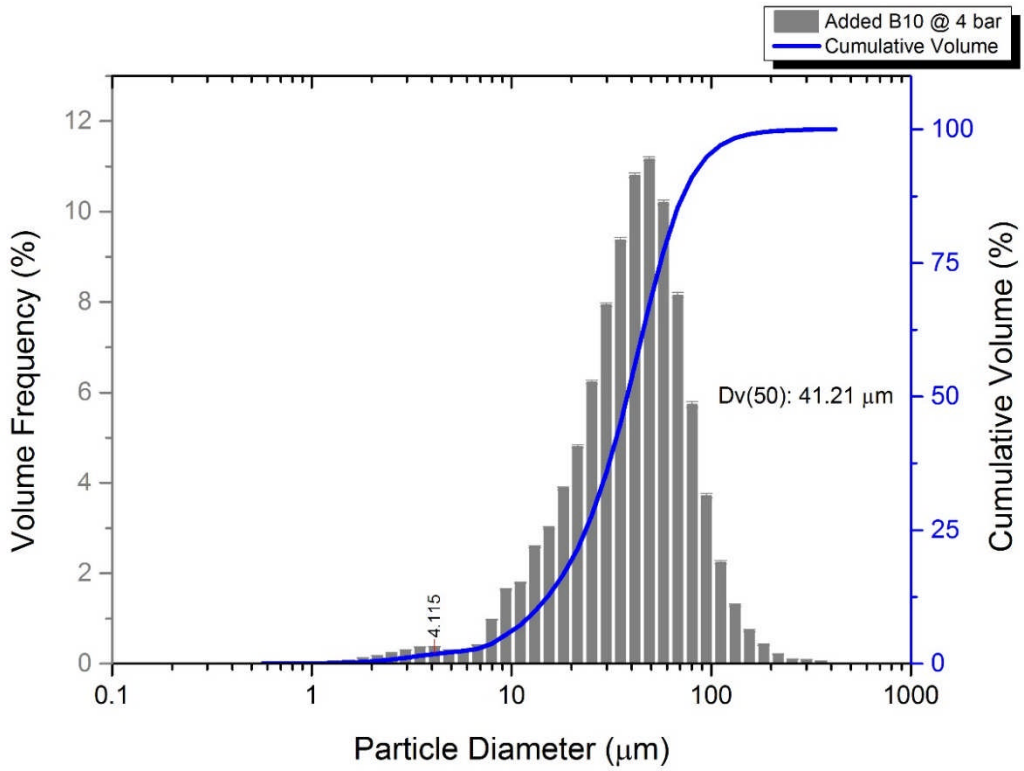


Figure 4-23: DSD of the water phase in B10 at 4 bar pressure

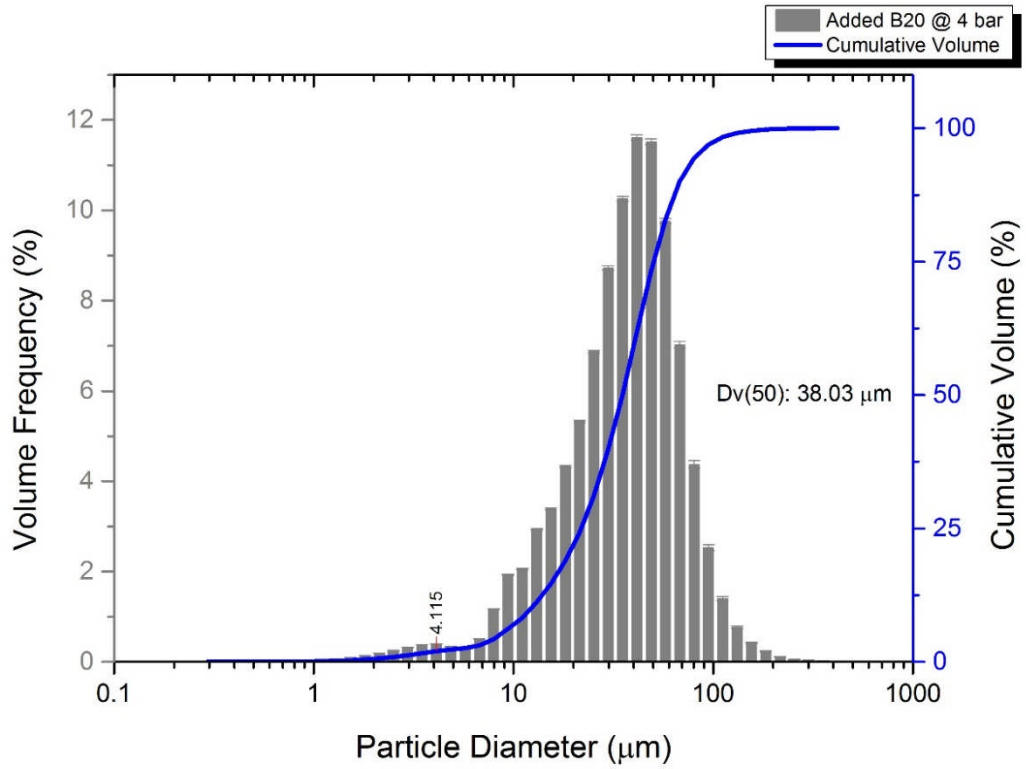


Figure 4-24: DSD of the water phase in B20 at 4 bar pressure

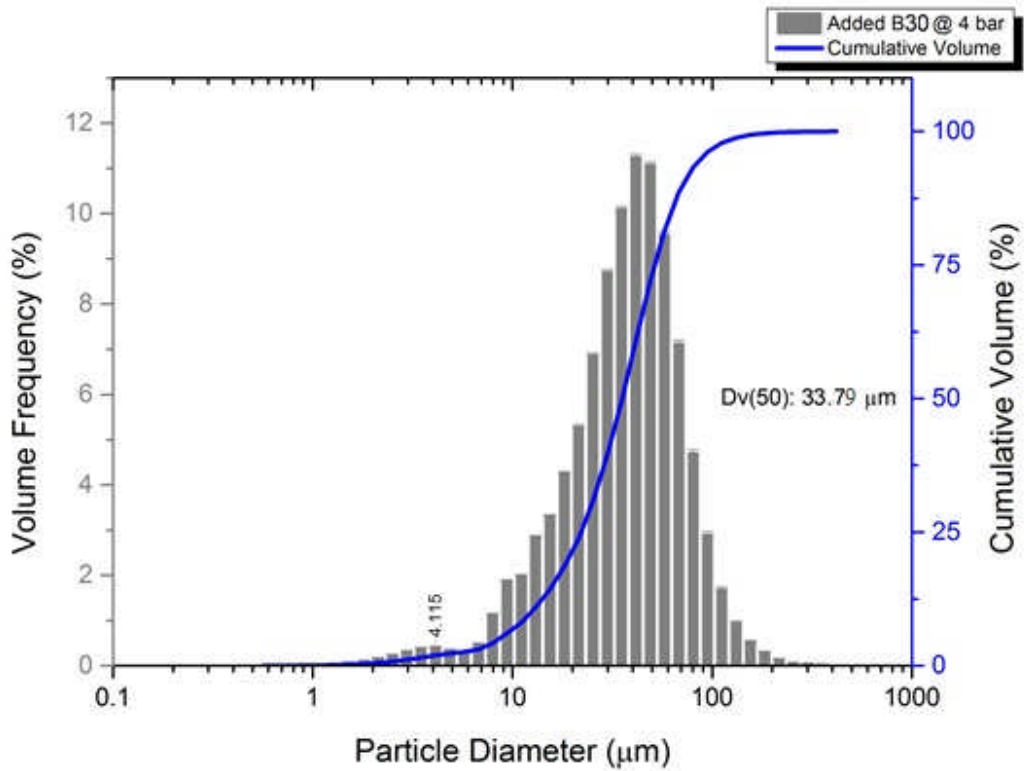


Figure 4-25: DSD of the water phase in B30 at 4 bar pressure

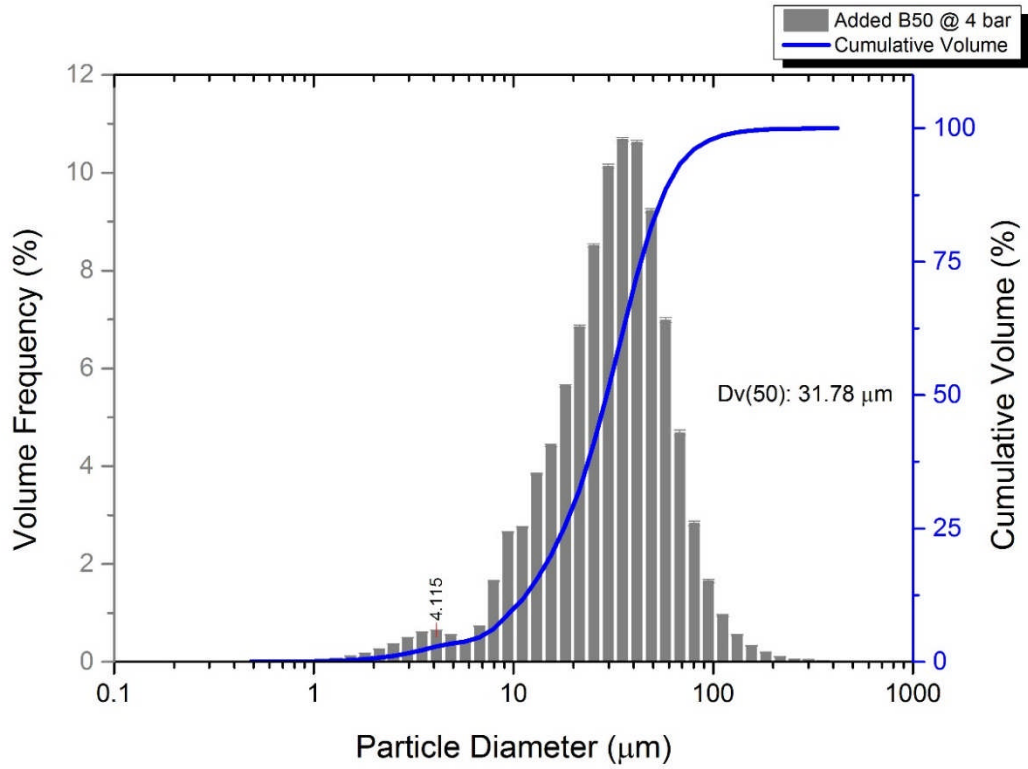


Figure 4-26: DSD of the water phase in B50 at 4 bar pressure

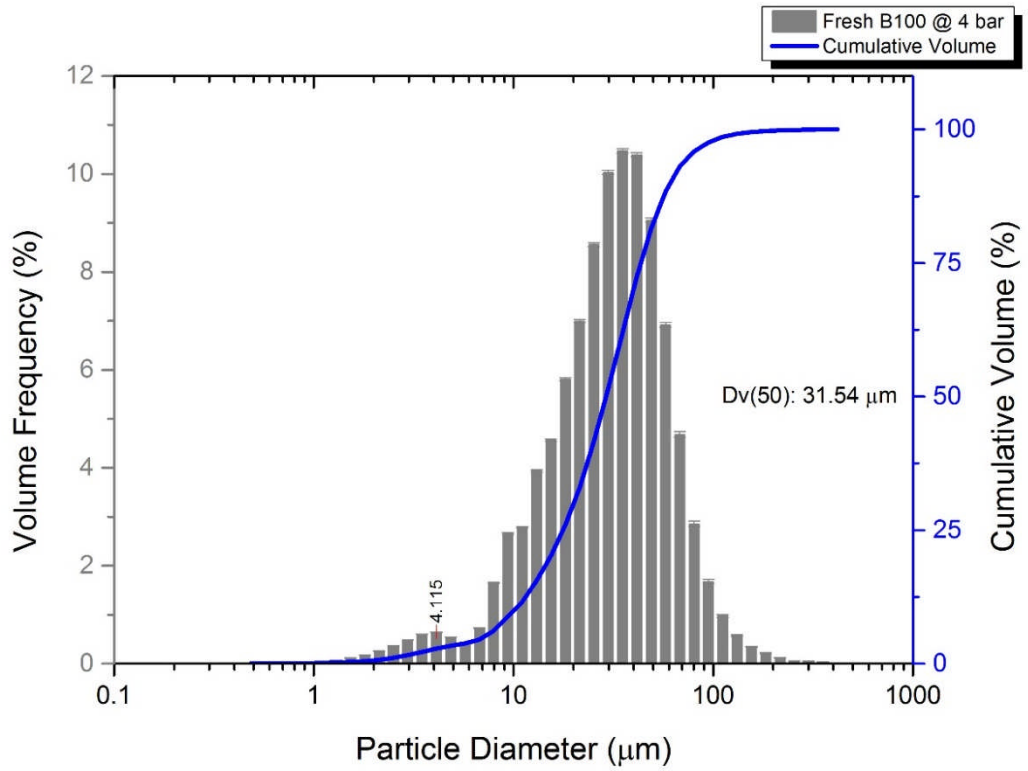


Figure 4-27: DSD of the water phase in B100 at 4 bar pressure

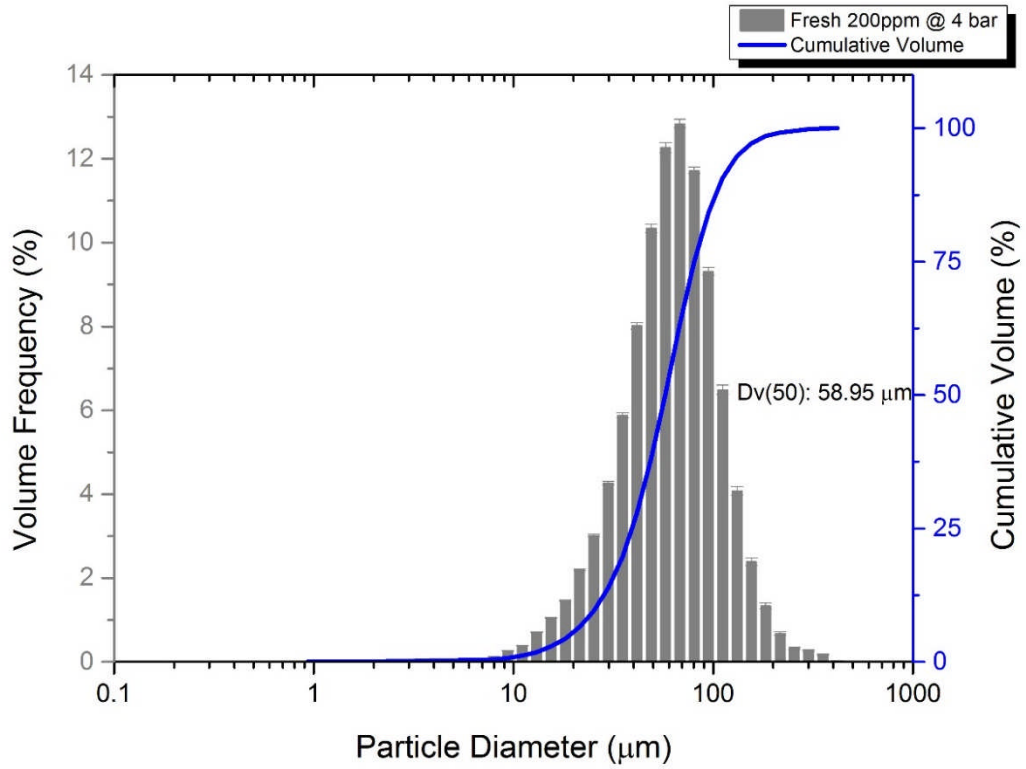


Figure 4-28: DSD of the water phase in M200 at 4 bar pressure

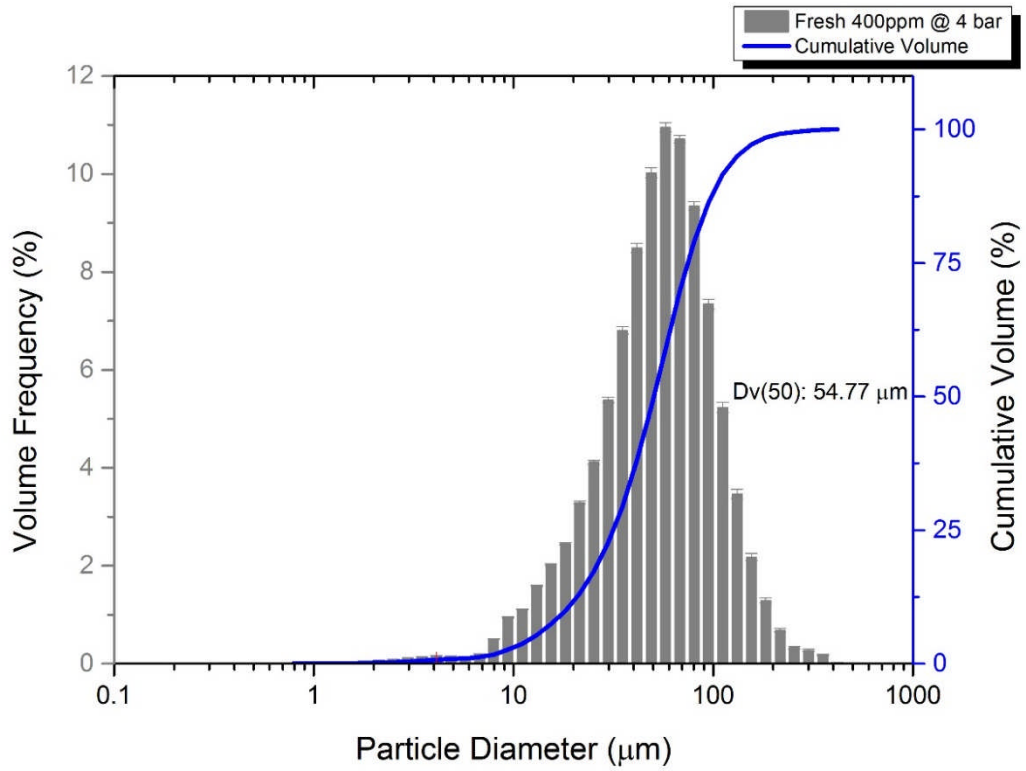


Figure 4-29: DSD of the water phase in M400 at 4 bar pressure

Figure 4-30 also compares the Dv_{50} values for two test conditions.

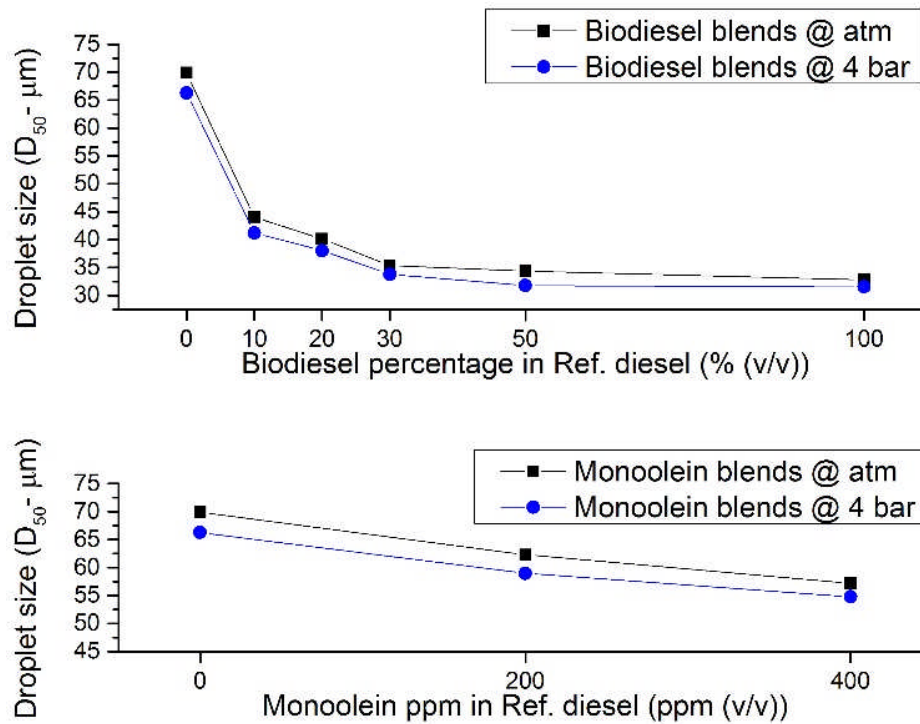


Figure 4-30: Dv_{50} of dispersed water droplets at atmospheric and 4 bar pressures in monoolein and bio-diesel blends

Based on the resulting graphs (Figure 4-22 to Figure 4-29), by increasing the static pressure during emulsion generation to 4 bar, size distributions become slightly wider and is shifted to the right side. Moreover, the small peaks around the size of 4 μm was detected on B10 and B20 in addition to B30, B50, and B100 (Figure 4-23 to Figure 4-27). Dv_{50} of the blends at the 4 bar pressure, Table 4-5, also confirm that by increasing the static pressure to 4 bar smaller droplet sizes were formed compared to atmospheric pressure (Table 4-4). This reduction was observed for all the test fuels. This is of practical significance because in diesel fuel engines, high pressures are increasingly used, meaning smaller droplet sizes are likely to be increasingly encountered.

4.5.3 DSEP rating

DSEP rating was performed on the test fuels based on the procedure explained in Section 4.3.3, however, the rates for all the test fuels were found to be zero except REF and B5 fuels (Table 4-6). All the blends were so cloudy that they could be rated at time = 0 such that the REF fuel was the only one that could acquire an initial DSEP rate of 82. Except B5, all the other blends remained cloudy for the dynamic DSEP rate as well.

Table 4-6: Dynamic DSEP of the test fuels

Test fuel	Time (<i>min</i>)					
	0	15	30	60	90	120
REF	82	98	100	100	100	100
B5	0	58	70	75	95	97
B100	0	0	0	0	0	0
M200	0	0	0	0	0	0

The initial DSEP value of the REF fuel decreased from 82 to zero by adding either monoolein or bio-diesel, such that it was concluded that the DSEP rating technique is incapable of differentiating between bio-diesel and monoolein regarding resistance to coalescence and changes in the settling velocity of the emulsified droplets in the fuel blends. The dynamic DSEP measurements could not clearly distinguish between monoolein and bio-diesel additives in water separation either. Moreover, during the dynamic measurements, it was noticed that the light beam of the turbidimeter was interacting with the emulsions and clear fuel was observed locally in the path of the light beam while the majority of the volume of the test fuel was still cloudy. Reliance on DSEP values was therefore concluded to be out of measurement capability.

4.5.4 Water separation via the sedimentation test

Table 4-7 summarises the volume of settled water at different time intervals for each of the fuel samples, and Table 4-8 illustrates the appearance of the samples after intervals of 3, 10, 90, and 300 min. This time series provides a semi-quantitative comparison of the fuel blends.







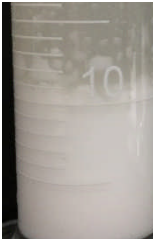



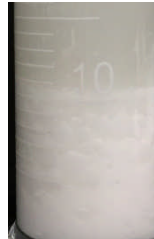













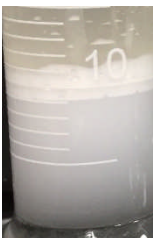


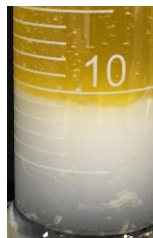


It was apparent that the bio-diesel blends produced longer settling times compared to the monoolein blends and the REF fuel, and water droplets were more stable in B20 and B50 compared to the other test fuels. This could be the result of the higher viscosity of the bio-diesel blends as well as their ability to stabilise water droplets of smaller size resulting in a reduction in the settling velocity of the dispersed water.

Visual assessment of the REF mixture revealed settled water that first appeared milky in colour but which gradually cleared. However, in the fuels containing bio-diesel and monoolein, progression from the milky phase to clear water was accompanied by a flocculation phase containing water. This was indicative of a resistance to coalescence associated with the presence of the surfactant or bio-diesel molecules at the interface of the water droplets. Comparing the fuel phases in each of the samples, B50 appeared clearer than the other blended fuels, which may be attributable to the relatively high capability of B50 to dissolve small water droplets.

Table 4-7: Water separation/settlement in the test fuels (*ml*)

Fuel ID	Time (<i>min</i>)																	
	1	2	3	4	5	6	7	8	9	10	20	30	60	90	120	180	240	300
REF	8	10	10	10	10	10	10	10	10	10	10	10	10	10	10	10	10	10
B5	4	9	10	10	10	10	10	10	10	10	10	10	10	10	10	10	10	10
B20	-	-	7	7	7-8	8	8-9	9	10	10	10	10	10	10	10	10	10	10
B50	-	-	7	8	9	9	10	10	10	10	10	10	10	10	10	10	10	10
M200	8	11	10	10	10	10	10	10	10	10	10	10	10	10	10	10	10	10
M325	-	5-7	7-9	7-9	10	10	10	10	10	10	10	10	10	10	10	10	10	10

Table 4-8: Visual assessment of water separation in fuel blends

	REF	B5	B20	B50	M200	M325
0 th min						
3 rd min						
10 th min						
90 th min						
300 th min						

4.6 Summary

In Chapter 3, the effects of bio-diesel and monoolein on the behaviour of diesel fuel were discussed, and the resultant impact on water-in-fuel emulsions was further explored in Chapter 4 with reference to bio-diesel and monoolein surfactant. Following construction of a bespoke emulsion generation test rig, online measurements of water droplet size distributions (DSD) in diesel containing bio-diesel and monoolein were undertaken. Water separation was also evaluated using the DSEP rating and sedimentation tests.

In existing test standards, specifically ISO 16332 and SAE J1488, monoolein surfactant is employed to adjust the IFT of the reference grade test fuel so as to mimic the presence of fuel additives including bio-diesel in petrol station diesel. However, the results reported herein, raise questions about the suitability of monoolein as an appropriate fuel additive for the test standard, because it does not behave comparably with bio-diesel. Fuel containing bio-diesel contained more dissolved water and led to higher viscosities (see Section 3.4.3) compared to the REF fuel and monoolein blends. This occurs even though bio-diesel acts like monoolein as a surface active agent reducing the fuel IFT and stabilising water droplets in the fuel such that flocculation occurs during water settlement. It is apparent that bio-diesel blends and emulsions are capable of maintaining a low IFT measured by tensiometry. However, this does not happen for monoolein blends due to differences in the molar ratios. This coupled with the higher viscosity in a bio-diesel blend leads to smaller water droplet sizes compared to monoolein blends.

The effect of the static pressure on droplet size distribution (DSD) was tested by applying 4 bar pressure on the fuel blends in the emulsion rig, revealing that higher pressures lead to a

decrease in the droplet size of the emulsion, which is independent of the type of additive (bio-diesel or monoolein).

This chapter also characterised emulsions using the DSEP rating. This technique is considered to be ineffective as an accurate method of evaluating water separation in diesel fuels containing surfactants. Based on the experimental data herein, evaluating the DSD of an emulsion is thought to be a more useful measure to control surfactant levels in fuel blends rather than the DSEP rating, water sedimentation, and IFT measurements.

CHAPTER 5

Design and Construction of the Coalescence Test Rig

5.1 Introduction

Evaluation of coalescing performance of a nonwoven filter media was key to building a relationship between structure and properties and therefore a new test rig was required to provide a means of instrumental characterisation. In this Chapter, the design, construction, and validation of the new coalescence test rig are explained. The test rig was then used for evaluating existing coalescence filters (benchmark samples in Chapter 6) as well as nonwoven media specifically developed as part of this research (Chapter 7). Existing methods such as those described in ISO 4020, ISO 16332 and SAE J1488 were briefly discussed in Section 2.5 of the literature review chapter because of their relevance to building the new test rig.

5.2 Scope

The aim was to provide a robust lab scale test rig to generate water in fuel emulsions and then to enable its circulation through a filter test housing accommodating a flat fabric sheet sample capable of acting as a fuel-water separator. Herein, separation means the removal of water droplets from the emulsion by a coalescence mechanism.

The test rig was designed to generate fine emulsified water droplets, i.e. with a Dv_{50} less than $25 \mu m$, and to challenge test filter samples at a face velocity close to what is encountered in the field, which is ca. $8 mm/s$.

5.3 Design of the new test rig

The first step in designing the coalescence test rig was to understand existing standard test methods for separation of water from diesel, as was explained in Section 2.5. To design the coalescence test rig the operational limitations of existing filtration test standards were

considered (see Section 2.5) and the following additional criteria for an alternative system were defined:

- Flexibility to conduct both coalescence efficiency and separation efficiency tests;
- A short test time of less than 24 h, manageable by an operator in a safe manner so that no significant online and automatic control systems are required;
- Ability to produce a uniform and steady fuel flow in a test system containing clean-up filters to provide a single-pass test in terms of water circulation;
- A filter housing capable of holding a flat sheet nonwoven filter medium and a barrier mesh medium, if required, for coalescence and separation tests;
- Ability to generate a water-in-fuel emulsion with the capability to control the water concentration at the upstream side of the filter housing;
- To challenge the test filter with water droplets in a fine size region;
- To have the capability to sample the test fuel for the purpose of water content measurement in the fuel at both the upstream and downstream sides of the filter housing in separation efficiency tests;
- To have a capability to easily drain and collect separated water.

The following sections explain the design and construction of the test circuits, filter housing and other key components of the new rig.

5.3.1 Filter housing design

Schematics of the filter housing are given in Figure 5-1. The final design that is shown enabled flat discs of nonwoven test sample to be held, as well as a plastic filter support and a barrier mesh (as required). This provided the flexibility to conduct either coalescence or separation tests.

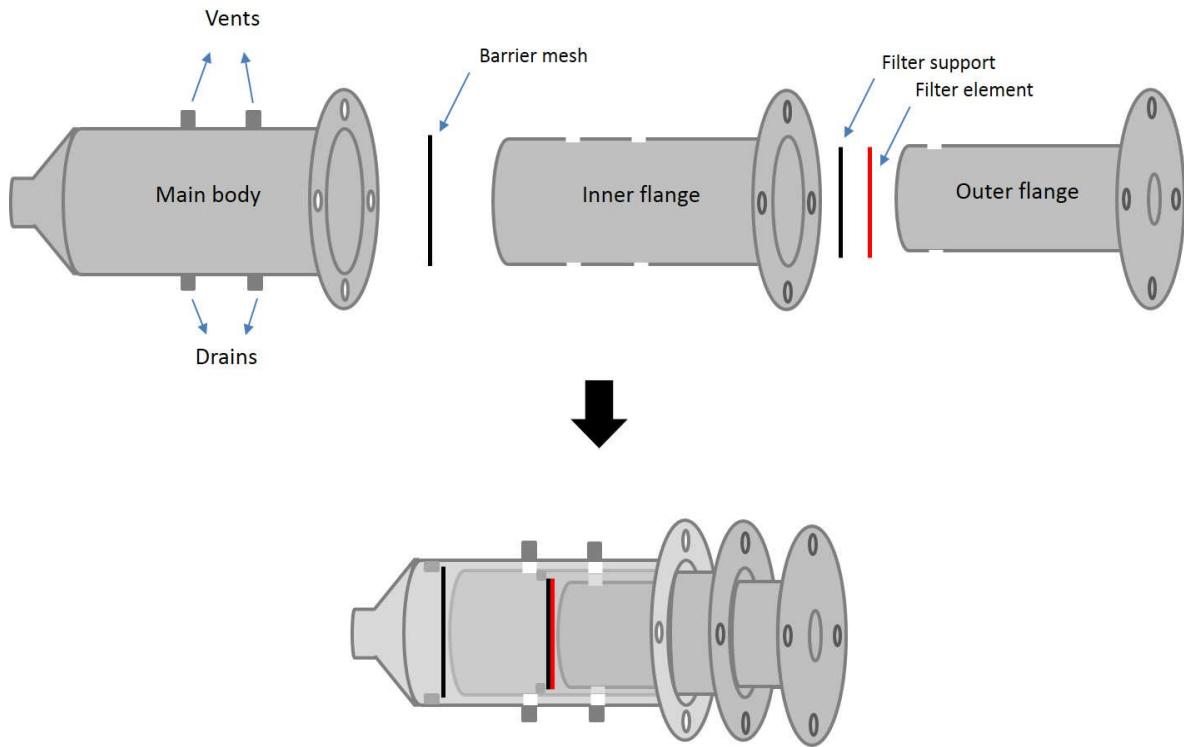


Figure 5-1: Initial design of the filter housing

The housing was composed of three cylindrical parts: the main body, inner flange (rear clamping flange), and outer flange (clamping flange), which could accommodate one or more of a filter fabric, filter support, and a barrier mesh disc. Figure 5-2 to Figure 5-5 demonstrate design details of the filter housing parts – all the dimensions are in *mm*. The two flanges are removable for ease of installation and removal of samples.

Part1 – outer flange (clamping flange)

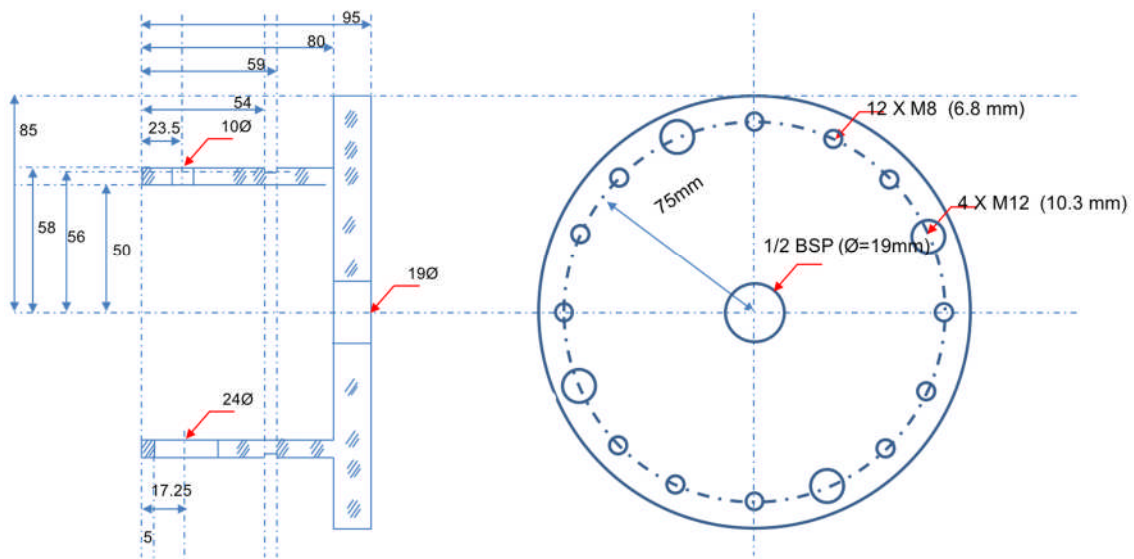


Figure 5-2: Design details of the outer flange of the filter housing

Part2 – inner flange (rear clamping flange)

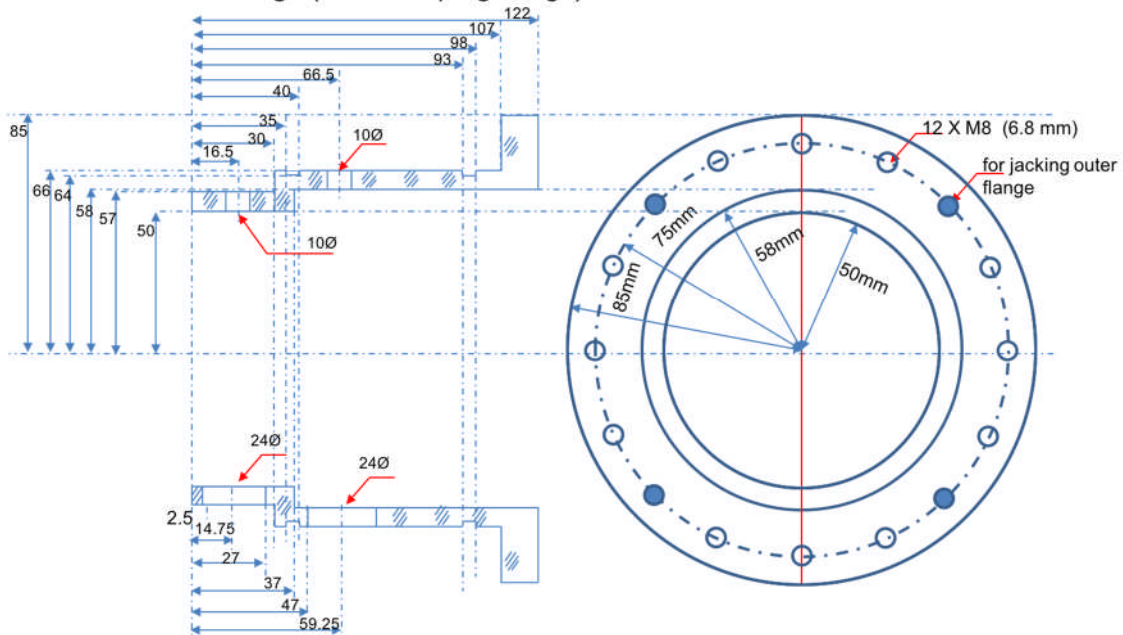


Figure 5-3: Design details of the inner flange of the filter housing

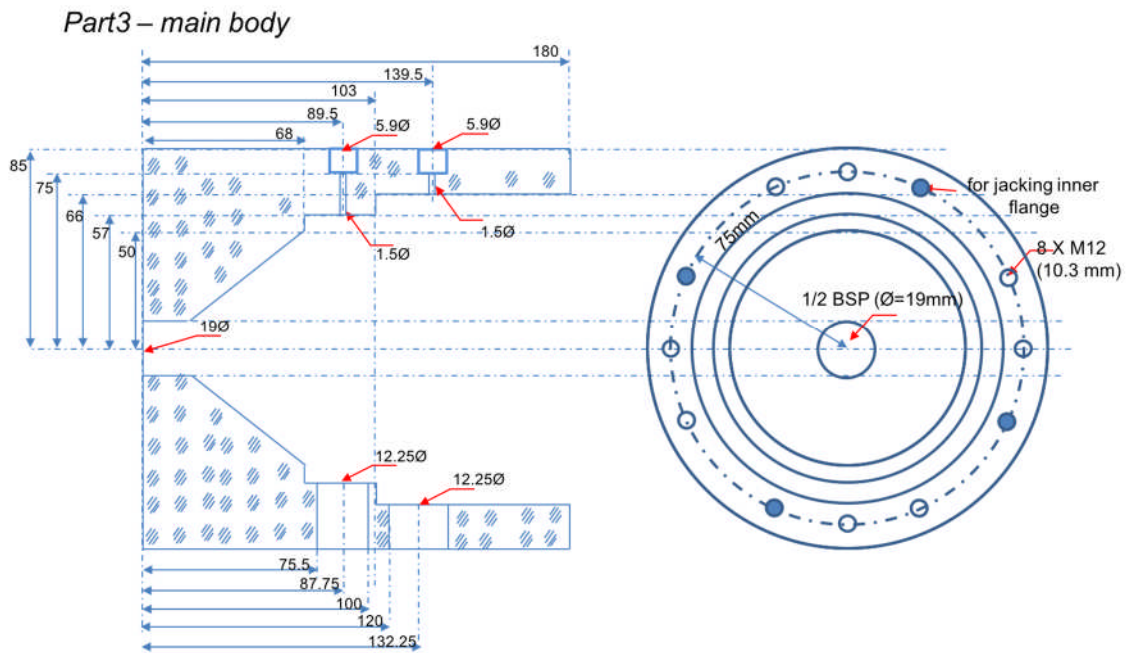


Figure 5-4: Design details of the main body of the filter housing

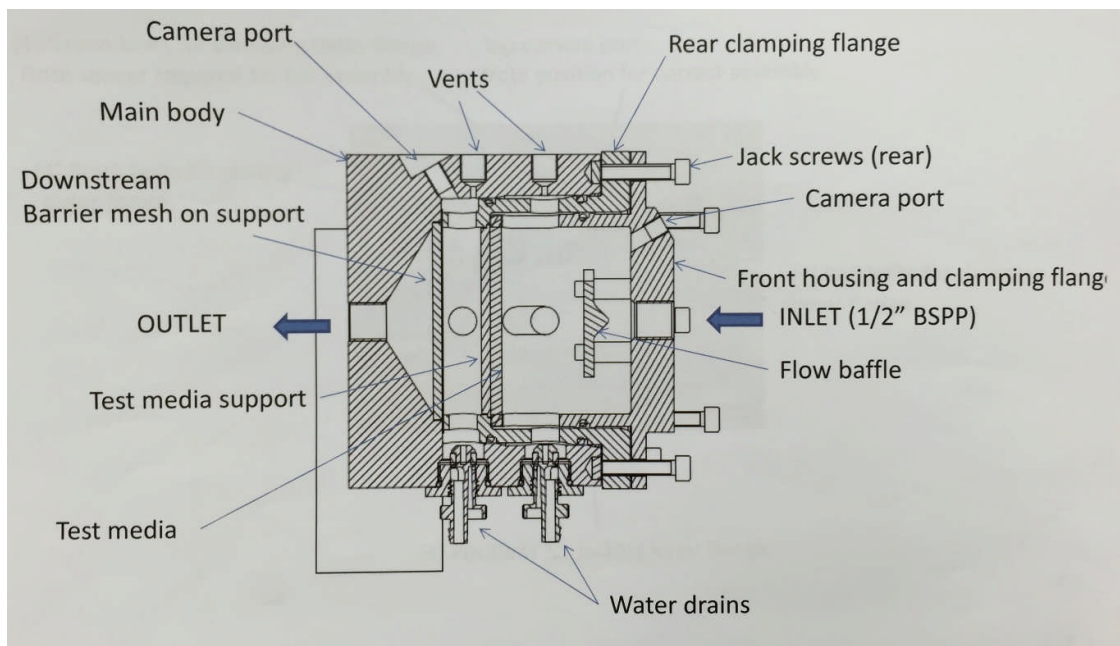


Figure 5-5: Design details of the new test filter housing with its three parts clamped together

The two flanges were screwed to the main body and O-rings placed on the outer surface of the flanges to provide proper sealing when the parts were screwed together. The inner flange together with the main body held the mesh disc (Figure 5-6 (B)) and the outer flange together with the inner one held the filter support (Figure 5-6 (A)) as well as the filter test sample. The use of filter support made of black polyethylene plastic was designed to prevent the test sample from collapsing under the flow pressure, and the barrier mesh was used to separate water droplets coming from the sample, which is required for a separation test. The barrier mesh was made of a disk of woven PET polyester fabric with pore size of $25\ \mu\text{m}$ laminated on a plastic support with the same specification of the filter support.

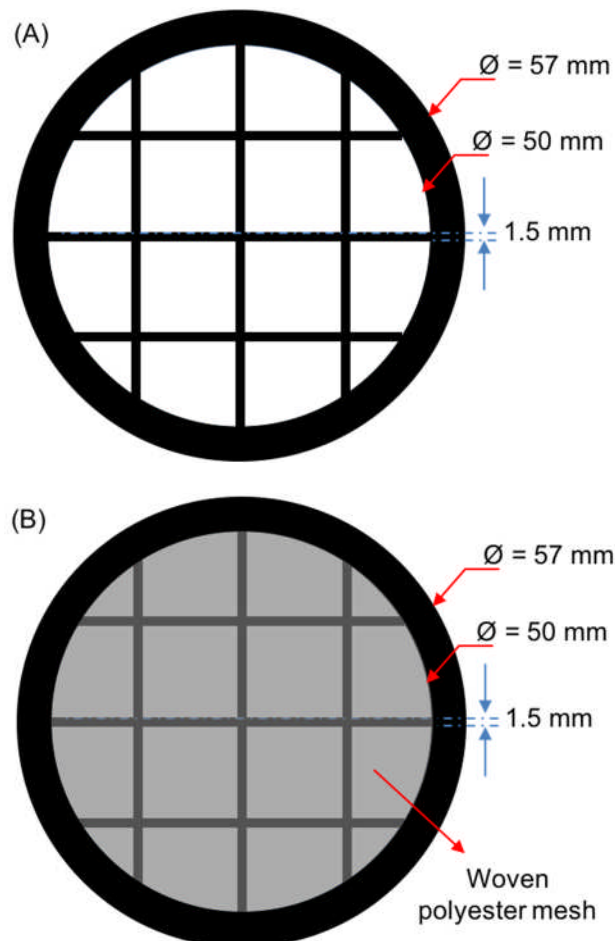


Figure 5-6: Design details of the filter support (A) and barrier mesh (B)

The flanges were designed to be removable using jack screws. The housing was provided with two vents to enable air bleeding as well as two drainage holes for collecting settled water from the both sides of the test sample during the test. The vents were blocked by bolts such that the operator could bleed the air by gradually unscrewing them. The downstream drain was connected to a portable collecting 250 ml bottle beneath the housing such that the bottle and the housing were filled with fluid during the test. The bottle were disconnected from the housing for discharging and/or measuring collected water after each test was complete. For the same aim, the upstream drain was connected to a hose instead of a bottle due to lack of space. Two camera ports on the housing facilitated monitoring both sides of the test filter during testing. Each test filter sample was cut to a circular shape with diameter of 11 cm and installed in the housing. A diameter of 10 cm was exposed to the flow after installation.

Two housing configurations were anticipated for evaluation, specifically use of the housing with and without a support mesh (Figure 5-7 and Figure 5-8).

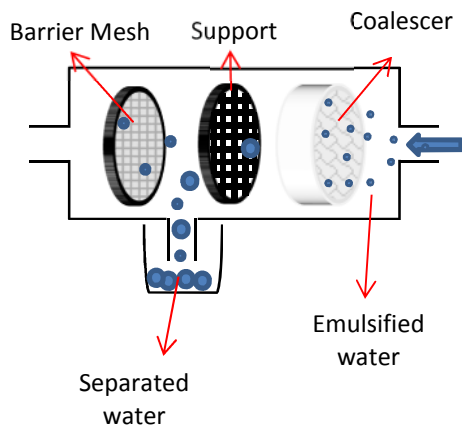


Figure 5-7: Housing configuration for the separation tests

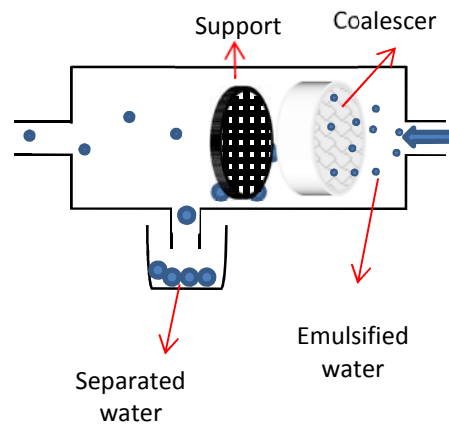


Figure 5-8 : Housing configuration for the coalescence tests

The former configuration was designed to conduct the separation tests in which water droplets are collected in the drainage bottle as a result of the coalescence and surface filtration at the barrier mesh. The latter configuration was designed for the coalescence tests in which water droplets are sufficiently large for gravitational settlement in the collection bottle are analysed to evaluate the coalescence efficiency of the filter.

5.3.2 Design of test system

The test system shown in Figure 5-9 was designed. The graphical symbols used to demonstrate the test system are in accordance with ISO 14617 (all parts) standard documents.

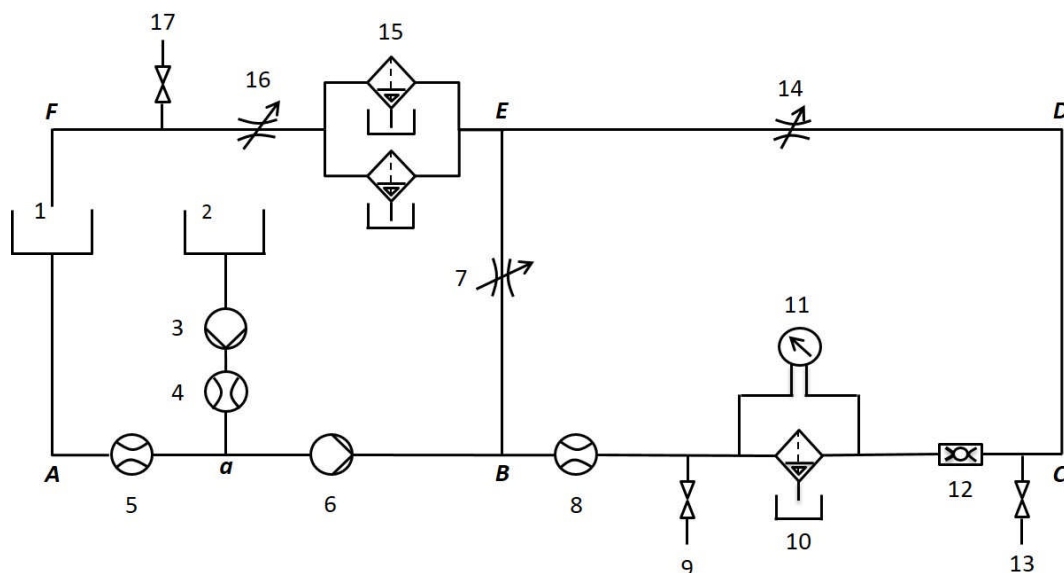


Figure 5-9: Schematic of the coalescing test rig built in-house for the efficiency tests

The test system components are as following:

- | | |
|-------------------------|-----------------------------------|
| 1- Fuel tank | 9, 13, 17- Sampler unit |
| 2- Water tank | 10- Parker test filter housing |
| 3- Water pump | 11- Monometer |
| 4, 5, 8- Flow meter | 12- Static mixer |
| 6- Main pump | 15- Two parallel clean-up filters |
| 7, 14- Adjustable valve | 16- Pressure valve |

The system comprises two circuits - the emulsion generation (ABEF) and filtration circuits (ACDF). The two circuits are connected to each other by a bypass line (BE) using a valve (7) to control the flow rate, as necessary. The inclusion of a bypass circuit was to maintain a constant pump flow rate if the flow in the filtration circuit was lower than required. This enabled a uniform water droplet size distribution (DSD) to be generated by the fuel pump for different filtration rates.

In the circuit, water-free fuel was fed from the fuel tank (1) into the pipeline by a pump (6) and passing through a flowmeter (5) and clean-up filters (15) and then returned into the fuel tank (1). Water held in the tank (2) was injected through an injector setup (a) into the upstream side of the pump to be mixed and pumped through the main pump (6). The water-in-fuel emulsion was introduced to the filter housing of the rig (10) in the filtration circuit. Water flow rate was controlled by a dosing pump (3) and was monitored by a flow meter (4). The clean-up filters ensured the water-free fuel could be returned to the fuel tank enabling a single-pass filtration test to be maintained. The performance of the clean-up filters were checked offline by titrating fuel samples (Section 3.3.3) taken from the sampling point (17). To change the static pressure as well as to facilitate air bleeding at the beginning of the test, a pressure valve (16) was incorporated.

In the emulsion generation circuit, assuming the valve (7) is open and valve (14) is closed, water was injected into the main stream and was emulsified into the fuel while the pump (6) generated a constant flow rate. The emulsion entered the filtration loop when the valve (7) was closed and the valve (14) was open. The flow rate in the open loop of BCDE is adjustable via the valves (7) and (14). In this circuit, the emulsion passes through a flowmeter (8) as well as the filter housing (10) and enters the emulsion generation loop again to pass through the clean-up filters and return into the fuel tank. Pressure drop across the filter was measured by a

differential pressure gauge (11), and water content of the fuel upstream and downstream of the filter housing was checked by sampling from points (9) and (13) using a titration procedure (see Section 3.3.3). To avoid any water settlement downstream of the filter in the pipeline, use of a static mixer (12) was included.

The design described herein, was suitable for both coalescence efficiency and separation efficiency tests as the main modifications needed to switch between these tests was done by simply modifying the configuration of the filter housing (see Section 5.3.1).

5.3.3 Test liquids

Deionised or distilled water with a surface tension about 72 mN/m , measured at a room temperature, i.e. $20^\circ\text{C} \pm 1.5^\circ\text{C}$, was used for the water injection. Test fuels of the same specifications given in Section 3.2 were used throughout. The fuel blends used in this work were prepared based on the procedure given in Section 3.3.1.

5.3.4 Filter sample

According to the filter housing design (Section 5.3.1) any filter sample cut in to a disc shape of 11 cm in diameter could be used in the test rig. The disk shape avoided variations due to anisotropy in the CD or MD directions. Samples were cut using a standard sample cutter.

5.3.5 Laboratory equipment

A Karl Fischer titration system (Section 3.3.3) and a tensiometry system (Section 3.3.2) were used to determine the water content and IFT of the test fuels. The laboratory where the test rig was located had a standard established fuel disposal system for the waste fuel as well as a proper ventilation system for extraction of the fuel vapour during the test rig operation.

5.3.6 Rig frame design

Figure 5-10 shows the design of the rig frame.

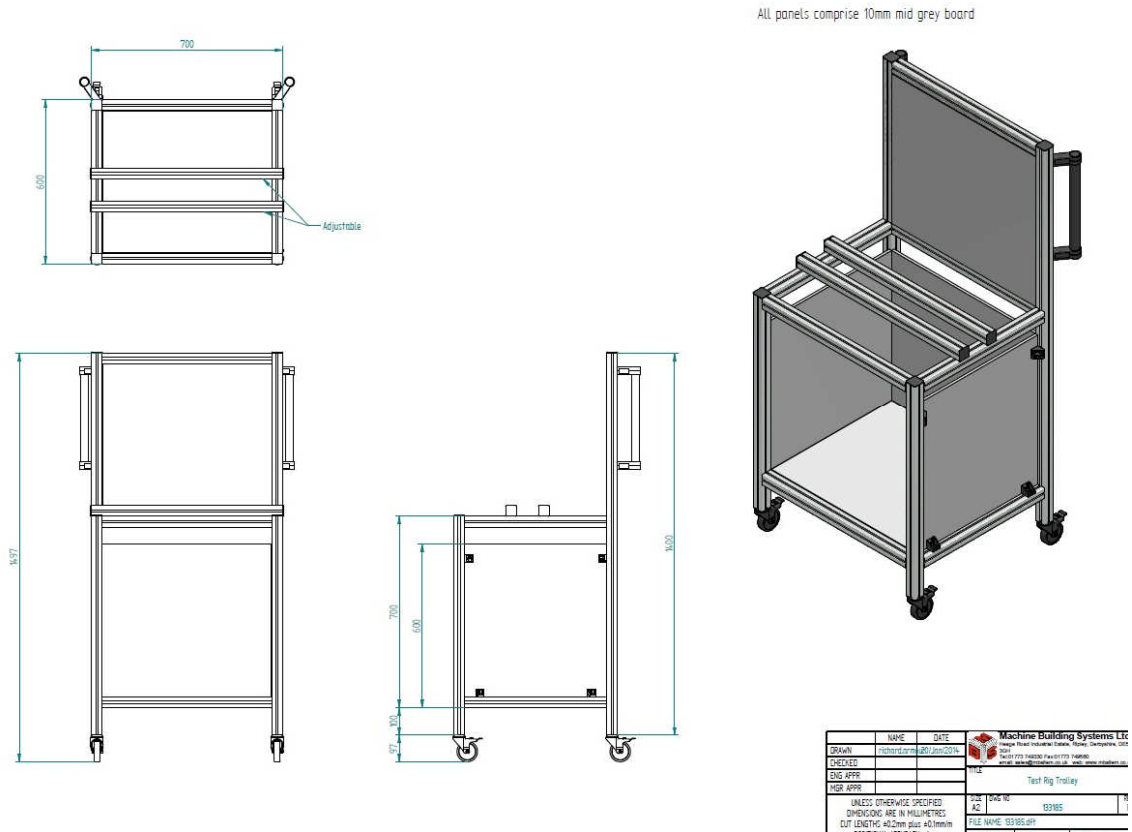


Figure 5-10: Frame (trolley) of the coalescence test rig

The frame was assembled from 40 mm × 40 mm light aluminium profiles secured at the joints with standard fasteners, universal fasteners and angle brackets. It was equipped with two handles and four wheels with a wheel brake to provide ease of relocation. The design of the housing as well as its construction was assisted by Machine Building Systems (UK).

5.3.7 Operating conditions and parameters for the test stand

5.3.7.1 Temperature

The rig was designed for evaluation of filter samples at room temperature of 23 °C □□□□□□.

All measurements were made under these conditions and in the same location.

5.3.7.2 Total test duration

The duration of both the coalescence and separation evaluations were fixed at 40 min, which included a period of 10 min pre-testing, 20 min water injection, and finally a 10 min fuel clean-up period. All evaluations were carried out under these fixed conditions. The period of water injection was defined as 20 min because the 250 ml water collection bottle could provide sufficient volume for water collection during this period at the designated water concentration and fuel flow rate explained below.

5.3.7.3 Volume of fuel

The volume of the test fuel was designed to be at least two times that of the test flow rate per minute for all the measurements. In so doing, there was always a sufficient volume of fuel to fill the system, whilst some fuel was left in the tank, which was needed to ensure steady fuel flow.

5.3.7.4 Test flow rate and filtration face velocity

As explained in Section 2.6.2, face velocity is one of the main parameters influencing the performance of coalescing filter media. In this work the velocity was maintained in the range 6 - 8 *mm/s* in accordance with guidance provided by Parker Hannifin. Therefore, given the fixed sample surface area, the main flow rate ranged between 2.8 and 3.8 *l/min*. Based on the designated tube size (316 Stainless steel, 9.525 mm outside diameter (OD) × 1.219 mm wall thickness (WT)) the Reynolds Number in the filtration zone (from sampling point 2 to sampling

point 3) was in the range of 5700 and 7700, which avoided creeping flow where sedimentation might otherwise be an issue.

5.3.7.5 Undissolved water concentration

Water concentration was defined as the concentration of undissolved water injected into the fuel intentionally during operation of the rig. The water concentration was maintained at 2500 *ppm*, in accordance with the value suggested by the SAE J1488 test procedure.

5.3.7.6 Operating procedure

Two possible operating procedures could be used to evaluate filters using the new rig: coalescence efficiency and separation efficiency, depending on which housing configuration was selected (Section 5.3.1). All other operating parameters such as flow rate, face velocity, water concentration, were kept constant throughout. The specific values used for each method are given in Section 5.5.

5.4 Construction of the test rig

The detailed specifications of the rig shown in Figure 5-11 are discussed with reference to Figure 5-9.

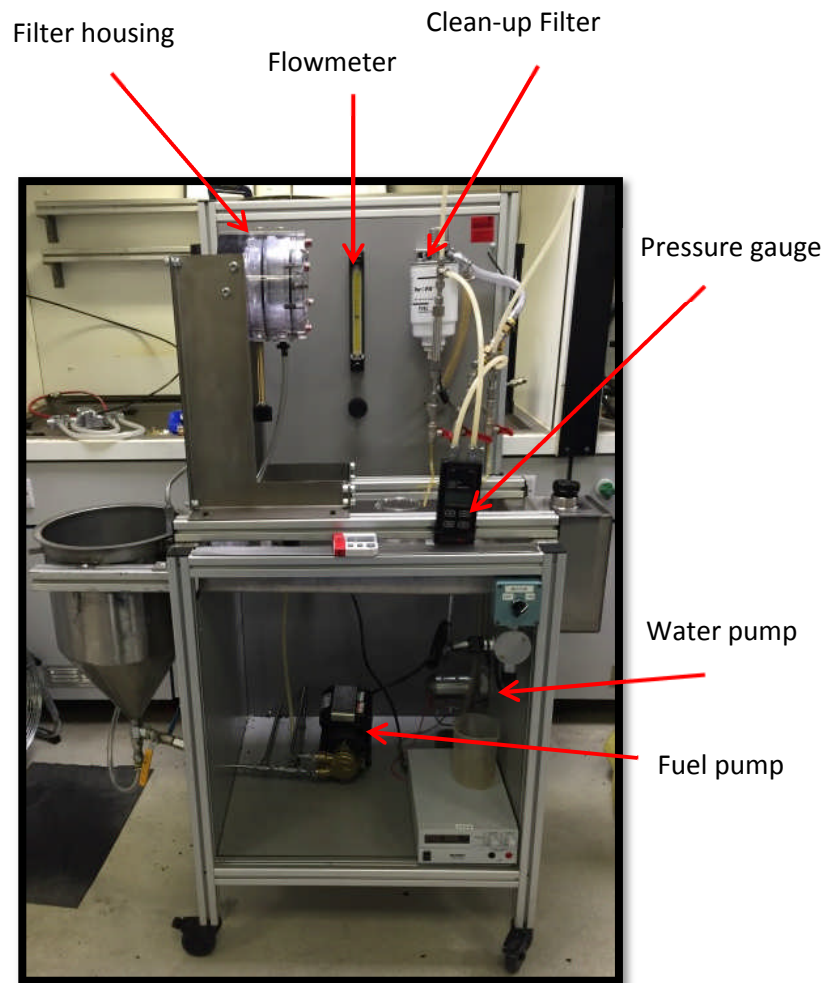


Figure 5-11: The coalescence test rig

5.4.1 Test stand tubing and fittings

316 Stainless steel 3/8" tube (3/8" OD \times .048" WT / 9.525 mm OD \times 1.219 mm WT) was used to build the fluid lines. All the connectors, tube couplings, elbows, and tees were stainless steel and chosen with compression fittings and connectable to 3/8" OD tubing. Tubing and the fittings were ordered from a Parker Hannifin distributor.

5.4.2 Fuel tank (1)

A stainless steel tank with 1 1/2" (139.7 mm) plastic screw cap and sloping bottom with dimensions of 250mm × 250mm × 350mm (length × width × height) was used for the fuel tank. The tank with a capacity around 22 litres was supplied by Jay Wolfe Metalwork Ltd. (UK). The tank was connected to the suction side of the main pump (6).

5.4.3 Main pump (6)

A RG4000 Stuart® centrifugal pump with 30 metres maximum head and 6.0 bar maximum working pressure was used in the test rig. The flow rate of the pump in the rig was 3.3 l/min which provided a face velocity of 7 mm/s at the surface of the test filter with diameter of 10 cm. This pump was chosen instead of the gear pump which was being used for the emulsion generation study (see Section 4.4.2.7 in Chapter 4). The gear pump was capable of generating water droplets with $Dv_{50} = 69.9 \mu\text{m}$ (see Section 4.5.2) while the Stuart® centrifugal pump could generate a DSD with a Dv_{50} of $14.28 \mu\text{m} \pm 0.02 \mu\text{m}$ (mean ± confidence level 95%) in the REF fuel measured (Figure 5-12) via The Insitac Wet Malvern® particle size analyser (Section 4.3.1) at 3.3 l/min.

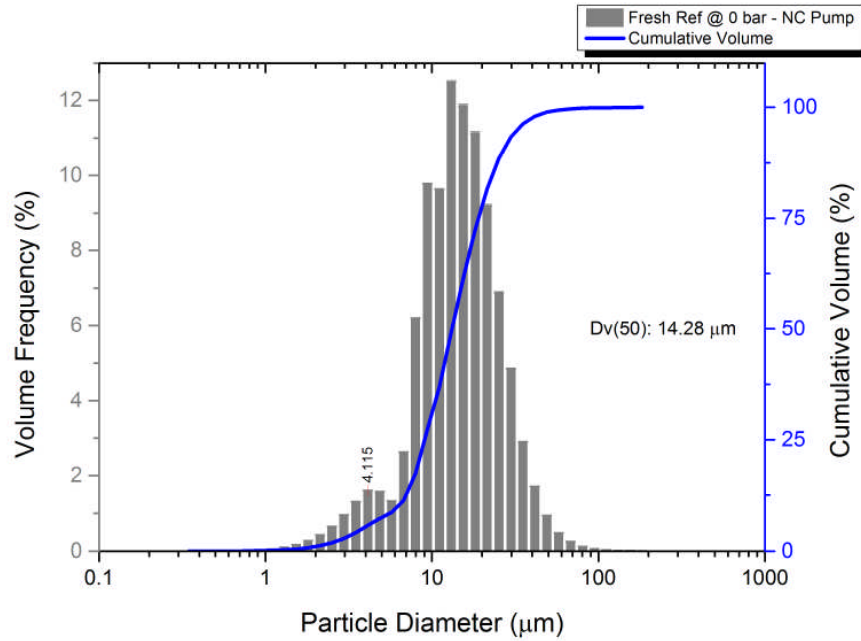


Figure 5-12: DSD of the water phase in REF at atmospheric pressure generated by the main fuel pump

Water was injected upstream of the fuel pump (6) by the peristaltic pump (3).

5.4.4 Water tank (2)

A stainless steel tank with a 1 1/2" (139.7 mm) plastic screw cap with dimensions of 150 mm × 150 mm × 250 mm (length × width × height) and a capacity around 5.5 litres was used for the water tank. Similar to the fuel tank, the water tank was built and supplied by Jay Wolfe Metalwork Ltd. (UK). The water tank was connected to the suction side of the main fuel pump, however, water was injected into the main stream using a peristaltic pump rather than relying only on the suction of the main pump.

5.4.5 Water pump (3)

A Watson-Marlow 313FD/D high flow peristaltic pump was employed for the water injection. A 100 r min⁻¹ pump, driven by 12V fixed speed DC motor via a reduction gearbox with a torque

of 6 kg/cm , was compatible with a tubing with 1.6 mm wall thickness and inner diameter from 0.5 mm to 8 mm . Changes in the water flow rate was achieved by using Norprene A-60-F tubes with a 1.6 mm wall thickness and different inner diameters of 0.8 mm , 1.6 mm , and 3.2 mm ($1/32''$, $1/16''$, and $1/32''$) along with changing the speed of the motor via changing the input voltage using a normal laboratory power supplier. To facilitate the water flow joining the main stream, a small plastic orifice with the hole diameter of 1 mm was placed in the Tee fitting (a).

5.4.6 Water flowmeter (4), and fuel flowmeters (5, 8)

A Porter F65-S-HR-A-157-1 flowmeter with a stainless steel float equipped with a standard cartridge control valve and with the capacity of 18 ml/min was used as the water flowmeter. The flowmeter was capable of measuring to $\pm 1\%$ accuracy between 0 and 18 ml/min . RCM digital display flow meters were used to give the main flow rates in both the emulsion and filtration circuits. The flow meters were chosen based on the required measurement ranges and accuracy of $\pm 1\%$ over the range of 0 to 10 l/min .

5.4.7 Adjustable valves (7, 14, 16)

Parker 6A-V6LR-SS stainless steel needle valves were used for the by-pass (7) and filtration circuit (14) valves. The purpose of these valves was to adjust the flow rate of the filtration circuit. The valve (16) can be used to temporarily put a back pressure on the clean-up filter and the whole circuit to vent air out at the beginning of the test. Moreover, it can be used to increase the pressure of the system if necessary. The flow could also be directed to each of the emulsion and filtration circuits by adjusting valves 7 and 14. This design allowed the flow rate in the filtration circuit to differ from that of the main pump whenever necessary. The flow rate of the pump in the emulsion generation circuit had to be kept at a constant rate to generate constant

droplet size distributions (DSD). Operation was possible under atmospheric or higher pressures using the designated pressure valve (16).

5.4.8 Sampler unites (9, 13, 17)

Sampler units were composed of a ball valve and required fittings to be connectable to 3/8" OD tubes (9.525 mm OD). Sampler units 9, 13, and 17 were placed in the system to extract samples from the upstream of the test filter as well as downstream of the clean-up filters to determine water concentration and to calculate separation efficiency.

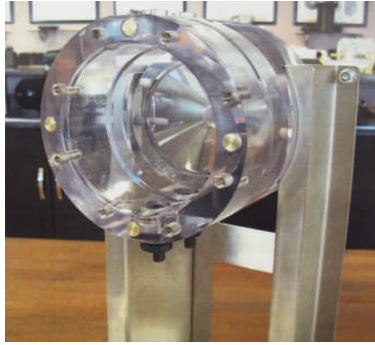
5.4.9 Parker test filter housing (10)

The filter housing shown in Figure 5-13, the design of which was detailed in Section 5.3.1 was built up by Parker Hannifin.

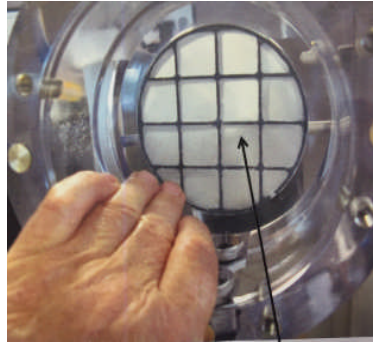


Figure 5-13: Filter housing of the coalescence test rig

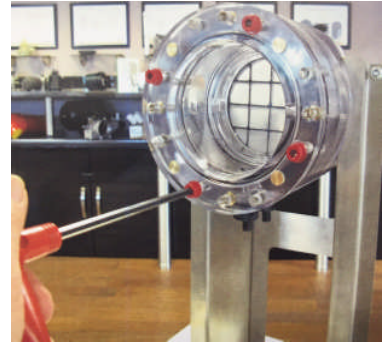
The housing was capable of being operated safely at 4 bar. The barrier mesh on the outlet of the housing was removable and consisted of a woven mesh with an open aperture size of $25\mu m$. Assembling and disassembling of the filter housing are explained in Figure 5-14.



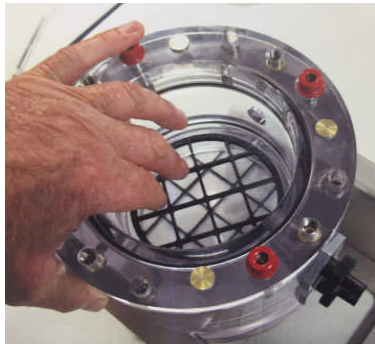
Main body



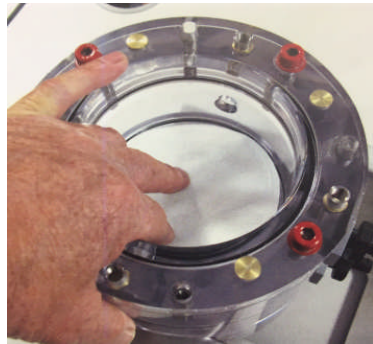
Barrier mesh installation



Inner flange installation



Filter support installation

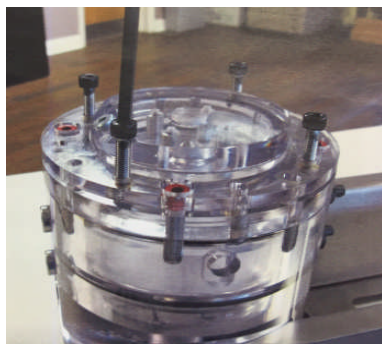


Filter medium installation



Outer flange installation

Water bottle and collection hose installation



Jack screws for disassembling flanges



Outer flange disassemble

Figure 5-14: Steps for assembling/disassembling the filter housing

5.4.10 Manometer

A Dwyer 490-1 Wet/Wet Handheld Digital Manometer with a measuring range of 0-103 kPa (with an accuracy of $\pm 2\%$) was used in the system. The device measured the differential pressure between the upstream and downstream sides of the housing during operation.

5.4.11 Static mixer (12)

A Statiflo series 100 motionless mixer, 3/8" NB with 6 removable elements, was chosen as the inline mixer of the test circuit to avoid settlement of dispersed droplets when taking samples from the downstream sampler (item No. 13 in Figure 5-9). The mixer was made of stainless steel components to minimise issues with corrosion.

5.4.12 Clean-up filters

Commercially available Parker D-MAX filters were used as clean-up filters in the system. The filters were intended to separate all undissolved water, i.e. maximum water content of 50 *ppm* (*v/v*) of water at the downstream of the clean-up filter is acceptable according to the SAE J1488, from the fuel before it is circulated back to the test tank enabling a single pass test. Two clean-up filters were used in parallel for assuring the clean fuel.

5.5 Test procedure

This section defines the procedures used to measure both the separation and coalescence efficiencies of flat sheet nonwoven filter media using the rig detailed in Sections 5.3 and 5.4. The numbered items refer to Figure 5-9.

5.5.1 Pre-test preparation

To reach to a steady state flow rate as well as to bleed air from the system, a 10 min pre-test procedure was implemented before any efficiency measurements were made. The pre-test procedure involved operating the rig without any water injection in the following order:

- 1) Check the IFT of the test fuel offline (see Section 3.3.2);
- 2) Fill the fuel tank with about 6 *l* of a test fuel (almost two times of the fuel low rate, i.e. 3.3 *l/min*);
- 3) Fill the water tank with 400 *ml* of the test water;
- 4) Cut a sample in circular shape with a diameter about 11 *cm*.
- 5) Install the test filter, filter support and the barrier mesh (if required) and connect water drainage bottle to the housing (Section 5.4.9);
- 6) Close the bypass valve (7) and open the valve (14) for the fuel circulation in the main circuit;
- 7) Reset the pressure gage
- 8) Prime the fuel pump (if required)
- 9) Start circulation at the test flow rate of 3.3 *l/min*, i.e. there is no pump velocity controller as such the test flow rate is always the same for all the tests;
- 10) Continue the fuel circulation to achieve a steady flow rate and bleed air from the system using vents on the housing and clean-up filters as well as creating a back pressure by means of the valve (16);
- 11) Take an initial sample from the sampling point (17) and measure water content of the fuel (see Section 3.3.3) and record the dissolved or base water content of the test fuel;

The pre-test can be followed by either separation efficiency test or coalescence efficient test which are explain in the following sections.

5.5.2 Separation efficiency measurement

The water separation efficiency measurements involved operation of the rig with the nonwoven test filter sample followed by a barrier mesh to retrieve any residual water from the exit flow 2 cm downstream of the coalescer. In this study the mesh had an aperture size of $25\mu m$. To obtain the separation efficiency measurements, the following steps were followed after running the pre-test for the first 20 minutes.

- 1) The filtration flow rate was adjusted using the valve (see Section 5.4.7)
- 2) The water flowmeter control valve was opened and the dosing pump started (3) to inject water at a flow rate of 8.25 ml/min , equivalent to 0.25% of the main flow rate, into the main stream. Once the water droplets reached the filter housing the timing clock was started. This point of the test was denoted as test time $t = 0$ and the differential pressure drop across the filter housing, Δp_0 was recorded;
- 3) Continue the injection and circulation for the next 20 min;
- 4) Samples were taken from points (9), and (13) every 5 min to obtain the total water content of the upstream and downstream samples up to the 20th minute. At each time point the differential pressure drop across the housing was also recorded.
- 5) Injection of the water was shut off at time $t = 20\text{ min}$ and the fuel circulation was continued for the next 10 min.
- 6) The differential pressure drop, flow rate and water concentration downstream of the clean-up filter was then determined at the end point of time $t = 30\text{ min}$.

- 7) Data was discarded if the dissolved water concentration downstream of the clean-up filter was more than 50 ppm (v/v) and the clean-up filter was checked accordingly.
- 8) The fuel pump was stopped, the housing disassembled and the filter medium was discarded.
- 9) The instantaneous water separation efficiency (%), η_i , the average water separation efficiency (%), η_{av} , as well as quality factor of the test filter was calculated based on Equation 5-1 to Equation 5-3:

$$\eta_i = \frac{c - c_i}{c} \times 100$$

Equation 5-1: Instantaneous water separation efficiency [48]

$$\eta_{av} = \frac{c - c_{av}}{c} \times 100 \quad , \quad c_{av} = \frac{\sum c_i}{n}$$

Equation 5-2: Average water separation efficiency [48]

$$QF = \frac{-\ln(1 - \eta_{av}/100)}{\Delta P_{20} - \Delta P_0}$$

Equation 5-3 Quality Factor [48]

Where:

c : Specified water concentration (ppm (v/v));

c_i : Downstream water concentration of sample (ppm (v/v));

n : Number of samples;

c_{av} : Average downstream water concentration (ppm (v/v));

ΔP_0 : Differential pressure drop across the filter housing at time $t = 0 \text{ min}$, (kPa);

ΔP_{20} : Differential pressure drop across the filter housing at time $t = 20 \text{ min}$, (kPa).

5.5.3 Coalescence efficiency test

This procedure was developed for the measurement of the coalescing performance of a test filter medium in coalescing water droplets in diesel fuel without the use of a barrier mesh medium.

The procedure was as follows:

- 1) The filtration flow rate was adjusted using the valves – as required (see Section 5.4.7)
- 2) The water flowmeter control valve was opened and the dosing pump (3) started to begin injection of water with a flow rate of 8.25 ml/min , i.e. 0.25% of the main flow rate, into the main stream. Once water droplets had reached the filter housing, the timing clock was started. This point was recorded as time $t = 0$ and the differential pressure drop across the filter housing, Δp_0 , was recorded;
- 3) Injection and circulation was continued for the next 20 min;
- 4) Water injection was completed at $t = 20$ and the fuel circulation was continued for the next 10 min.
- 5) The differential pressure drop at $t = 20$, Δp_{20} , was recorded;
- 6) The differential pressure drop and the flow rate at the end was at time $t = 30$ was controlled to be stable.
- 7) The fuel pump was stopped and the housing disassembled, then the filter medium was discarded.
- 8) The volume of water settled in the collection bottle was determined (M_{Cd});
- 9) The volume of water remaining in the water tank was obtained (M_R);
- 10) The volume of water injected into the mainstream was determined ($M_{IU} = 400 - M_R$)

11) Finally, the coalescence efficiency as well as the quality factor of the filter was calculated by Equation 5-4 and Equation 5-5.

$$\varepsilon = \frac{M_{Cd}}{M_{IU}} \times 100$$

Equation 5-4: Coalescence efficiency

$$QF = \frac{-\ln(1 - \eta_{av}/100)}{\Delta P_{20} - \Delta P_0}$$

Equation 5-5 Quality Factor

5.6 Test stand validation

The validation of the new rig was performed at the maximum flow rate of the filtration circuit (with valve 7 closed – see Figure 5-9) and with the filter housing fitted with a straight hose. The validation procedure was based on that described in ISO 16332:2006 and SAE J1488:2010. Operation of the system was conducted using pump (item 6 in Figure 5-9) with a flow rate of 3.3 *l/min* using the following systematic procedure:

- 1) The main pump was started and fluid was circulated in the filtration circuit while the bypass valve (7) was closed.
- 2) The base water concentration of the test fuel (dissolved water) was measured using Karl Fischer titration, (see Section 3.3.3), and reported as *ppm_v* (volumetric fraction).
- 3) Water injection was started at 0.25% of the main flow rate (2500 *ppm (v/v)*).
- 4) A circulation time of 10 min was implemented to stabilise the system.

- 5) Samples were taken (approximately 50ml) at sampling points (9, 13, 17) every 20 min for 1 hr (starting from the water injection) to validate the injection system, static mixer, and clean-up filters respectively.
- 6) Analysis of each sample was conducted using Karl Fischer titration, (see Section 3.3.3), and the water content reported as ppm_v . The undissolved water content of each sample was calculated by deducting the based water content of the fuel measured at stage 2 (above).
- 7) Operation was satisfactory if: (a) the undissolved water content of the samples from the upstream and downstream of the filter housing were equal to the injected water concentration with maximum 12% variation (2200 ppm to 2800 ppm (v/v) (SAE J1488)) and (b) if the undissolved water content of the sample from the clean-up filter was lower than 50 ppm (v/v).

Each of these steps were followed to validate the operating stability of the coalescence rig and Table 5-1 shows typical results. The data clearly indicate that the satisfactory operating criteria defined in step 7 above, had been met, such that further experimental work could proceed.

Table 5-1: The validation results of the coalescence test rig

Sampling time (min)	Upstream ppm (v/v)	Downstream ppm (v/v)	Clean-up ppm (v/v)
20	2711	2690	6
40	2397	2751	6
60	2488	2370	2
Mean	2532	2604	5
SE (ppm (v/v))	93.23	118.04	1.33

5.7 Summary

To enable different nonwoven coalescing water separators to be studied, this Chapter has reported the design and development of a new coalescence rig. The design included a carefully designed filter housing that allowed dynamic observation of water droplet removal and ease of assembly and disassembly. All components of the rig were made from materials compatible with diesel and bio-diesel fuel and water content and IFT measurements were designed to be conducted offline. Robust procedures for determining coalescence and separation efficiencies were developed based on existing standard methods. The validation study confirmed that reliable data could be obtained, based on strict operating performance criteria, enabling efficiency measurements to be undertaken with different nonwoven filter media in subsequent chapters.

CHAPTER 6

Characterisation of Meltblown Depth Coalescence Fuel

Filter Media

6.1 Introduction

As discussed in Section 2.4.2.2, multilayer nonwoven coalescing media, particularly meltblowns, are commonly encountered in water-diesel separation applications because of their ability to manage the coalescence of water droplets within their structure. However, this performance has not been systematically studied in public domain literature and there is only limited data relating to the importance of the fabric configurations. Accordingly, the main purpose of the work reported in this chapter was to study multilayer nonwoven depth coalescing filter media to understand their geometry and the associated effects on separation and coalescence efficiencies. Industrially sourced coalescence fabric samples were characterised regarding their geometry as well as their separation and coalescing performance. The procedures used for conducting the coalescence evaluations are explained in Chapter 5 and the methodologies employed to evaluate nonwoven fabric properties are reported in Section 6.3. To reflect current industrial practice and trends the samples studied herein comprised meltblown nonwoven fabrics.

6.2 Test filter media and test fuels

Four coalescing cartridge filters denoted as WB, B16, B41, and B45 (Figure 6-1), were supplied by Parker Racor, UK. Each was produced from multilayers of industrially manufactured poly(butylene terephthalate) (PBT) meltblown (thermally bonded and non-bonded fabrics) and poly(ethylene terephthalate) (PET) spunbond fabrics.



Figure 6-1: An example of the benchmark sample

The outer and inner most layers of the filter comprised thermally point-bonded spunbond poly(ethylene terephthalate) (PET) fabric, denoted as SB strips, to support and hold the meltblown layers together around the centre core. Some of the meltblown strips were thermally bonded, denoted as MB strips. Non-bonded meltblown strips are denoted as CM strips. The CM strips were functioning specifically as depth coalescers. Table 6-1 lists the number of strips in each of the filter samples.

Table 6-1: Number of fabric windings in the test filter packs

Filter ID	Number of SB strips	Number of MB strips	Number of CM strips
WB	2	3	2
B16	2	0	1
B41	2	5	1
B45	2	3	1

The layers of the filters were cut to narrow width strips (about 5 cm width) wound on to a robust plastic cylindrical support mesh (centre core) at a specified angle – winding angle α (Figure 6-2). The winding angle, dictated whether the strip left an open layer below (Figure 6-2 (a)), or a closed layer in which the fabric strip was wound either side by side Figure 6-2 (b)), or in an overlapped fashion (Figure 6-2 (c)). Depends on the angle α , the length of the strips varied to cover the whole width of the filter.

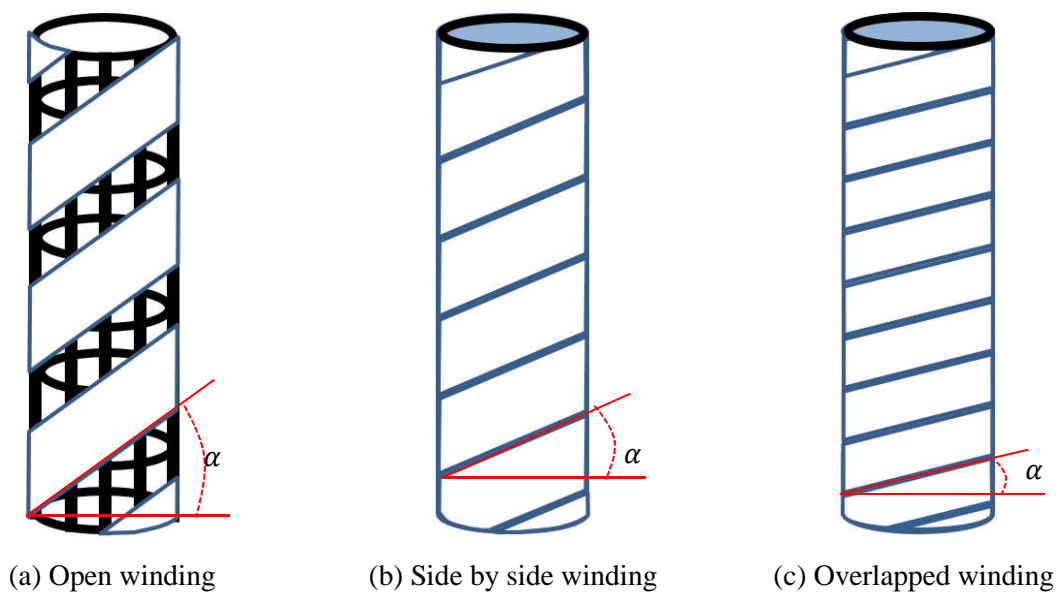


Figure 6-2: Schematic of different strip arrangements when assembling the coalescence filters

In the case of the overlapped configuration (Figure 6-2 (c)), the wound strips formed more than one layer over the support. The structural specifications of the filters produced are given in Table 6-2 to Table 6-5. The strips in each pack are labelled from the outer strip, 1, towards the most inner most strip adjacent to the filter support. When installed in to a filter circuit, the flow direction is always towards the centre core.

Table 6-2: Layer specification of the WB filter

Strip	Material	winding type	number of layers
1	Spunbond PET	Overlapped	3
2	Non-bonded Meltblown	Side by side	1
3	Thermally bonded PBT	Overlapped	2
4	Thermally bonded PBT	Overlapped	2
5	Thermally bonded PBT	Overlapped	2
6	Non-bonded Meltblown	Side by side	1
7	Spunbond PET	Overlapped	3

Table 6-3: Layer specification of the B16 filter

Strip	Material	winding type	number of layers
1	Spunbond PET	Overlapped	2
2	Non-bonded Meltblown PBT	Side by side	1
3	Spunbond PET	Overlapped	3

Table 6-4: Layer specification of the B41 filter

Strip	Material	winding type	number of layers
1	Spunbond PET	Overlapped	2
2	Thermally bonded PBT	Overlapped	2
3	Thermally bonded PBT	Overlapped	2
4	Thermally bonded PBT	Overlapped	2
5	Thermally bonded PBT	Overlapped	2
6	Thermally bonded PBT	Overlapped	2
7	Non-bonded Meltblown	Side by side	1
8	Spunbond PET	Overlapped	3

Table 6-5: Layer specification of the B45 filter

Strip	Material	winding type	number of layers
1	Spunbond PET	Overlapped	2
2	Thermally bonded PBT	Overlapped	4
3	Thermally bonded PBT	Overlapped	2
4	Thermally bonded PBT	Overlapped	2
5	Non-bonded Meltblown PBT	Side by side	1
6	Spunbond PET	Overlapped	3

Configurations of the media and strips coding are explained in Table 6-6 where strips of the B series and WB media are denoted by B and WB subscripts respectively. The strip codes used for these filters are adapted from codes used by the supplier (Parker Ltd.). Characterisations of the strips are reported in the next part. Based on the manufacturing specifications, spunbond strips (SB_B) used in B16, B41, and B45 samples (B series samples) are from the same fabric batch. This is the case for the non-bonded meltblown stripes (CM_B) too. This is why the SB

and CM strips are coded all the same in these filters. Spunbond and non-bonded meltblown strips in WB samples were from the same fabric batch too.

Table 6-6: Strip specification of the benchmark media

Media ID	Strips number and configuration towards the centre core (→ Fuel flow direction)							
	1	2	3	4	5	6	7	8
B16	SB _B	CM _B	SB _B					
B41	SB _B	MB15	MB5	MB15	MB20	MB30	CM _B	SB _B
B45	SB _B	MB5	MB15	MB30	CM _B	SB _B		
WB	SB _{WB}	CM _{WB}	MB1	MB2	MB3	CM _{WB}	SB _{WB}	

6.3 Experimental methods and apparatus

This section reports the test methods and equipment employed to characterise nonwoven strips of the filters regarding their physical and chemical properties. These properties include area density, thickness, air permeability, porosity, pore size distribution. ATR-FTIR and DSC analysis were also performed to confirm identities of the material used in the filter media.

6.3.1 Determination of area density (GSM)

The European Standard BS EN 29073-1:1992 [137] was used for area density (mass per unit area ($g \cdot m^{-2}$) - GSM) measurements. GSM of each layer of the filters was measured using a METTLER TOLEDO balance with accuracy of four decimal places with five replicates per sample. The samples size for this measurement was a rectangle of 20 mm × 30 mm.

6.3.2 Calliper or thickness

BS EN ISO 9073-2:1997 [138] was used as a reference to determine thickness of nonwovens while 0.5 kPa pressure is applied on specimens with a surface area of 2,500 mm². In this work,

thickness of the filter strips was measured via a THWING-ALBERT thickness gauge calibrated according to the BS EN ISO 9073-2:1997 standard. Based on the recommendations in the standard, at least ten replicates were measured to report the average thickness of the filter strips.

6.3.3 Air permeability

BS EN ISO 9073-15:2008 is the standard test method for determination of air permeability for nonwovens based on measuring an airflow passing through a sample disk with a fixed area, between 20 and 50 cm². The airflow is defined as the air permeability of the sample expressed in (l/m²/s) at a constant differential pressure, 100, 125, or 200 Pa, across the sample (Equation 6-1). Based on the Darcy's law the measured flow rate is used to calculate the intrinsic permeability constant, k (m²), of the sample [34]:

$$\phi = \frac{k}{\mu} \times \frac{\Delta p}{L}$$

Equation 6-1: Air flow rate [34]

Where:

ϕ : Air flow rate (l/m²/s);

μ : Air viscosity(Pa. s);

Δp : Differential Pressure (Pa);

L : Sample Thickness (m).

To characterise air permeability of the filters and their strips, five specimens were tested with LabAir FX3300 instrument. Following the standard procedure, the test area of 50 cm² was employed for this measurement. The fabric samples were not structurally open and fragile and were able to tolerate the recommended range of the pressure drop up to 200 Pa. Moreover, BS EN ISO 9237:1995 [139], the test method for the determination of the permeability of textile

fabrics to air, also clearly recommends the 200 Pa pressure drop for testing industrial fabrics. Therefore, the test differential pressure of 200 Pa was employed for this measurement.

6.3.4 Determination of density, bulk, solidity, and porosity of nonwovens

Density of a fabric is defined as the weight of mass of fibres in gram per unit volume of the fabric in cubic meter, ρ_w ($\frac{kg}{m^3}$), and web bulk, β_w ($\frac{m^3}{kg}$), is defined as the reciprocal of the fabric density (Equation 6-2) [34]:

$$\rho_w = \frac{GSM}{L}; \beta_w = \frac{1}{\rho_w}$$

Equation 6-2: Density and web bulk of nonwoven fabrics [34]

The solidity of a nonwoven, \aleph ($\frac{m^3}{m^3}$), is also defined as the volume of fibre per unit volume of the fabric, and porosity, ε ($\frac{m^3}{m^3}$), refers to the inverse concept of the solidity and is defined as the volume of the void space per unit volume of the fabric which can be calculated from the Equation 6-3 [34]:

$$\aleph = \frac{GSM}{L \times \rho_m}; \varepsilon = 1 - \aleph$$

Equation 6-3: Solidity and porosity of nonwoven fabrics [34]

Where:

ρ_m : Material density ($\frac{kg}{m^3}$).

In this study density of PBT and PET were assumed as $1.39 \frac{g}{cm^3}$ and $1.31 \frac{g}{cm^3}$ respectively throughout.

6.3.5 Pore size characterisation

ASTM F316-3(2013) standard test procedure recommends measurement methods to characterise membrane filters in relation to their pore sizes via bubble point and mean flow pore sizing tests, which are also being used for the characterisation of nonwovens as well [34]. In the bobble point test, a test fabric saturated with a specific test fluid with a known surface tension and density is fastened in a sample chamber where compressed air is flown perpendicular to the surface of the fabric and passes through it with an increasing flow rate. As the liquid is filled up the void volume of the fabric, it generates a pressure drop across the sample at each air flow rate. While the pressure increases air eventually can push the liquid out of pores with maximum size and a bubble is observed rising through the fabric sample. This pressure is recorded to calculate the maximum pore size of the test fabric using the Equation 6-4.

$$d = \frac{4\gamma_{lv} \cos \theta}{\Delta p} \times 10^6$$

Equation 6-4: Pore size of nonwoven fabrics [34]

Where:

d : Pore diameter (μm);

γ_{lv} : Surface tension of the test fluid (N/m);

θ : Contact angle between the test liquid and pore wall (degree);

Δp : Air pressure drop (Pa);

The mean flow tests is a test by which bubble point pore size, mean flow pore size and pore size distribution of a test sample can be measured. The sample preparation in this test is the same as the bobble point test while after determination of the bobble point, the test is continuing to reach to the maximum pressure determined by the user (Δp_{max}). The pore sizes at all the pressures ranged from zero to the maximum pressure drop, Δp_{max} , are calculated using

Equation 6-4 and the size distribution is reported. In addition to the bubble point pore size and the size distribution, a mean flow pore size is reported as well. To calculate the mean flow pore size, a pressure drop across the sample in the wet test, i.e. when fabric is saturated with the test fluid, is compared to a dry test (when the test fabric is not in contact with any liquid) when the flow rate in the wet test reaches to 50% of the maximum flowrate in the dry test, i.e. mean flow pressure drop. Maximum flow rate is recorded when the maximum determined pressure drop in the dry test is met (Figure 6-3). The mean flow pore size can also be measured via Equation 6-4 at the detected mean flow pressure. To run the mean flow test, there are two test methods of wet-dry and dry-wet tests. In the former mode the wet test is immediately followed by a dry test while in the dry-wet mode, the sample has to be saturated before the wet test is commissioned. The mean flow pore size is not the mean pore size of the sample as a flow through a small pore can be disproportionately smaller than flow from a larger pore.

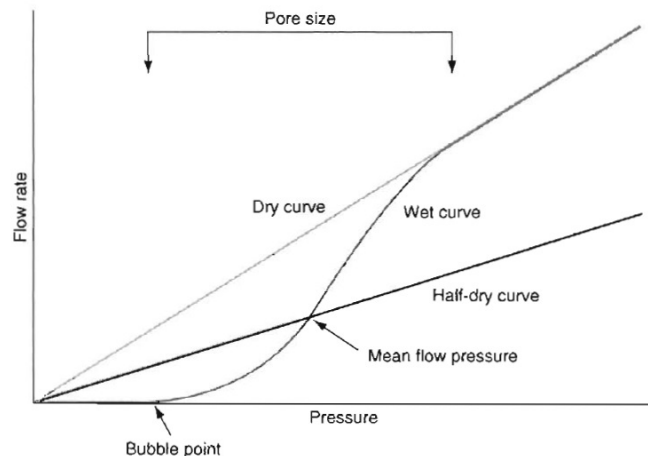


Figure 6-3: Determination of mean flow pore size [34]

Capillary flow porometry® in the wet-up – dry-up mode, as described above, was used to measure pore size distribution of the filter strips. The test was performed with at least three replicates for the each of the strips. The maximum pressure, (Δp_{max}), to be defined for each

test (Table 6-6) could vary for different strips, i.e. spunbond (SB), thermally bonded (MB), and non-bonded (CM) strips, due to difference in their structure (open or close structure). Therefore, the maximum pressure, (Δp_{max}), was define by conducting a trial prior to actual tests as 4 kPa, 6 kPa, and 8 kPa for spunbond (SB) strips, non-bonded (CM) strips, and thermally bonded (MB) strips respectively.

6.3.6 Fourier transform infrared spectroscopy - attenuated total reflectance (FTIR - ATR)

Fourier transform infrared spectrometer (FTIR) is the most prevalent spectrometer by which infrared spectrum of a matter can be measured and plotted. The infrared spectrum is “a plot of measured infrared intensity versus wavelength (or wavenumber) of light” during the light-matter interaction [140-144]. The infrared spectrum is a part of the electromagnetic spectrum and has a lower frequency, ν , ($1.9 \times 10^{13} - 1.2 \times 10^{14} \text{ Hz}$) and longer wavelength, λ , ($2500 - 16000 \text{ nm}$) than the visible spectrum. All objects which have a temperature above absolute zero radiate waves in the infrared region and matters having chemical bonds in their structure can absorb a fraction of the infrared radiation depending on their chemical compositions. Chemical functional groups of a matter, such as $C = O$, CH_3 , etc., can maintain their chemical properties in different molecules such that they absorb the infrared radiation at the same wavelength regardless of the molecule chemical structure. This future is utilised in infrared spectroscopy to identify unknown materials or confirm their identities.

Fourier transform infrared spectrometer (FTIR) consists of a light source, an interferometer which send the light in the infrared region to a sample, a detector able to measure intensity of the light versus time for all the radiated wavelengths transmitted from the sample, and a

processor which convert the intensity-time spectrum to the intensity-frequency spectrum using a Fourier transform mathematical function [141]. The output is a plot of measured infrared intensity versus wavelength. The infrared intensity can be reported as either transmittance (T - % - Equation 6-5), or Absorbance (A - unit less - Equation 6-6), and the X-axis can be either wavelength or the reciprocal of the wavelength called as wavenumber (cm^{-1}),

$$T = I/I_0$$

Equation 6-5: Infrared intensity in transmittance [141]

Where:

I : Light intensity with a sample in the infrared beam,

I_0 : Light intensity with no sample in the infrared beam (background).

$$A = \log\left(\frac{1}{T}\right)$$

Equation 6-6: Infrared intensity in absorbance [141]

Attenuated Total Reflection (ATR) is a common sampling technique for nonwovens samples [141]. In this technique no specific sample preparation is required, however, an ATR accessory is needed. An IR beam in the ATR probe is directed onto a special crystal with a high refractive index which generate “evanescent waves” into the sample held in contact with it. While the sample absorbs energy, the evanescent wave is attenuated and returns to the crystal, exits and then is directed to the detector in the IR spectrometer.

In this project, ATR-FTIR was performed using a Perkin Elmer FTIR spectrometer to confirm identities of strips of the benchmark filter media. Measurements were taken in the mid-infrared region, wavenumber between $4000 - 400 \text{ cm}^{-1}$ with a resolution of 4 cm^{-1} and interval scanning of 2 cm^{-1} . For each spectrum 64 scans were averaged. For each measurement,

separate background measurement was performed. The media strips subjected to this experiment are listed in Table 6-7.

Table 6-7: filter Strips for the ATR-FTIR analysis

Media ID	Strips ID					
B16, B41, B45	SB _B	CM _B	MB5	MB15	MB20	MB30
WB	SB _{WB}	CM _{WB}	MB1	MB2	MB3	

6.3.7 Differential scanning calorimetry (DSC)

DSC, Differential Scanning Calorimetry, is a technique to study thermal transitions of a polymer such as glass transition, crystallization, and melting transition. By this technique, thermal profile of a sample placed in a pan is compared with that of an empty pan (reference pan) both subjected to a controlled temperature program [145, 146]. The calorimetry plots the excess heat flow required for the sample pan to keep its temperature increasing at the same rate as the reference pan [145]. A plot goes down when the thermal transition is endothermic, such as glass transition and melting point, and it goes up when the transition is exothermic such as crystallization.

In this study, DSC was used in conjunction with ATR-FTIR to confirm identity of the benchmark filter samples, and a PerkinElmer Jade calorimetry was employed for this experiment. The system components include sample cell consists of two heaters on which the sample and reference pans are accommodated on the right and left sides of the chamber, cooling accessories, and controller computer with an associated software. Following the instrument instruction, it was calibrated using Zinc and Indium pans, with known weight, melting temperature and enthalpy change. The software was programed to control temperature of the

samples from 30°C to 440°C with the rate of 20 °C/*min*. Output of the test was normalized heat flow (*W/g*) – temperature (°C) graphs. Glass transition and melting temperatures of the samples were compared with corresponding temperature of a literature reference value to confirm identity of the benchmark samples.

6.3.8 Scanning electron microscopy (SEM) and fibre diameter measurement

The scanning electron microscopy uses a focused and high energy electron beam being scanned over surface of a sample and detects returned signals using proper detectors for qualitative or semi-quantitative analyses [147]. A matter exposed to a beam of high energy electrons, primary electrons, can emit different types of signals including secondary electrons which are the electrons from surface of the sample excited by the primary electrons. These electrons are being used to generate a 2-D images displaying spatial variations in the morphology of the sample. In a conventional SEM microscopy magnification ranges from 20X to approximately 30,000X, and spatial resolution ranges from 50 to 100 nm. A sample have to be electrically conductive to prevent charge build-up on its surface, and the sample chamber is vacuumed in a conventional SEM microscopy. Such that, electrically insulating samples have to be coated by conductive materials such as carbon, gold, or other metals.

During the course of this study a JEOL JSM-6610 LV scanning electron microscope (SEM) (JEOL Ltd.; Tokyo, Japan) with an accelerating voltage between 2 kV and 15 kV was used in order to record morphological features of individual medium with magnifications of 750x, 100x, or 5000x. For the SEM imaging, the samples were cut in small squares (5 × 5 *mm*) and coated with a 30 nm layer of gold using a Quorum Q150RS sputter coater (Quorum Technologies Ltd.; East Sussex, UK). The SEM images were used for the fibre diameter

measurements of the filter media using the ImagePro software and for each sample at least 50 measurements were taken.

6.3.9 Determination of wetting tension of nonwoven strips

The aim of this experiment was to conduct a simple and quick test to indicate whether the benchmark filter media experiences any hydrophilicity treatment or not. Determination of the exact wetting tension (surface tension) of the media was not in the focus of this examination, such that, the BS ISO 8296:2003 standard method for determination of wetting tension of plastics was employed with some modifications as below.

BS ISO 8296:2003 indicates a series of mixtures of solvents (inks) of gradually increasing surface tension kept in separate dropper bottled. The inks are applied to the surface of a sample placed on the ground plate of a hand-coater and are immediately spread by drawing a wire bar of the coater depositing a 12 μm ink film on the sample. The inks are applied from a low surface tension and the ink film is observed if it holds together for 2 seconds. If the film is break below 2 seconds, an ink with a lower surface tension must be applied, and if it wets the surface for more than 2 seconds, one with a higher surface tension is applied. The surface tension of an ink that comes nearest to wetting the surface for 2 seconds is recorded as the wetting tension of the plastic film. In this project, however, samples were nonwoven sheets with porous surfaces. Therefore, the hand coater mentioned in the standard test procedure was not used and instead of evaluating the ink films, ink drops were observed if they can wet the surface in less than 5 seconds, i.e. the concept is similar to that of testing for oil repellency of textile fabrics, BS EN ISO 14419:2010.

For this test, Arcotest test inks were used which covered surface tension range from 30 mN/m to 105 mN/m . Inks were put on the surface of each layer by means of a pipette with fixed drop volume of 25 μl .

All the steps of the test were conducted under fume cupboard as some of the inks were toxic. Three to five drops (25 μl) of each ink were put on the surface of each layer by means of the pipette. The droplets were observed to see if they can completely wet the surface in 5 sec. The surface energy of the test sample was defined as a range that the lower limit is the surface tension of the ink being absorbed in just below 5 seconds (denoted as “Y” in the result table) and the upper limit is the surface tension of the next liquid with a higher surface tension which cannot be absorbed in 5 seconds (denoted as “N” in the result table).

6.3.10 Separation performance evaluation

A pilot study was conducted to record separation efficiency of the benchmark samples (WB, B16, B41, B45) using the purpose-built coalescence test rig explained in Chapter 5 according to the test procedure explained in Section 5.5.2 of that chapter. All the tests were conducted at the same filtration flowrate of 3.3 l/min and water concentration of 2500 \pm 300 $ppm(v/v)$, (see Section 5.5) using the reference grade diesel fuel (REF fuel) with specification defined in Section 3.2 of the third chapter of this thesis. The IFT and based water content of the test fuel were in the ranges of 31.24 \pm 0.73 mN/m (*mean \pm SE*) and 49.13 \pm 2.79 $ppm(v/v)$ (*mean \pm SE*) respectively. As it was previously discussed in Section 5.5.2, a barrier mesh medium was used for this test at downstream of the test filter, such that the separation efficiency of the mesh itself was evaluated as well.

6.3.11 Coalescence performance evaluation

The coalescence efficiency test of the benchmark samples were performed based on the procedure explained in the Section 5.5.3 of the Chapter 5. For this test, the coalescence test rig was used and it was prepared for the test based on the procedure explained in the Section 5.5.1. The benchmark samples WB, B16, B41, and B45 were tested in triplicates using the reference grade diesel fuel (REF fuel) with specification defined in Section 3.2 and following to the test procedure (Section 5.5.3).

6.4 Results and discussions

The filter media explained in the Section 6.2 were characterised regarding their nonwoven properties based on the procedures explained in the Section 6.3. The benchmark filter media were supplied by the sponsor of the project in cartridge form and the media were cut of the cartridge core to be tested for the different properties. The following sections are discussing the results of the characterisations.

6.4.1 Determination of area density (GSM)

Following the test procedure explained in the Section 6.3.1, average GSM of the media as well as their strips (*mean* \pm SE) are reported in Table 6-8 and Table 6-9 respectively, the test was performed with at least five replicates per sample.

Table 6-8: Average GSM of the benchmark filter media

Media No.	Area Density ($g. m^{-2}$)
WB	865.53 \pm 16.54
B16	599.18 \pm 16.39
B41	795.77 \pm 13.26
B45	674.65 \pm 8.85

Table 6-9: Average GSM of strips of the benchmark filter media

Area Density ($g. m^{-2}$)							
Strip	WB	Strip	B16	Strip	B41	Strip	B45
SB _{WB}	28.19 \pm 1.16	SB _B	50.67 \pm 1.57	SB _B	50.67 \pm 1.57	SB _B	50.67 \pm 1.57
CM _{WB}	212.94 \pm 36.52	CM _B	274.99 \pm 18.31	MB15	14.01 \pm 0.29	MB5	15.34 \pm 0.62
MB1	53.89 \pm 3.07	SB _B	50.67 \pm 1.57	MB5	15.34 \pm 0.62	MB15	14.01 \pm 0.29
MB2	54.39 \pm 2.37			MB15	14.01 \pm 0.29	MB30	54.28 \pm 1.62
MB3	32.22 \pm 0.84			MB20	54.89 \pm 1.03	CM _B	274.99 \pm 18.31
CM _{WB}	212.94 \pm 36.52			MB30	54.28 \pm 1.62	SB _B	50.67 \pm 1.57
SB _{WB}	28.19 \pm 1.16			CM _B	274.99 \pm 18.31		
				SB _B	50.67 \pm 1.57		

Based on the results (Table 6-8), WB sample had the highest area density compared to other media which is mainly because of having two non-bonded layers (CM_{WB}) in its structure. The CM strips have higher area density than other strips as well (Table 6-9).

6.4.2 Calliper or thickness

Table 6-10 and Table 6-11 lists the average thickness (*mean* \pm SE) of the media and their strips respectively.

Table 6-10: Average thickness of the benchmark filter media

Media No.	Thickness (<i>mm</i>)
WB	8.6 ± 0.1
B16	6.7 ± 0.1
B41	7.0 ± 0.1
B45	6.8 ± 0.0

Table 6-11: Average thickness of strips of the benchmark filter media

Thickness (μm)							
Strip	WB	Strip	B16	Strip	B41	Strip	B45
SB _{WB}	221 ± 9	SB _B	560 ± 19	SB _B	560 ± 19	SB _B	560 ± 19
CM _{WB}	3010 ± 191	CM _B	3800 ± 160	MB15	100 ± 1	MB5	131 ± 3
MB1	521 ± 8	SB _B	560 ± 19	MB5	131 ± 3	MB15	100 ± 1
MB2	383 ± 8			MB15	100 ± 1	MB30	470 ± 5
MB3	172 ± 1			MB20	488 ± 7	CM _B	3800 ± 160
CM _{WB}	3010 ± 191			MB30	470 ± 5	SB _B	560 ± 19
SB _{WB}	221 ± 9			CM _B	3800 ± 160		
				SB _B	560 ± 19		

Table 6-11 elucidates that the thickness of the media is mainly governed by the CM layers, such that WB sample shows the highest thickness (Table 6-10). The bonded strips, MB strips, have obviously lower thickness compared to the fluffy CM layers (Table 6-11).

6.4.3 Air permeability

Table 6-12 and Table 6-13 reports the average air permeability (*mean* ± SE) of the media and their strips respectively.

Table 6-12: Average air permeability of the benchmark filter media

Media No.	Air Permeability ($l. m^{-2}. s^{-1}$)
WB	184.8 ± 4.2
B16	697.6 ± 32.4
B41	160.85 ± 3.21
B45	219.33 ± 4.29

Table 6-13: Average air permeability of strips of the benchmark filter media

Air Permeability ($l. m^{-2}. s^{-1}$)							
Strip	WB	Strip	B16	Strip	B41	Strip	B45
SB _{WB}	6147 ± 173.24	SB _B	4866 ± 98.87	SB _B	4866 ± 98.87	SB _B	4866 ± 98.87
CM _{WB}	3056 ± 252.59	CM _B	2140 ± 181.85	MB15	453.4 ± 8.14	MB5	1006.8 ± 35.83
MB1	1412±41	SB _B	4866 ± 98.87	MB5	1006.8 ± 35.83	MB15	453.4 ± 8.14
MB2	1236±55			MB15	453.4 ± 8.14	MB30	1436 ± 119.77
MB3	460±7			MB20	873.6 ± 25.88	CM _B	2140 ± 181.85
CM _{WB}	3056 ± 252.59			MB30	1436 ± 119.77	SB _B	4866 ± 98.87
SB _{WB}	6147 ± 173.24			CM _B	2140 ± 181.85		
				SB _B	4866 ± 98.87		

Table 6-12 shows that among the samples, B16 has the most open structure and the highest air permeability belongs to this medium ($\approx 698 l. m^{-2}. s^{-1}$). On the other hand, sample B41 which has the greatest number of layers showed the lowest permeability ($\approx 161 l. m^{-2}. s^{-1}$). Table 6-13 also shows that the bonded strips used in all the media have different permeability ranged from about $400 l. m^{-2}. s^{-1}$ to about $1500 l. m^{-2}. s^{-1}$, while the non-bonded strips (CM strips) showed a much higher permeability about $2140 - 3556 l. m^{-2}. s^{-1}$.

6.4.4 Determination of density, bulk, solidity, and porosity of benchmark media

Following the procedure explained in the Section 6.3.4, density, bulk, solidity, and porosity of the benchmark samples were calculated based on their corresponding thickness and GSM results reported in previous sections. Results related to the filter packs and strips of the WB and B series samples are given in Table 6-14, Table 6-15, and Table 6-16 respectively.

Table 6-14: Density, bulk, solidity, and porosity of benchmark media

Media No.	density($\frac{kg}{m^3}$)	bulk($\frac{m^3}{kg}$)	solidity($\frac{m^3}{m^3}$)	Porosity($\frac{m^3}{m^3}$)
WB	101.0	9.9×10^{-3}	0.08	0.92
B16	88.9	1.1×10^{-2}	0.07	0.93
B41	113.0	8.8×10^{-3}	0.09	0.91
B45	99.1	1×10^{-2}	0.08	0.92

Table 6-15: Density, bulk, solidity, and porosity of strips of the WB medium

Strip No.	density($\frac{kg}{m^3}$)	bulk($\frac{m^3}{kg}$)	solidity($\frac{m^3}{m^3}$)	Porosity($\frac{m^3}{m^3}$)
SB _{WB}	127.6	7.8×10^{-3}	0.09	0.91
CM _{WB}	70.7	1.4×10^{-2}	0.05	0.95
MB1	103.4	9.7×10^{-3}	0.08	0.92
MB2	142.0	7×10^{-3}	0.11	0.89
MB3	187.3	5.3×10^{-3}	0.14	0.86
CM _{WB}	70.7	1.4×10^{-2}	0.05	0.95
SB _{WB}	127.6	7.8×10^{-3}	0.09	0.91

Table 6-16: Density, bulk, solidity, and porosity of strips of the B16, B41, and B45 media

Media No.	density($\frac{kg}{m^3}$)	bulk($\frac{m^3}{kg}$)	solidity($\frac{m^3}{m^3}$)	Porosity($\frac{m^3}{m^3}$)
SB _B	90.4	1.1×10^{-2}	0.07	0.93
MB5	117.1	8.5×10^{-3}	0.09	0.91
MB15	140.1	7.1×10^{-3}	0.11	0.89
MB20	112.5	8.9×10^{-3}	0.09	0.91
MB30	115.5	8.7×10^{-3}	0.09	0.91
CM _B	72.4	1.4×10^{-2}	0.06	0.94

Table 6-14 confirms that the B16 and B41 samples have the highest and the lowest porosity among other benchmark media, which is in agreement with the air permeability results (Section 6.4.3). Regarding the strips (Table 6-15 and Table 6-16), the fluffy CM strips have a high porosity while the bonded MB strips have lower porosity. The SB strips showed medium porosity in related to the other media.

6.4.5 Pore size characterisation

Bubble point mean flow and smallest detected pore sizes of the strips of media (*mean* \pm *SE*) are reported in Table 6-17, Table 6-18, and Table 6-19 respectively.

Table 6-17: Average bubble point pore size of strips of the benchmark filter media

Pore size – Bubble Point (μm)							
Strip	WB	Strip	B16	Strip	B41	Strip	B45
SB _{WB}	755 ± 58.3	SB _B	303.4 ± 27	SB _B	303.4 ± 27	SB _B	303.4 ± 27
CM _{WB}	233.2 ± 37.5	CM _B	289.6 ± 41	MB15	26.8 ± 0.9	MB5	16.5 ± 1.4
MB1	72.4 ± 3.5	SB _B	303.4 ± 27	MB5	16.5 ± 1.4	MB15	26.8 ± 0.9
MB2	68.3 ± 1.2			MB15	26.8 ± 0.9	MB30	95.6 ± 19.1
MB3	21.9 ± 1.3			MB20	42.2 ± 4.1	CM _B	289.6 ± 41
CM _{WB}	233.2 ± 37.5			MB30	95.6 ± 19.1	SB _B	303.4 ± 27
SB _{WB}	755 ± 58.3			CM _B	289.6 ± 41		
				SB _B	303.4 ± 27		

Table 6-18: Average mean flow pore size of strips of the benchmark filter media

Pore size –Mean flow (μm)							
Strip	WB	Strip	B16	Strip	B41	Strip	B45
SB _{WB}	388.3 ± 84.9	SB _B	72.6 ± 2.3	SB _B	72.6 ± 2.3	SB _B	72.6 ± 2.3
CM _{WB}	50.1 ± 7.8	CM _B	57.3 ± 10.3	MB15	11.8 ± 0.2	MB5	6.7 ± 0.3
MB1	23.3 ± 2.9	SB _B	72.6 ± 2.3	MB5	6.7 ± 0.3	MB15	11.8 ± 0.2
MB2	24.7 ± 0.9			MB15	11.8 ± 0.2	MB30	24.2 ± 1.8
MB3	8.4 ± 0.5			MB20	16.4 ± 0.8	CM _B	57.3 ± 10.3
CM _{WB}	50.1 ± 7.8			MB30	24.2 ± 1.8	SB _B	72.6 ± 2.3
SB _{WB}	388.3 ± 84.9			CM _B	57.3 ± 10.3		
				SB _B	72.6 ± 2.3		

Table 6-19: Average smallest detected pore size of strips of the benchmark filter media

Pore size –smallest detected pore size (μm)							
Strip	WB	Strip	B16	Strip	B41	Strip	B45
SB _{WB}	10.2 ± 1.2	SB _B	9 ± 0.9	SB _B	9 ± 0.9	SB _B	9 ± 0.9
CM _{WB}	5.1 ± 0.5	CM _B	7.5 ± 0.4	MB15	5.5 ± 0.6	MB5	5.3 ± 0.3
MB1	6.2 ± 0.6	SB _B	9 ± 0.9	MB5	5.3 ± 0.3	MB15	5.5 ± 0.6
MB2	5.9 ± 0.2			MB15	5.5 ± 0.6	MB30	8.8 ± 1.2
MB3	3.6 ± 0.3			MB20	6.2 ± 1	CM _B	7.5 ± 0.4
CM _{WB}	5.1 ± 0.5			MB30	8.8 ± 1.2	SB _B	9 ± 0.9
SB _{WB}	10.2 ± 1.2			CM _B	7.5 ± 0.4		
				SB _B	9 ± 0.9		

Results in Table 6-17 to Table 6-19 elucidate that the SB strips of the media sandwiching the other strips in between have the largest pore sizes which indicates these strips are not intended to be functioning as a coalescer or droplet capturer media in a filter and they are mainly intended to provide structural stability to the media. The non-bonded (CM) strips, however, are put in the second rank in having large pore sizes. This can be attributed to the required coalescing functionality of the strips to provide an open structure through their thickness to the droplets and give them required time and space to be coalesced to larger drops. MB layers, on the other hand, have relatively smaller size pores in their structure, such that they seem to be given a functionality to capture small size incoming droplets and deliver them to the CM layer in the filter. It has to be kept in mind that the pore size of the non-bonded (CM) strips is measured while the fabric is under the air pressure during the test, i.e. up to 6 kPa (see Section 6.3.5), and because the fabric is non-bonded, the calculated pore size might be smaller than what it actually is without applying the pressure.

6.4.6 Fourier transform infrared spectroscopy - attenuated total reflectance (FTIR - ATR)

Strips of the benchmark filter media (Table 6-7) were tested for the ATR-FTIR analysis as described in the Section 6.3.6. This analysis along with the DSC analysis explained in the Section 6.3.7 was performed to confirm identities of the strips claimed by the supplier. It has been claimed that the SB strips of both B series and WB media are made of PET and the other strips are made of PBT polymers.

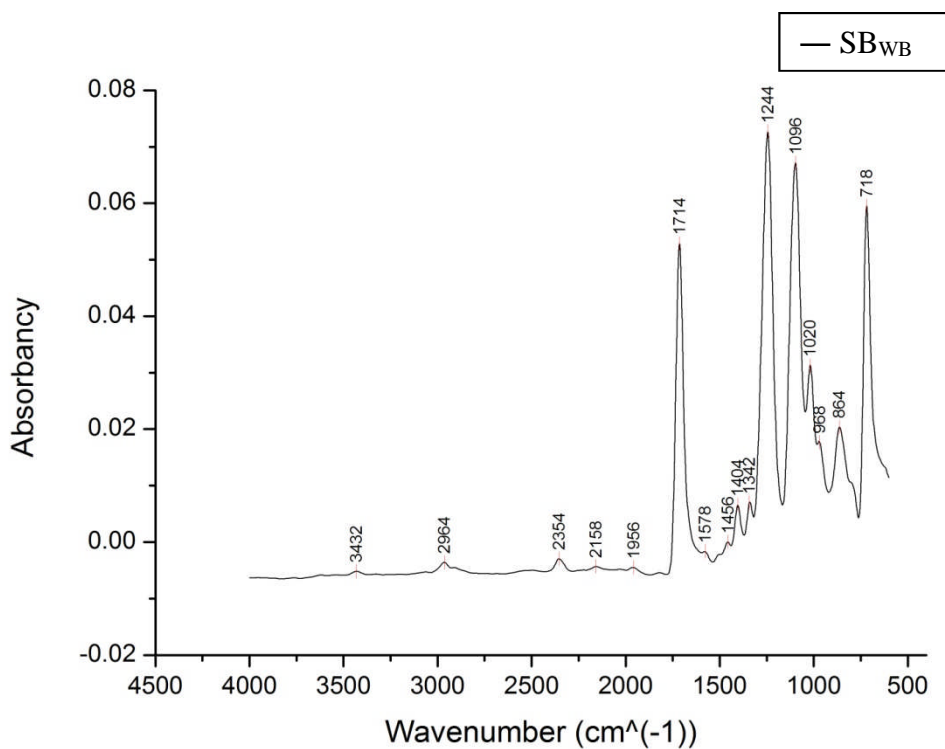


Figure 6-4: ATR-FTIR spectrum for WB filter - SB_{WB} strip (for codes see Table 6-6)

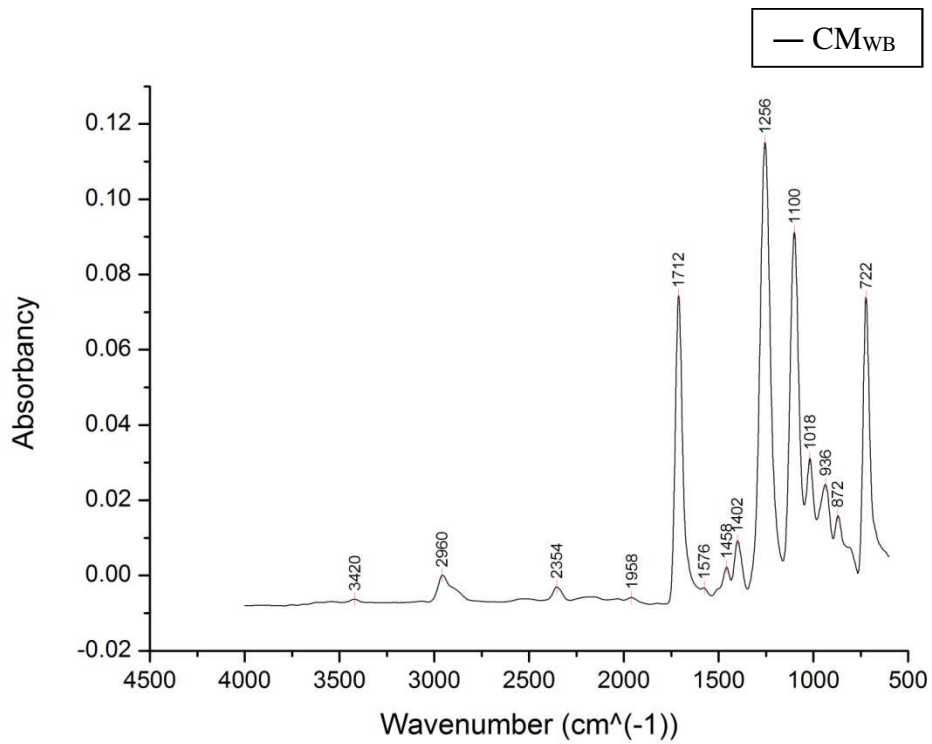


Figure 6-5: ATR-FTIR spectrum for WB filter - CM_{WB} strip (for codes see Table 6-6)

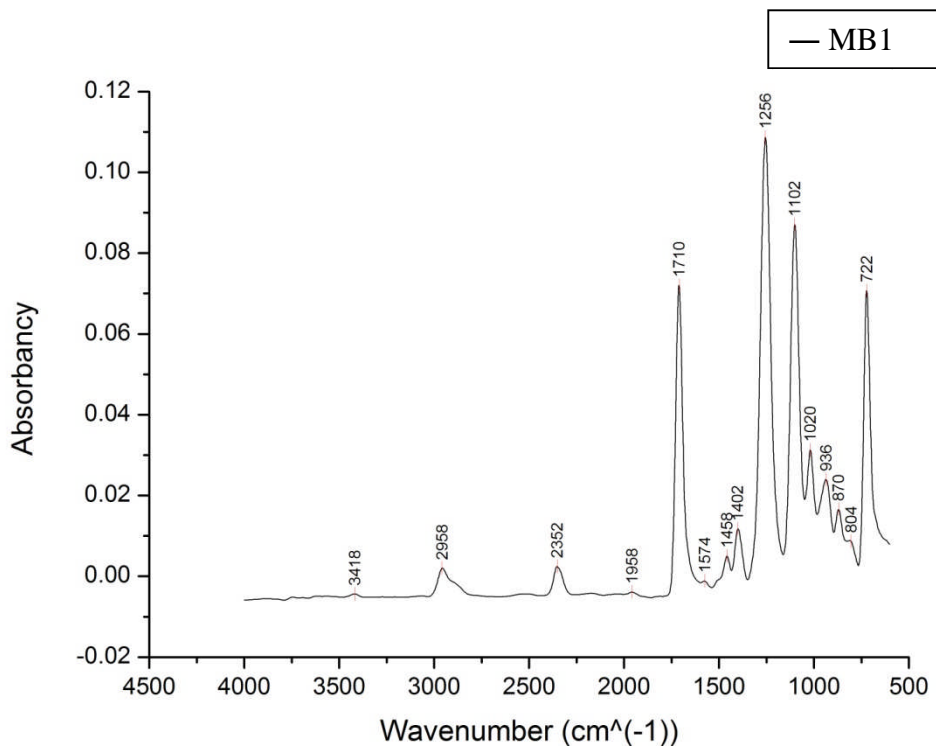


Figure 6-6: ATR-FTIR spectrum for WB filter - MB1 strip (for codes see Table 6-6)

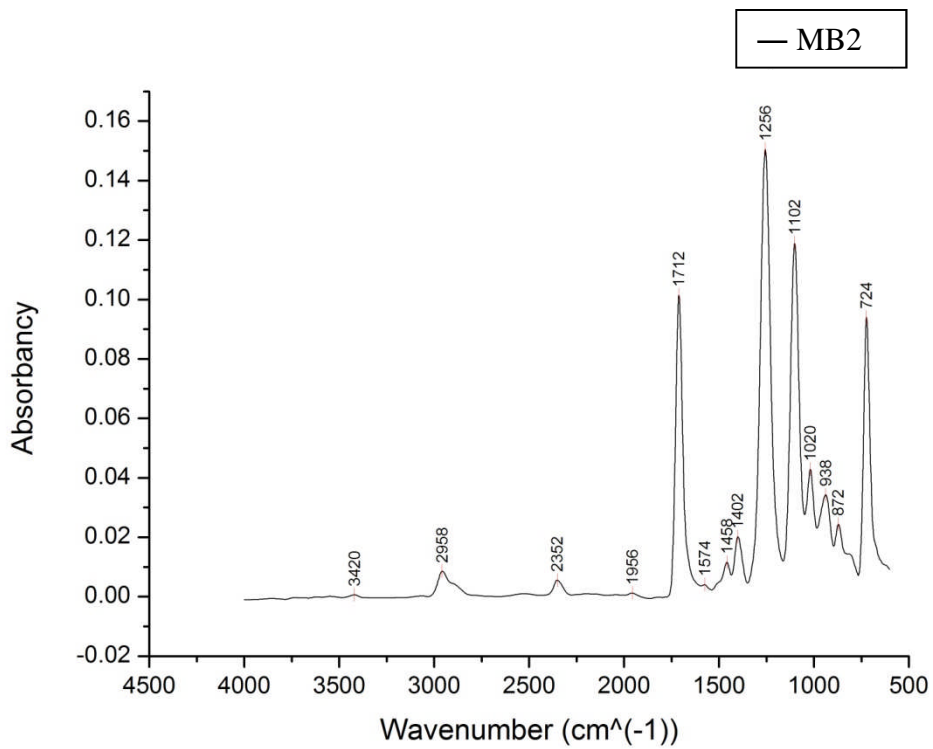


Figure 6-7: ATR-FTIR spectrum for WB filter-MB2 strip (for codes see Table 6-6)

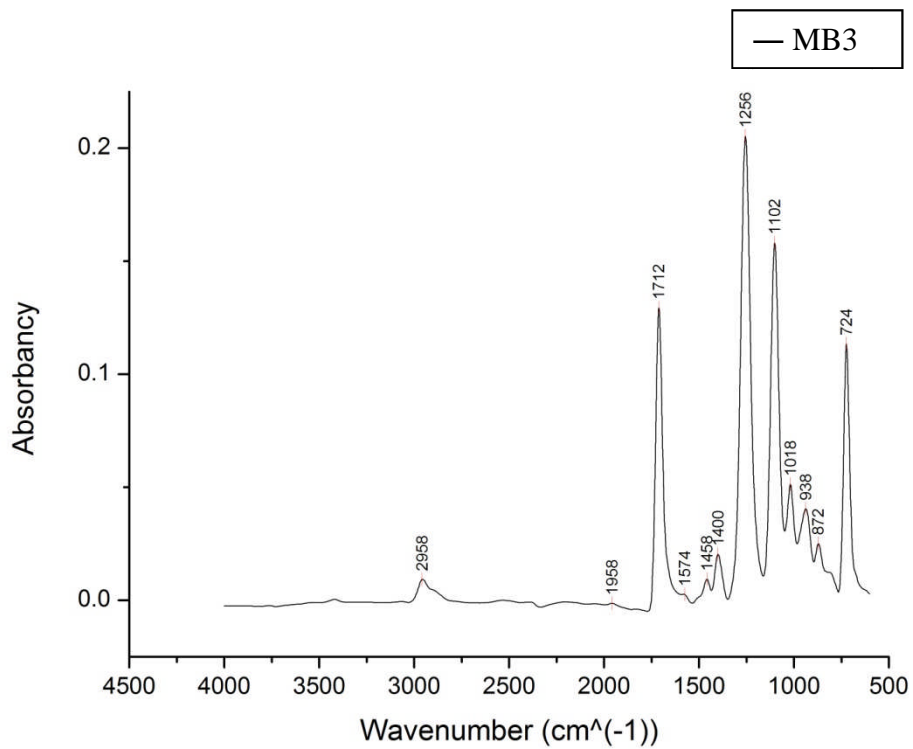


Figure 6-8: ATR-FTIR spectrum for WB filter - MB3 strip (for codes see Table 6-6)

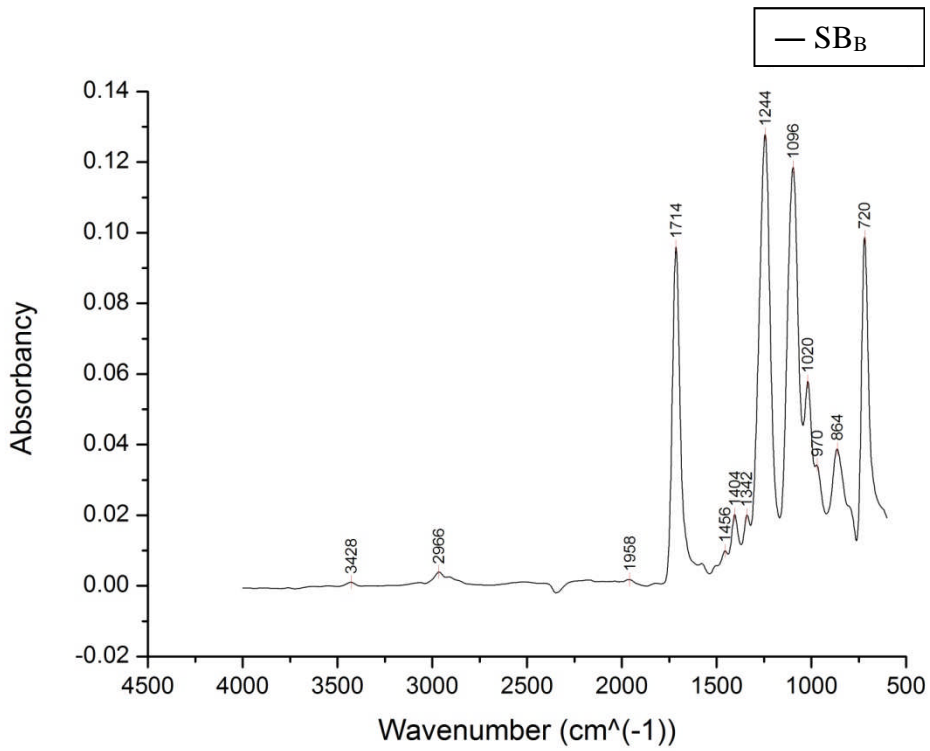


Figure 6-9: ATR-FTIR spectrum for B filters -SB_B strip (for codes see Table 6-6)

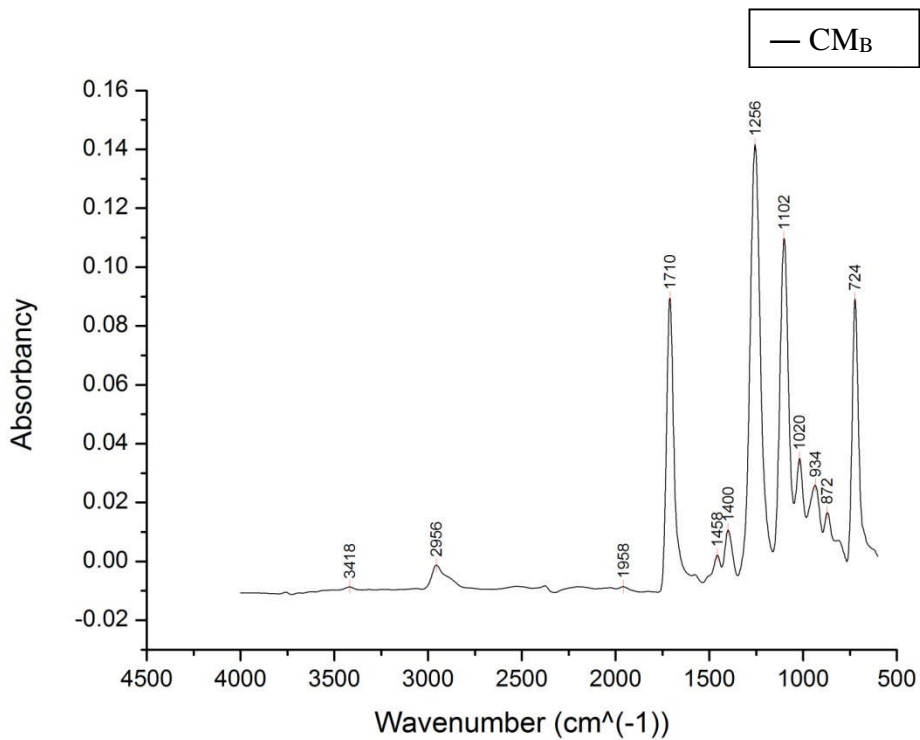


Figure 6-10: ATR-FTIR spectrum for B filters -CM_B strip (for codes see Table 6-6)

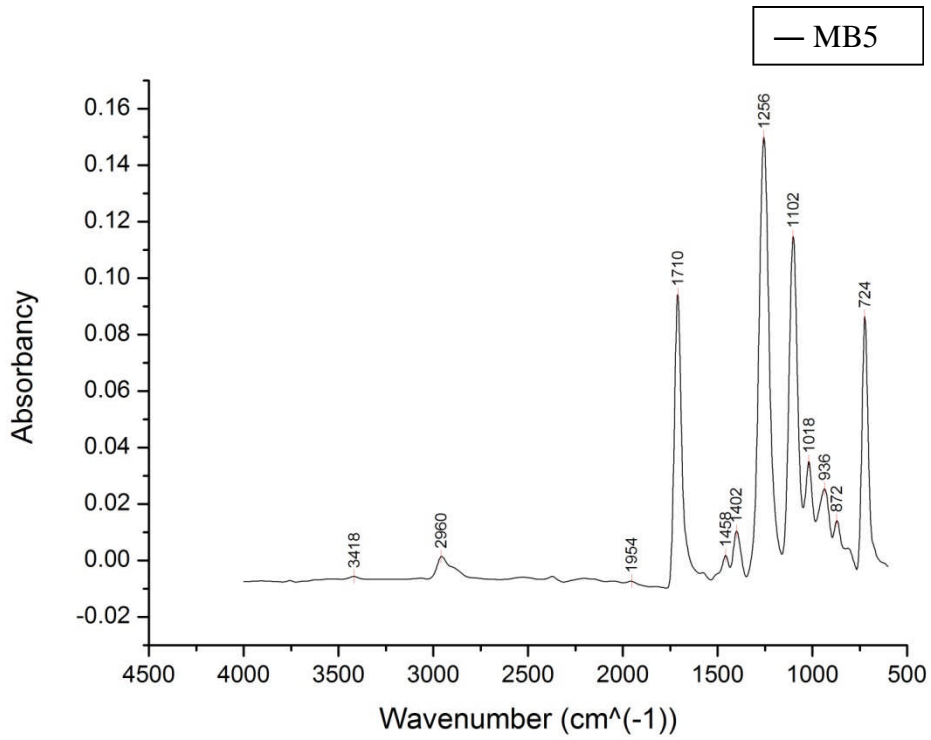


Figure 6-11: ATR-FTIR spectrum for B filters - MB5 strip (for codes see Table 6-6)

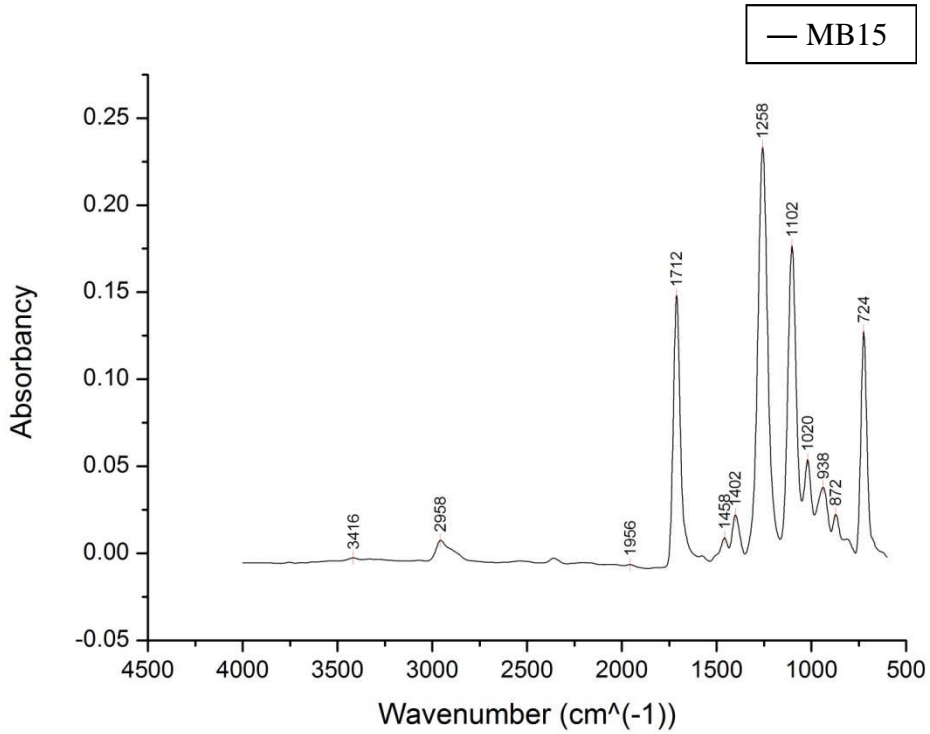


Figure 6-12: ATR-FTIR spectrum for B filters - MB15 strip (for codes see Table 6-6)

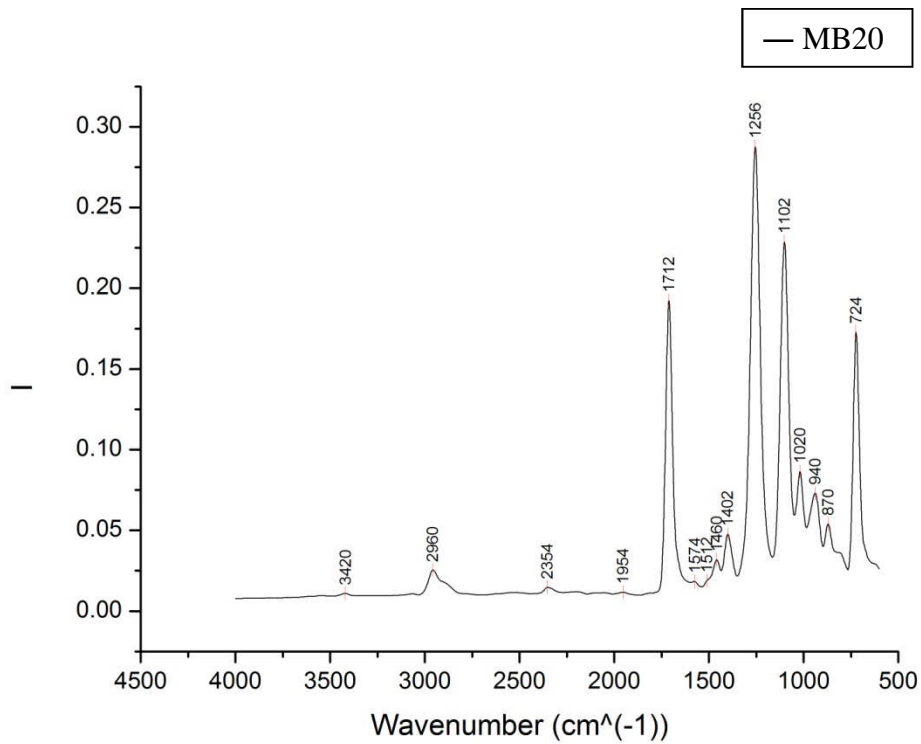


Figure 6-13: ATR-FTIR spectrum for B filters - MB20 strip (for codes see Table 6-6)

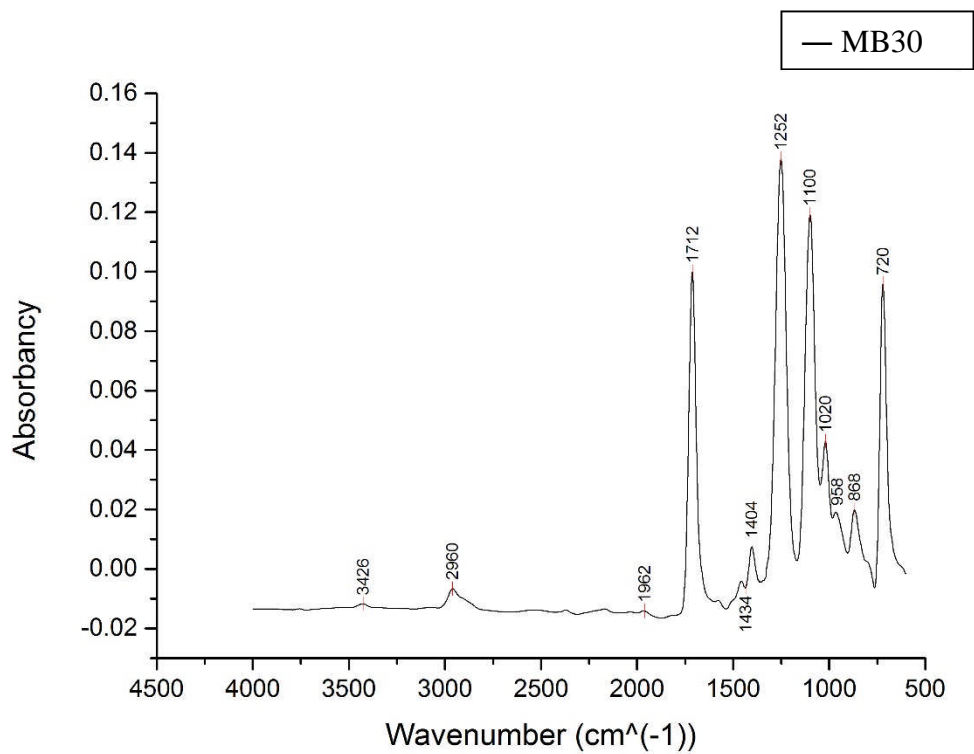


Figure 6-14: ATR-FTIR spectrum for B filters - MB30 strip (for codes see Table 6-6)

Table 6-20: main FTIR spectra peaks for all coalescer layers (cm^{-1}) (for codes see Table 6-6)

Filter strips										
SB _{WB}	CM _{WB}	MB1	MB2	MB3	SB _B	CM _B	MB5	MB15	MB20	MB30
718	722	722	724	724	720	724	724	724	724	720
864	872	870	872	872	864	872	872	872	870	868
968	936	936	938	938	970	934	936	938	940	958
1020	1018	1020	1020	1018	1020	1020	1018	1020	1020	1020
1096	1100	1102	1102	1102	1096	1102	1102	1102	1102	1100
1244	1256	1256	1256	1256	1244	1256	1256	1258	1256	1252
1342	-	-	-	-	1342	-	-	-	-	-
1404	1402	1402	1402	1400	1404	1400	1402	1402	1402	1404
1456	1458	1458	1458	1458	1456	1458	1458	1458	1460	1434
1714	1712	1710	1712	1712	1714	1710	1710	1712	1712	1712
1956	1958	1958	1956	1958	1958	1958	1954	1956	1954	1962
2964	2960	2958	2958	2958	2966	2956	2960	2958	2960	2960
3432	3420	3418	3420	3420	3428	3418	3418	3416	3420	3426

The Figure 6-4 to Figure 6-14, as well as Table 6-20 confirmed that CM and MB layers of the media have the same chemical composition which is different from that of SB layers. Utilising references to the IR peaks of the chemical groups in the literature of the topic, [148-150], the detected IR peaks of the CM and MB layers are very similar to ones for PBT, Table 6-21, while the SB layers did not show the peaks related to ethylene glycol, so that the hypothesis of SB layers are made of PET polymer could not be rejected by this analysis.

Table 6-21: Band assignment of main peaks of PET/PBT polymer

Wavenumber (cm^{-1})	Bond assignment
722-730	Out of plane deformation of two carbonyl substituent on the aromatic ring [148-150]
850-870	Out of plane of benzene group [148-150]
970-980	C-O stretching of glycol [148-150]
1017-1020	In-plane vibration of benzene [148-150]
1090	Mainly due to ester C=O stretching [148, 149]
1230-1270	C(O)-O stretching of ester group [148-150]
1340	CH ₂ wagging of glycol [148, 149]
1370	CH ₂ wagging of glycol [148, 149]
1408-1410	Aromatic skeletal stretching band. Ring in-plane deformation [148-150]
1450	Aromatic skeletal stretching bands [150]
1710-1720	C=O stretching (conjugated with the ring) [148-150]
1950	Aromatic summation band [150]
2960	Aliphatic C-H stretching [150]
3440	O-H stretching of diethylene glycol end-group [150]

To confirm the results of the FTIR analysis, DSC analysis was conducted which revealed the results reported in the next section.

6.4.7 Differential scanning calorimetry (DSC)

To confirm the results acquired by the FTIR analysis, samples from SB and MB strips were analysed by DSC to confirm the hypothesis that the SB strips are made of PET and MB and CM strips are made of PBT polymers. The CM samples were not analysed as no difference between them and MB layers was noticed by the FTIR analysis. Figure 6-15 and Figure 6-16 show the resulted spectra for the SB_{WB} and MB30 strips respectively.

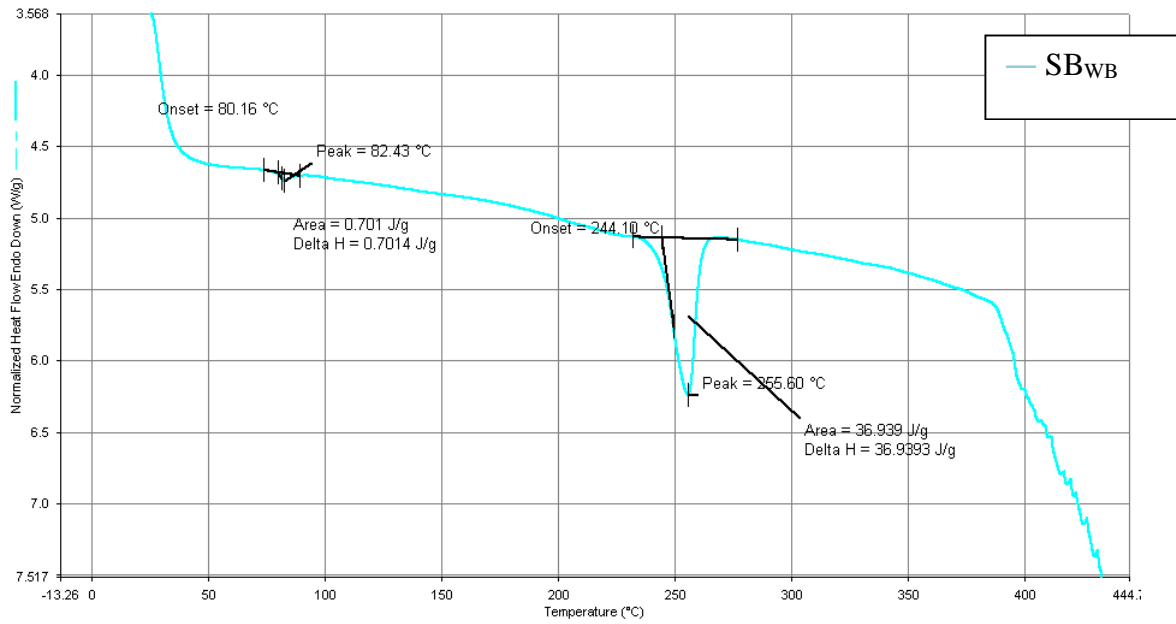


Figure 6-15: DSC graph for SB_{WB} strip (for codes see Table 6-6)

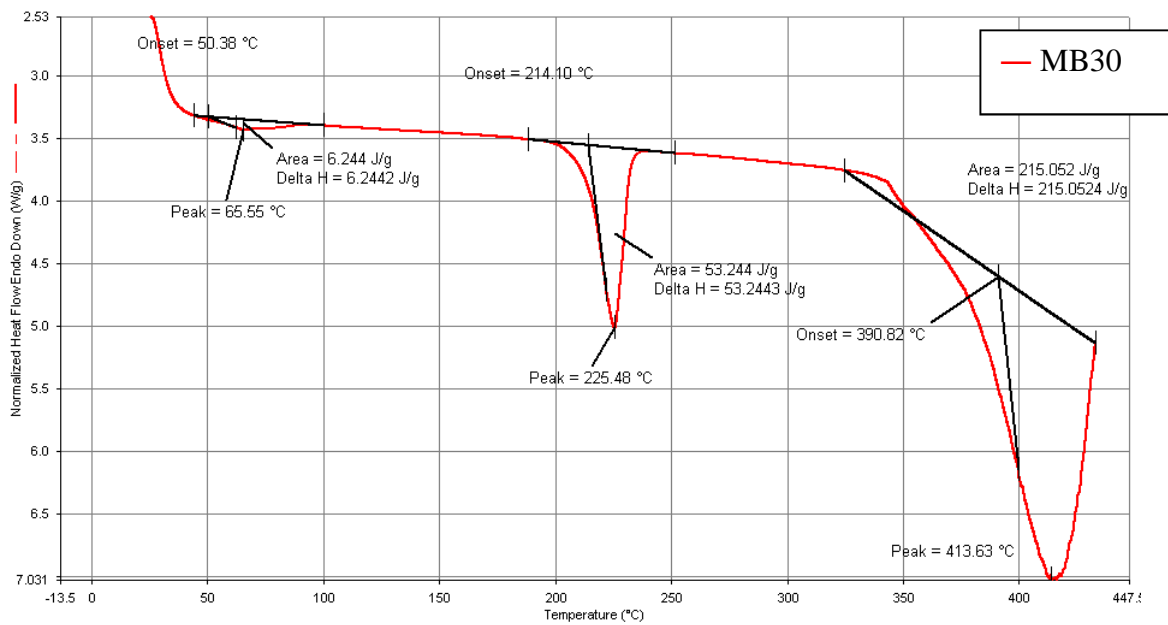


Figure 6-16: DSC graph for MB30 strip (for codes see Table 6-6)

The results (Figure 6-15 and Figure 6-16) show melting point around 255°C and 225°C for the SB_{WB} and MB30 strips respectively which is similar to that of PET and PBT polyesters based

on the literature. This results are similar to those of the FTIR analysis hence could not reject the manufacturers' claim about the polymeric composition of the trips.

6.4.8 Fibre diameter measurement

Figure 6-17 and Figure 6-18 show the SEM images of the strips of the WB and B series media respectively. Average fibre diameters ($\mu\text{m} \pm SE$) of the strips are listed in Table 6-22 as well.

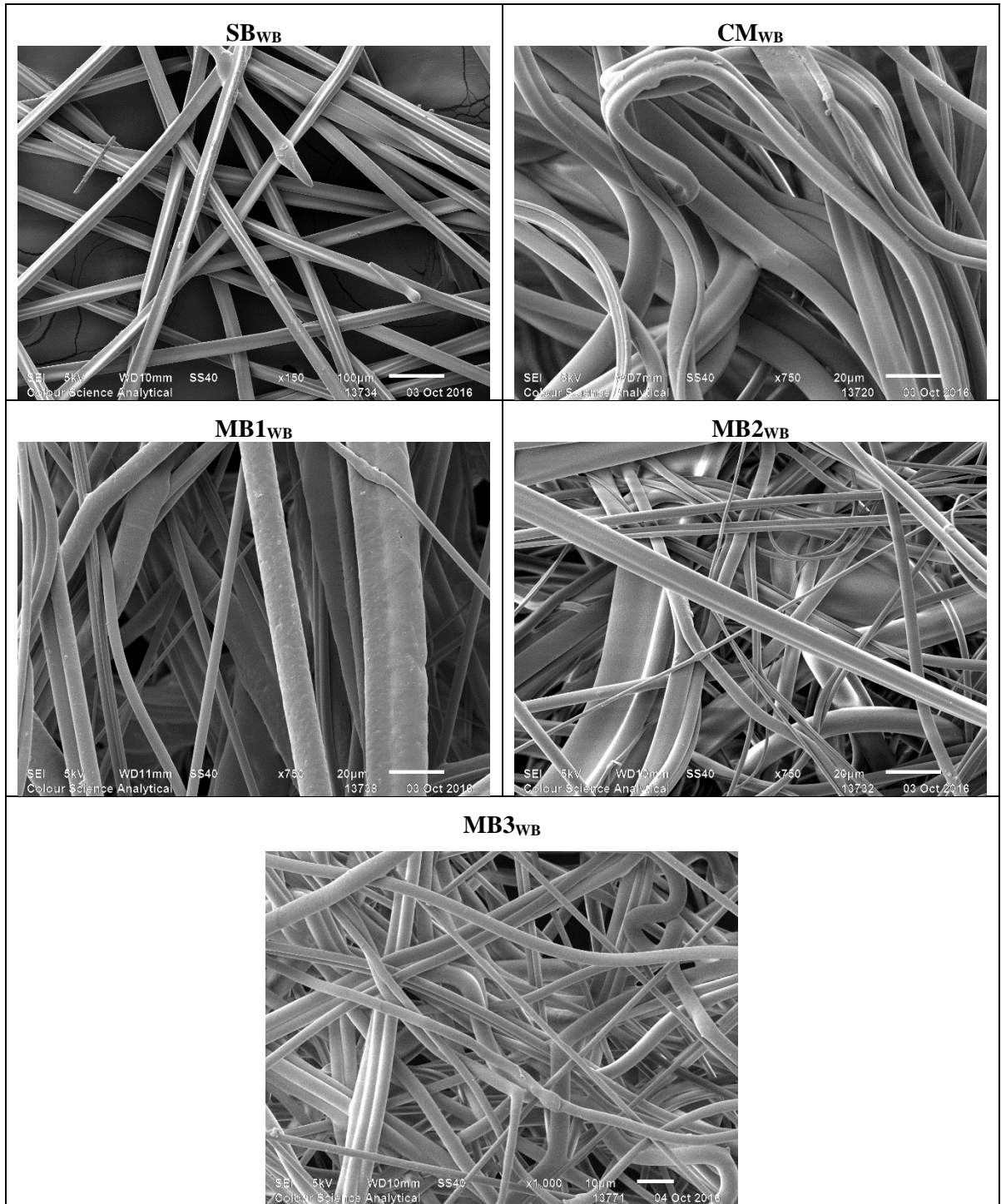


Figure 6-17: SEM images of the WB filter strips (for codes see Table 6-6)

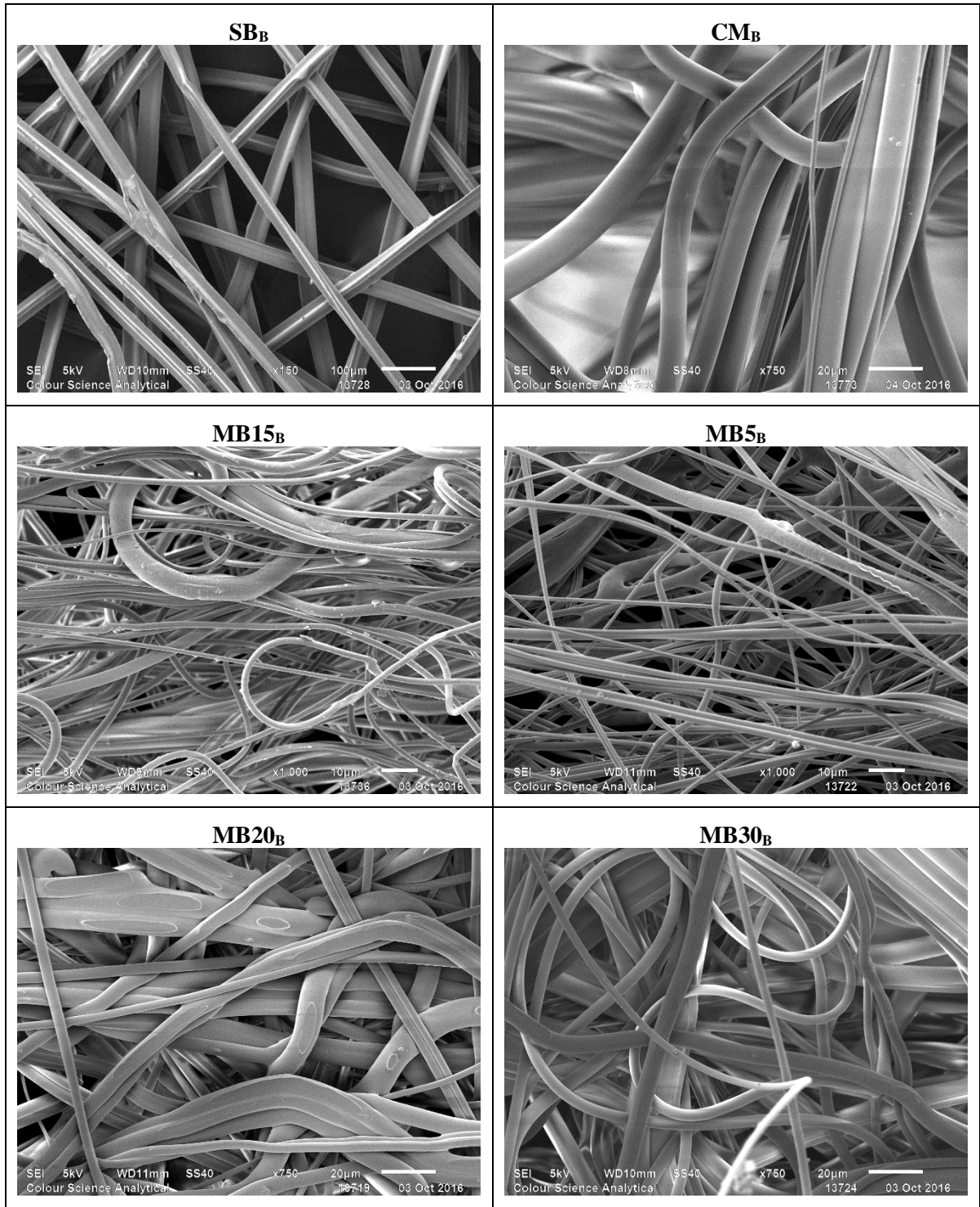


Figure 6-18: SEM images of the B series sample strips (for codes see Table 6-6)

Based on the fibre images (Figure 6-17 and Figure 6-18) and in accordance with the strips manufacturing specifications, no specific binder or surface additives were observed on the

surface of the fibres and the images clearly confirmed the spunbond and meltblown configuration of the strips. Differences between SB, CM, and MB strips are obvious in the images and are in agreements with the results discussed before, e.g. open structure of SB strips, compact and fluffy configuration of MB and CM strips respectively.

Table 6-22: Average fibre diameters of strips of the benchmark filter media (for codes see Table 6-6)

Fibre diameter (μm)							
Strip	WB	Strip	B16	Strip	B41	Strip	B45
SBWB	28.7 ± 0.4	SBB	34 ± 0.6	SBB	34 ± 0.6	SBB	34 ± 0.6
CMWB	6 ± 0.5	CMB	9.1 ± 0.8	MB15	2.2 ± 0.1	MB5	2.1 ± 0.1
MB1	5.4 ± 0.7	SBB	34 ± 0.6	MB5	2.1 ± 0.1	MB15	2.2 ± 0.1
MB2	3.3 ± 0.3			MB15	2.2 ± 0.1	MB30	5.3 ± 0.5
MB3	3.4 ± 0.2			MB20	5.2 ± 0.4	CMB	9.1 ± 0.8
CMWB	6 ± 0.5			MB30	5.3 ± 0.5	SBB	34 ± 0.6
SBWB	28.7 ± 0.4			CMB	9.1 ± 0.8		
				SBB	34 ± 0.6		

Results of the fibre diameter measurements (Table 6-22) elucidate the spunbond layers of the media have the largest average fibre diameter ranged from $28 \mu m$ to $34 \mu m$ which is much greater than that of meltblown fibres. The results also show that the fluffy meltblown strips (CM) are made of fibres slightly coarser than that of the MB strips, i.e. fibre diameter ranged between $2 \mu m$ and $6 \mu m$ in MB strips versus fibre diameters between $6 \mu m$ and $10 \mu m$ in CM strips.

6.4.9 Determination of wetting tension of nonwoven strips

The results of the wetting tension test on WB and B series media are reported in Table 6-23 and Table 6-24 respectively.

Table 6-23: Wetting energy test for the WB filter (for codes see Table 6-6)

Layer ID	Ink with specific surface tension (mN/m)							Layer wetting tension range (mN/m)
	42	48	52	57	60	64	66	
SB _{WB}	Y	Y	Y	N	N	N	-	52-57
CM _{WB}	Y	Y	Y	N	N	N	-	52-57
MB1 _{WB}	Y	Y	Y	Y	N	N	N	57-60
MB2 _{WB}	Y	Y	Y	Y	N	N	N	57-60
MB3 _{WB}	Y	Y	Y	Y	N	N	N	57-60

Table 6-24: Wetting energy test for the B filters (for codes see Table 6-6)

Layer ID	Ink with specific surface tension (mN/m)							Layer wetting tension range (mN/m)
	42	48	52	57	60	64	66	
SB _B	Y	N	N	-	-	-	-	42-48
CM _B	Y	Y	Y	N	N	N	-	52-57
MB5 _B	Y	Y	Y	Y	N	N	N	57-60
MB15 _B	Y	Y	Y	Y	N	N	N	57-60
MB20 _B	Y	Y	Y	Y	N	N	N	57-60
MB30 _B	Y	Y	Y	Y	N	N	N	57-60

Results in Table 6-23 and Table 6-24 confirmed that the strips have not experienced specific hydrophilic treatments and all the surface tension of the strips were lower than $60 mN/m$. Analysis of the exact wetting tension of the strips was not within the scope of this research,

however, the different detected ranges of wetting tensions can be attributed to the different surface morphology and structure of the strips which affecting the wicking properties of the media differently.

6.4.10 Separation performance evaluation

Table 6-25 lists the separation efficiency, η_{av} – Equation 5-2, results of the benchmark samples as well as the barrier mesh.

Table 6-25: Separation efficiency of the benchmark filters measured in the flat configuration with the hydrophobic mesh using the REF diesel fuel

ID.	ΔP_0 (kPa)	ΔP_{20} (kPa)	$\Delta P_{20} - \Delta P_0$ (kPa)	η_{av} (%)
WB	27.1	30.2	3.1	99.75
B16	22.0	22.5	0.5	99.23
B41	27.5	31.4	3.9	99.77
B45	25.3	27.6	2.3	99.59
Mesh	3.1	3.1	-	44.46

Table 6-25 shows very high separation efficiencies for all the benchmarks greater than 99% although, following the previous results, structure of the media are different. Based on the separation efficiency test procedure explained in Chapter 5 of the thesis (Section 5.5.2), the separation efficiency of the media is measured while the barrier mesh is installed in the housing. Such that, contribution of the barrier mesh in the overall separation efficiency of the media was measured following the procedure described in Section 6.3.10, and an efficiency about 44% was measured (Table 6-25). This level of contribution was considered high and probably the reason for the very high similar separation efficiency of the WB and B series media. Therefore, it was decided to measure the coalescence efficiency of the media instead of

carrying on with the separation efficiency to eliminate effects of the barrier mesh and also focusing of the coalescence performance of media which is of main interest in this research. This strategy was followed in the other courses of this study involved with evaluating coalescence efficiency of nonwoven filter media.

6.4.11 Coalescence performance evaluation

The coalescence performance of the benchmark media, coalescence efficiency, ε - Equation 5-4, and quality factor, QF - Equation 5-5, is listed in Table 6-26.

Table 6-26: Coalescence efficiency of the benchmark filters measured in the flat configuration using the REF diesel fuel without using the hydrophobic mesh

ID.	ΔP_0 (kPa)	ΔP_{20} (kPa)	$\Delta P_{20} - \Delta P_0$ (kPa)	ε (%)	QF
WB	24.45 ± 0.15	27.3 ± 0	2.85 ± 0.15	18.92 ± 2.25	0.073 ± 0.0059
B16	22.25 ± 0.05	22.38 ± 0.02	0.13 ± 0.03	21.18 ± 1.18	2.009 ± 0.5212
B41	27.05 ± 0.25	31 ± 0.1	3.95 ± 0.15	23.2 ± 1.51	0.067 ± 0.0024
B45	25.15 ± 0.05	27.6 ± 0.1	2.45 ± 0.05	20.85 ± 0.15	0.095 ± 0.0011

Analysis of the coalescence efficiency of the media (Table 6-26) by a single-factor ANOVA showed that there is no significant statistical difference between the coalescence performance of the media ($P = 0.3658$, $\alpha = 0.05$). This led to the conclusion that having compact meltblown fibre layers (MB layers) functioning as capturing layers does not significantly affect the coalescence efficiency of a media, i.e. comparing the structure of B16 medium with other three media. Moreover, having addition layer of a fluffy layer close to the upstream side of a medium, i.e. similar to the structure of the WB sample compared to the other media, does not significantly improve the coalescence efficiency either. This can be attributed to the fact that

the coalesced drop at the upstream side are re-emulsified when they are pushed through the other compact layers towards the downstream side of the filter.

The same analysis on the quality factor of the media showed significant difference between the media overall performances ($P = 0.0143$, $\alpha = 0.05$). This can be attributed to the low pressure drop across the B16 medium compared to the other media. This also confirm the hypothesis suggesting the coalescence performance of a medium is mainly governed by the fluffy and non-bonded coalescer layer of the medium and having a multi-layer of compact capturing layer does not help the overall coalescence performance of the medium, within the specifications followed in this research.

6.5 Summary

This chapter was dedicated to evaluation of existing multilayer depth coalescing water separation filter media in terms of their nonwoven characteristics as well as water separation and coalescence efficiencies. For this study four filters denoted as WB, B16, B41, and B45 and their constituent nonwoven strips were evaluated regarding their polymer identity, area density, thickness, air permeability, pore size, fibre diameter, wetting tension, bulk and porosity. The separation and coalescence efficiencies of the media were evaluated as well as using the purpose-built test rig explained in the previous chapter.

The material characterisation testing (FTIR and DSC) was performed to check the polymeric identity of the media. Results confirmed that the media are composed of multilayer PBT meltblown fibre strips winded on to a robust plastic cylindrical support mesh while two PET spunbond strips are holding the meltblown layers together. The media also were recognised as hydrophobic media (no hydrophilicity treatment) by conducting a wetting tension test. The PBT strips used in the media were of two kinds: thin bonded strips with a thickness less than

500 μm and a mean flow pore size less than 25 μm , mainly intended for capturing small droplets, and thick fluffy strips with a thickness about 3 to 4 mm and a mean flow pore size about 50 μm functioning as coalescers. The samples ranged from relatively open structure, i.e. B16 with SMS (spunbond – meltblown – spunbond) structure to packed structure such as B41 with eight strips or WB with seven layers including two fluffy coalescing layers.

The separation efficiency tests elucidated high efficiency more than 99% for all the benchmark samples which was attributed to the contribution of the barrier mesh installed in the filter housing for this test. This was considered misleading in terms of evaluation coalescence efficiency of the media based on this test. Therefore, the coalescence efficiency test, which evaluate ability of the media in water coalescence without effects of the barrier mesh was substituted. The results of this tests showed that although the structure of the media are different, their coalescence performances are not significantly different ($P = 0.36$, $\alpha = 0.05$), however, the B16 sample which has no bonded strips in its structure showed the best quality factor compared to the other media ($QF = 2.01$), i.e. B41 showed the best efficiency (23.85%) but a lower quality factor ($QF = 0.07$).

Based on these results and considering limitations and variations within the experimental works of this study, i.e. specific test conditions as well as the design and dimensions of the filter housing, it was concluded that the coalescence performance of a medium might be mainly governed by the coalesce layer of the medium (a fluffy and non-bonded layer), such that evaluation of non-bonded meltblown media with enhanced coalescing performance was put on the agenda as the next stage of the research which is discussed in the next chapter in details.

CHAPTER 7

Effects of Fibre Hydrophilicity and Meltblown Fabric Geometric Configurations on the Performance of Depth Coalescing Fuel Filter Media

7.1 Introduction

The hypothesis confirmed in Chapters 3 and 4 that bio-diesel can stabilise water droplets of smaller sizes compared to mineral diesel and its blends with diesel leads to highly challenging water separation conditions. The results in Section 6.4.11 revealed that the coalescence efficiency of multilayer depth coalescing media can be mainly governed by the non-bonded meltblown nonwoven coalescer layers rather than the bonded meltblown nonwovens mainly functioning to capture water droplets. It was also discovered that the maximum coalescing efficiency of existing commercially sourced samples using REF diesel is only about 24%.

Therefore, there is a need to improve coalescing efficiency by understanding the effects of nonwoven fabric properties on coalescence performance. Accordingly, the main aim of this chapter was to investigate the effects of key properties believed to be influential, specifically fibre hydrophilicity as well as macro-structural features of the fabric. These properties were selected because of the significant attention they have received in the literature (Section 2.6.2). To ensure a systematic investigation of key properties minimising confounding factors, this work is based on studying the coalescence behaviour of a single layer of PBT meltblown fabric representative of that found in industrial systems.

7.2 Test filter media and test fuels

Samples were prepared from 100% poly(butylene terephthalate) (PBT) meltblown fabrics (PMB coalescers) supplied in a 20 m role (width of 50 cm) by the sponsor of this project. The meltblown fabric was characterised using the methodologies given in Section 7.3.1 and the results are reported in Table 7-6 and Table 7-7. The fuel blends used to determine the

coalescing performance of the PMB media were the same diesel and bio-diesel fuels specified in Section 3.2 and prepared using the procedure in Section 3.3.1.

7.3 Experimental methods and apparatus

This section reports the experimental methods and apparatus used to characterise the PMB media in respect of hydrophilicity, physical properties, macrostructure, and coalescence performance.

7.3.1 Modification of the surface wettability

The wetting behaviour of the PBT meltblown fabrics was modified by alkaline hydrolysis using the procedure detailed by Wang et al. [98]. This involved treatment with a sodium hydroxide (NaOH)/methanol solution in which PBT polymer chains are attacked by hydroxide ions (OH^-) present in the solution and end groups of carboxyl or hydroxyl are formed on the carbonyl carbons of the ester linkage of the PBT polymer, such that hydrophilicity is increased [98, 151-153]. In the alkaline hydrolysis method, surface modification of fibres in depth of fabrics is ensured compared to other techniques such as coating [154] or plasma treatment [155-157].

The hydrolysis treatment bath was prepared by dissolving different concentrations of NaOH into solutions of methanol (50% *v/v*) and deionized water (50% *v/v*). PBT fabric samples were cut into squares of 20 cm × 20 cm, and then immersed in the treatment bath for 10 min without stirring (liquor ratio of 1:100). The bath temperature (T) was controlled at 40°C for NaOH concentrations of 0.25, 1, and 3 mol/l, or 35°C for a NaOH concentration of 3 mol/l. Three replicates per sample were prepared. Samples codes corresponding to each condition are listed in Table 7-1. PMB-0-40 refers to control fabrics treated at 40°C with no NaOH dissolved in the solution.

Table 7-1: Sample codes for the hydrolysis test conditions

NaOH concentration (mol/L)	Treatment bath temperature T(°C)	
	35	40
0	-	PMB-0-40
0.25	-	PMB-0.25-40
1	-	PMB-1-40
3	PMB-3-35	PMB-3-40

For each sample, the solution was prepared in a glass vial and preheated to the specified temperature before immersion. The bath temperature was maintained during treatment using temperature control equipment consisting of a thermocouple, PID controller (proportional integral derivative controller), and a hotplate. Samples were washed after treatment (10 min) by immersion in distilled water for 1 h, then quickly immersed in HCl solution (0.1 mol/l), and then soaked again in distilled water until a pH of 7 was achieved after rinsing. Finally, samples were dried in air for 24 h, followed by vacuum drying overnight at 20 °C.

7.3.1.1 Wettability characterisation

The wettability of each sample (PMP, PMB-0, PMB-0.25, PMB-1, and PMB-3) was characterised by the L/H ratio (lipophilicity/hydrophilicity) in accordance with Kulkarni et al. [96], based on the modified Washburn's equation, Equation 7-1.

$$L/H = \frac{S_o \eta_o \rho_w^2 \gamma_w}{S_w \eta_w \rho_o^2 \gamma_o}$$

Equation 7-1: Modified Washburn's equation [96]

η , γ , and ρ in Equation 7-1 denote viscosity, surface tension, and density of the penetrating liquid respectively, and S is the slope of the wetting curve plotting the square mass, m^2 , of the penetrating liquid at time t . The subscript “ o ” refers to oil and “ w ” refers to water. The m^2 - t curve is generated experimentally by conducting a liquid absorption test via tensiometry.

In principle, the L/H ratio is related to the wicking performance of a medium when it is in contact with an oil compared to when it is in contact with water, such that in

Equation 7-2, the terms θ_o and θ_w refer to the advancing contact angles of the oil and water phases.

$$L/H = \frac{\cos \theta_o}{\cos \theta_w}$$

Equation 7-2: Fundamental equation of the L/H ratio [96]

Kulkarni et al. [96], developed their equation (Equation 7-1) by solving Equation 7-2 using Washburn’s equation, (

Equation 7-3) to substitute the contact angles, which require difficult and complex measurements, usually with significant errors on the non-ideal porous/rough surface of a fibrous substrate while the effect of gravity is ignored too.

$$h^2 = \frac{r_{eff} \cos \theta \gamma t}{2\eta}$$

Equation 7-3: Washburn’s equation [96]

Where:

h : is the height of liquid rising in the fabric by wicking

r_{eff} : is the effective capillary radius in the medium.

A Kruss K100 force tensiometry instrument operating in absorption measurement mode was used to plot the wetting curves of the test samples using deionised water and REF diesel fuel. A test specimen was cut in 1 cm × 1 cm, and was hung on the measuring probe connected to the balance of the tensiometer. To commence measurements, the probe descended into the vessel containing 50 ml of the test liquid until the lower edge of the sample touched the liquid surface and the balance detected liquid contact (sensitivity of 0.005 gf). Once the surface was detected, the mass of the liquid penetrating the sample was recorded and plotted every 2 s for 1 min. At least six specimens from each sample in two groups of three were evaluated. One group was tested using distilled water, and the other one was tested using REF diesel. The slope of each wetting curve was calculated by line fitting the initial wetting kinetics of the curves. Table 4-2 summarises the samples studied.

Table 7-2: Samples prepared for wettability evaluations (for sample codes see: Table 7-1)

Sample ID	Description
PMB	Untreated
PMB-0-40	Alkali-treated
PMB-0.25-40	Alkali-treated
PMB-1-40	Alkali-treated
PMB-3-350	Alkali-treated
PMB-3-40	Alkali-treated

7.3.1.2 Characterisation of treated and untreated nonwoven coalescing media

The treated and untreated PBT meltblown samples were characterised in relation to their properties according to the standard test procedures via instruments listed in Table 7-3. All test

procedures, excluding the bursting strength, are detailed in Section 6.3. Results were analysed using single factor ANOVA and statistical T-testing.

Table 7-3: Nonwoven characterisation test procedures

Property	Unit	Standard No.	Testing Instrument
Area Density (GSM)	$g.m^{-2}$	BS EN 29073-1:1992	METTLER TOLEDO balance
Thickness	mm	BS ISO 9073-2:1996	THWING-ALBERT gauge
Air Permeability	$l.m^{-2}.s^{-1}$	EDANA 140.1-81	LabAir FX3300
Pore size –Bubble point	μm	ASTM F316	Capillary flow porometry®
Pore size –Mean flow	μm	ASTM F316	Capillary flow porometry®
Fibre diameter	μm	FESEM	JEOL JSM-6610 LV
Bursting strength	kPa	ISO 13938-2:1999	James Heal

Air permeability measurements were made at 200 Pa pressure difference based on 20 cm² samples using the procedure described in Section 6.3.3. The pore size distribution in each sample was determined according to the methodology in Section 6.3.5. Mean fibre diameter was determined using SEM images and image analysis (Image-Pro software) using the methodology described in Section 6.3.8. Bursting strength is an important parameter for filter fabrics because of the multi-axial forces that are inevitably imposed on the substrate during use. Accordingly, the bursting strength was determined.

Bursting strength test methodology

A James Heal pneumatic bursting strength tester was used to evaluate samples based on BS EN ISO 13938-2:1999 standard test procedure. Each sample was clamped over an expanding diaphragm using a circular clamping ring such that a sample area of 50 cm² was achieved. The apparatus equipped with a compressed air system, applied an increasing air pressure to the

underside of the diaphragm, causing distension of the diaphragm as well as the overlying fabric. The pressure increased smoothly until the test specimen bursts within 20 ± 5 s. The resulting bursting strength is defined as maximum pressure applied to the test specimen until the test specimen ruptures minus the diaphragm pressure (diaphragm correction). The height at burst is defined as the displacement of the test fabric at its peak position at the bursting pressure. All data is based on three replicates per sample.

7.3.2 Effect of geometrical arrangement to the coalescing media

During use, a nonwoven coalescing fabric will be compressed by the fuel flow against the filter support such that its effective porosity under load is likely to be reduced from its nominal value determined in load-free conditions. It is therefore instructive to understand how such variations in macrostructure and fabric dimensions can affect coalescence performance.

Accordingly, PBT meltblown samples with different macro structural formats were compared using the efficiency test methodology described in Section 5.5.3 using REF diesel. Initially, the coalescence efficiency of the single layer PMB media operating in tandem with a filter support as in the conventional filter sample arrangement (Section 5.3.1) and (Figure 7-1), was determined. The results were then compared with data obtained using alternative configurations of the same fabric in which the fabric porosity was modulated. Once any differences in coalescence performance were established, it was possible to study the underlying relationships between the fabric configuration and performance.

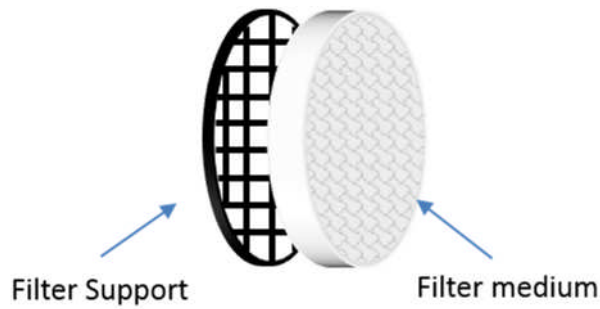


Figure 7-1: Control filter sample arrangement in the filter housing for the coalescence efficiency test

Details of the different filter assemblies and evaluation methodologies will now be explained. Note that the associated results for each set of conditions are presented in Section 7.4. In the alternative arrangements that will now be described, the rationale was to provide increased solid surface area to promote coalescence performance and/or to reduce the pressure drop, since both govern the operating efficiency of the coalescer.

7.3.2.1 Double layer of PMB media operating in tandem with a filter support

In the first alternative assembly, the conventional filter configuration was modified by the addition of a second identical meltblown PMB fabric to make a dual layer configuration (Figure 7-2).

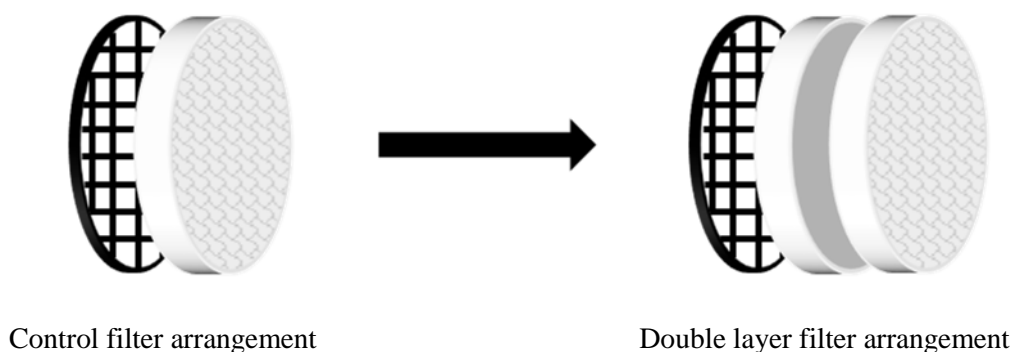


Figure 7-2: Single (control) and double layer filter assemblies operating with a support layer

It was reasoned that this would substantially increase the surface area available for water removal via coalescence. This arrangement is denoted as “double layer” throughout. The coalescing performance of the double layer was then compared with the single layer control.

7.3.2.2 Surface hairiness: single layer of PMB media with projecting surface fibres in tandem with a filter support

By providing projecting fibres or hairiness on the surface of the filter fabric it was reasoned that this could lead to comparable coalescence performance (since the total solid surface area was unaffected), combined with a reduced pressure drop, due to the higher overall fabric porosity.

To prepare the samples, the control filter sample arrangement was maintained, but the surface of the medium on the downstream side (facing the filter support) was mechanically disrupted by light rotary pressure to produce a ‘hairy’ surface (Figure 7-3) such that approximately twice the thickness of the control sample was achieved.

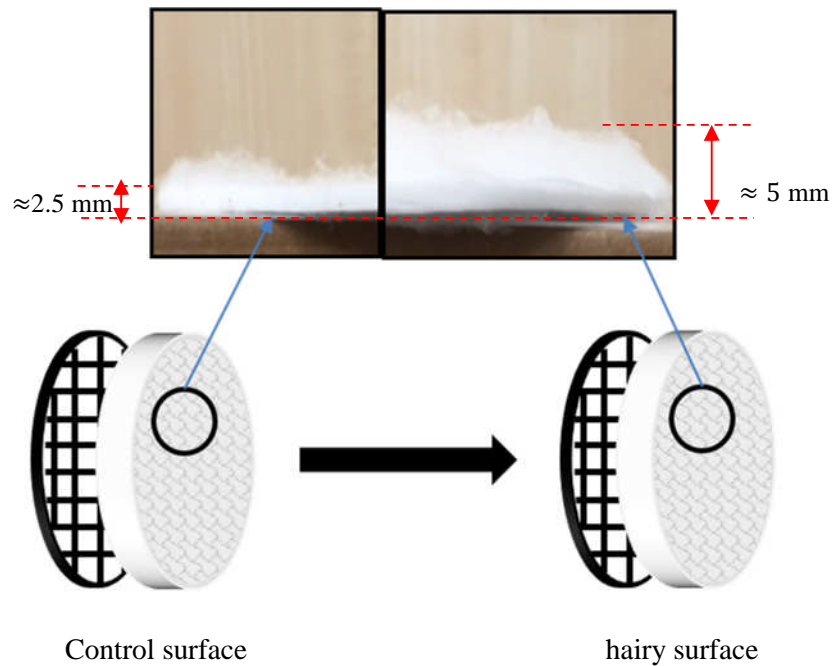


Figure 7-3: Single (control) layer filter assembly with a hairy surface operating with a support layer

The coalescence performance was then compared to the conventional single layer filter assembly.

7.3.2.3 Static porosity: double layers of PMB media with a spacer in tandem with a filter support

During dynamic operation, the meltblown fabric is likely to be compressed due to the pressure of fluid flow. Therefore, in an effort to stabilise the porosity of the fabric (static porosity) and determine the coalescence efficiency a porous spacer was inserted between two layers of PMB fabric (Figure 7-4(b)). To accomplish this, a 100 cm² porous spacer disk was manufactured from PMMA (Perspex) sheet of 5 mm thickness, and cut to the same size as the filter fabric using a FB730 Laser cutter (CadCam Technology Ltd., UK). The disk was intended to be a porous spacer, therefore, it was manufactured with randomly arranged holes. For this aim, 25

holes were of a diameter of 10 mm, 10 holes with a diameter of 5 mm, and 10 holes with diameter of 2 mm.

Furthermore, to understand the effect of the spacer itself on the coalescence efficiency, regardless of its location in the arrangement, measurements were also made with the spacer placed on the upstream side of the filter (Figure 7-4(a)).

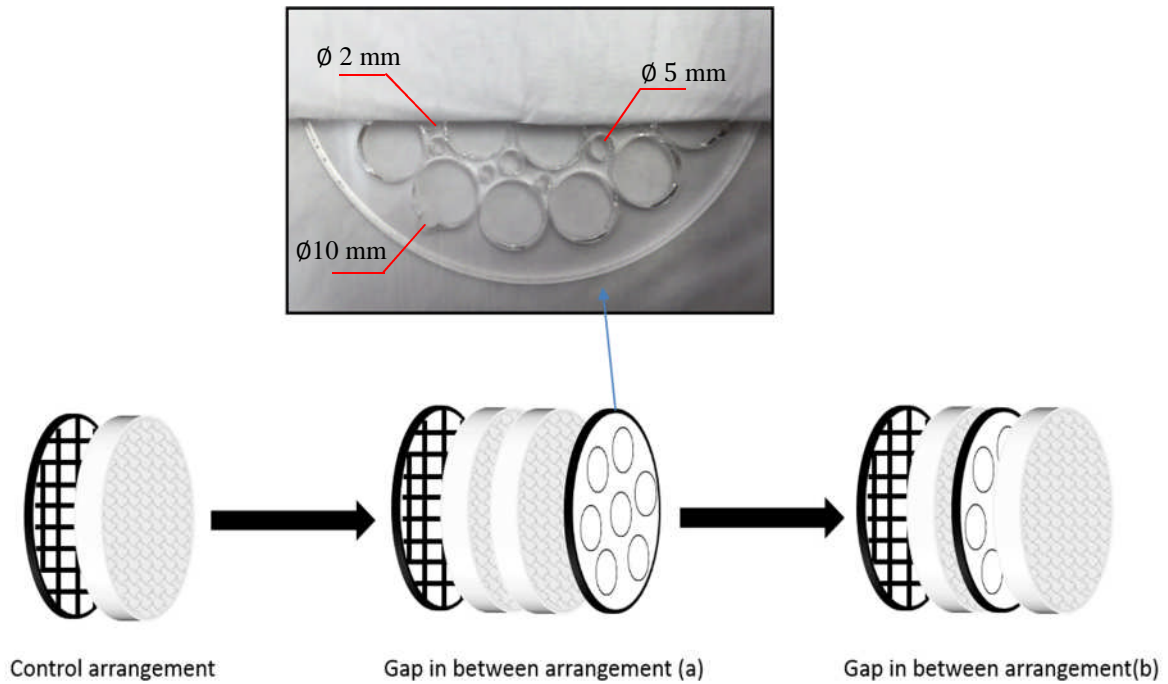


Figure 7-4: Generation of a 'gap in between' arrangement using a porous spacer disk

The filter support was also placed in the housing such that during an efficiency test, the two filter fabrics were compressed against the spacer and the filter support. Herein, the spacer simulates a porous structure inside the medium with a 5 mm gap (thickness of the spacer) maintained between the two filter fabrics, which remain interconnected by the holes cut in the spacer.

7.3.2.4 Dynamic porosity: single layer of PMB media without filter support (bowing arrangement)

By removing the filter support, during operation, the fabric is not mechanically supported and is therefore likely to partially deform and ‘bow’ due to the applied forces imposed in the same direction as the liquid flow. Since the fabric will not be compressed against a rigid surface, the deformation can be expected to maximise the effective porosity of the fabric during operation (dynamic porosity). It was instructive to understand how such conditions would affect coalescence efficiency. In this arrangement (denoted as “bowing arrangement”), the filter support was taken off the filter housing, such that the filter medium was not compressed against the support during the efficiency test. As the fuel flowed through the fabric and because there was no filter support in place to limit freedom of movement, a bowing deformation was generated in the fabric while it remained robustly clamped in the filter housing (Figure 7-5).

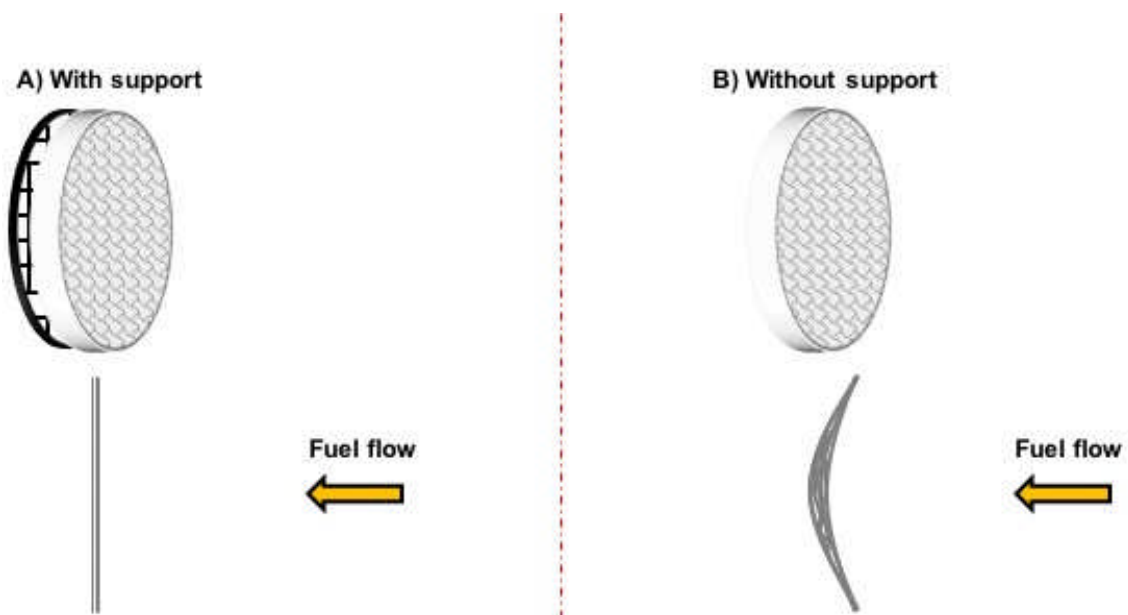


Figure 7-5: Bowing arrangement

7.3.2.5 Results

Table 7-4 summarises the influence of the different filter assemblies on the coalescence efficiency, ε - Equation 5-4, using the REF diesel fuel.

Table 7-4: Effect of different filter arrangements on the coalescence efficiency

Sample arrangement	ε (%)
Control	25
Double layer	38
Surface hairiness	34
Static porosity	22
Dynamic porosity	62

Marked differences were observed in coalescence behaviour amongst the various configurations despite the retention of what was in effect the same meltblown filter medium. Interestingly, an almost 150% increase in coalescence efficiency was observed in the dynamic porosity arrangement compared with the control arrangement. This surprising result led to further investigation of the bowing effect and to the development of methods to better characterise the structure as will now be explained.

7.3.3 configurational characterisation of the bowing configuration

The bowing configuration associated with evaluation of filters in dynamic porosity conditions (no filter support being used) was characterised using semi-quantitative methods. In the bowing arrangement, the configuration of the fabric is deformed dynamically when placed in the housing subjected to dynamic liquid flow. Consequently, offline characterisation of the medium's configuration to capture this effect was impractical. Moreover, the filter housing of the coalescence test rig was of cylindrical shape, which meant that deformation and

visualisation of the sample could not readily be recorded. Owing to these limitations, two methodologies were employed: (a) use of a convex filter support (Figure 7-8) in to which a filter medium could be placed and (b) simple transparent perspex filter housing (Figure 7-7) with a square cross section in to which a filter medium could be placed to aid visualisation.

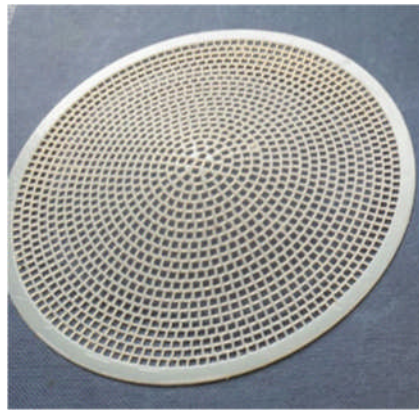


Figure 7-6: 3D printed convex filter supports

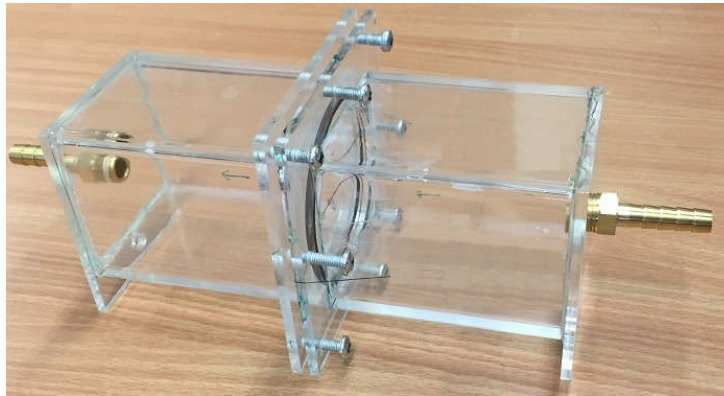


Figure 7-7: Modified filter housing to aid visualisation of the bowing arrangement

Both the convex filter support and the pilot filter housing were made in-house. To compare the coalescence performance results of a medium supported by the convex filter support with that of the medium supported by a flat filter support and eliminate possible errors associated with

the aperture size and thickness of the supports, a flat support with the same thickness and aperture size as the convex one was built (Figure 7-8). Both the flat and convex filter supports were 2 mm thick and designed in CAD software (SolidWorks) and Objet 1000 3D printed (Stratasys, US) from ABS-M30i polymer. Each had an open area of more than 85% and square apertures of 2 mm x 2 mm. The convex support had a maximum internal height of 15 mm at its centre.

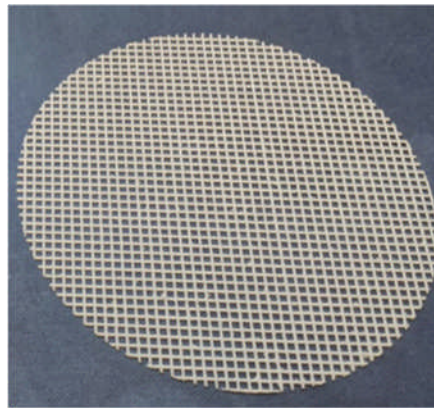


Figure 7-8: 3D printed flat filter supports

The pilot filter housing was composed of an inlet hose, upstream and downstream flanges, and an outlet hose. The detailed design of the housing is shown in Figure 7-9. The housing was designed to be simply connected to a fluid source such as tap water or compressed air using a hose such that the fluid could easily run through the filter medium clamped in the middle and cause the bowing deformation. The housing with a square cross section was chosen to facilitate measuring deformations of the test medium with a ruler by an operator with a relatively high accuracy.

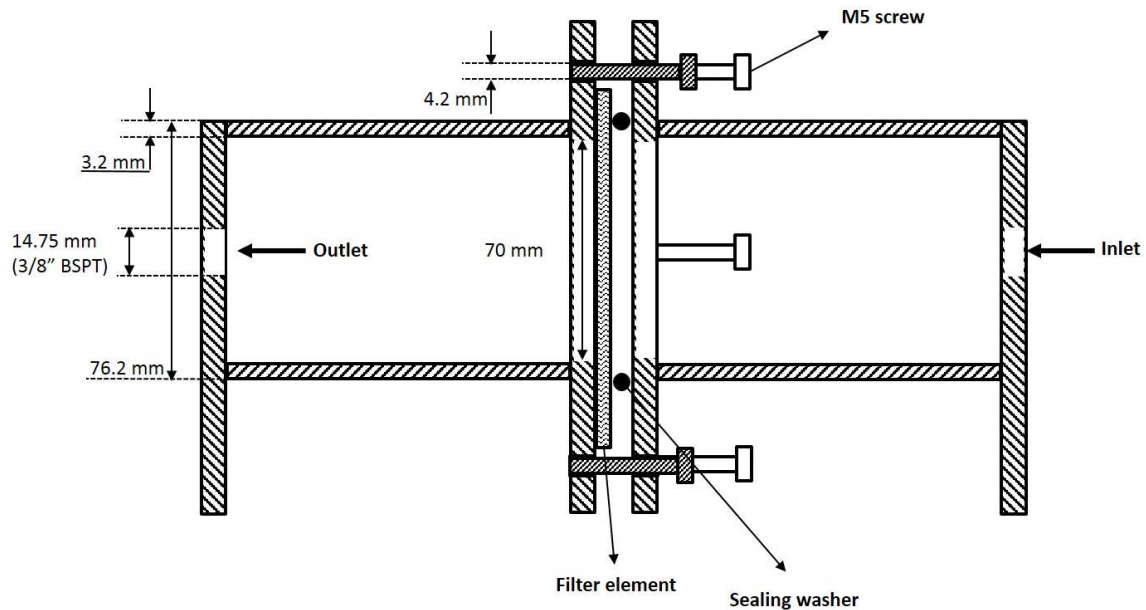


Figure 7-9: detailed design of the filter housing for the bowing characterisations

To characterise the bowing configuration employing the aforementioned methodologies, three sets of experiments were conducted. Firstly, coalescence performance was measured on the coalescence test rig using the 3D printed convex and flat filter supports to see if the bowing shape itself was affecting the performance of the filter media. Secondly, untreated PMB media were clamped into the pilot housing to simulate the bowing deformation using compressed air any dynamic changes in the sample thickness were measured as the fluid passed through (air-flow experiment). A final experiment was conducted using the same pilot housing (Figure 7-7 and Figure 7-9) wherein water was used as the flow fluid medium to induce deformation of the test sample (water-flow experiment). For the air-flow experiment, to enable capture of the deformation during bowing followed by offline measurement of the sample, filter samples were first immersed in poly(vinyl acetate) (PVA) adhesive (volume ratio of PVA/water = 1:3). Residual adhesive was removed using a pad mangle with a nip to nip distance of 1 mm and a padding pressure of 0.5 bar, before being clamped in the housing (Figure 7-10). Compressed

air was then used to generate a fluid flow at a velocity similar to that encountered in the normal filter housing, causing the sample to bow. As the air stream continued to be directed at the sample for at least 30 min, water was gradually evaporated leading to adhesive fixation of the bowed configuration of the filter fabric. The dry sample was then removed and cut in half such that the deformation through the sample thickness could be observed. Samples were manufactured at flow rates and pressures of 44 cm/s and 11.9 mbar, and 18 cm/sec and 3.7 mbar respectively. In both cases, bowing deformation was observed similar to that visually observed in the coalescence test rig.

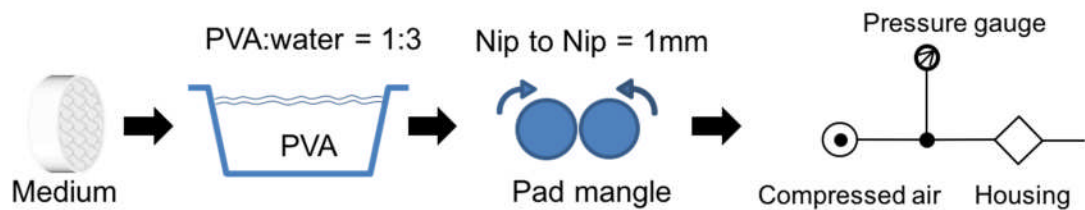


Figure 7-10: Methodology used to capture the bowed filter fabric configuration under dynamic flow conditions

In water-flow experiment, the fabric deformation was not fixed and changes in thickness of the centre of the test medium were directly recorded. The experiment was conducted by connecting the inlet hose to a water supply, with the filter housing over a lab sink such that the outlet water could be directly removed to waste. The convex deformation of the fabric on the downstream side was carefully measured using a ruler from outside of the Perspex housing. The same procedure could not be applied to measure the concave deformation of the medium due to lack of visibility. Therefore, A measuring flag (Figure 7-11) made of flexible plastic, $7\text{ mm} \times 20\text{ mm}$, was clamped upstream the filter medium using a stitch yarn such that the flag

is positioned on the centre of the medium and concave deformation of the medium is measurable.

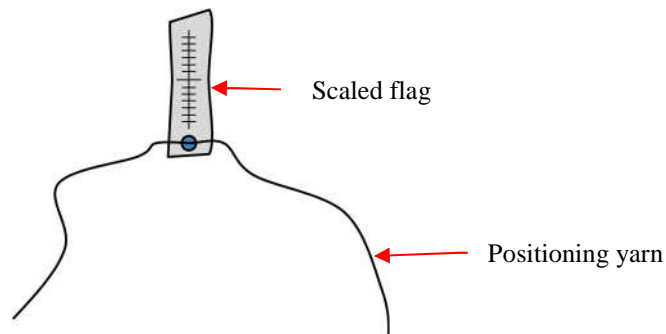


Figure 7-11: Measuring flag used for measuring for concave deformation of the medium

The maximum deformation was measured for each sample by subtracting the convex and concave deformations given the dry thickness of the fabric. The water flow rate always remained constant at 2 l/min.

7.3.4 Evaluation of coalescing performance: flat vs. bowing configurations

Two sets of experiments were performed to evaluate the coalescence performance of hydrolysis-treated PMB samples in the control filter arrangement, and untreated PMB samples in the bowing filter arrangement. In both cases, the coalescence performance was compared with that of the untreated PMB fabric in the control arrangement. All the coalescence efficiency tests were performed in triplicate for each sample following the procedure in Section 5.5.3.

For these measurements, the REF and M200 fuels were used to characterise the coalescence performance. The REF fuel was used for all the media while M200 was used only for PMB, PMB1 and PMB3 samples to see if the presence of surfactant in the fuel affected the performance of the hydrolysed samples. For the coalescence efficiency measurements using the bowing arrangement, the Ref, B5, B20, B50, M200, M325, and M400 fuels were used to

characterise the untreated PMB samples and the results were compared with that of untreated PMB media in the same fuel blends but this time, in the control sample arrangement (flat configuration).

7.4 Results and discussion

This section details the results of the characterisations performed on the treated and untreated PMB meltblown samples, as well as the coalescence efficiency measurements on the flat and bowed configuration samples using REF diesel and bio-diesel blends.

7.4.1 Surface wettability modifications of the filter medium

The wettability of the PMB meltblown fibres was modified using the procedure in Section 7.3.1 based on six average wetting curves (mean \pm SE), i.e. three water curves and three diesel curves, for each sample (listed in Table 7-1). Three replicates were made per sample. Figure 7-12 to Figure 7-17 show the water and diesel curves for the test samples, and the wetting slopes obtained by line fitting the initial wetting kinetics of each average curve are shown in Figure 7-18 to Figure 7-23. The slope values and the calculated L/H ratios are reported in Table 7-5. Figure 7-12 and Figure 7-13, the water curves demonstrate the repellency of the hydrophobic samples, and in Figure 7-18 and Figure 7-19 the slope of the water curves show the repellency slopes of those samples.

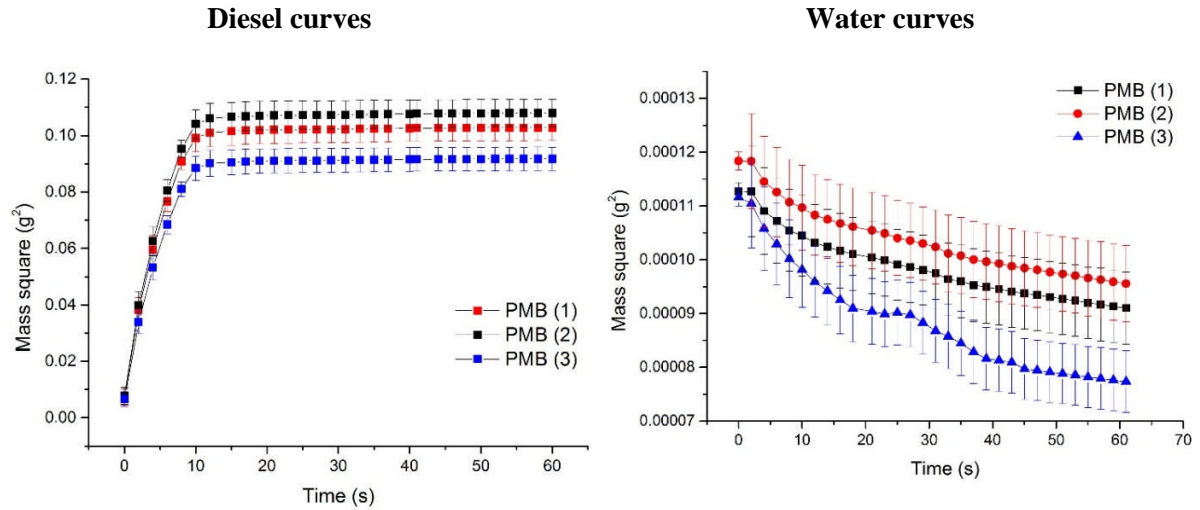


Figure 7-12: Wetting curves and repellency of the untreated PMB samples in REF diesel and distilled water respectively (see Table 7-1 for the sample code)

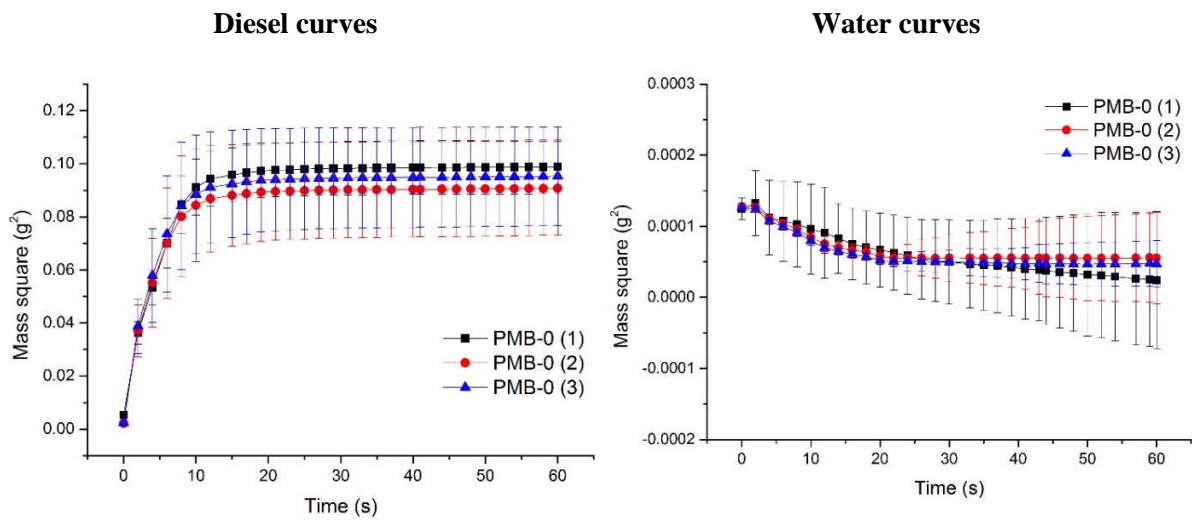


Figure 7-13: Wetting curves and repellency of the PMB-0-40 in REF diesel and distilled water respectively (see Table 7-1 for the sample code)

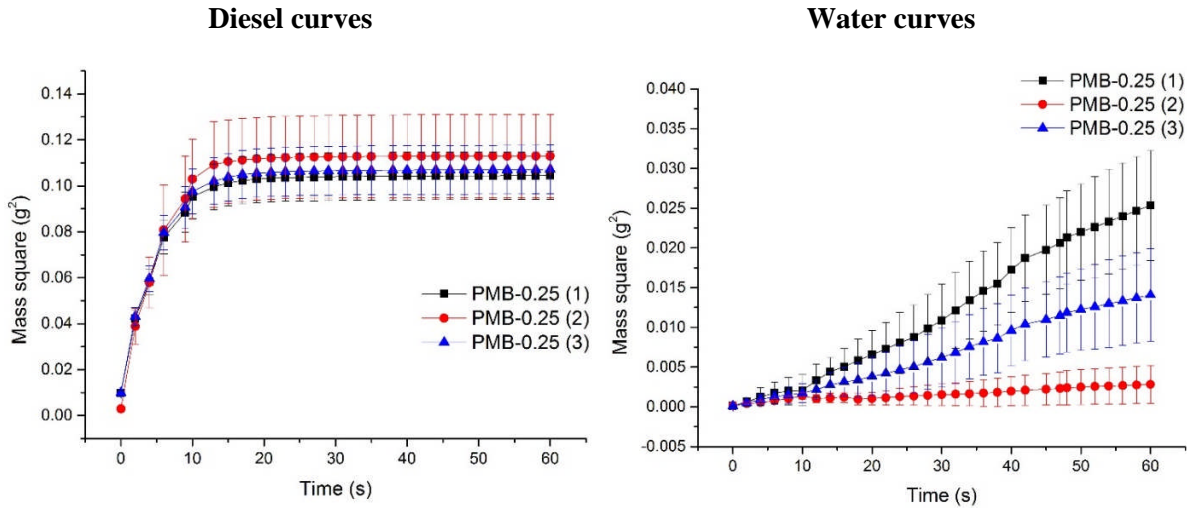


Figure 7-14: Wetting curves of the PMB-0.25-40 in distilled water and REF diesel (see Table 7-1 for the sample code)

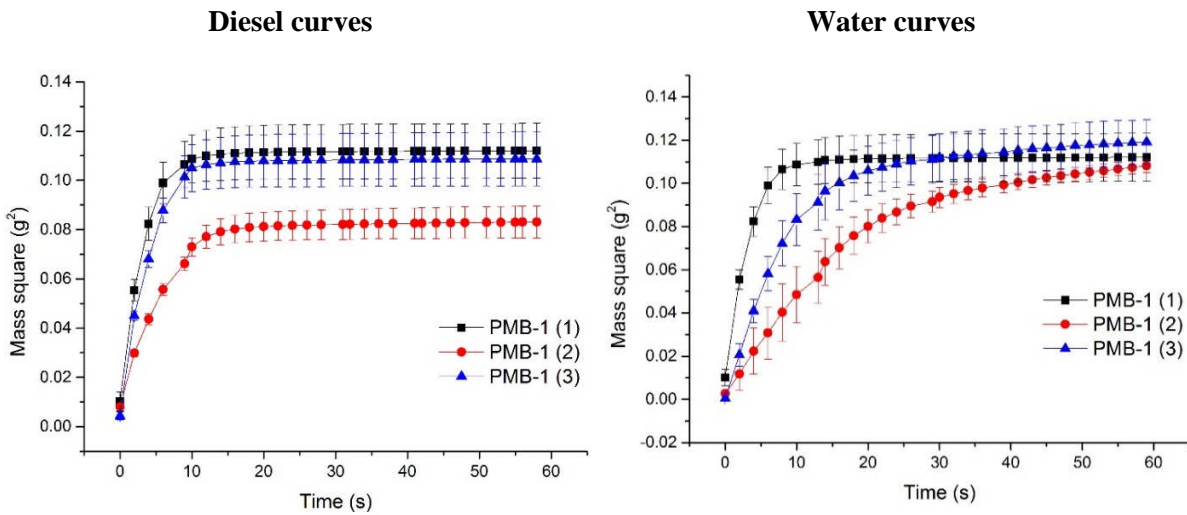


Figure 7-15: Wetting curves of the PMB-1-40 in distilled water and REF diesel (see Table 7-1 for the sample code)

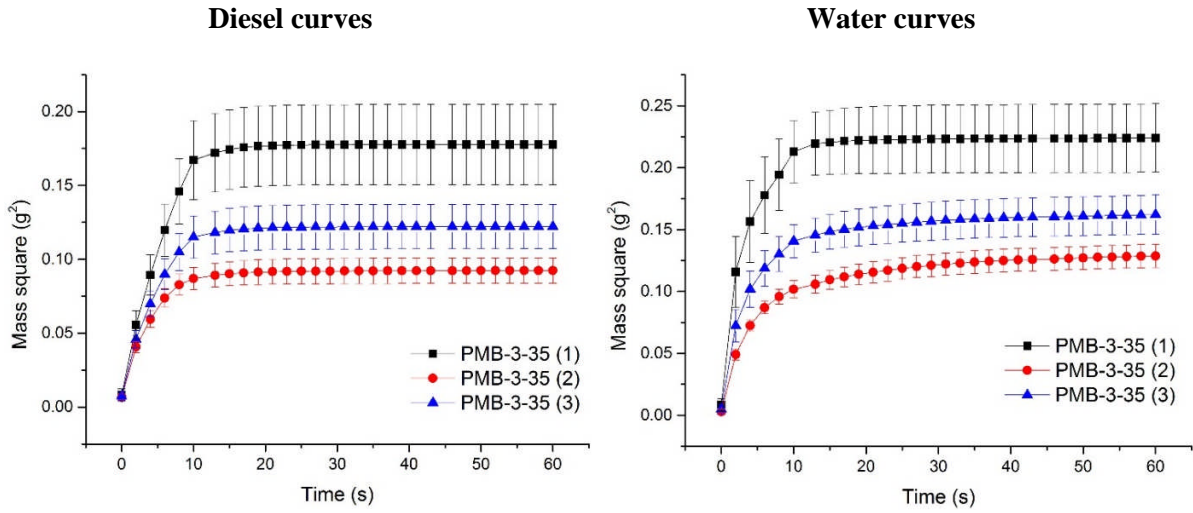


Figure 7-16: Wetting curves of the PMB-3-35 in distilled water and REF diesel (see Table 7-1 for the sample code)

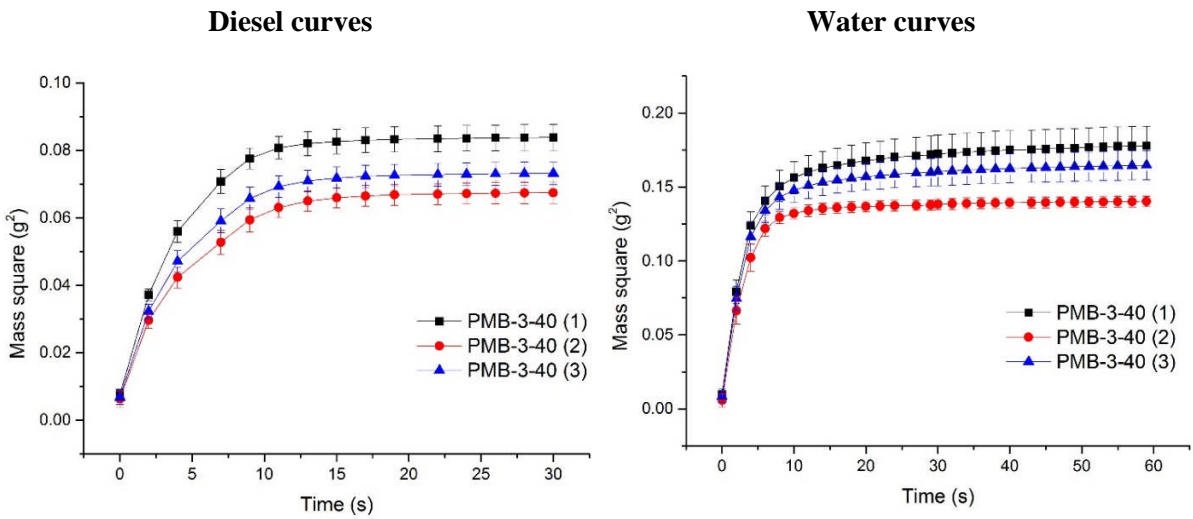


Figure 7-17: Wetting curves of the PMB-3-40 in distilled water and REF diesel (see Table 7-1 for the sample code)

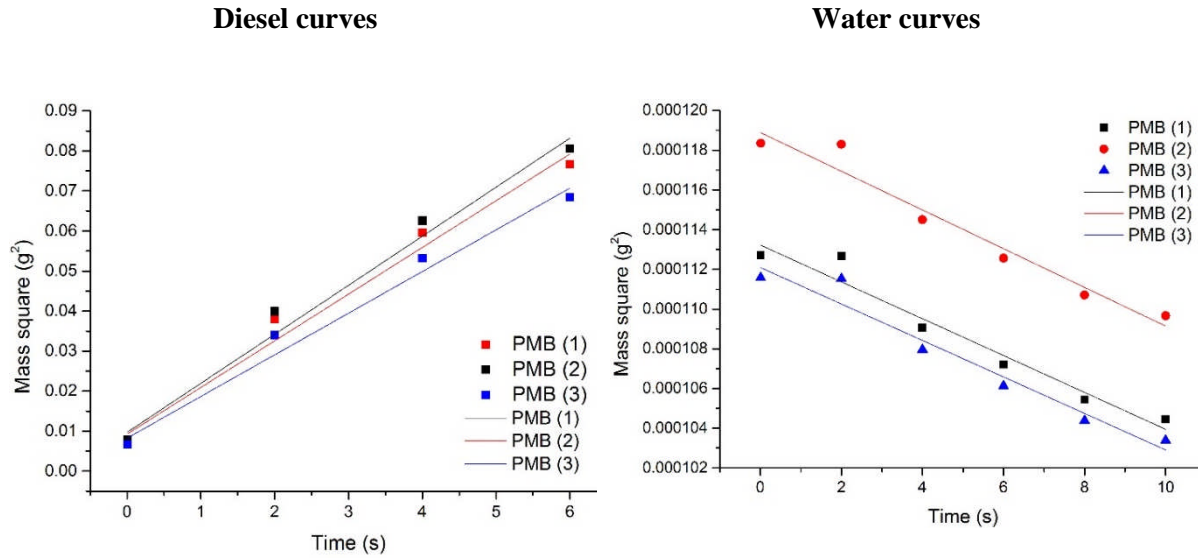


Figure 7-18: Wetting and repellency slopes of the untreated PMB samples in REF diesel and distilled water respectively (see Table 7-1 for the sample code)

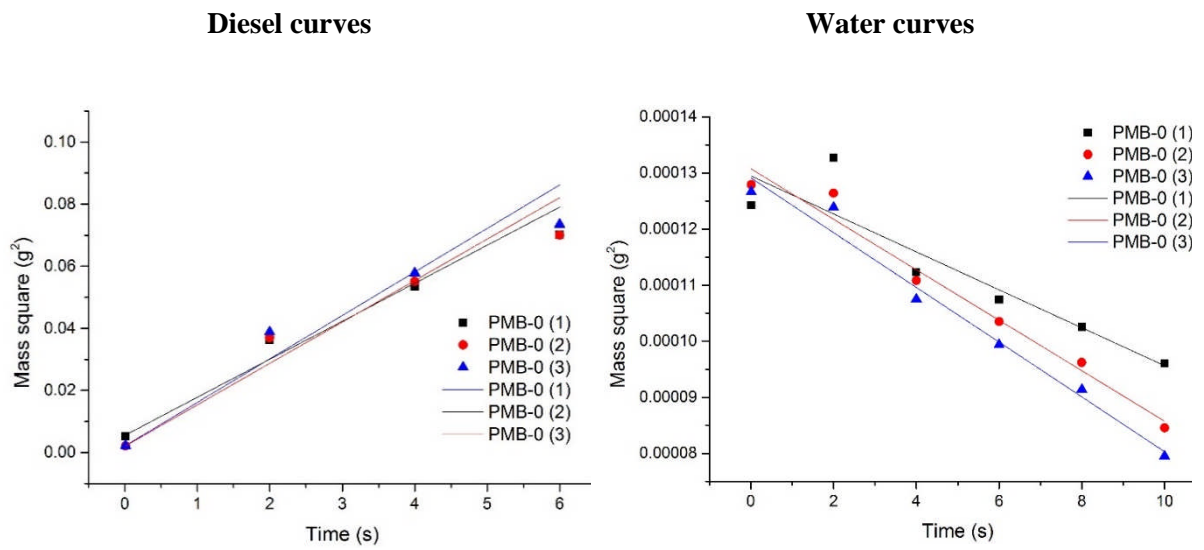


Figure 7-19: Wetting and repellency slopes of the PMB-0-40 in REF diesel and distilled water respectively (see Table 7-1 for the sample code)

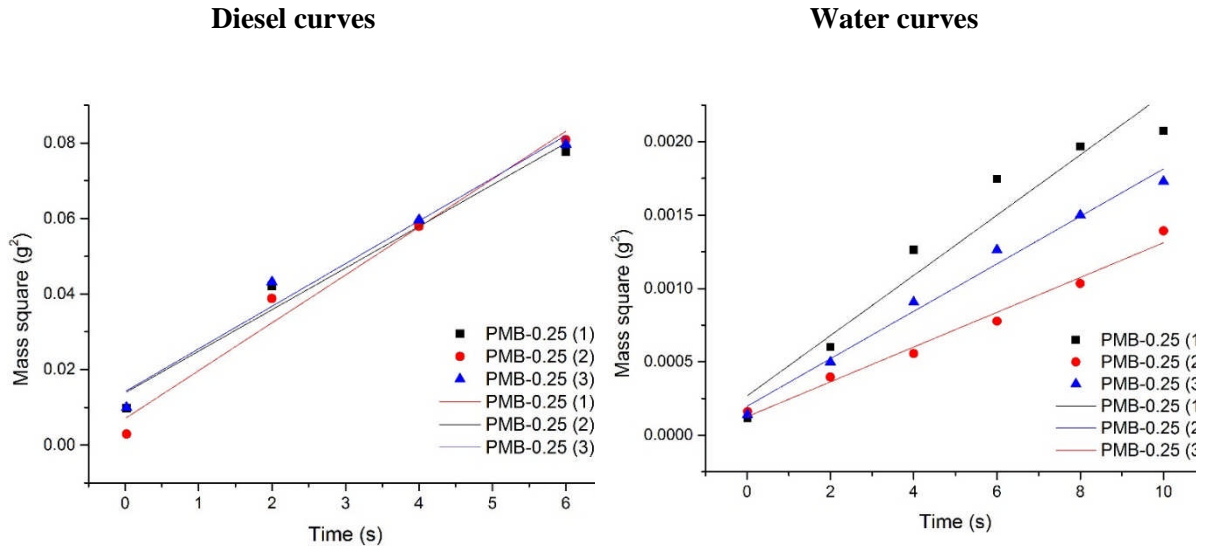


Figure 7-20: Wetting slope of the PMB-0.25-40 in distilled water and REF diesel (see Table 7-1 for the sample code)

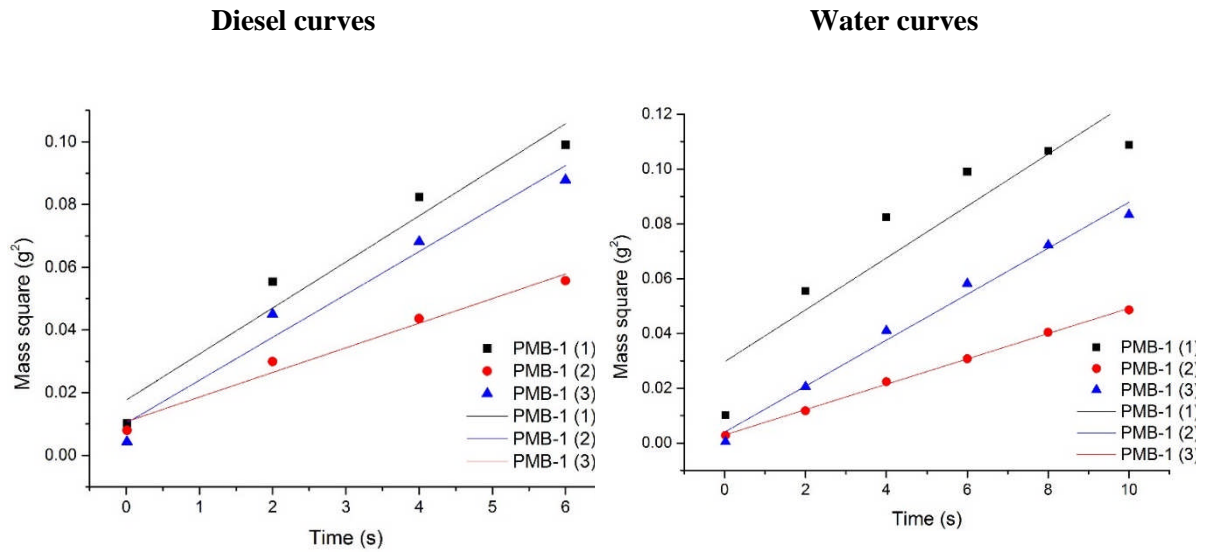


Figure 7-21: Wetting slope of the PMB-1-40 in distilled water and REF diesel (see Table 7-1 for the sample code)

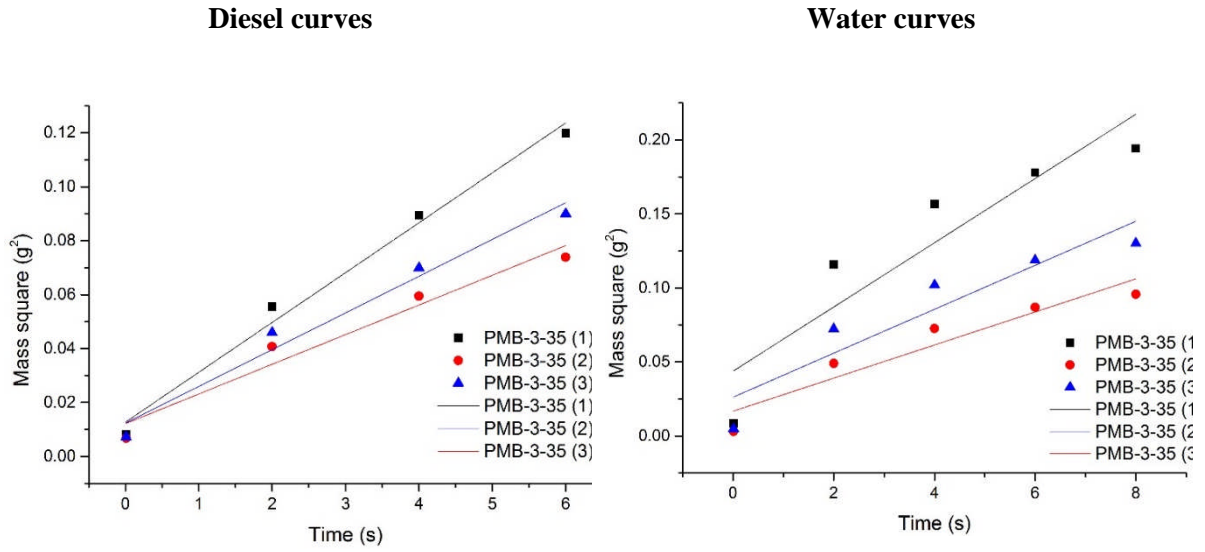


Figure 7-22: Wetting slope of the PMB-3-35 in distilled water and REF diesel (see Table 7-1 for the sample code)

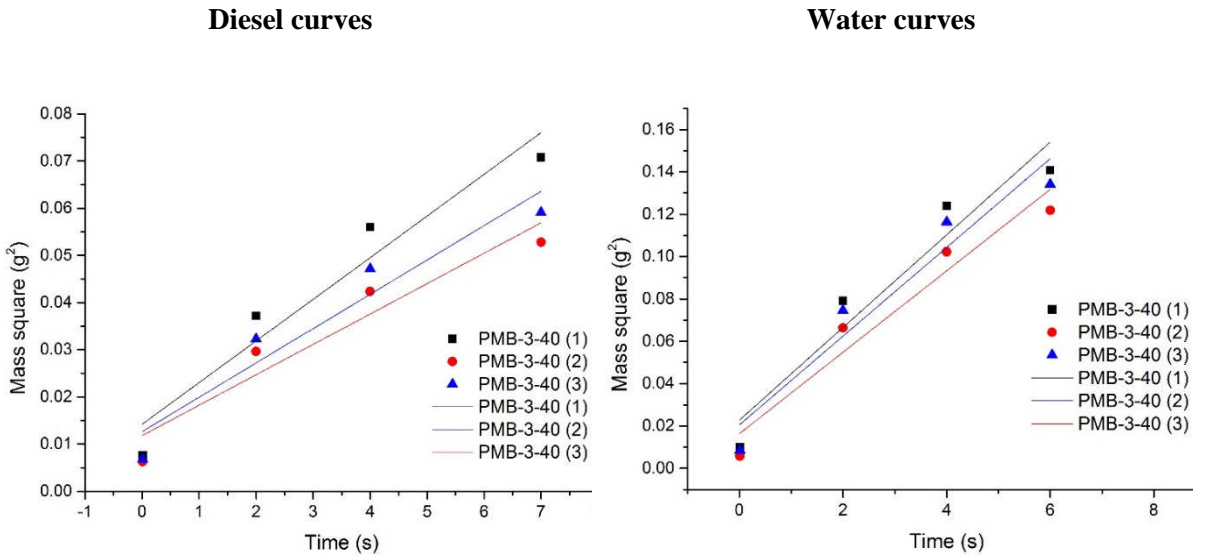


Figure 7-23: Wetting slope of the PMB-3-40 in distilled water and REF diesel (see Table 7-1 for the sample code)

The alkaline hydrolysis treatment resulted in a wider range of wetting behaviour in the PMB meltblown samples (Table 7-5). The negative L/H ratios for PMB and PMB-0-40 is attributable to the hydrophobicity of the material as well as buoyancy forces leading to a negative slope.

As the result, the water curves of the untreated fabrics demonstrate their water repellency. The average slope in the water curves of the PMB-0 samples tended to be closer to negative than the PMB samples, which is consistent with the fact that the PMB-0 samples had a more open structure than the PMPs in the thickness direction, which can be expected to affect the capillary radius and therefore capillary pressure and wicking. The positive L/H ratios are indicative of a high degree of surface hydrophilicity and wetting propensity in the structure compared the negative L/H ratios. Amongst positive L/H ratios, smaller value, e.g. 4.3 for PMB-3-40, denotes better hydrophilicity than greater value, e.g. 918.72 for PMB0.25-40.

Table 7-5: L/H values for test filter fabrics (for codes see: Table 7-1)

ID	S_o	R	S_w	R	L/H
PMB	0.011 ± 0.0005	0.99	-0.00000094 ± 0.00000002	0.96	-148828.08 ± 9250.76
PMB-0-40	0.013 ± 0.0005	0.97	-0.000004 ± 0.0000004	0.93 ± 0.04	-39182.84 ± 5772.76
PMB-0.25-40	0.0117 ± 0.0005	0.97	0.00016 ± 0.00003	0.95 ± 0.02	918.72 ± 125.73
PMB-1-40	0.012 ± 0.002	0.97 ± 0.01	0.007 ± 0.001	0.95 ± 0.05	19.93 ± 0.52
PMB-3-35	0.014 ± 0.002	0.98 ± 0.01	0.016 ± 0.003	0.87 ± 0.01	11.24 ± 0.47
PMB-3-40	0.0075 ± 0.0007	0.93 ± 0.01	0.0207 ± 0.0008	0.94 ± 0.01	4.43 ± 0.26

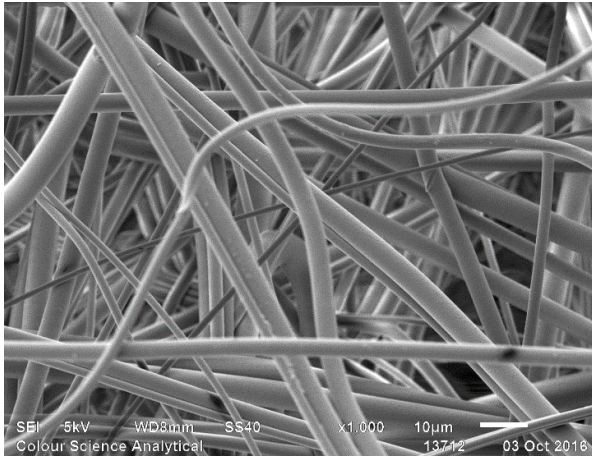
Table 7-6 and Table 7-7 report the dimensional and physical properties of the untreated and alkali-treated PMB filter samples, and Figure 7-24 to Figure 7-29 show typical SEM images from which fibre diameter measurements were made.

Table 7-6: Dimensional and structural properties of the filter fabrics (for codes see: Table 7-1)

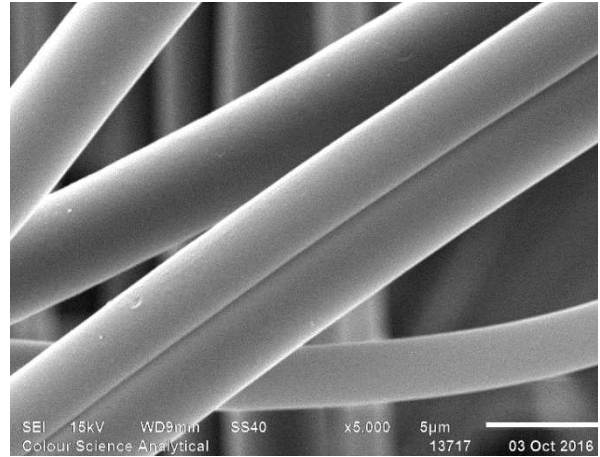
ID.	Area Density ($g \cdot m^{-2}$)	Thickness (mm)	Air Permeability ($l \cdot m^{-2} \cdot s^{-1}$)	Pore size – Bubble point (μm)	Pore size – Mean flow (μm)	Mean fibre diameter (μm)
PMB	228.3 ± 2.14	2.7 ± 0	119.42 ± 1.5	33.6 ± 1.2	8.8 ± 0.2	3.6 ± 0.4
PMB-0-40	225.34 ± 0.11	3 ± 0	130.1 ± 3.45	34.3 ± 1.8	8.6 ± 0.3	3.1 ± 0.2
PMB-0.25-40	229.35 ± 1.25	3.1 ± 0.1	132.8 ± 2.98	35.9 ± 1	8.5 ± 0.1	3.6 ± 0.3
PMB-1-40	231.26 ± 4.91	3.3 ± 0.2	137.67 ± 5.36	34.4 ± 1	8.9 ± 0.1	3.5 ± 0.2
PMB-3-40	232.52 ± 10.98	2.9 ± 0.2	137.5 ± 16.39	34.1 ± 1.3	8.9 ± 0.2	3.6 ± 0.3
PMB-3-35	237.05 ± 5.8	3 ± 0.2	132.25 ± 3.3	34.4 ± 2.2	9 ± 0.1	3.6 ± 0.2

Table 7-7: Bursting strength of the filter fabrics (b) (for codes see: Table 7-1)

Sample	Mean bursting strength ($kPa \pm SE$)	Mean height at burst ($mm \pm SE$)	Mean time to burst ($S \pm SE$)
PMB	351.73 ± 8.88	19.83 ± 0.39	20.42 ± 0.78
PMB-0-40	363.2 ± 16.89	19.53 ± 0.19	21.77 ± 0.72
PMB-0.25-40	351.9 ± 7.53	19.5 ± 0.1	20.27 ± 0.2
PMB-1-40	350.13 ± 10.86	19.6 ± 0.25	21.17 ± 0.37
PMB-3-40	349.75 ± 1.5	19.37 ± 0.09	20.1 ± 0.06
PMB-3-35	348.94 ± 1.95	19.2 ± 0.06	20.1 ± 0.06

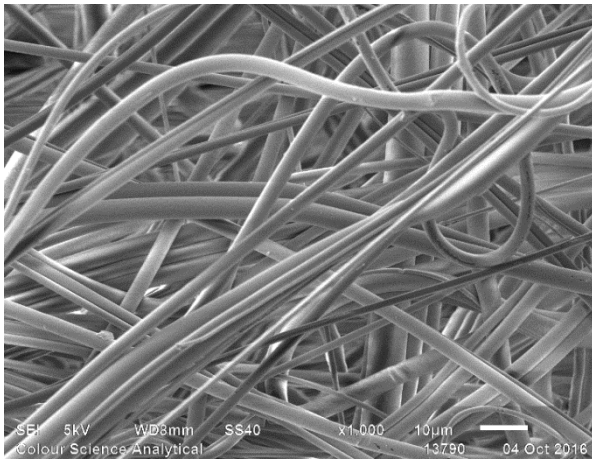


PMB (x1000)

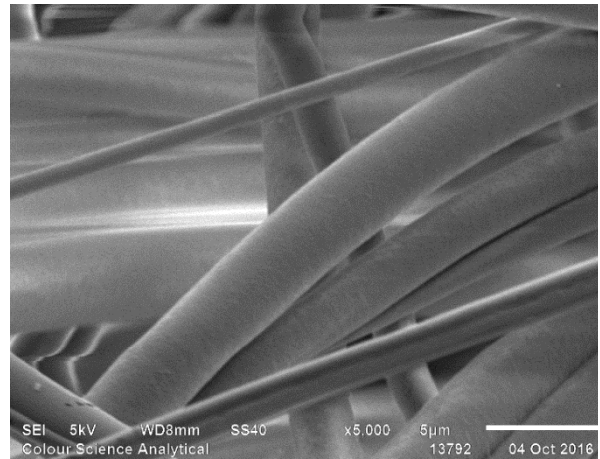


PMB (x5000)

Figure 7-24: SEM images of the untreated PMB sample (see Table 7-1 for the sample code)

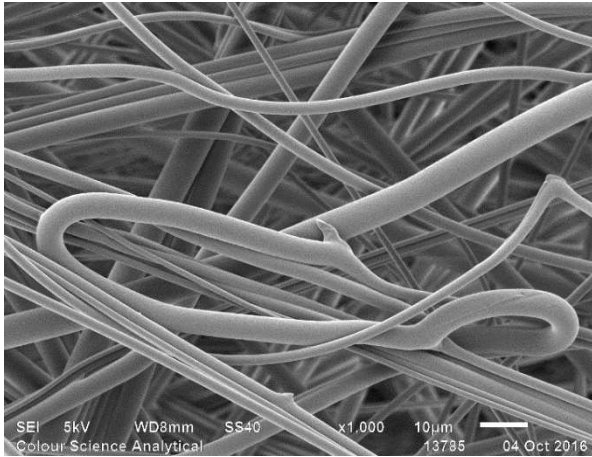


PMB-0 (x1000)

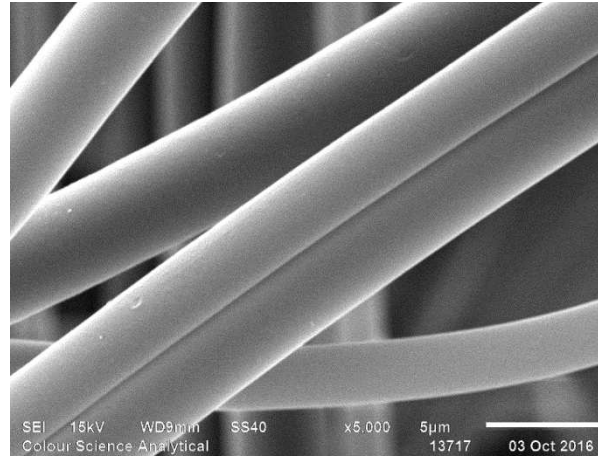


PMB-0 (x5000)

Figure 7-25: SEM images of the PMB-0-40 sample (see Table 7-1 for the sample code)

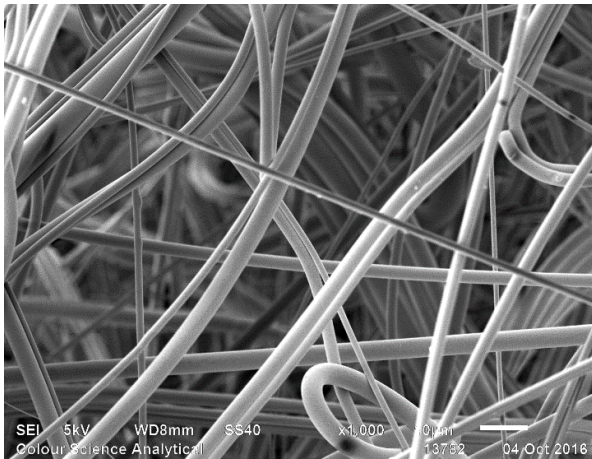


PMB-0.25 (x1000)

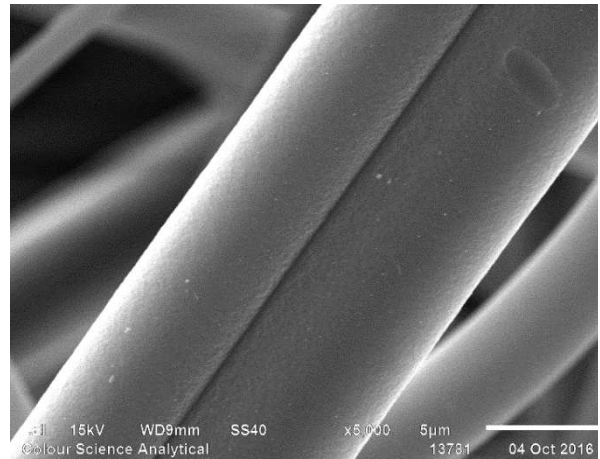


PMB-0.25 (x5000)

Figure 7-26: SEM images of the PMB-0.25-40 sample (see Table 7-1 for the sample code)



PMB-1 (x1000)



PMB-1 (x5000)

Figure 7-27: SEM images of the PMB-1-40 sample (see Table 7-1 for the sample code)

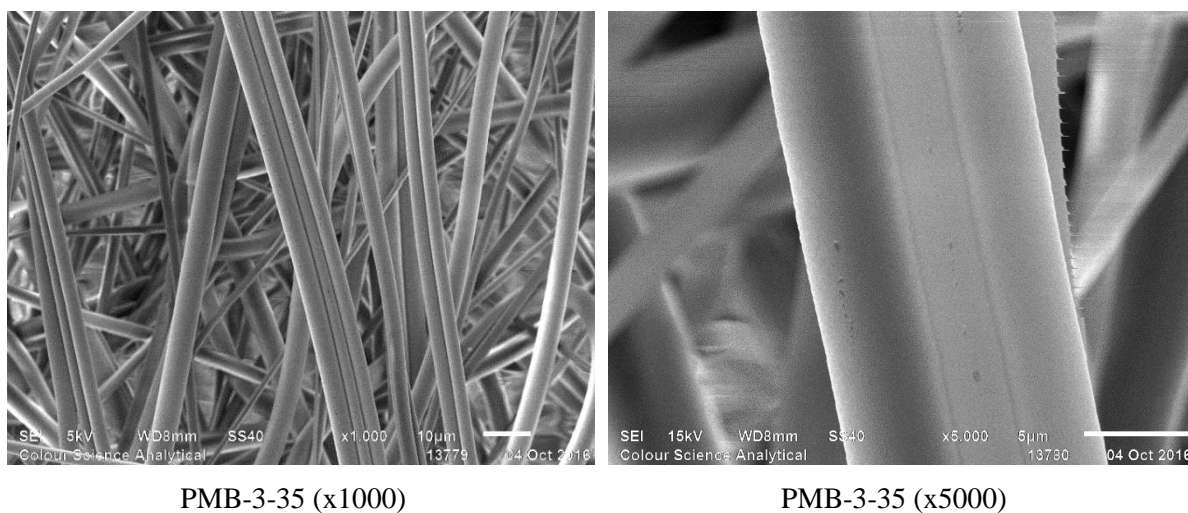


Figure 7-28: SEM images of the PMB-3-35 sample (see Table 7-1 for the sample code)

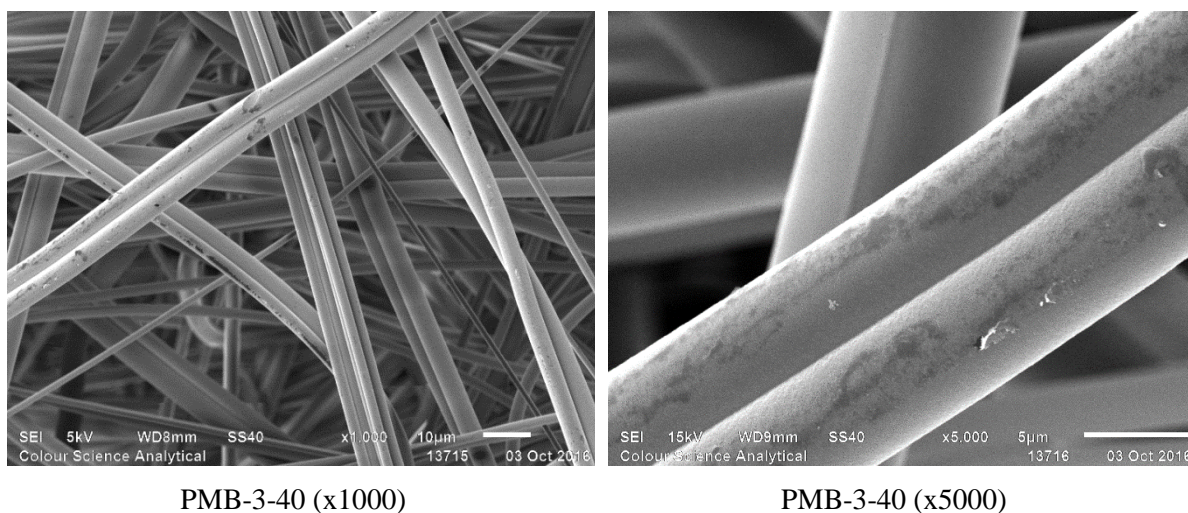


Figure 7-29: SEM images of the PMB-3-40 sample (see Table 7-1 for the sample code)

A single factor ANOVA of the pore size, areal density, and bursting strength data of treated and untreated samples revealed no significant differences between the samples (P -value > 0.05). A t -test analysis of PMB and PMB-0-40 showed only significant differences in thickness (P -value = 0.0008) and air permeability (P -value = 0.004) of the samples at a confidence level of 95%. This was anticipated since no direct changes were made to the structure of the

meltblown samples other than slight structural agitations applied on PMB-0 samples due to the treatment procedure, confirmed by a slight difference in fabric thickness and permeability.

To detect any possible relationship between changes in the structure of the alkali-treated samples and their coalescence performance, all properties of the alkali-treated samples (PMB-0s, PMB-1s, and PMB-3s) were analysed by one-way ANOVA test, which confirmed no significant differences between the PMB-0 samples and the other treated samples (P-value > 0.05). Thus, it could be concluded that NaOH-treatment of the PBT samples did not significantly alter the physical or mechanical properties of the filter fabric, such that any differences in coalescence performance of the samples could be attributed mainly to chemical differences affecting wettability. The SEM images (Figure 7-24) visually showed no noticeable mechanical damage/change on the surface of the treated samples compared to PMB untreated fabric, which is in agreement with the analysis on the structural characterisation results above.

7.4.2 Structural characterisation of the bowing configuration

Table 7-8 show results for the coalescence efficiency, ϵ - Equation 5-4, of the PMB medium using the 3D printed spacer filter supports, compared with the conventional flat filter support.

Table 7-8: Coalescence efficiency of the filter fabric using 3D printed spacer filter support

Sample arrangement	ϵ (%)
Control (black support)	31.5
3D printed convex support	37.5
3D printed flat support	33

Use of a convex filter support design appeared to slightly affect the coalescence efficiency of the filter, however, the effect was very small compared to large increase in efficiency resulting

from the bowing configuration (Section 7.3.2.5). These initial results suggested that the high efficiency obtained in the bowing configuration could be attributed to the dynamic change that takes place in filter's effective porosity, rather than bowing shape per se. This was confirmed with the results of the air-flow and water-flow characterisation works reported in Section 7.3.3. Figure 7-30 demonstrates the changes that took place in the configuration of the filter medium under the pressure of liquid passing through in the water-flow experiment. Figure 7-31 shows examples of the typical bowing deformation that took place in PMB samples (fixed using PVA adhesive). Figure 7-31 also shows the changes in the thickness of the PMB medium as the bowing deformation occurs.

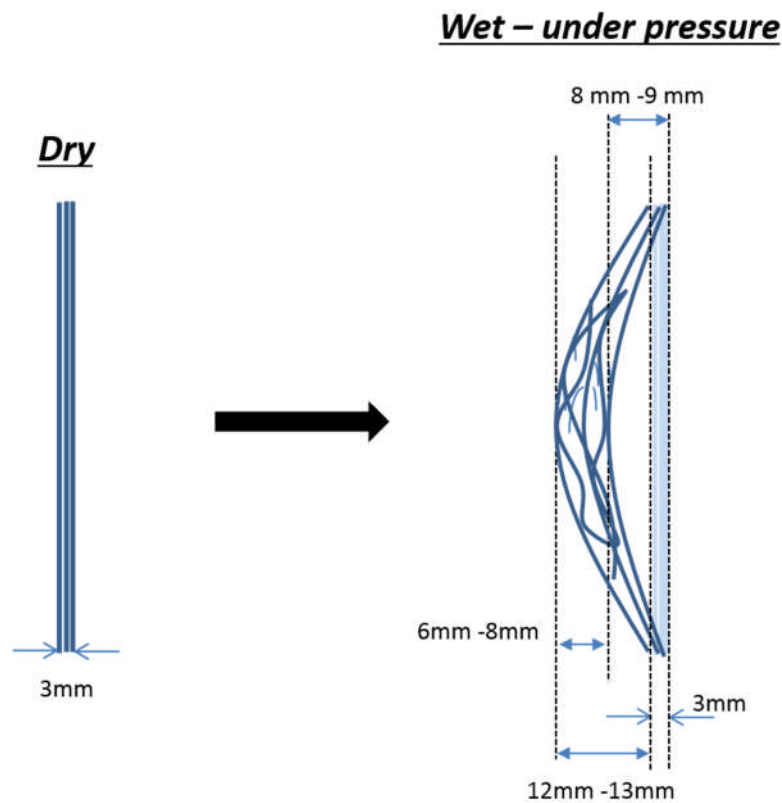


Figure 7-30: Magnitude of filter deformation during the bowing arrangement observed in the water flow-through experiment

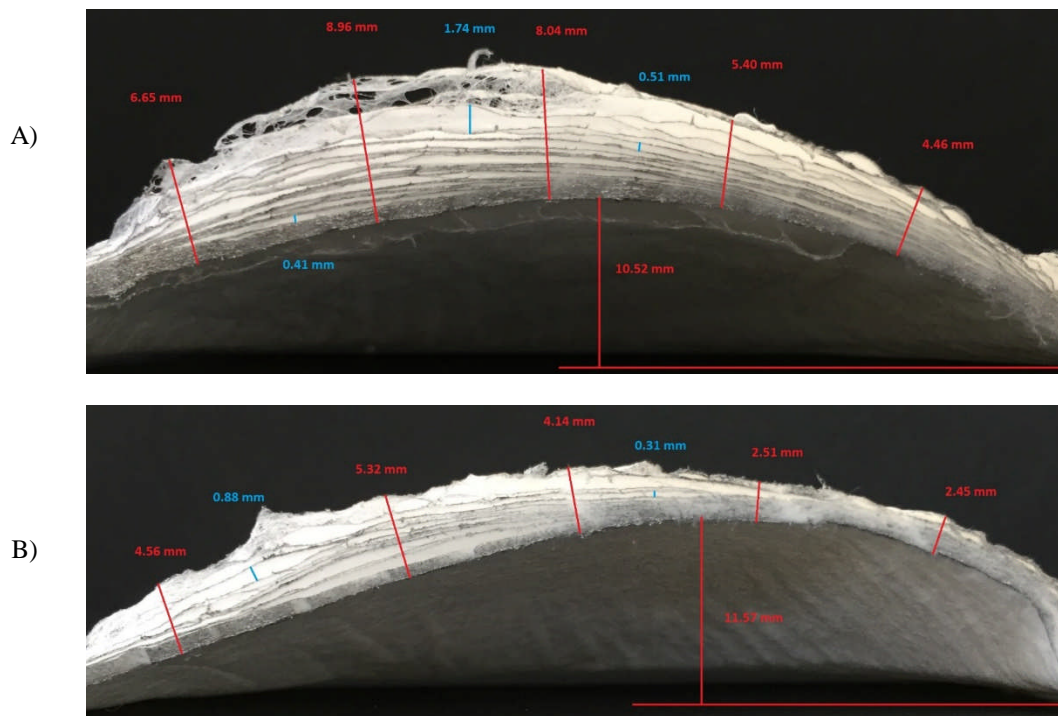


Figure 7-31: Changes in the thickness of the PMB medium as a result of the bowing deformation: performed at air pressure and velocity of A) 11.9 mbar and 44 cm/s, B) 370 Pa and 18 cm/s

The bowing deformation resulting from the use of water as the flowing fluid show that the increase in thickness due to bowing deformation can be substantial. In this case thickness increased from 2.6 mm (Table 7-6) to near 8 mm. This is in agreement with the results of the experiment conducted using compressed air, which showed that the thickness of the flat PMB medium could increase to near 9 mm resulting in an increase in the fabric porosity from 93% to 98% (Table 7-9).

Table 7-9: Structural measurement of the flat and bowed PMB media under dynamic conditions

Sample	density ($\frac{kg}{m^3}$)	bulk ($\frac{m^3}{kg}$)	solidity ($\frac{m^3}{m^3}$)	porosity ($\frac{m^3}{m^3}$)
PMB - flat	86.2	1.1×10^{-2}	0.07	0.93
PMB- bowed	25.4	3.9×10^{-2}	0.02	0.98

This dramatic increase in porosity can be attributed to an intrinsic feature of meltblown media, which have a multi-layered, laminar internal structure, wherein it is possible for the fluid flow to delaminate layers leading to bowing, without breakage or collapse of the fabric.

7.4.3 Coalescing performance of new filter media arrangements

7.4.3.1 Alkali-treated PMB fabrics with increased wettability in a flat configuration

Figure 7-32 to Figure 7-34 and Figure 7-35 to Figure 7-37 report the coalescence efficiency, pressure drop, and quality factor of the alkaline treated PMB samples in the control filter arrangement (flat configuration) as a function of the wettability for the REF and M200 fuels respectively.

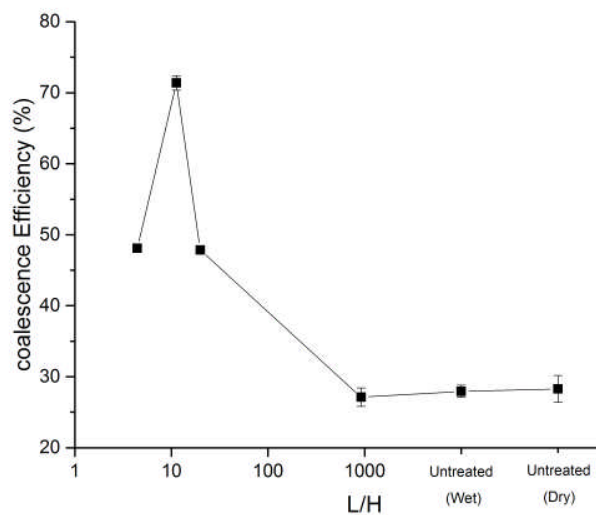


Figure 7-32: Effect of wettability (L/H) on coalescence efficiency of the PMB media using REF diesel fuel (source Table 9-6 in Appendix (A))

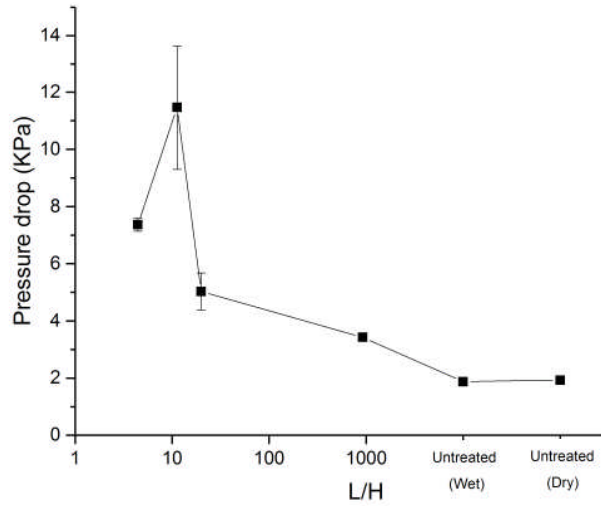


Figure 7-33: Effect of wettability (L/H) on pressure drop of the PMB media using REF diesel fuel (source Table 9-6 in Appendix (A))

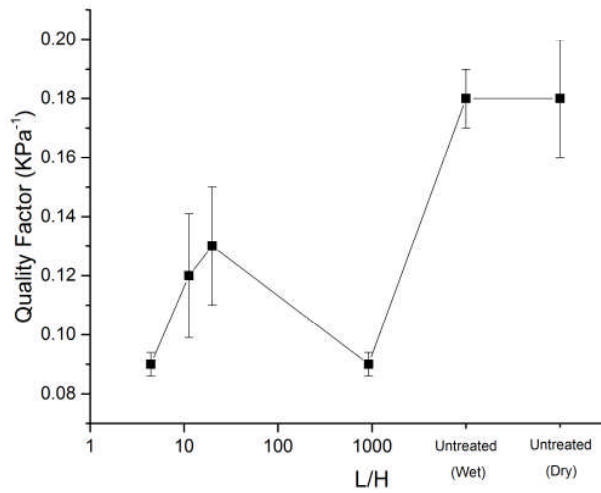


Figure 7-34: Effect of wettability (L/H) on quality factor of the PMB media using REF diesel fuel (source Table 9-6 in Appendix (A))

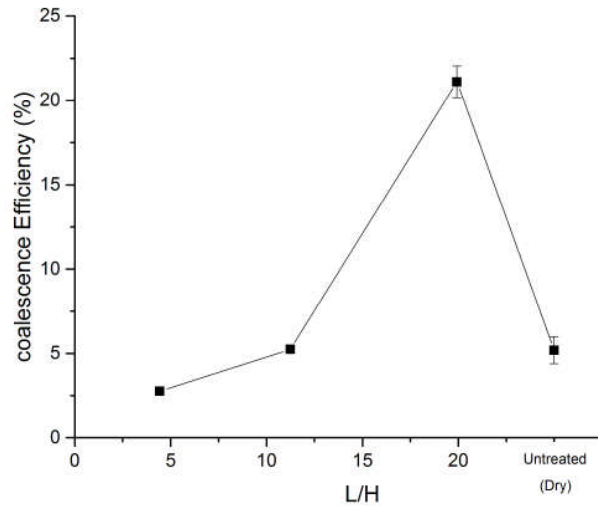


Figure 7-35: Effect of wettability on coalescence efficiency of the PMB media using M200 fuel (source Table 9-7 in Appendix (A))

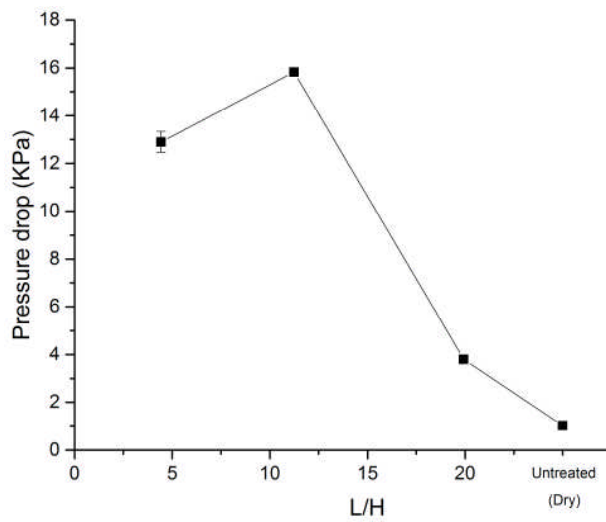


Figure 7-36: Effect of wettability on pressure drop of the PMB media using M200 fuel (source Table 9-7 in Appendix (A))

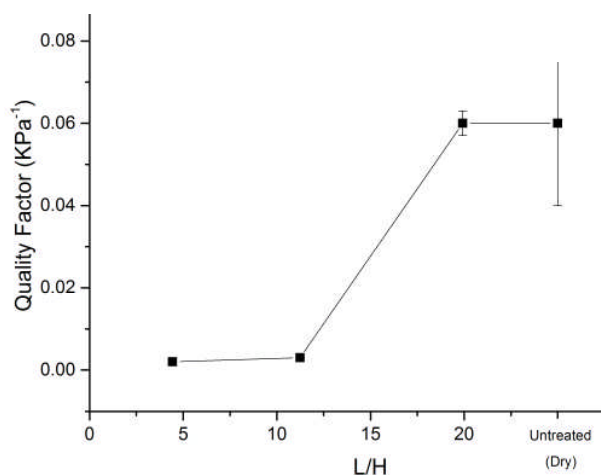


Figure 7-37: Effect of wettability on quality factor of the PMB media using M200 fuel (source Table 9-7 in Appendix (A))

With reference to Figure 7-32 to Figure 7-34, the coalescence efficiency of untreated PMB filter fabrics using the REF fuel was found to increase as the hydrophilicity (L/H) increased, however, the maximum efficiency was obtained at a L/H ratio between 4 and 20 (Figure 7-32 and Table 9-6 in Appendix A). This is in agreement with the belief that optimal coalescence is achieved at an “intermediate” hydrophilicity (see Section 2.6.2.2). However, it is interesting to note that this was not accompanied by an increase in the quality factor (Figure 7-34), because the pressure drop (Figure 7-33) increased due to greater retention of water within the filter. Thus, in practice, increasing the wettability of fibres alone is not a satisfactory approach because of the increase in the pressure drop as the optimum hydrophilicity for coalescence is approached ($4 < L/H < 20$). Referring to Figure 7-38, such filters with the ability to enhance coalescence also promote the formation of large droplets due to the increased work of adhesion (W_A in Section 2.4.2.2) and they become so well attached that they are not easily removed (Figure 7-38 c). Consequently, the water droplets retained by the filter occupy the internal void space leading to an increase in the pressure drop. By further increasing the hydrophilicity, $L/H=4.43$, the work of adhesion as well as work of spreading, W_S (Section 2.4.2.2), are further

increased such that the captured droplets spread more readily throughout the fibrous network (Figure 7-38 b). In this case, there is likely to be re-emulsification due to the reduction in the Laplace pressure (see Section 2.3.1.3) and a larger droplet curvature. Additionally, under these circumstances fewer incoming droplets will be captured such that the pressure drop (Figure 7-33) and the coalescence efficiency (Figure 7-32) are found to decrease.

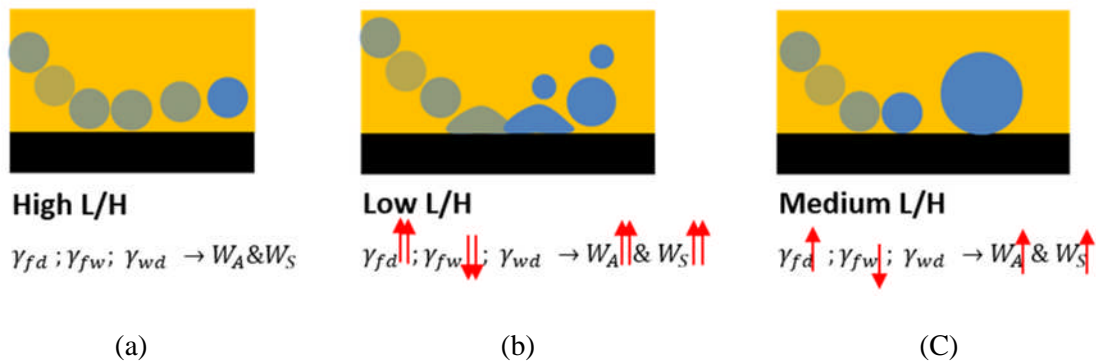


Figure 7-38: Schematic of the water droplet interactions that are believed to take place with fibre surfaces of low (a), high (b), and medium (c) hydrophilicity, when immersed in REF diesel fuel. Where, γ_{fd} , γ_{fw} , γ_{wd} , W_A , and W_S are the interfacial tensions of fibre-diesel, fibre-water, water-diesel, work of adhesion, and work of spreading respectively

In the presence of surfactant, which occurs using the M200 fuel (Figure 7-35 to Figure 7-37), increasing the fibre wettability up to a L/H ratio of 20, results in bigger water droplets and an increase in the pressure drop (Figure 7-33 and Table 9-7). However, when the hydrophilicity was high, lower coalescence efficiency and increases in high pressure drops, of up to 55% observed in terms of the static pressure downstream of the medium at a L/H ratio of 11 and 4 (Figure 7-33 and Table 9-7 in Appendix A). This can be attributed to a sharp increase in both the work of adhesion and the work of spreading within the fabric due to an increase in the surface energy of the fibres as a result of surface modification by the Alkali treatment as well as reduction in the interfacial tension of the water droplets as a result of surfactant molecules (Figure 7-39). This results in retention of water inside the medium as well as further drop in

liquid spreading which leads to a greater pressure drop and re-emulsification of small droplets resulting in low coalescence efficiency.

Comparing the results of the REF and M200 fuels in Figure 7-32 to Figure 7-34 and Figure 7-35 to Figure 7-37, it can be concluded that the maximum coalescence efficiency for the same filter medium is achieved over different hydrophilicity ranges. For the REF, the preferred range is therefore $L/H \approx 11$ and for M200, the preferred value of $L/H \approx 20$. This highlights the practical challenge that exists in engineering a universally applicable high performance coalescing medium based solely on the modulation of fibre hydrophilicity.

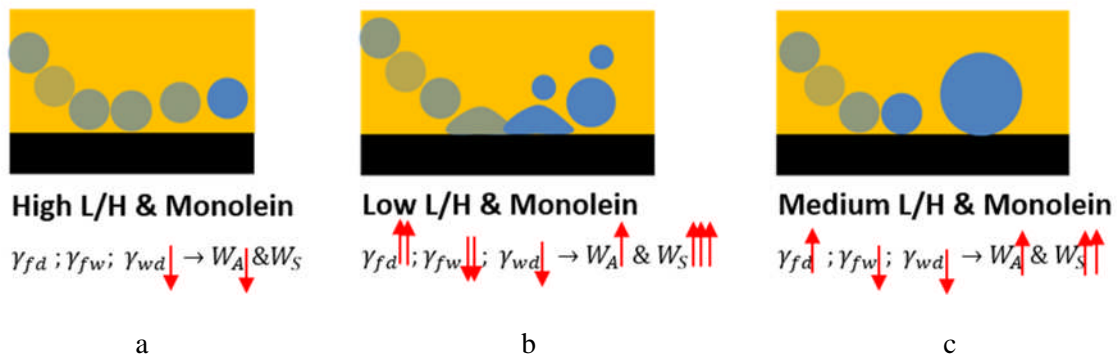


Figure 7-39: Schematic of water droplet interactions with the fibre surface with a low (a), high (b), and medium (c) hydrophilicity, immersed in a monolein blended diesel fuel (M200), where $\gamma_{fd}, \gamma_{fw}, \gamma_{wd}, W_A$, and W_S are the interfacial tension of fibre-diesel, fibre-water, water-diesel, work of adhesion, and work of spreading respectively

7.4.3.2 Untreated PMB filter fabrics in the bowing configuration

Table 7-10 and Table 7-11 report the average coalescence efficiencies, ε - Equation 5-4, and quality factor, QF - Equation 5-5, of untreated PMB filter fabrics in the flat and bowing configurations respectively.

Table 7-10: Coalescence efficiency of the untreated PMB in the flat configuration for different fuel blends

Test fuel	ΔP_0 (kPa)	ΔP_{20} (kPa)	$\Delta P_{20} - \Delta P_0$ (kPa)	ε (%)	QF
REF	25.37 ± 0.4	27.33 ± 0.41	1.93 ± 0.1	28.28 ± 1.885	0.18 ± 0.02
B5	23.6 ± 0.06	25.07 ± 0.03	1.47 ± 0.03	6.22 ± 0.15	0.031 ± 0.0037
B20				<1	
B50				<1	
M200	28.7 ± 0.3	29.73 ± 0.47	1.03 ± 0.17	5.19 ± 0.801	0.058 ± 0.0204
M325				<1	
M400				<1	

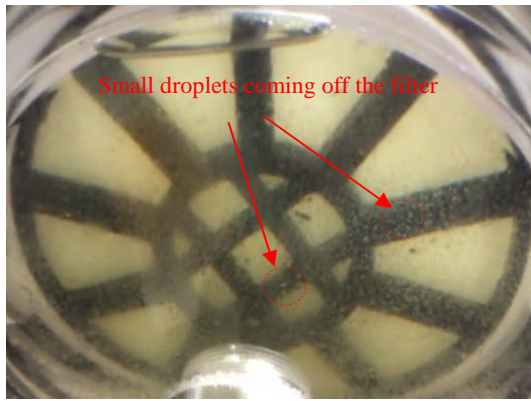
Table 7-11: Coalescence efficiency of the untreated PMB in the bowing configuration for different fuel blends

Test fuel	ΔP_0 (kPa)	ΔP_{20} (kPa)	$\Delta P_{20} - \Delta P_0$ (kPa)	ε (%)	QF
REF	23.4 ± 0.17	24.3 ± 0.12	0.85 ± 0.1	69.75 ± 2.302	1.562 ± 0.2615
B5	22.13 ± 0.03	22.4 ± 0.06	0.27 ± 0.07	53.03 ± 2.134	3.099 ± 0.5327
B20	22.37 ± 0.19	22.73 ± 0.17	0.37 ± 0.03	45.97 ± 1.169	1.702 ± 0.1259
B50	22.53 ± 0.09	23.5 ± 0.06	0.97 ± 0.15	7.37 ± 0.434	0.082 ± 0.01
M200	27.23 ± 0.15	27.8 ± 0.15	0.57 ± 0.07	54.43 ± 2.142	1.442 ± 0.2222
M325	21.53 ± 0.03	21.87 ± 0.03	0.33 ± 0.03	32.41 ± 0.473	1.198 ± 0.1166
M400	21.53 ± 0.09	21.63 ± 0.11	0.1 ± 0.04	28.37 ± 0.466	2.75 ± 0.5131

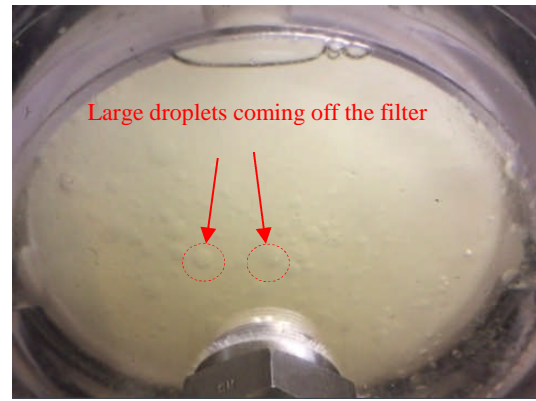
Referring to the data in Table 7-10, the fabrics evaluated in the conventional flat configuration were completely disarmed in B20, B50, M325, and M400, i.e. their initial wetting characteristics as well as media structure were not instrumental in controlling associated coalescence efficiency – because of the effect of the fuel. In practice, this meant that no settled water could be observed in the collection bottle during testing. However, the results for samples

measured using the same fuels but in the bowing configuration (Table 7-11) were substantially improved in terms of water coalescence efficiency.

It was apparent that bowing of the fabric greatly enhances the coalescence efficiency irrespective of the fuel blend, and whether or not bio-diesel or monoolein was present. Remarkably, this was also associated with a corresponding improvement of the quality factor when challenged with fuel blends containing surfactants. This impressive improvement is of great practical significance because of the possibility to provide a universal filter media. The observed effects can be attributed to the increase in the porosity of the filter (P=98%) as it bows during dynamic operation, as compared to the initial flat state, (93%) (Section 7.4.2). In the bowing configuration, the internal layers of the meltblown are partially delaminated due to the forced flow such that each layer is able to act as an independent coalescing medium, maintaining the efficiency of small water droplet capture. The coalesced droplets do not so readily blind the pore volume of the filter because of the increased porosity, and the transport of large droplets through the structure for collection appeared to be enhanced as a result of the large pore sizes. Thus, the larger pores resulting from bowing appeared to provide transport channels for the coalesced droplets to facilitate their transport from one side to the other without re-emulsification or excessive retention, avoiding a large pressure drop. Therefore, much larger water droplets were seen to fall out of the bowed configuration during the coalescence test (Figure 7-40), leading to a low pressure drop and much higher quality factor.



Flat configuration



Bowing configuration

Figure 7-40: Comparison between coalesced water droplets coming off the flat and bowing filter configurations at a same filtration test condition

Owing to the discovery of the remarkable benefits of promoting a bowing configuration in relation to coalescence efficiency and pressure drop, a further study was conducted to determine technical routes for industrial exploitation of the effect, as explained in Appendix B. In Appendix B, reinforcement of the medium in the bowing configuration is discussed to demonstrate feasible routes for scaling up of the new configuration.

7.5 Summary

In this chapter, experimental work was conducted to study the coalescence performance of poly(butylene terephthalate) (PBT) meltblown nonwoven filter fabrics with modified wetting characteristics achieved by alkaline hydrolysis. In so doing, fibre surface properties were modified independently of fabric structure. Additionally, the effects of geometrical modifications to the filter medium were also explored, and in particular dynamic deformation of the filter fabric due to the forced flow conditions existing during the coalescence process were exploited to induce bowing. Remarkably, inducing a bowing configuration of the fabric

was found to increase the coalescence performance by almost 150% compared to the conventional flat configuration that is currently used in practice.

The coalescence efficiency and the quality factor of alkaline treated fabrics were analysed as a function of their wettability using the purpose-built coalescence test rig using both the REF and M200 diesel fuels. Although a maximum coalescence efficiency could be achieved at a particular L/H ratios and fibre hydrophilicity, the quality factor of the untreated (hydrophobic) samples remained significantly higher ($P > 0.001$) than the hydrophilic alkali treated variants. The reduction in the quality factor in the case of alkali treated media was even more pronounced in the presence of surfactants present in the fuel. This was attributed to water droplets being retained by the filter resulting in an increased pressure drop and re-emulsification in water. It was also established, that optimal wetting behaviour of fibres were consistent with achieving maximal coalescence efficiency is not the same for REF diesel and M200 fuel. This suggests that a universal filter medium with a high coalescence performance cannot rely solely on tuning fibre wetting properties.

In relation to the coalescence efficiency of the same fabric operating in a bowing configuration, remarkably high coalescence efficiency was obtained for the REF diesel, bio-diesel and monoolein blends. This was attributed to the increase in fabric porosity 93% to 98% that results from partial delamination of the fabric under dynamic conditions, which provides greater volume for the accommodation and transport of large water droplets. Also noteworthy is that the bowing configuration also assisted coalescence efficiency in fuels blended with surfactants for both untreated and alkali-treated samples - conditions that were found to disarm the ability of the fabric to coalesce when presented in a flat configuration.

CHAPTER 8

Conclusions

8.1 General Conclusion

Fuel-water coalescing filters are crucially required in diesel engines to reduce the maximum total water content of diesel to a value acceptable by the Original Equipment Manufacturers (OEMs). The ISO and SAE water separation test methods evaluate water separator filters using a reference grade diesel fuel whose properties are modulated by blending surfactant in the form of monoolein as a surrogate for bio-diesel and other fuel additives. However, there is no universally applicable filter that can fully satisfy current industrial requirements because of differences in fuel additive compositions (bio-diesel and surfactants) as well as water content of the fuel from one region to another. Meltblown nonwoven fabrics are promising structure for use as coalescing media due to their small mean fibre diameter and high solid surface area for capturing water droplets from a fuel stream. Therefore, if these characteristics together with high porosity can be designed in relation to characteristics of fuel and water-in-fuel emulsion then there is an opportunity to produce enhanced universal coalescing media for use in separation of water from standard fuel in new diesel engines.

Initially, the properties of reference grade fuel influenced by addition of bio-diesel and monoolein were investigated in Chapter 3 and this provided evidence that the effects of adding monoolein and bio-diesel to a reference fuel are therefore not the same. The interfacial tension (IFT), dissolved water content and viscosity of bio-diesel blends are substantially affected by addition of bio-diesel, even at low concentrations of only 5% (v/v). However, by contrast, addition of monoolein was only found to affect the IFT of the fuel. It was established that monoolein does not saturate the interface of water and fuel at an IFT higher than 2 mN/m , while the interface reaches saturation point in fuels containing more than 20% bio-diesel, i.e.

>B20, such that the IFT of the fuel blends is maintained between 12 and 13 mN/m even in the case of B100. This can be attributed to the molar ratio of the bio-diesel in the fuel blends, which is much greater than monoolein in the monoolein blends. Whilst the fuel properties of blends containing bio-diesel or surfactants have been reported before, this research provided comparative data on fuel properties associated with blends of diesel/bio-diesel and diesel/monoolein. This is particularly important given the widespread use of monoolein in the ISO and SAE water separation test methods.

Having successfully characterised bio-diesel and monoolein blends, the properties of emulsified water in these blends were further investigated in Chapter 4. It was important to determine how the water droplet size distribution (DSD) changes when a water-in-fuel emulsion is generated in bio-diesel and monoolein blends. Accordingly, a bespoke emulsion generation test rig was constructed and online measurements of water DSDs in diesel containing bio-diesel and monoolein were undertaken. Water separation was also evaluated using the DSEP rating and sedimentation tests.

It was established that although bio-diesel acts like monoolein as a surface active agent reducing the fuel IFT and stabilising water droplets, bio-diesel blends and emulsions are capable of maintaining a low IFT measured by tensiometry. However, this does not happen for monoolein blends due to differences in the molar ratios. This coupled with the higher viscosity in a bio-diesel blend leads to smaller water droplet sizes compared to monoolein blends. The effect of the static pressure on DSD was tested by applying 4 bar pressure on the fuel blends in the emulsion rig, revealing that higher pressures lead to a decrease in the droplet size of the emulsion, which is independent of the type of additive (bio-diesel or monoolein).

In existing test standards, specifically ISO 16332 and SAE J1488, emulsions are characterised using the DSEP rating. It was appeared that this technique is ineffective as an accurate method of evaluating water separation in diesel fuels containing surfactants. Based on the experimental data herein, evaluating the DSD of an emulsion is thought to be a more useful measure to control surfactant levels in fuel blends rather than the DSEP rating, water sedimentation, and IFT measurements.

Following the results reported in Chapter 3 and Chapter 4, questions about the suitability of monoolein as an appropriate fuel additive for the test standard were raised, because it does not behave comparably with bio-diesel. Therefore, to evidence coalescing performance of nonwoven water separator media in bio-diesel and monoolein blends, the design and development of a new coalescence rig was reported in Chapter 5. The rig composed of a carefully designed filter housing that allowed dynamic observation of water droplet removal, and procedures for determining coalescence and separation efficiencies of flat-sheet nonwoven media were developed based on existing standard methods. All components of the rig were made from materials compatible with diesel and bio-diesel fuel and water content and IFT measurements were designed to be conducted offline. The validation study confirmed that reliable have been obtained for efficiency measurements undertaken with different nonwoven filter media throughout.

In parallel to the fuel and emulsion studies, industrially sourced coalescence filter samples were characterised in Chapter 6 regarding their configuration as well as their separation and coalescing performance. This provided an understanding about structure of existing multilayer nonwoven depth coalescing filter media and the associated effects on separation and coalescence efficiencies. Four filters denoted as WB, B16, B41, and B45 were evaluated regarding their polymer identity, area density, thickness, air permeability, pore size, fibre

diameter, wetting tension, bulk and porosity. The separation and coalescence efficiencies of the media were evaluated using the purpose-built coalescence test rig using reference grade diesel fuel.

The characterisations confirmed that the media were composed of multilayer PET spunbond and PBT meltblown, evidenced by FTIR and DSC, with hydrophobic surface properties, confirmed by a wetting tension test. The media were employed thin bonded fabrics with thicknesses less than $500\ \mu\text{m}$ and mean flow pore sizes less than $25\ \mu\text{m}$, mainly intended for capturing water droplets. They also had thicker fluffy layers with thicknesses about 3 to 4 mm and mean flow pore sizes about $50\ \mu\text{m}$ functioning as coalescers. High separation efficiency, i.e. more than 99%, measured for all the filters highlighted the contribution of the barrier mesh installed in the filter housing for this test. Accordingly, the coalescence efficiency tests were conducted on the filters showing similar coalescence performances ($P = 0.36$, $\alpha = 0.05$) despite different layer arrangements. Amongst filters, the B16 sample showed the best quality factor, ($QF = 2.01$), owing to its open structure, i.e. it has no bonded layer in its structure. Consequently, it was established that the coalescence performance of media originates from the bulky non-bonded layers (coalescers).

Finally, having successfully conducted the fuel, emulsion, and benchmark study as well as constructed a reliable coalescence test rig, the coalescence performance of non-bonded PBT meltblown nonwoven filter fabrics was studied in Chapter 7 regarding their surface wetting and structural characteristics. The surface modifications were achieved by alkaline hydrolysis so that fibre surface properties were modified independently of fabric structure. For the first time, in this research the configurational modifications to the filter medium was in particular dynamic deformation of the filter fabric due to the forced flow conditions existing during the

coalescence process. This was exploited to induce bowing and eliminate filter compression against the filter support which normally occurs in the industrial application.

The coalescence efficiency and the quality factor of alkaline treated fabrics were analysed as a function of their wettability using the purpose-built coalescence test rig using both the REF and M200 diesel fuels. The quality factor of the untreated (hydrophobic) samples remained significantly higher ($P > 0.001$) than the hydrophilic alkali treated variants even though a maximum coalescence efficiency could be achieved at a particular L/H ratios and fibre hydrophilicity. The presence of surfactants present in the fuel deteriorated the quality factor more in the case of alkali treated media. It was established, that water droplets being retained by the filter resulting in an increased pressure drop and re-emulsification in water. For the first time, this research established, that optimal wetting behaviour of fibres consistent with achieving maximal coalescence efficiency is not the same for REF diesel and M200 fuel. This suggests that a universal filter medium with a high coalescence performance cannot rely solely on tuning fibre wetting properties.

In relation to the coalescence efficiency of the same fabric operating in a bowing configuration, remarkably high coalescence efficiency, i.e. by almost 150% compared to the conventional flat configuration, was obtained for the REF diesel, bio-diesel and monoolein blends. It was established, that the fabric porosity increased from 93% in the flat configuration to 98% in the bowing configuration that results from partial delamination of the fabric under dynamic conditions. This provides greater volume for the accommodation and transport of large water droplets. Also for the first time, in this research the bowing configuration assisted coalescence efficiency in fuels blended with surfactants that were found to disarm the ability of the fabric to coalesce when presented in a flat configuration.

8.2 Recommendations for further work

To further understand water-fibre interactions in coalescing process for fuel-water separation application and provide greater understanding of coalescing performance of nonwoven fuel-water separators in real practical environments, the following additional areas of research can be identified:

- Study of bio-diesel and monoolein at the molecular level to characterise resistance they induce to coalescence of water droplets.
- The fuel and emulsion study provided herein was conducted at room temperature. In practice, this can be the temperature at which the challenging water separation could happen, i.e. starting the engine after not being operated for a long time (e.g. at the morning). The challenging water separation also could happen at a higher temperature, e.g. when the engine is refuelled and water enters the warm fuel. Therefore, the same fuel and emulsion study conducted in this work could be employed at a higher temperature, e.g. 40°C, to characterise bio-diesel and monoolein blends in the similar situations.
- The current study provided a comprehensive analysis on coalescence performance of PBT meltblown media using fresh bio-diesel and monoolein blends. Further to the coalescence efficiency profile, using aged fuel blends would be of interests in future studies to assist understanding effects of fuel properties on the media performance.
- The current study provided a robust and reliable test stand required to measure separation/coalescence efficiency of flat-sheet fuel-water separator media for research and product development purposes. This instrument is design to circulate fuel through a medium at room temperature. There is scope to develop this instrument in order to be more flexible in modulating fuel temperature to simulate a real filtration condition in a test.

- Further to the design of the coalescence test rig, it can be improved to vibrate filter housing during the test and to simulate the same condition for the filter that occurs in a vehicle.
- The current study provided a novel analysis of media structure, and the bowing configuration was evidenced to be remarkably instructive to improve coalescence efficiency in different fuel blends compare to untreated and alkali-treated media in the flat configuration. Testing alkali-treated media in the bowing configuration would further help to design a universal media structure for fuel-water separation.
- The current work provided a comprehensive experimental data in relation to coalescence performance of nonwoven structure in separation of emulsified water in diesel fuel blended with surfactants. These results could be exploited for computer simulations to assist design of enhanced coalescing water separators.
- Ultimately, employing the same research methodology to test other types of coalescing filters such as pleated wetlaid composite media may provide a route to identify optimum structure and properties of these media in relation to coalescence performance.

Appendix (A)

Source Tables of the Figures Presented In the Text

Table 9-1: Interfacial tension (IFT) of the test fuels

Test Fuel	IFT ($mN/m \pm SE$)	Test Fuel	IFT ($mN/m \pm SE$)
REF	31.24±0.73	M200	18.8 ± 0.21
B5	17.37±0.38	M325	12.75 ± 0.15
B10	14.38±0.11	M400	11.4 ± 0.21
B15	13.23±0.12	M600	6.05 ± 0.13
B20	12.94±0.1	M1000	2.18 ± 0.12
B30	12.35 ± 0.1		
B50	12.31±0.23		
B100	13.17±0.13		

Table 9-2: Water content of the test fuels

Test Fuel	Water content ($ppm(\frac{v}{v}) \pm SE$)	Test Fuel	Water content ($ppm(\frac{v}{v}) \pm SE$)
REF	49.13±2.79	M200	50.28±4.45
B5	54.94±4.1	M325	50.97±3.95
B10	68.47±4	M400	50.97±3.95
B15	79.2±0.88	M600	51.74±2.71
B20	90.34±3.03	M1000	51.06 ± 1.6
B30	123.78 ± 3.4		
B50	183.16±11.65		
B100	403.94±24.89		

Table 9-3: Water saturation level values of the bio-diesel blends

Test Fuel	Saturation level (ppm($\frac{v}{v}$) \pm SE)
REF	46.84 \pm 1.53
M400	48.13 \pm 2.31
B5	84.3 \pm 1.49
B50	400.77 \pm 11.8
B100	1186.67 \pm 25.69

Table 9-4: Density values of test fuels at 25°C

Test Fuel	Density (kg/m³)	Test Fuel	Density (kg/m³)
REF	829.07	M400	829.05
B5	831.33	M1000	829.13
B10	834.12		
B15	836.38		
B20	838.97		
B50	853.61		
B100	878.17		

Table 9-5: Kinematic and dynamic viscosity values of the test blends at 25°C

Test Fuel	Kinematic viscosity (mm^2/s)	Density (kg/m^3)	Dynamic viscosity ($mPa \cdot s$)
REF	4.137	829.07	3.43
B5	4.140	831.33	3.44
B20	4.424	838.97	3.71
B50	5.313	853.61	4.54
B100	6.561	878.17	5.76
M400	4.079	829.05	3.38
M1000	4.027	829.11	3.34

Table 9-6: Coalescence efficiency of the untreated and alkali-treated PMB media measured in the flat configuration using the REF diesel fuel (see Table 7-1 for the sample code)

ID.	ΔP_0 (kPa)	ΔP_{20} (kPa)	$\Delta P_{20} - \Delta P_0$ (kPa)	ε (%)	QF
PMB	-148828.08 \pm 9250.76	25.37 \pm 0.4	1.93 \pm 0.1	28.28 \pm 1.885	0.18 \pm 0.02
PMB-0-40	-39182.84 \pm 5772.76	24.64 \pm 0.1	1.88 \pm 0.04	27.93 \pm 0.858	0.18 \pm 0.01
PMB-0.25-40	918.72 \pm 125.73	25.6 \pm 0.06	3.43 \pm 0.03	27.12 \pm 1.297	0.09 \pm 0.004
PMB-1-40	19.93 \pm 0.52	25.07 \pm 0.37	5.03 \pm 0.65	47.87 \pm 0.329	0.13 \pm 0.02
PMB-3-35	11.24 \pm 0.47	26.37 \pm 1.32	11.47 \pm 2.17	71.38 \pm 1.021	0.12 \pm 0.021
PMB-3-40	4.43 \pm 0.26	26.7 \pm 0.1	7.37 \pm 0.23	48.1 \pm 0.433	0.09 \pm 0.004

Table 9-7: Coalescence efficiency of the untreated and alkali treated PMB media in the flat configuration using the M200 fuel (see Table 7-1 for the sample code)

ID.	L/H	ΔP_0 (kPa)	$\Delta P_{20} - \Delta P_0$ (kPa)	ε (%)	QF
PMB	-148828.08 ± 9250.76	28.7 ± 0.3	1.03 ± 0.17	5.19 ± 0.801	0.06 ± 0.02
PMB-1-40	19.93 ± 0.52	24.17 ± 0.09	3.8 ± 0.12	21.11 ± 0.93	0.06 ± 0.003
PMB-3-35	11.24 ± 0.47	29 ± 01	15.83 ± 0.09	5.24 ± 0.204	0.003 ± 0.0001
PMB-3-40	4.43 ± 0.26	23.3 ± 01	12.9 ± 0.44	2.77 ± 0.066	0.002 ± 0.0001

Appendix (B)

Reinforcement of the Bowing Configuration

Following to the discovery of the bowing configuration and its remarkable role in relation to coalescence efficiency and pressure drop, and further to the structural characterisation of the bowing configuration discussed in Section 7.3.3, reinforcement of the medium structure in this configuration was studied in this section. As explained in Section 6.2, coalescing filter media are wound on to a robust plastic cylindrical support mesh (centre core) to ensure robust structure of the filter during its lifetime. Therefore, the rationale of the experiment was to initiate a feasibility study on determining technical routes for industrial exploitation of the bowing configuration as durability of the structure is ensured. Details of the different filter assemblies and evaluation methodologies will now be explained.

10.1 Dynamic porosity with back support: single layer of PMB media with upstream filter support

A 100 cm² support disk (Figure 10-1) was manufactured from PMMA (Perspex) sheet of 5 mm thickness, and cut to the same size as the filter fabric using the same Laser cutter explained in Section 7.3.2.3.

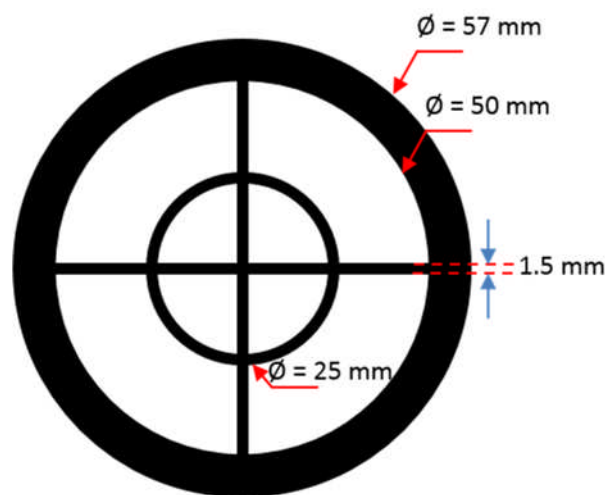


Figure 10-1: Design details of the filter support

The disk was intended to be placed at upstream of the filter medium and upstream layer of the medium was carefully stitched to the support (Figure 10-2) without disturbing the medium structure.



Figure 10-2: Dynamic porosity arrangement with back support

Once the media is assembled in the filter housing (see Section 5.3.1) and fuel is passing through, the bowing configuration is formed while the upstream side of the medium is supported accordingly (Figure 10-3).

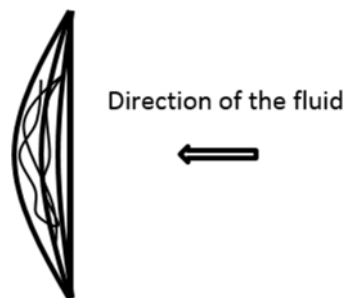


Figure 10-3: The bowing configuration in dynamic porosity arrangement with back support

The coalescence efficiency test (Section 5.5.3) was performed on this structure to ensure the high efficiency associated with the bowing configuration (control dynamic porosity) - see Section 7.4.3.2 - is maintained while the structure is supported.

10.2 Local dynamic porosity: single layer of PMB media with reinforced configuration via local stitches

In this configuration, no filter support was used, however, the filter medium was reinforced as it was stitched through its thickness at the same locations as in the dynamic porosity with back support (Figure 10-4 and Figure 10-2).

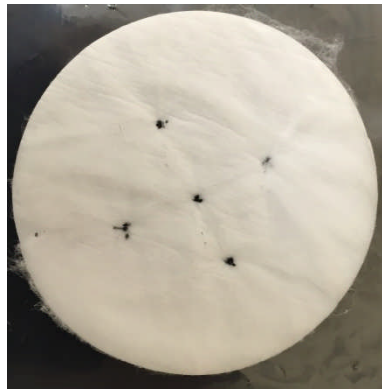


Figure 10-4: Local dynamic porosity arrangement

Once the media is assembled in the filter housing (see Section 5.3.1) and fuel is passing through, the local bowing configuration is formed (Figure 10-5).

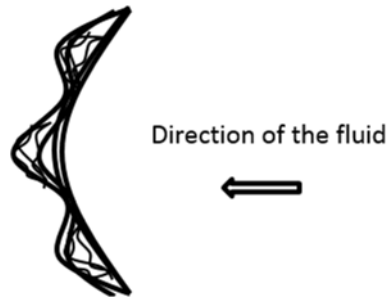


Figure 10-5: The bowing configuration in local dynamic porosity arrangement

For this arrangement, the coalescence efficiency test (Section 5.5.3) was performed to see whether the high efficiency associated with the bowing configuration (control dynamic porosity) - see Section 7.4.3.2 - is maintained while the structure is reinforced.

10.3 Results

Table 10-1 summarises the influence of the different reinforcement arrangements on the coalescence efficiency, ε - Equation 5-4, using the REF diesel fuel.

Table 10-1: Effect of different filter arrangements on the average coalescence efficiency

Sample arrangement	ε (%)
Control dynamic porosity	65.8
Dynamic porosity with back support	65.9
Local dynamic porosity	67.1

The same coalescence behaviour was observed amongst the three configurations and it was established that the new configurations maintain the coalescence performance of the dynamic porosity configuration while their structures are reinforced. These promising results was

considered as initiative of further investigations towards commercialisation of the bowing configuration. The results were reported to the industrial sponsor of the project to proceed with more experiments in their site.

References

1. Asmus, A.F. and B.F. Wellington, *Diesel engines and fuel systems*. 1995.
2. Gilles, T., *Automotive Engines: Diagnosis, Repair, Rebuilding*. 2014: Cengage Learning.
3. EPA, u.s.e.p.a., *Federal register (Tier 4)*. Federal register, 2004. **69**(124).
4. commission, E., *Emissions from heavy duty vehicles (Euro VI)* Official Journal of the European Union, 2011. **54**.
5. commission, E., *Emissions from light passenger and commercial vehicles (Euro 6)* Official Journal of the European Union, 2016. **59**.
6. (ATSDR), A.f.T.S.a.D.R., *Toxicological profile for fuel oils*. 1995, U.S. Department of Health and Human Services, Public Health Service.: Atlanta, GA.
7. Kumara, R.S. and P. Rajkumarb, *Characterization of minerals in air dust particles in the state of tamilnadu*.
8. Lif, A. and K. Holmberg, *Water-in-diesel emulsions and related systems*. Advances in colloid and interface science, 2006. **123**: p. 231-239.
9. Lin, C.-Y. and S.-A. Lin, *Effects of emulsification variables on fuel properties of two- and three-phase biodiesel emulsions*. Fuel, 2007. **86**(1): p. 210-217.
10. Johnson, T.V., *Review of Diesel Emissions and Control*. 2010.
11. Petiteaux, M. and G. Monsallier, *Impacts of Biodiesel Blends on Fuel Filters Functions, Laboratory and Field Tests Results*. 2009, SAE Technical Paper.
12. Pangestu, F.D. and C.M. Stanfel, *Media for Water Separation from Biodiesel-Ultra Low Sulfur Diesel Blends*. SAE International Journal of Fuels and Lubricants, 2009. **2**(1): p. 305-316.
13. Stone, W., G. Bessee, and C. Stanfel, *Diesel Fuel/Water Separation Test Methods—Where We Are and Where We Are Going*. SAE International Journal of Fuels and Lubricants, 2009. **2**(1): p. 317-323.
14. (BSI), B.S.I., *BS EN 590:2013- Automotive fuels - Diesel - Requirements and test methods*. 2013, British Standards Institution (BSI).

15. Shields, C. *Chemical and Thermal Stability of Nonwoven Filtration Media In Fluid Power Applications NCFP I05-19.2*. in *Proceedings of the national conference on fluid power*. 2005.
16. Shields, C. *Design and Performance of Diesel Fuel Filters*. 2005.
17. Shields, C., *High efficiency fuel filter*. 2006, Google Patents.
18. Association, A.W.W., *Internal Corrosion of Water Distribution Systems, 2 Edition*. 1996: American Water Works Association.
19. EPA, u.s.e.p.a. *Air Emissions*. 2014 [cited 2014 5/22/2014].
20. Tang, T.-W., Y.-Y. Ku, and C.L. Chen, *Impacts of Biodiesel Blends on Fuel Filters of High Pressure Common Rail (HPCR) System*. 2016, SAE Technical Paper.
21. Stone, W., G. Bessee, and C. Stanfel, *Diesel Fuel/Water Separation Test Methods—Where We Are and Where We Are Going*. SAE International Journal of Fuels and Lubricants, 2009. **2**(2009-01-0875): p. 317-323.
22. Knothe, G., *Biodiesel and renewable diesel: a comparison*. Progress in Energy and Combustion Science, 2010. **36**(3): p. 364-373.
23. Timilsina, G.R. and A. Shrestha, *How much hope should we have for biofuels?* Energy, 2011. **36**(4): p. 2055-2069.
24. Aatola, H., Larmi, M., *Hydrotreated vegetable oil (HVO) as a renewable diesel fuel: trade-off between NOx, particulate emission, and fuel consumption of a heavy duty engine*. SAE paper, 2008(2008-01): p. 2500.
25. Atadashi, I., M. Aroua, and A.A. Aziz, *Biodiesel separation and purification: a review*. Renewable Energy, 2011. **36**(2): p. 437-443.
26. Atabani, A.E., Silitonga, A.S., *A comprehensive review on biodiesel as an alternative energy resource and its characteristics*. Renewable and sustainable energy reviews, 2012. **16**(4): p. 2070-2093.
27. Basha, S.A., K.R. Gopal, and S. Jebaraj, *A review on biodiesel production, combustion, emissions and performance*. Renewable and Sustainable Energy Reviews, 2009. **13**(6): p. 1628-1634.
28. Yoshino, F.J., G.A. Marques, and F. Ferrari, *Water Separation Challenge for Brazilian Diesel Engine*. 2013, SAE Technical Paper.
29. Yoshino, F.J., Moreira, F., *Double stage pre-filter diesel water separator*. Blucher Engineering Proceedings, 2015. **2**(1): p. 199-207.
30. Stanfel, C. and F. Cousart, *Coalescence media for separation of water-hydrocarbon emulsions*. 2008, US Patents 2009/0178970.
31. Chase, G. and P. Kulkarni, *Mixed hydrophilic/hydrophobic fiber media for liquid-liquid coalescence*. 2010, US Patents 2010/0200512.
32. Bansal, S., Von Arnim, V., *Effect of fibrous filter properties on the oil-in-water-emulsion separation and filtration performance*. Journal of hazardous materials, 2011. **190**(1): p. 45-50.

33. Moses, S. and K. Ng, *A visual study of the breakdown of emulsions in porous coalescers*. Chemical engineering science, 1985. **40**(12): p. 2339-2350.
34. Wadsworth, L.C. and I.M. Hutten, *Handbook of Nonwoven Filter Media*. 2007: Access Online via Elsevier.
35. Uppal, R., Bhat, G., *Meltblown nanofiber media for enhanced quality factor*. Fibers and Polymers, 2013. **14**(4): p. 660.
36. Lalagiri, M., Bhat, G., *Filtration Efficiency of Submicrometer Filters*. Industrial & Engineering Chemistry Research, 2013. **52**(46): p. 16513-16518.
37. Hassan, M.A., Yeom, B.Y., *Fabrication of nanofiber meltblown membranes and their filtration properties*. Journal of Membrane Science, 2013. **427**: p. 336-344.
38. Kaur, S., Gopal, R., *Next-generation fibrous media for water treatment*. MRS bulletin, 2008. **33**(01): p. 21-26.
39. Stanfel, C. and F. Cousart, *Coalescence media for separation of water-hydrocarbon emulsions*. 2009, Google Patents.
40. Stanfel, C. and F. Cousart, *Coalescence media for separation of water-hydrocarbon emulsions*. 2011, Google Patents.
41. Stanfel, C.M. and F.D. Pangestu, *Separation media and methods especially useful for separating water-hydrocarbon emulsions having low interfacial tensions*. 2012, Google Patents.
42. Stanfel, C.M. and F.D. Pangestu, *Separation modules including media for separating water-hydrocarbon emulsions having low interfacial tensions*. 2013, Google Patents.
43. Wieczorek, M.T., B.M. Verdegan, and S. Dawar, *Multi-layer coalescing media having a high porosity interior layer and uses thereof*. 2013, Google Patents.
44. Wieczorek, M., Shults, T., *Two stage fuel water separator and particulate filter utilizing pleated nanofiber filter material*. 2013, Google Patents.
45. Russell, S.J., *Handbook of nonwovens*. 2007: CRC Press Boca Raton, FL.
46. Koslow, E.E., J.D. Miller, and K.M. Williamson, *Coalescing filter for removal of liquid aerosols from gaseous streams*. 1988, Google Patents.
47. Brown, R. and T. Wines, *Improve suspended water removal from fuels*. Hydrocarbon Processing, 1993. **72**: p. 95-95.
48. (ISO), I.O.f.S., *ISO/TS 16332:2006: Diesel engines -- Fuel filters -- Method for evaluating fuel/water separation efficiency*. 2006.
49. Moorthy, K., *Effect of surface energy of fibers on coalescence filtration*. 2007, University of Akron.
50. Schütz, S., Winkler, D., *Water/Diesel Separation. Part 2: Impact of Fuel Additives on the Physical Properties of Water/Diesel Emulsions*.
51. Fahim, M.A., T.A. Al-Sahhaf, and A. Elkilani, *Fundamentals of petroleum refining*. 2009: Elsevier.

52. Collins, C.D., *Implementing phytoremediation of petroleum hydrocarbons*, in *Phytoremediation*. 2007, Springer. p. 99-108.
53. Eucar, C. and J.R.C.o.t.E. Commission, *Well-To-Wheels Analysis Of Future Automotive Fuels And Powertrains In The European Context-WELL-to-WHEELS Report Version 2c*. Joint Research Centre of the EU Commission, 2007.
54. Golovitchev, V. and J. Yang. *The Construction of Combustion Models for RME Biodiesel fuel for ICE Application*. in *ICBT-2008*. 2008.
55. Panis, L.I., Rabl, A. Diesel or petrol? *An environmental comparison hampered by uncertainty*. in *Proceedings of 11th International Symp. Transport and Air Pollution. Mitteilungen Institut fur Verbrennungskraftmaschinen und Thermodynamik*. Ed. P. Sturm, Technische Universitat Graz, Austria. 2002.
56. Tiddy, G.J., *Surfactant-water liquid crystal phases*. *Physics reports*, 1980. **57**(1): p. 1-46.
57. Cousart, F. and C. Stanfel, *Coalescence media for separation of water-hydrocarbon emulsions*. 2009, Google Patents.
58. Liao, Y. and D. Lucas, *A literature review on mechanisms and models for the coalescence process of fluid particles*. *Chemical Engineering Science*, 2010. **65**(10): p. 2851-2864.
59. Walstra, P., *Principles of emulsion formation*. *Chemical Engineering Science*, 1993. **48**(2): p. 333-349.
60. Patel, S.U. and G.G. Chase, *Separation of water droplets from water-in-diesel dispersion using superhydrophobic polypropylene fibrous membranes*. *Separation and Purification Technology*, 2014. **126**(0): p. 62-68.
61. He, Y., Howes, T., *Experimental study of drop-interface coalescence in the presence of polymer stabilisers*. *Colloids and Surfaces A: Physicochemical and Engineering Aspects*, 2002. **207**(1-3): p. 89-104.
62. Somasundaran, P., *Encyclopedia of Surface and Colloid Science*. 2006: Taylor & Francis.
63. Pan, N. and P. Gibson, *Thermal and moisture transport in fibrous materials*. 2006: CRC Press.
64. Hansen, F.K., *The measurement of surface energy of polymers by means of contact angles of liquids on solid surfaces*. A short overview of frequently used methods. University of Oslo, Oslo, 2004.
65. Rama, D.D., *Fluid Mechanics And Machinery*. 2007: New Age International (P) Limited.
66. Ramesh, K.S. and P. Dusan, *Fundamentals of heat exchanger design*. John Wiley & Sons. 2003.
67. Kocherginsky, N.M., C.L. Tan, and W.F. Lu, *Demulsification of water-in-oil emulsions via filtration through a hydrophilic polymer membrane*. *Journal of Membrane Science*, 2003. **220**(1-2): p. 117-128.

68. Christov, N.C., Ganchev, D. N., *Capillary mechanisms in membrane emulsification: oil-in-water emulsions stabilized by Tween 20 and milk proteins*. Colloids and Surfaces A: Physicochemical and Engineering Aspects, 2002. **209**(1): p. 83-104.
69. Lehr, F., M. Millies, and D. Mewes, *Bubble-Size distributions and flow fields in bubble columns*. AIChE Journal, 2002. **48**(11): p. 2426-2443.
70. Hsü, K.J., *Physics of Sedimentology: Textbook and Reference*. 2013: Springer Berlin Heidelberg.
71. Daniel, S., M.K. Chaudhury, and J.C. Chen, *Fast drop movements resulting from the phase change on a gradient surface*. Science, 2001. **291**(5504): p. 633-636.
72. Fregolente, P.B.L., L.V. Fregolente, and M.R. Wolf Maciel, *Water content in biodiesel, diesel, and biodiesel–diesel blends*. Journal of Chemical & Engineering Data, 2012. **57**(6): p. 1817-1821.
73. He, B., Thompson, J.C., *Moisture absorption in biodiesel and its petro-diesel blends*. Applied engineering in agriculture, 2007. **23**(1): p. 71-76.
74. Shin, C. and G. Chase, *Water-in-oil coalescence in micro-nanofiber composite filters*. AIChE journal, 2004. **50**(2): p. 343-350.
75. Sutherland, K.S. and G. Chase, *Filters and Filtration Handbook*. 2011: Elsevier Science.
76. Butler, I., *The nonwoven fabrics handbook*. 1999: INDA, Association of the Nonwoven Fabrics Industry.
77. Purchas, D. and K. Sutherland, *Handbook of filter media*. 2002: Elsevier.
78. Kulkarni, C.V., Wachter, W., *Monoolein: a magic lipid?* Physical Chemistry Chemical Physics, 2011. **13**(8): p. 3004-3021.
79. Ramskill, E.A. and W.L. Anderson, *The inertial mechanism in the mechanical filtration of aerosols*. Journal of Colloid Science, 1951. **6**(5): p. 416-428.
80. Davies, C.N., *Air filtration*. 1973.
81. Spurny, K.R., *Aerosol Filtration Science at the end of the 20th Century*. Chapter, 1997. **2**: p. 13-234.
82. Goldsmith, S., *High Efficiency Air Filter Media-Synthetic and Glass Media*. INDA-Filtration 2004, 2004.
83. Stanfel, C., *Fuel filtration: Protecting the diesel engine*. Filtration & Separation, 2009. **46**(3): p. 22-25.
84. A, D.J., *Glass fiber filter tubes*. 1966, Google Patents.
85. Ayers, W.R., *Water removing filter media*. 1986, Google Patents.
86. Alptekin, E. and M. Canakci, *Determination of the density and the viscosities of biodiesel–diesel fuel blends*. Renewable Energy, 2008. **33**(12): p. 2623-2630.
87. Bari, S., T.H. Lim, and C.W. Yu, *Effects of preheating of crude palm oil (CPO) on injection system, performance and emission of a diesel engine*. Renewable Energy, 2002. **27**(3): p. 339-351.

88. Ricco, M. and S.M. Borrione, *Device for controlling the flow of a high-pressure pump in a common-rail fuel injection system of an internal combustion engine*. 2003, Google Patents.
89. Karabektas, M., G. Ergen, and M. Hosoz, *The effects of preheated cottonseed oil methyl ester on the performance and exhaust emissions of a diesel engine*. Applied Thermal Engineering, 2008. **28**(17–18): p. 2136-2143.
90. Sutherland, K., *Filtration overview: A closer look at depth filtration*. Filtration & Separation, 2008. **45**(8): p. 25-28.
91. Schick, M.J., *Surface Characteristics of Fibers and Textiles*. Vol. 7. 1977: CRC Press.
92. Basu, S., *A Study on Effect of Wetting on Mechanism of Coalescence in a Model Coalescer*. Journal of Colloid and Interface Science, 1993. **159**(1): p. 68-76.
93. Miljkovic, N., Enright, R., *Jumping-droplet-enhanced condensation on scalable superhydrophobic nanostructured surfaces*. Nano letters, 2012. **13**(1): p. 179-187.
94. Hodgson, K.T. and J.C. Berg, *The effect of surfactants on wicking flow in fiber networks*. Journal of Colloid and Interface Science, 1988. **121**(1): p. 22-31.
95. Fries, N. and M. Dreyer, *An analytic solution of capillary rise restrained by gravity*. Journal of colloid and interface science, 2008. **320**(1): p. 259-263.
96. Kulkarni, P.S., S.U. Patel, and G.G. Chase, *Layered hydrophilic/hydrophobic fiber media for water-in-oil coalescence*. Separation and Purification Technology, 2012. **85**: p. 157-164.
97. Patel, S.U., Kulkarni, P., *Glass fiber coalescing filter media augmented with polymeric submicron fibers and modified with angled drainage channels*. Separation and Purification Technology, 2013. **120**: p. 230-238.
98. Wang, Z., C.W. Macosko, and F.S. Bates, *Tuning Surface Properties of Poly (butylene terephthalate) Melt Blown Fibers by Alkaline Hydrolysis and Fluorination*. ACS applied materials & interfaces, 2014. **6**(14): p. 11640-11648.
99. Beard, K.V. and H.T. Ochs, *Collection and coalescence efficiencies for accretion*. Journal of Geophysical Research: Atmospheres (1984–2012), 1984. **89**(D5): p. 7165-7169.
100. Pinsky, M., A. Khain, and M. Shapiro, *Collision efficiency of drops in a wide range of Reynolds numbers: Effects of pressure on spectrum evolution*. Journal of the atmospheric sciences, 2001. **58**(7): p. 742-764.
101. (ISO), I.O.f.S., *BS ISO 4020:2001- Road vehicles. Fuel filters for diesel engines. Test methods*. 2001.
102. International, S., *J1488-201010: Emulsified Water/Fuel Separation Test Procedure*. 2010.
103. Murgia, S., F. Caboi, and M. Monduzzi, *Addition of hydrophilic and lipophilic compounds of biological relevance to the monoolein/water system II—13 C NMR relaxation study*. Chemistry and physics of lipids, 2001. **110**(1): p. 11-17.
104. International, S., *Coarse Droplet Water/Fuel Separation Test Procedure*. 2010.

105. Tat, M.E. and J.H. Van Gerpen, *The kinematic viscosity of biodiesel and its blends with diesel fuel*. Journal of the American Oil Chemists Society, 1999. **76**(12): p. 1511-1513.
106. Yuan, W., Hansen, A., *Temperature-dependent kinematic viscosity of selected biodiesel fuels and blends with diesel fuel*. Journal of the American Oil Chemists' Society, 2005. **82**(3): p. 195-199.
107. Viswanadam, G. and G.G. Chase, *Water–diesel secondary dispersion separation using superhydrophobic tubes of nanofibers*. Separation and Purification Technology, 2013. **104**: p. 81-88.
108. Patel, S.U. and G.G. Chase, *Gravity orientation and woven drainage structures in coalescing filters*. Separation and Purification Technology, 2010. **75**(3): p. 392-401.
109. Patel, S.U., Kulkarni, P., *The effect of surface energy of woven drainage channels in coalescing filters*. Separation and Purification Technology, 2012. **87**(0): p. 54-61.
110. Yang, X., H. Wang, and G.G. Chase, *Performance of hydrophilic glass fiber media to separate dispersed water drops from ultra low sulfur diesel supplemented by vibrations*. Separation and Purification Technology, 2015. **156**: p. 665-672.
111. Yang, X., Zhang, X., *Vibration assisted water-diesel separation by electrospun PVDF-HFP fiber mats*. Separation and Purification Technology, 2016. **171**: p. 280-288.
112. Agarwal, S., Von Arnim, V., *Role of surface wettability and roughness in emulsion separation*. Separation and Purification Technology, 2013. **107**: p. 19-25.
113. Agarwal, S., Von Arnim, V., *Effect of Fibrous Coalescer Geometry and Operating Conditions on Emulsion Separation*. Industrial & Engineering Chemistry Research, 2013. **52**(36): p. 13164-13170.
114. Patel, S.U., S.U. Patel, and G.G. Chase, *Electrospun Superhydrophobic Poly (vinylidene fluoride-co-hexafluoropropylene) Fibrous Membranes for the Separation of Dispersed Water from Ultralow Sulfur Diesel*. Energy & Fuels, 2013. **27**(5): p. 2458-2464.
115. Kulkarni, P.S., Patel, S., *Coalescence filtration performance of blended microglass and electrospun polypropylene fiber filter media*. Separation and Purification Technology, 2014. **124**(0): p. 1-8.
116. Krasinski, A. and P. Wierzba, *Removal of Emulsified Water from Diesel Fuel Using Polypropylene Fibrous Media Modified by Ionization during Meltblow Process*. Separation Science and Technology, 2015. **50**(10): p. 1541-1547.
117. Rajgarhia, S.S., S.C. Jana, and G.G. Chase, *Separation of Water from Ultralow Sulfur Diesel Using Novel Polymer Nanofiber-Coated Glass Fiber Media*. ACS Applied Materials & Interfaces, 2016. **8**(33): p. 21683-21690.
118. Manzo, G.M., Wu, Y., *Comparison of nonwoven glass and stainless steel microfiber media in aerosol coalescence filtration*. Separation and Purification Technology, 2016. **162**: p. 14-19.
119. Shin, C., G. Chase, and D. Reneker, *The effect of nanofibers on liquid–liquid coalescence filter performance*. AIChE journal, 2005. **51**(12): p. 3109-3113.

120. Shin, C., *Filtration application from recycled expanded polystyrene*. Journal of Colloid and Interface Science, 2006. **302**(1): p. 267-271.
121. Hajra, M., K. Mehta, and G. Chase, *Effects of humidity, temperature, and nanofibers on drop coalescence in glass fiber media*. Separation and purification technology, 2003. **30**(1): p. 79-88.
122. Shields, C., *Micro/Nanofiber Media for Biopharmaceutical Filtration*. Vortrag FILTECH, Page II-428, 2005.
123. Chase, G.G., *Improved microfiber filter performance by augmentation with nanofibers*. 2007, SAE Technical Paper.
124. Wang, J., Ponting, M., *Processing-structure-property relationships of novel fibrous filters produced by a melt-process*. Journal of materials science, 2016. **51**(1): p. 188-203.
125. Wang, J., Ponting, M., *Manufacturing of polymer continuous nanofibers using a novel co-extrusion and multiplication technique*. Polymer, 2014. **55**(2): p. 673-685.
126. Wang, J., Ponting, M., *Fuel filtration properties and mechanism of a novel fibrous filter produced by a melt-process*. Journal of Membrane Science, 2017. **526**: p. 229-241.
127. Hartland, S., *Surface and interfacial tension: measurement, theory, and applications*. 2004: CRC Press.
128. Lee, D. and E. Scholz, *Karl Fischer Titration: Determination of Water*. 2012: Springer Berlin Heidelberg.
129. MacLeod, S.K., *Moisture determination using Karl Fischer titrations*. Anal. Chem, 1991. **63**(10): p. 557-566.
130. (ISO), I.O.f.S., *Methods of test for petroleum and its products. BS 2000-189/190. Crude petroleum and liquid or solid petroleum products. Determination of density or relative density. Capillary-stoppered pycnometer and graduated bicapillary pycnometer methods*. 2004, BSI.
131. (ISO), I.O.f.S., *ISO 3105:1994: Petroleum products. Transparent and opaque liquids. Determination of kinematic viscosity and calculation of dynamic viscosity*. 1994.
132. (ISO), I.O.f.S., *BS EN ISO 3104:1996: Methods of test for petroleum and its products. Petroleum products. Transparent and opaque liquids. Determination of kinematic viscosity and calculation of dynamic viscosity*. 1996.
133. Lopes, S.M. and T. Cushing, *The Influence of Biodiesel Fuel Quality on Modern Diesel Vehicle Performance*. 2012, SAE Technical Paper.
134. Standardization, t.I.O.f., *ISO 13320:2009 - Particle size analysis - Laser diffraction methods*. 2009.
135. DAGORN-SCAVINER, C., J. Gueguen, and J. Lefebvre, *Emulsifying properties of pea globulins as related to their adsorption behaviors*. Journal of Food Science, 1987. **52**(2): p. 335-341.
136. Standardization, t.I.O.f., *ISO 13320:2009 - Particle size analysis - Laser diffraction methods*. 2009.

137. (BSI), B.S.I., *BS EN 29073-1:1992, ISO 9073-1:1989 - Methods of test for nonwovens. Methods of test for nonwovens. Determination of mass per unit area.* 1992, British Standards Institution (BSI).
138. (BSI), B.S.I., *BS EN ISO 9073-2:1997 - Textiles -Test methods for nonwovens -Part 2: Determination of thickness.* 1997, British Standard.
139. (ISO), I.O.f.S., *BS EN ISO 9237:1995: Textiles. Determination of the permeability of fabrics to air.* 1995.
140. Smith, B.C., *Infrared spectral interpretation: a systematic approach.* 1998: CRC press.
141. Smith, B.C., *Fourier transform infrared spectroscopy.* CRC, Boca Raton, FL, 1996.
142. A C. Tracey, B.D.F. *Infrared spectroscopy: A potential quality assurance method for composite bonding surface preparation.* 2012.
143. Smith, B.C., *Fundamentals of Fourier Transform Infrared Spectroscopy.* 1995: Taylor & Francis.
144. Thermo, N., *Introduction to fourier transform infrared spectrometry.* Thermo Nicolet Corporation, 2001.
145. Höhne, G., W. Hemminger, and H.-J. Flammersheim, *Theoretical fundamentals of differential scanning calorimeters,* in *Differential scanning calorimetry.* 2003, Springer. p. 31-63.
146. Höhne, G., W. Hemminger, and H.J. Flammersheim, *Differential Scanning Calorimetry.* 2003: Springer.
147. Amelinckx, S., Van Dyck, D., *Electron microscopy: principles and fundamentals.* 2008: John Wiley & Sons.
148. Andanson, J.M. and S.G. Kazarian. *In situ ATR-FTIR Spectroscopy of Poly (ethylene terephthalate) Subjected to High-Temperature Methanol.* in *Macromolecular symposia.* 2008. Wiley Online Library.
149. ANA, P.M. and S. Catherine, *Report of an interlaboratory comparison from the European Reference Laboratory for Food Contact: ILC002 2013-Identification of polymeric materials.* 2013.
150. Holland, B.J. and J.N. Hay, *The thermal degradation of PET and analogous polyesters measured by thermal analysis–Fourier transform infrared spectroscopy.* *Polymer,* 2002. **43**(6): p. 1835-1847.
151. Greaves, P. and B. Saville, *Microscopy of textile fibres.* 1995: BIOS Scientific.
152. Mather, R.R. and R.H. Wardman, *Chemistry of Textile Fibres.* 2011: Royal Society of Chemistry.
153. Pastore, C. and P. Kiekens, *Surface characteristics of fibers and textiles.* 2000: CRC Press.
154. Zambianchi, L., P. Bonaguidi, and G. Mari, *Filter for the removal of substances from blood products.* 2010, Google Patents.

155. Wei, X., Zhao, B., *CF 4 plasma surface modification of asymmetric hydrophilic polyethersulfone membranes for direct contact membrane distillation*. Journal of membrane science, 2012. **407**: p. 164-175.
156. Fernández-Blázquez, J.P., Fell, D., *Superhydrophilic and superhydrophobic nanostructured surfaces via plasma treatment*. Journal of colloid and interface science, 2011. **357**(1): p. 234-238.
157. Kim, E.J., Yeo, G, *Preparation of surface-modified poly (butylene terephthalate) nonwovens and their application as leukocyte removal filters*. Journal of Biomedical Materials Research Part B: Applied Biomaterials, 2009. **90**(2): p. 849-856.